University of Southampton

Faculty of Natural Sciences

Theory and practice of singlet nuclear magnetic resonance

by

Michael Charles Douglas Tayler

M.A. M.Sci. Hons. (Cantab.)

A dissertation submitted in partial satisfaction

of the requirements for the degree of

Doctor of Philosophy

September, 2012 A.D.

Committee in charge:

Prof. Malcolm H. Levitt, FRS (chair)

Prof. Geoffrey Bodenhausen (examiner)

Dr. Jörn Werner (co-examiner)

UNIVERSITY OF SOUTHAMPTON

ABSTRACT

FACULTY OF NATURAL SCIENCES
SCHOOL OF CHEMISTRY

Doctor of Philosophy

THEORY AND PRACTICE OF SINGLET NUCLEAR MAGNETIC RESONANCE

by Michael Charles Douglas Tayler

Sensitivity is a signature problem of NMR. In its most basic description, an NMR experiment involves encoding information into an ensemble of nuclear spins followed by readout at a later time. The sensitivity is the extent to which the information content is distinguishable from system noise.

Principal factors that determine sensitivity are ensemble initialisation or polarisation, detection efficiency and relaxation effects that occur in between. This thesis addresses the last of these by examining opportunities of nuclear singlet states. Singlet states are exchange-antisymmetric quantum states of spin-1/2 pairs that, under favourable conditions, are the slowest-relaxing spin states of the NMR ensemble. In certain cases, singlet states may also exceed the relaxation times of isolated spins-1/2.

The goal of the work is to explore 'singlet NMR' as concept. The fundamentals of coherent control in a spin-1/2 pair are studied in depth, from which pulse sequences to generate and take advantage of singlet states are discussed. Several new methods for singlet excitation and detection are introduced. Existing methods are discussed within an overview context. Basic principles of singlet relaxation are also presented. Singlet lifetimes depend strongly on the correlation between magnetic fields at the nuclear spin pair sites and are sensitive most to the local magnetic environment. This can be used to retrieve information on local molecular structure and motion. Study of the relaxation relax rates may also help one determine the dominant singlet relaxation mechanisms for a given spin pair environment. This information may help one design molecules for maximum longevity of nuclear spin order.

Contents

AUTHOR'S DECLARATION

Theory and practice of singlet nuclear magnetic resonance

by

Michael Charles Douglas Tayler

I declare that this thesis, and the work presented within are both my own, and have been generated by me as the result of my own original research. I confirm this work was done while wholly in candidature for a research degree at the University of Southampton.

Where I have consulted the published work of others, this is always clearly attributed. Where I have quoted from the work of others, the source is always given. With the exception of such quotations, this thesis is entirely my own work. Where the thesis is based on work done by myself jointly with others, a substantial part is my own original work and I have made clear exactly what was done by others.

Published parts of this work are detailed on the page opposite.

Signed _____ Date _____

LIST OF PAPERS

Material in this thesis is published or being prepared for publication in the following papers:

1. **Determination of torsional angles using nuclear singlet relaxation**
   M. C. D. Tayler, S. Marie, A. Ganesan and M. H. Levitt
   J. Am. Chem. Soc., vol. 132, 24, pp. 8225-8227, 2010.

2. **Singlet nuclear magnetic resonance of nearly equivalent spins**
   M. C. D. Tayler and M. H. Levitt
   Phys. Chem. Chem. Phys., 13, pp. 5556-5560, 2011.

3. **Paramagnetic relaxation of nuclear singlet states**
   M. C. D. Tayler and M. H. Levitt
   Phys. Chem. Chem. Phys., 13, pp. 9128-9130, 2011.

4. **Direct nuclear singlet hyperpolarisation via dissolution DNP**
   M. C. D. Tayler, I. M.-Rius, M. I. Kettunen, K. M. Brindle, M. H. Levitt and G. Pileio
   J. Am. Chem. Soc., vol. 134, 18, pp. 7668-7671, 2012.

5. **Hyperpolarised singlet NMR on a small-animal imaging scanner**
   C. Laustsen, G. Pileio, **M. C. D. Tayler**, L. J. Brown, R. C. D. Brown, M. H. Levitt and J.-H. Ardenkjær-Larsen
   Magn. Reson. in Med,, vol. 68, 4, pp. 1262-1265, 2012.

6. **Long-lived nuclear spin order accessed via isotope shifts**
   M. C. D. Tayler and M. H. Levitt
   Submitted to publisher, September 2012.

7. **Heteronucleus-induced symmetry-switching in singlet NMR**
   M. C. D. Tayler, G. Pileio and M. H. Levitt
   Submission in preparation.

ACKNOWLEDGEMENTS

The feeling after finally completing this thesis is one of enormous relief! It is also one of enormous thanks, towards the many people who have helped me achieve it.

I wish foremost thanks to Malcolm Levitt, my supervisor during this time, whose unique style, expertise, kindness and supreme level of support has made working in the group such a pleasure. I also could not have asked for a more stimulating research subject; I recall my interview in Southampton four years ago, where Malcolm assured that there was 'still a lot to work out' about singlet NMR. He was not wrong! I am grateful to all from Malcolm's lab, past and present, whom I have met. All have been very supportive, especially Marina Carravetta, Peppe Pileio, Maria Concistrè, Salvo Mamone and Jiří Bočan.

Outside the group I acknowledge the collaborators who share a part in this work. In chronological order: Ganesan and Sabrina Marie (Chemistry, Southampton), who synthesised deuterium-labelled amino acids; to Lynda and Richard Brown (Chemistry, Southampton), who produced us labelled carbon-13 compounds; Chris Laustsen (Aarhus) and Jan-Henrik Ardenkjær-Larsen (DTU Denmark and GE Healthcare) with whom plus an MRI scanner some basic studies of singlet hyperpolarisation were made; Kevin Brindle's group (Biochemistry, Cambridge Univ. and Cancer Research UK), in particular Irene Marco-Rius, for their enthusiasm in exploring the in vivo potential of our work; Neil Wells, for generously lending me his NMR spectrometer at weekends and Ole Johannessen (Southampton) for repairs to / advice on instrumentation and hardware, plus his general lab humour.

I also wish to thank James Keeler. It was by attending his lectures in undergraduate physical chemistry that I became interested in NMR. That led somehow to me working in his research group during my masters' year, and from there to Southampton. Thank you James for initially recommending me to Malcolm and your continued kind support since.

Another thank you to Irene, for looking after and taking good care of me, especially throughout the writing-up period and making sure that I finished on-time and in-health.

Final words are reserved for those who have looked after me not just in the recent years but throughout my whole life. While no amount of words can express my true thankfulness, a special thank you goes to my parents, Clive and Judith, for giving me unlimited support, encouragement and love. Without that, all the many wonderful things that have happened in my life probably would not have come about.

A short direction to avoid dejection
By variations in occupations
And prolongation of relaxation
And combinations of recreations
And disputation on the state of the nation

In adaptation to your station
By invitations to friends and relations
By evitation of amputation
By permutation in conversation
And deep reflection
You'll avoid dejection

Lewis Carroll, *Rules and Regulations*

1 Introduction

1.1 Memory

Rather like the human mind, many systems in nature keep only a limited memory of their history. In statistical physics, in the same way that one visualises the 'drunkard' forgetting his route during a random walk from the pub, macroscopic or *ensemble* properties can become 'forgotten' as their microscopic constituents lose synchrony with one another through time.[1] Such processes of information loss are irreversible; for instance, the disappearance of temperature or concentration gradients in a solution (the loss of positional order, due to Brownian translational diffusion), or the melting of a liquid crystal (loss of orientational order). Time-dependent changes in macroscopic nonequilibria such as these are called *ensemble relaxation* phenomena, for they return the bulk system to an equilibrium state.

Ensemble relaxation (or simply 'relaxation') is a major issue in nuclear magnetic resonance (NMR) techniques.[2, 3, 4, 5, 6] An NMR system comprises a macroscopic collection of atomic nuclei, the *spin ensemble*, whose microscopic property is the nuclear spin angular momentum. This angular momentum gives an incredible power to the scientist. If we think as physicists, we view the resulting bulk property, *nuclear magnetisation*, as a 'storage device' on which wealths of physical data may be recorded (see fig. 1.1). With NMR in the clinic, one may obtain images inside the human body more safely, more sensitively, and with greater detail than surgical or ionisation routes.[7] One can record maps showing blood velocity through the circulatory system with striking clarity. In the laboratory,

NMR spectroscopy is the premier tool for gathering information about molecular geometry, three-dimensional structure, functionality of biomolecules inside cells and microscopic motion. If we really think of NMR systems as a 'memory', we may indeed use them to execute algorithms and perform computation![8]

Relaxation is crucial aspect in almost all NMR experiments; it can act as both a help and as a hindrance. To encode information into the spin ensemble, creating a nonequilibrium state, it is usual to start from a known and consistent equilibrium. Rapid relaxation is in this context beneficial, in the sense that the spin memory is 'wiped clean' quickly so there are no long waiting periods before an experiment can start. This speeds up the more laborious 'multi-scan' NMR experiments where repeated readouts of the spin memory are combined to improve overall signal-to-noise, or shorten the time needed to collect higher-dimensional or arrayed datasets, for example in spin-spin correlation (COSY) experiments used for molecular structure elucidation.[4, 11] On the other hand, fast relaxation generally implies a shorter spin memory timescale during the experiment itself. In that case the complexity and maximum duration of encoding can be rather limited.

This view implies there is a trade-off to be made between sensitivity and time. However, it is not the spectroscopist who decides the speed of relaxation. Spin memory loss is governed by the microscopic motion processes that cause decoherence of the ensemble, principally molecular reorientation, exchange and collisions.[14] Most of these processes are inherent to the system under study, and not possible to change, in general, except by significantly altering the physical state or chemical composition. Furthermore, while relaxation may be artificially accelerated, for instance by doping the system with paramagnetic substances,[14] on which I will say more later, it is much more difficult to do the opposite to the ensemble, *i.e.* to 'remove' relaxation mechanisms that are intrinsic.

Having said this, opportunities to prolong the spin memory do exist in some circumstances. A familiar example to those in the NMR field is how spin relaxation rates depend on the relative orientation between nuclear magnetisation and its external magnetic environment. For magnetisation of isolated spins, the component parallel to an uniform external field (called *longitudinal* magnetisation) relaxes with a time constant we call T_1. Magnetisation perpendicular to the applied field (called *transverse* magnetisation) often decays with a faster time constant $T_2 \leq T_1$.[3, 4] The relation $T_2 \leq T_1$ implies spin memory may be preserved for longer times by confinement in the guise of longitudinal magnetisa-

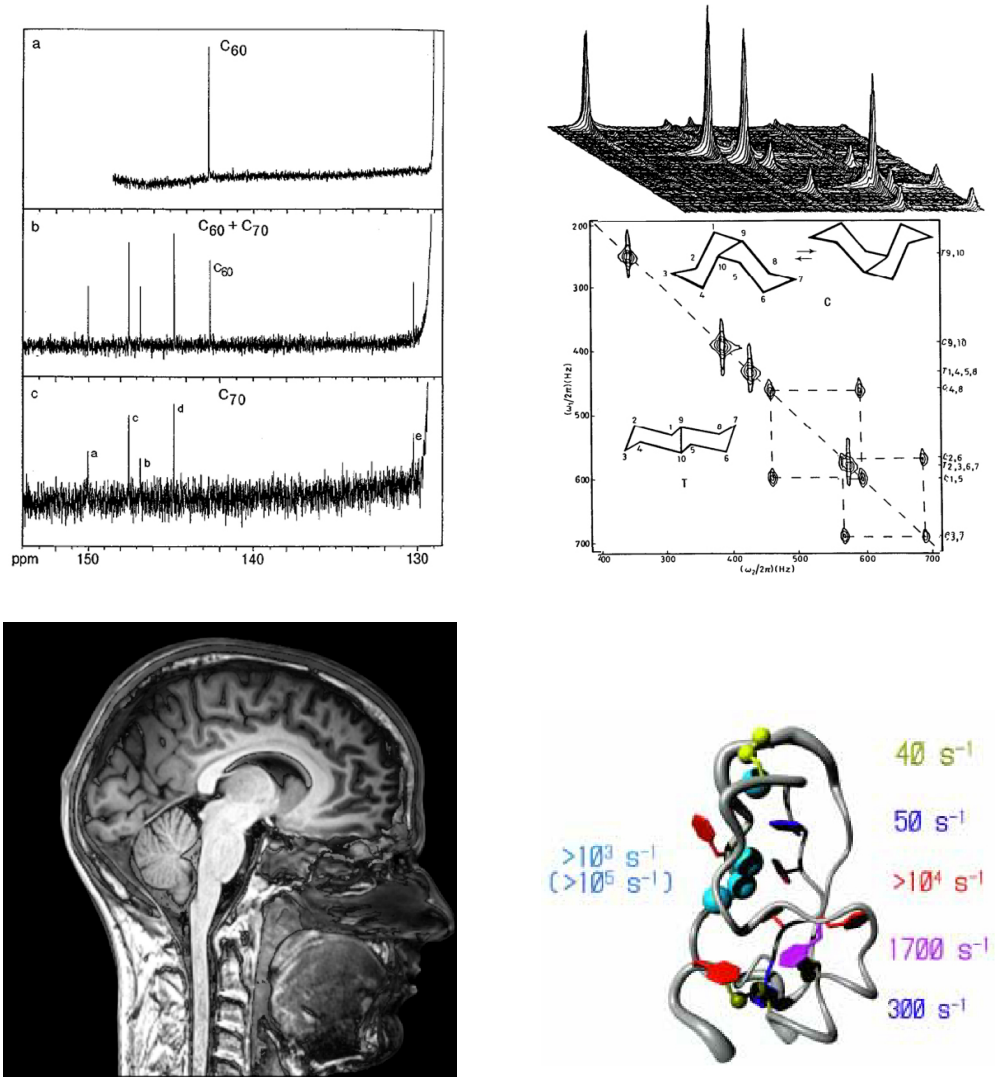

Figure 1.1: Information provided by nuclear magnetic resonance, from the simple to the intricate. Clockwise from top-left: Compelling proof for the fullerene structures of C_{60} and C_{70} obtained by ^{13}C NMR spectroscopy;[9, 10] Ernst's Fourier-transform spectroscopy,[11] an instrumental advance in sensitivity, which also opened up the field of multidimensional spectroscopy. The off-diagonal peaks in the above spectrum give information on the chemical exchange between cis- and trans-decalin isomers; NMR determination of intramolecular rate processes and mechanism of action in the basic pancreatic trypsin inhibitor protein (BPTI, MW $\approx$ 6500 g/mol). Structural studies by NMR are now viable and routine on proteins in excess of MW $= 10^5$ g/mol;[12] noninvasive single-scan 'echo-planar' imaging of water or fat content in living matter.[13]

tion, where possible. This is now common practice in NMR experiments where long waiting periods between initial memory encoding and readout are required, where a delay may be required for self-diffusion, bulk flow, or a chemical reaction to occur. The earliest example of this was Hahn's *stimulated echo* sequence, developed as far back as the 1950s.[15]

Longer-lived states

The work in this thesis pursues how memory times longer than T_1 are possible by exploiting *singlet states* between pairs of nuclei. The singlet is a 'non-magnetic' or 'spin-zero' configuration shared between two nuclei with individual angular momenta $\pm\hbar/2$. These states may exhibit, in certain circumstances, lifetimes exceeding T_1 by an order of magnitude.[16, 17] The correlation between the angular momenta of the pair allows the composite state to escape many relaxation mechanisms, so that it decays more slowly than each nucleus in isolation.

As just two spin-1/2 nuclei are required, singlet states are common to find in a wide variety of molecules, from small polyatomics to proteins. The first experimental demonstration of long-lived singlet states in a polyatomic molecule was made in 2004 by Carravetta and Levitt for the pair of protons in 2,3-dibromothiophene.[18, 19] To brief summarise the development of the field since, (to mid 2012), there have been over 100 peer-reviewed publications on singlet NMR, concerning in roughly equal proportion methodology for exciting singlet states, theory and rationale of the relaxation properties and applied technology. Several reviews are available.[16, 17, 20, 21] Some achievements speak for themselves:

- The world record singlet lifetime of a polyatomic molecule is 26 minutes, for $^{15}N_2O$ (^{15}N-nitrous oxide).[22, 23] The ^{15}N T_1 in the same system is less than 3 minutes.

- The largest extension in spin lifetime via singlet states is 37 times T_1, as has been observed for a proton pair in a partially deuterated saccharide molecule.[24, 25]

- Proton singlet lifetimes have been measured for Ubiquitin,[26, 27] the most-commonly studied protein.

- Singlet NMR opens the study of self-diffusion of large molecules to timescales an order of magnitude slower than those conventionally probed by NMR.[25, 28, 29]

- Several experimental demonstrations made for preserving hyperpolarised (very strongly magnetised) samples for potential use *in vivo*.[30, 31, 32]

Thesis outline and structure

The remainder of this chapter introduces singlet NMR more formally to the reader within the context of its main challenge: to overcome, without change to the system's composition or bulk conditions, the frustrations of low signal strength in NMR caused by undesirably short relaxation times. One may regard 'singlet NMR' as achieving for NMR what we might wish for an improved memory performance of our brains and computers: to keep track of information over longer periods of time, accomplish goals more efficiently and solve more challenging problems.

My chosen starting point is the perspective of the NMR ensemble as an information storage device, where I summarise (in brief) the important quantum mechanical formalisms used to understand NMR spectroscopy, namely the *state space* concept, the *density operator* and how nuclear spin order is manipulated during an experiment. This is followed by a discussion about sensitivity in NMR, its enhancement using singlet states and the interface of singlet NMR with other existing or competing practices. An idea of the current state of singlet NMR will be outlined through a summary of existing work done by others.

After this introductory chapter the thesis contains two technical chapters in which new material is presented. The first of these (chapter 2) is a roundup of methodology to excite the potentially long-lived nuclear singlet states, dealing with how to convert between 'ordinary' nuclear magnetisation and singlet spin order, and vice versa. As well as discussing new methods, I will indicate where improvements are available to existing ones. The second chapter (chapter 3) is focused on understanding the factors that contribute to long singlet lifetimes. At present, the mechanisms of singlet relaxation are not well understood and there is limited experimental data to analyse. Can one predict systems where singlet states will be longest-lived? May one establish how a given functional group may extend or reduce spin relaxation times? The findings are rounded off with a short chapter summarising the prospects of singlet NMR and suggesting the likely future direction of the topic.

1.2 What is spin memory?

In its most basic description, NMR exploits atomic nuclei that have spin angular momenta quantum number I greater than zero.[4] A spin with $I > 0$ has $(2I + 1) > 1$ distinct orientations, according to quantum mechanics, and as many distinct energy states.[33] These degrees of freedom provide a capacity for data storage. NMR relies on a practical ability to manipulate the statistical occupation of these states to encode and retrieve information.

1.2.1 The foundations: spin states

While some of earth's abundant isotopes, most notably ^{12}C and ^{16}O, have nonmagnetic or spin-zero nuclei, (*i.e.* with total angular momentum quantum number $I = 0$), most have finite spin. Isotopes ^{1}H, ^{13}C, ^{15}N, ^{19}F and ^{31}P are 'spin-half' ($I = 1/2$). Spin $I = 1/2$ nuclei have very simple structure. For a single isolated nucleus, quantisation defines two distinguishable angular momentum states $|l, m\rangle$,

$$|1/2, +1/2\rangle \equiv |\alpha\rangle \qquad \text{and} \qquad |1/2, -1/2\rangle \equiv |\beta\rangle\,, \tag{1.1}$$

where $l \equiv I$ and m denotes the angular momentum projection onto a global, space-fixed quantisation axis. Distinguishable in this context means the states are orthogonal. The nuclear wavefunction is free to inhabit any superposition of the states, provided that superposition is normalised. This vector space of $|\psi\rangle$ is known as a *Hilbert space*:

$$|\psi\rangle \;=\; c_\alpha\,|\alpha\rangle + c_\beta\,|\beta\rangle \;\Leftrightarrow\; \begin{pmatrix} c_\alpha \\ c_\beta \end{pmatrix} \qquad \text{with} \qquad |c_\alpha|^2 + |c_\beta|^2 = 1. \tag{1.2}$$

In more physical terms the complex number coefficients c_α and c_β give the orientation of a polarisation vector in three-dimensional space: $\boldsymbol{P} = (P_x, P_y, P_z)$. Components of $\boldsymbol{P}$ are the expectation values of the Pauli matrices,[34] given by

$$\sigma_x = \begin{pmatrix} 0 & 1 \\ 1 & 0 \end{pmatrix} \qquad \sigma_y = \begin{pmatrix} 0 & -\mathrm{i} \\ \mathrm{i} & 0 \end{pmatrix} \qquad \sigma_z = \begin{pmatrix} 1 & 0 \\ 0 & -1 \end{pmatrix}. \tag{1.3}$$

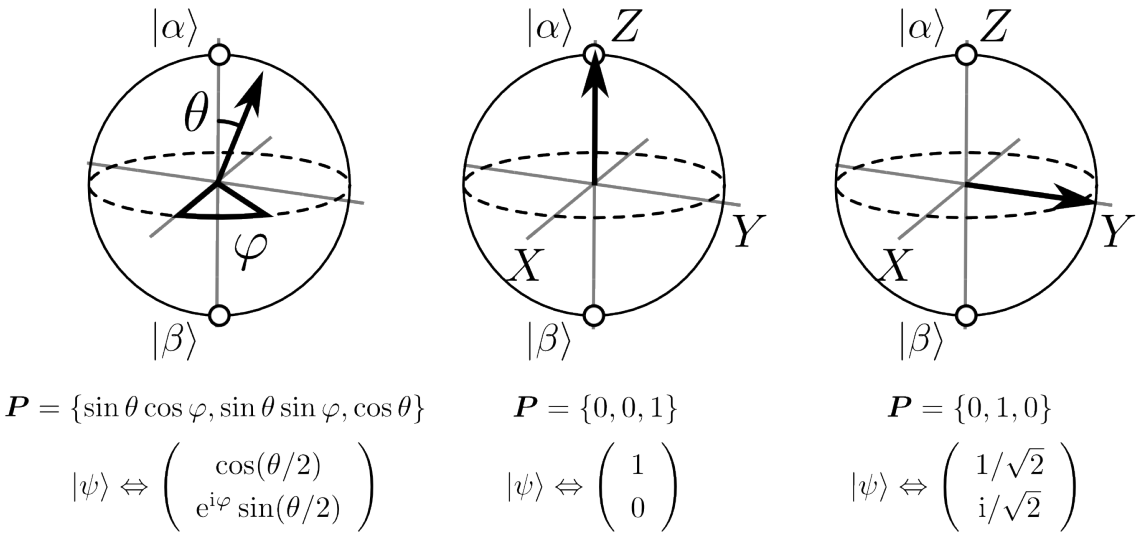

Figure 1.2: The 'Bloch sphere' gives a simultaneous geometric representation of wavefunction $|\psi\rangle$ and the polarisation vector $\boldsymbol{P}$.[35] To within a global phase factor, all normalised states lie on the sphere's surface, where the spin state is denoted by the arrow head.

The components of the polarisation vector are given by

$$P_i = \langle \sigma_i \rangle = \langle \psi | \sigma_i | \psi \rangle \,, \tag{1.4}$$

and range between -1 and 1. Proportional to $\boldsymbol{P}$ is the nuclear magnetic moment, denoted by

$$\boldsymbol{\mu} = (\mu_x, \mu_y, \mu_z) = \frac{1}{2}\gamma\hbar\boldsymbol{P}, \tag{1.5}$$

where the constant of proportionality, γ, is the gyromagnetic ratio of the isotope.[4]

This basic example highlights the first crux of NMR: how there exist quantised, orthogonal states of a *memory*, (a vector space), that are connected to a *physical observable* (the classical nuclear polarisation, or magnetic moment). For the spin-1/2 this correspondence is explicit if one writes $|\psi\rangle$ using the spherical coordinates of $\boldsymbol{P}$, *i.e.* $\boldsymbol{P} = (\sin\theta\cos\varphi, \sin\theta\sin\varphi, \cos\theta)$. This gives the so-called *Bloch sphere* projection between the wavefunction

$$|\psi\rangle = \cos(\theta/2)\,|\alpha\rangle + \mathrm{e}^{\mathrm{i}\varphi}\sin(\theta/2)\,|\beta\rangle \Leftrightarrow \begin{pmatrix} \cos(\theta/2) \\ \mathrm{e}^{\mathrm{i}\varphi}\sin(\theta/2) \end{pmatrix} \tag{1.6}$$

and $\boldsymbol{P}$ (see fig. 1.2). Applying Eq. (1.6) to eq. (1.4), it is clear that

$$P_x = \begin{pmatrix} \cos(\theta/2) & \mathrm{e}^{-\mathrm{i}\varphi}\sin(\theta/2) \end{pmatrix} \begin{pmatrix} 0 & 1 \\ 1 & 0 \end{pmatrix} \begin{pmatrix} \cos(\theta/2) \\ \mathrm{e}^{\mathrm{i}\varphi}\sin(\theta/2) \end{pmatrix} = \sin\theta\cos\varphi \tag{1.7a}$$

$$P_y = \begin{pmatrix} \cos(\theta/2) & \mathrm{e}^{-\mathrm{i}\varphi}\sin(\theta/2) \end{pmatrix} \begin{pmatrix} 0 & -\mathrm{i} \\ \mathrm{i} & 0 \end{pmatrix} \begin{pmatrix} \cos(\theta/2) \\ \mathrm{e}^{\mathrm{i}\varphi}\sin(\theta/2) \end{pmatrix} = \sin\theta\sin\varphi \tag{1.7b}$$

$$P_z = \begin{pmatrix} \cos(\theta/2) & \mathrm{e}^{-\mathrm{i}\varphi}\sin(\theta/2) \end{pmatrix} \begin{pmatrix} 1 & 0 \\ 0 & -1 \end{pmatrix} \begin{pmatrix} \cos(\theta/2) \\ \mathrm{e}^{\mathrm{i}\varphi}\sin(\theta/2) \end{pmatrix} = \cos\theta. \tag{1.7c}$$

In general a collection of N spins (such as the nuclei residing in a molecule), whose momenta are $I_1, I_2 \ldots I_N$, span $(2I_1+1)(2I_2+1)\ldots(2I_N+1)$ orthogonal states:

$$|\psi\rangle \Leftrightarrow \begin{pmatrix} c_1^{(1)} \\ \vdots \\ c_{2I_1+1}^{(1)} \end{pmatrix} \otimes \begin{pmatrix} c_1^{(2)} \\ \vdots \\ c_{2I_2+1}^{(2)} \end{pmatrix} \otimes \ldots \otimes \begin{pmatrix} c_1^{(N)} \\ \vdots \\ c_{2I_N+1}^{(N)} \end{pmatrix}. \tag{1.8}$$

Labels '1', '2' ... 'N' distinguish each nucleus. For example, two coupled spins-1/2 share $2\times 2 = 4$ states, therefore the spin wavefunction occupies a four-dimensional Hilbert space, these being $|\alpha_1\rangle\otimes|\alpha_2\rangle$, $|\alpha_1\rangle\otimes|\beta_2\rangle$, $|\beta_1\rangle\otimes|\alpha_2\rangle$ and $|\beta_1\rangle\otimes|\beta_2\rangle$. We return to these product states and their representations in due course.

1.2.2 Spin dynamics

The above vector-space picture, despite its seeming 'abstract' perspective, is fundamental and it is essential to keep in mind. The dynamics in Hilbert space obey Schrödinger's time-dependent equation

$$\mathrm{d}\,|\psi(t)\rangle\,/\mathrm{dt} = -\mathrm{i}H(t)\,|\psi(t)\rangle\,, \tag{1.9}$$

which says that under a known Hamiltonian, H, the nuclear environment's energy characteristic, an initially-known ket state evolves in a deterministic way:

$$|\psi(t_b)\rangle = U(t_b;t_a)\,|\psi(t_a)\rangle = \underbrace{\exp\Big[-\mathrm{i}\int_{t_a}^{t_b}\mathrm{d}t' H(t')\Big]}_{\text{'the propagator'}}\,|\psi(t_a)\rangle\,. \tag{1.10}$$

By knowing the determinism of $|\psi\rangle$, according to quantum mechanics, all physical

observables can be known, or predicted. By corollary, if all physical observables are predictable they must *also* be controllable, at least as far as $H(t)$ is controllable by the spectroscopist. This is NMR's second crux. Eq. (1.9) says the problem of manipulating the spin states equates to choosing an appropriate time-dependence for the Hamiltonian. While that task might seem complex, the vector space is 'closed' (finite-dimensional) meaning exact solutions are quite often and easily obtained.

1.2.3 Spin order

The questions of what information can be stored in 'spin memory', and how, require some further explanation. In NMR one is usually dealing with a macroscopic ensemble of nuclei, not a handful. In ensemble dynamics, one deals with the statistical evolution of the bulk. In general, at any given time the states of individual nuclei are not known.

A complete statistical description of the NMR ensemble is achieved by the wavefunction outer product $\overline{\rho} = \overline{|\psi\rangle\langle\psi|}$, often called the 'density operator', where overbar ('$\overline{}$') denotes an average over all particles.[3, 4, 34, 36] Properties of $\overline{\rho}$ are apparent upon expansion in the Hilbert ket basis:

$$\overline{\rho}(t) \;=\; \overline{|\psi(t)\rangle\langle\psi(t)|} \;=\; \sum_{i,j} \overline{c_j^*(t)c_i(t)}\,|j\rangle\langle i|. \tag{1.11}$$

The right-hand side of eq. (1.11) shows $\overline{\rho}$ expressed as a linear superposition of orthogonal projection operators between states, the number of which equals the square of the Hilbert space dimension. The meaning of the operators is indicated by their respective coefficients:

- Ket-bra products with a common index are the *population operators* of the basis. Their expectation is equal to the probability of finding a randomly chosen particle in a pure state $|i\rangle$; $\langle\overline{|i\rangle\langle i|}\rangle \equiv \overline{\langle|i\rangle\langle i|\rangle} = |c_i|^2$.

- The projection operators between orthogonal states are *transition operators*, otherwise called *coherences*. Coherence $|i\rangle\langle j|$ between states $|i\rangle$ and $|j\rangle$ (where $\langle i|j\rangle = 0$) is said to exist if there is a nonzero expectation value of $(c_j^* c_i) = (|c_i|e^{-i\varphi_i}|c_j|e^{i\varphi_j})$, which implies there is statistical correlation in the phases of states $|i\rangle$ and $|j\rangle$. 'Coherence' is to say $|i\rangle$ and $|j\rangle$ are in a coherent superposition.

Populations and coherences are collectively known as 'spin order'. If n is the dimension

of the Hilbert space, these must constitute (n^2-1) degrees of freedom for information storage in the ensemble. The 'minus 1' originates from the constraint on the total population as unity: $\sum_i |c_i|^2 = 1$.

1.2.4 Observables

Spin order quantifies the bulk ensemble state and therefore determines the expectation value of bulk physical observables. For any quantum mechanical operator, Q, the ensemble expectation value $\overline{Q}$ is found by projection onto $\overline{\rho}$, using the formula

$$\overline{Q} = \frac{\overline{\langle\psi|Q|\psi\rangle}}{\overline{\langle\psi|\psi\rangle}} \equiv \frac{\overline{\mathrm{Tr}(|\psi\rangle\langle\psi|\,Q)}}{\mathrm{Tr}(\overline{\rho})} = \frac{\mathrm{Tr}(\overline{\rho}Q)}{\mathrm{Tr}(\overline{\rho})}. \tag{1.12}$$

This states that $\overline{Q}$ is obtainable via the inner product between $\overline{\rho}$ and Q. We have already used this formula (on the previous page) to explain the meaning of coherence; the inner product in this case picks the relevant matrix element of $\overline{\rho}$ between the states.

In NMR a very important observable is the bulk magnetisation, or net magnetic moment of the ensemble. This is the detectable quantity in the NMR experiment.[4] From eq. (1.5) the Cartesian components magnetisation are defined by $M_x = N_A\overline{\mu_x} \equiv \gamma\hbar N_A\overline{\langle\sigma_x\rangle}/2$, $M_y = \gamma\hbar N_A\overline{\langle\sigma_y\rangle}/2$, $M_z = \gamma\hbar N_A\overline{\langle\sigma_z\rangle}/2$, per mole ($N_A$ is the Avogadro constant). For a single spin-1/2 nucleus, it may be shown that coherence between $|\alpha\rangle$ and $|\beta\rangle$ generates the bulk transverse magnetisations M_x and M_y, and that a net population difference $(|\alpha\rangle\langle\alpha| - |\beta\rangle\langle\beta|)$ corresponds to longitudinal magnetisation M_z.

1.2.5 Evolution of observables

To keep track of time evolution in the density operator, and thereby predict the future of observables, several analytical approaches are available. The most common are listed below:

- The pure state wavefunctions $|\psi\rangle$ are propagated in Hilbert space using eq. (1.10). Then the outer product $|\psi\rangle\langle\psi|$ is made, then the ensemble average.

- The above is done using the matrix representation of a pure-state density operator $|\psi\rangle\langle\psi|$. $\overline{\rho}$ is represented as a square matrix $\boldsymbol{\rho}$ where the populations $(\boldsymbol{\rho})_{ii}$ appear on

the diagonal and the coherences off-diagonal: [36]

$$\overline{\boldsymbol{\rho}}(t))_{ij} = \langle j|\rho(t)|i\rangle = \overline{c_j^*(t)c_i(t)} \equiv (\overline{\boldsymbol{\rho}}(t))_{ji}^* \qquad \mathrm{Tr}(\overline{\rho}) = 1; \tag{1.13}$$

$$\boldsymbol{\rho}(t_b) \;=\; \boldsymbol{U}(t_b;\, t_a) \cdot \boldsymbol{\rho}(t_a) \cdot \boldsymbol{U}^\dagger(t_b;\, t_a). \tag{1.14}$$

Observables may be evolved directly (Heisenberg mechanics), seeing that all observable operators relate to $\overline{\boldsymbol{\rho}}$ by projection:

$$\boldsymbol{Q_i}(t_b) \;=\; \boldsymbol{U}(t_b;\, t_a) \cdot \boldsymbol{Q_i}(t_a) \cdot \boldsymbol{U}^\dagger(t_b;\, t_a). \tag{1.15}$$

- The density operator is propagated in *Liouville space*. Liouville space differs from Hilbert space by its representation of operators by vectors. A predefined operator basis is chosen, usually the ket-bra basis $\{|j\rangle\langle i|\}$. In this formulation the $(n \times n)$ matrix representation of ρ is flattened to a $(1 \times n^2)$-dimensional vector. For $n = 2$,

$$\boldsymbol{\rho} = \underbrace{\begin{pmatrix} \rho_{11} & \rho_{12} \\ \rho_{21} & \rho_{22} \end{pmatrix}}_{\text{matrix}} \qquad \xrightarrow{\text{flatten}} \qquad \left.\begin{pmatrix} \rho_{11} \\ \rho_{12} \\ \rho_{21} \\ \rho_{22} \end{pmatrix}\right\} \text{ vector.} \tag{1.16}$$

Time evolution in Liouville space is represented via a *super-propagator* matrix $\hat{\boldsymbol{U}}$ (super-operator) acting on the vector representation: [37]

$$\boldsymbol{\rho}(t_b) \;=\; \hat{\boldsymbol{U}}(t_b;\, t_a) \cdot \boldsymbol{\rho}(t_a) \tag{1.17}$$

$$\hat{\boldsymbol{U}}(t_b;\, t_a) \;=\; \exp\Big[-\mathrm{i}\int_{t_a}^{t_b} \mathrm{d}t' \hat{\boldsymbol{H}}(t')\Big], \tag{1.18}$$

where 'hat' denotes the super-operator. The dimension of $\hat{\boldsymbol{U}}$ is the square of the size of the operator basis, *c.f.* :

$$\boldsymbol{\rho} = \begin{pmatrix} U_{11} & U_{12} & U_{11} & U_{12} \\ U_{11} & U_{12} & U_{11} & U_{12} \\ U_{11} & U_{12} & U_{11} & U_{12} \\ U_{11} & U_{12} & U_{11} & U_{12} \end{pmatrix} \cdot \begin{pmatrix} \rho_{11} \\ \rho_{12} \\ \rho_{21} \\ \rho_{22} \end{pmatrix}. \tag{1.19}$$

Observables are propagated directly by

$$Q(t_b) \quad = \quad \hat{\boldsymbol{U}}(t_b; t_a) \cdot Q(t_a), \tag{1.20}$$

or alternatively by the scalar product between the vector representations of Q and $\rho(t)$, for this product equates to the inner product given in eq. (1.12).[3, 37, 38]

I will use all of these methods in the following chapters. In essence they are the same, though Liouville space is usually preferred as this offers the most elegant and notationally compact route to solving the spin dynamics, and is the more intuitive of Heisenberg mechanics. Although the matrix representations of superoperators are relatively large, their size scaling as the number of pure states to the fourth power, they can have many computational rewards. First the superoperator matrix elements are usually related to commutators of the angular momentum operators and are fast to compute. The matrices are also often sparse. In some situations, the superoperator matrices may also be block-diagonal, and only a reduced part need to be exponentiated and propagated. Evolutions restricted to a subspace of the total dimension require less computational effort than full density matrix propagation.[39, 40] Liouville space is also most adept when one needs to account for relaxation, exchange and other bulk phenomena.[14]

Note whilst both Q and ρ have representations that depend on the basis chosen, the scalar $\mathrm{Tr}(\overline{\rho}Q)$ is independent of basis, so any orthonormal operator basis is valid. This emphasises that Liouville space regards an operator basis simply as a 'list' of all possible observables for the spin system. Whether these operators are chosen to correspond to definite or sharp observables is of lesser importance.

1.2.6 Coherent control versus decoherence

Generally speaking each member of the ensemble evolves under its own individual Hamiltonian, as a result of local perturbations in the magnetic surroundings. In solution, microscopically fluctuating fields may arise from the fact that the spins are not static in their environment, but reorient themselves during random molecular tumbling. The result of this is decoherence between the spins, where spins in each molecule evolve asynchronously from the rest and spin order is gradually lost.

Relaxation is the irreversible form of decoherence that drives spin order towards to a

stationary, equilibrium state. A formal introduction to the subject is deferred until chapter 3 of this thesis, but in general is treatable in two ways. The more sophisticated and thorough method, suitable for the ensemble endpoint view, is the Liouvillian treatment of relaxation by Wangsness, Bloch and Redfield (WBR) [41, 42] and Abragam.[2, 14] The Hamiltonian H experienced by each molecule is separable into a uniform, coherent part, $H_0 \equiv \overline{H}$ and a perturbative stochastic part $H_1 = (\overline{H} - H_0)$ that encompasses incoherent time-dependent fluctuations. WBR theory formalises an evolution according to the Liouvillian differential equation

$$\frac{\mathrm{d}}{\mathrm{d}t}\overline{\rho(t)} = (\hat{L}_0 + \hat{\Gamma})\overline{\rho(t)} \tag{1.21}$$

where the *coherent Liouvillian* $\hat{L}_0$ defines the in-phase evolution and depends only upon the uniform Hamiltonian H_0:

$$\hat{L}_0(t) \quad = \quad -\mathrm{i}\hat{\tilde{H}}_0(t). \tag{1.22}$$

The hat '$\hat{}$' signifies a commutation superoperator such that $\hat{H}\overline{\rho(t)} = H\overline{\rho(t)} - \overline{\rho(t)}H$ and tilde '$\tilde{}$' the Larmor frame (see §3.1.1).[3, 14] The other part is the so-called relaxation or *incoherent Liouvillian* that depends only on H_1:

$$\hat{\Gamma}(t) \quad = \quad -\overline{\int_{-\infty}^{0} \mathrm{d}\tau\, \hat{\tilde{H}}_1(t+\tau)\hat{\tilde{H}}_1(t)}. \tag{1.23}$$

One may alternatively deal with relaxation in the fashion of Hilbert space by formulating a matrix containing transition probabilities between spin states via Fermi's golden rule.[34] Fermi's rule (though the rule was in fact derived by Dirac [43]) states a perturbative Hamiltonian H_1 induces transitions between a pair of states $|p\rangle$ and $|q\rangle$ at a rate

$$R_{qp} \quad = \quad 2\pi \left|\langle q|H_1|p\rangle\right|^2 j(\omega_{pq}) \tag{1.24}$$

(in angular units) where $j(\omega_{pq})$ is the power spectral density of fluctuation at the transition frequency $\omega_{pq} = \langle p|H_0|p\rangle - \langle q|H_0|q\rangle$. Although both formalisms are equivalent in a theoretical sense, the WBR formalism is overall more convenient to handle.

Note that spin relaxation is distinct from *time-reversible* decoherence that frequently

occurs in NMR, particularly in the solid state. In solids, where molecular motion is frozen out, anisotropic spin evolution is reversible using techniques such as the spin echo, for example.[15] Only time-irreversible decoherence characterises spin relaxation and, notably, requires fluctuations at the transition frequency between spin states. The spectral density is explicit in the Fermi treatment, while the Liouvillian formalism obtains this through the time correlation integral.

1.3 Structure of the NMR experiment

The view in §1.2 boils down to the NMR system as a closed quantum ensemble where evolutions of spin order and observables behave as a problem in linear algebra. A graphical summary of the formalism is given in fig. 1.3 (for more depth, see ref. [3]). The ensemble state, or density operator, is controllable in its evolution because it can be steered in a predictable way by applying a carefully chosen time-dependent Hamiltonian. Despite the seemingly reduced information content $\overline{\rho}$ maintains a 'complete' statistical definition of the system, for according to eq. (1.12) it contains all physically significant information about the ensemble.

A general experimental scheme for NMR is given in fig. 1.4 outlining three basic stages: initialisation (a preparatory stage), encodement (the information storage part) and detection (the readout of observables), following in chronological order from left to right. These are briefly described as follows:

- *Initialisation*

  Initialisation prepares spin order for the 'encoding' stage. If the spin populations are initially all the same, coherent encoding is not possible since $\overline{\rho}$ remains stationary under unitary propagation, as the density matrix $\boldsymbol{\rho}$ is proportional to a unit matrix, $\boldsymbol{E}$. The goal of initialisation is to create a population asymmetry between spin states.

  Population asymmetry in the form of longitudinal magnetisation can be obtained by placing the sample can be within a static magnetic field denoted $\boldsymbol{B^0} = (0, 0, B^0)$, where B^0 usually exceeds the magnitude of all other spin interactions by several order of magnitude, and waiting until thermal equilibrium is reached. The spin order relaxes to a net magnetisation parallel to the field, where populations are given by the Boltzmann distribution:

$$\overline{\rho}_{\text{eq}} = \exp(-H/k_BT) \,/\, \text{Tr}(\exp(-H/k_BT)). \tag{1.25}$$

  Here T is the temperature, and k_B is Boltzmann's constant. The approximate Hamiltonian in this case is $H = -\hbar\gamma B^0\sigma_z/2$, which corresponds to the Zeeman energy $E = -\boldsymbol{\mu}\cdot\boldsymbol{B^0}$ of a magnetic moment in the field.

  Consider, as an example, protons in a room temperature (300 K) sample placed in a

Hilbert space

Elements

- $n = (2I_1 + 1)(2I_2 + 1)\dots(2I_N + 1)$ orthogonal kets $|i\rangle$
- norm: $\langle i|j\rangle = \delta_{ij}$

Representation

- pure state wavefunction $|\psi\rangle$ as n-dimensional vector
  $|\psi(t)\rangle = \sum_j c_j(t)\,|j\rangle \quad \Leftrightarrow \quad \mathbf{c} = (c_1\, c_2\, \dots\, c_n)^{\mathrm{T}}$
- n^2 linearly-independent operators each as $n \times n$ matrices
  $Q^k\,|\psi(t)\rangle = \sum_{i,j} Q^k_{ij} c_j(t)\,|j\rangle \quad \Leftrightarrow \quad (\mathbf{Q}^k)_{ij} = \langle i|Q^k|j\rangle$
- density operator as matrix
  $\overline{\rho}(t) = \sum_{i,j} \overline{c_j^*(t) c_i(t)}\,|j\rangle\,\langle i| \quad \Leftrightarrow \quad (\overline{\boldsymbol{\rho}})_{ij} = \overline{c_j^*(t) c_i(t)}$

Equation of Motion:

- $\mathrm{d}\,|\psi(t)\rangle\,/\mathrm{dt} = -\mathrm{i}H(t)\,|\psi(t)\rangle \quad \Leftrightarrow \quad \dot{\mathbf{c}} = -\mathrm{i}\mathbf{H}\mathbf{c}$
- $\mathrm{d}\rho(t)/\mathrm{dt} = -\mathrm{i}\Big(H\rho - \rho H\Big) \quad \Leftrightarrow \quad \dot{\boldsymbol{\rho}} = -\mathrm{i}(\mathbf{H}\boldsymbol{\rho} - \boldsymbol{\rho}\mathbf{H})$

Propagation:

- $U(t_b;\, t_a)\,|\psi\rangle = \exp[-\mathrm{i}\int_{t_a}^{t_b} H(t')\,\mathrm{d}t']\,|\psi\rangle$
- $\rho(t_b) = U(t_b;\, t_a)\rho(t_a)U^T(t_b;\, t_a) \quad \Leftrightarrow \quad \boldsymbol{\rho}(t_b) = \boldsymbol{U}\boldsymbol{\rho}(t_a)\boldsymbol{U}^T$
- $Q(t_b) = U(t_b;\, t_a)Q(t_a)U^T(t_b;\, t_a) \quad \Leftrightarrow \quad \boldsymbol{Q}(t_b) = \boldsymbol{U}\boldsymbol{Q}(t_a)\boldsymbol{U}^T$

Multiple propagation:

- $U_M \dots U_2 U_1 \rho(t) U_1^T U_2^T \dots U_M^T \quad \Leftrightarrow \quad \boldsymbol{U}_M \dots \boldsymbol{U}_2\boldsymbol{U}_1\boldsymbol{\rho}(t)\boldsymbol{U}_1^T\boldsymbol{U}_2^T\dots\boldsymbol{U}_M^T$

Liouville space

Elements:

- n^2 basis operators: $Q^{ij} = |j\rangle\,\langle i|$
- norm: $\mathrm{Tr}(\boldsymbol{Q}^{ij\,\dagger}\boldsymbol{Q}^{kl}) = \delta_{ik}\delta_{jl}$

Representation:

- operators as n^2-dimensional vector
  $\rho = \sum_k \mathrm{Tr}(\boldsymbol{Q}^{k\dagger}\boldsymbol{\rho})Q^k \quad \Leftrightarrow \quad \boldsymbol{\rho} = (\rho_1\, \rho_2\, \dots\, \rho_{n^2})^{\mathrm{T}}$
- n^4 linearly-independent superoperators each as $n^2 \times n^2$ matrices

Equation of Motion:

- $\mathrm{d}\rho(t)/\mathrm{dt} = -\mathrm{i}\hat{H}(t)\rho(t)$

Propagation by superoperator:

- $\hat{U}(t_b;\, t_a) = \exp[\int_{t_a}^{t_b} -\mathrm{i}\hat{H}(t')\,\mathrm{d}t'] \qquad \hat{\boldsymbol{U}} = \boldsymbol{U} \otimes \boldsymbol{U}$
- $\rho(t_b) = \hat{U}(t_b;\, t_a)\rho(t_a) \quad \Leftrightarrow \quad \boldsymbol{\rho}(t_b) = \hat{\boldsymbol{U}}\boldsymbol{\rho}(t_a)$
- $Q(t_b) = \hat{U}(t_b;\, t_a)Q(t_a) \quad \Leftrightarrow \quad \boldsymbol{Q}(t_b) = \boldsymbol{U}\boldsymbol{Q}(t_a)$

Multiple propagation:

- $\hat{U}_M \dots \hat{U}_2\hat{U}_1\rho(t) \quad \Leftrightarrow \quad \hat{\boldsymbol{U}}_M \dots \hat{\boldsymbol{U}}_2\hat{\boldsymbol{U}}_1\boldsymbol{\rho}(t)$

Figure 1.3: From the spin system to observables: a quick-reference guide to linear algebra in NMR.

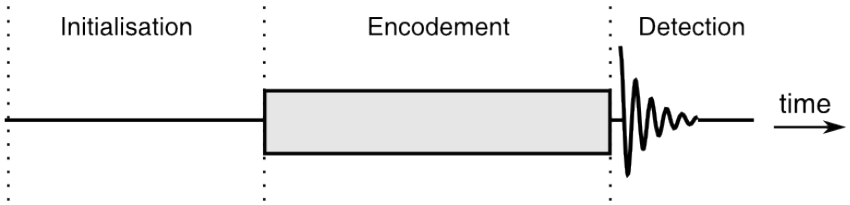

Figure 1.4: General structure of an NMR experiment, summarised in three basic stages.

typical magnetic field $B^0 = 5$ T. The density operator approximates to

$$\rho_{\text{eq}} \approx E - \frac{1}{k_B T} H \qquad (\text{for } k_B T \gg |\hbar\gamma B^0|) \tag{1.26a}$$

$$= E + \frac{\hbar\gamma B^0}{2k_B T}\sigma_z \tag{1.26b}$$

$$= \left(\frac{1}{2} + \frac{\hbar\gamma B^0}{2k_B T}\right)\Big(|\alpha\rangle\langle\alpha|\Big) + \left(\frac{1}{2} - \frac{\hbar\gamma B^0}{2k_B T}\right)\Big(|\beta\rangle\langle\beta|\Big). \tag{1.26c}$$

where E is the unity operator defined by $E|\psi\rangle = |\psi\rangle$.

Protons have nearly the largest $|\gamma|$ of all nuclei but the difference $|\hbar\gamma B^0/k_B T|$ is still very small, only of order 10^{-5}. While this difference is small, it usually suffices because it is compensated by very large number of spins (typically $10^{20} - 10^{23}$ spins).

- *Encoding*

  During this stage information is written into spin memory. The form of the encoding is a time-dependent Hamiltonian, in general expressed by

$$H(\{\omega_1, \omega_2 \ldots\}, t) = \omega_1(t)Q_1 + \omega_2(t)Q_2 + \ldots, \tag{1.27}$$

  where the coefficients $\omega_i(t)$ of each operator are related by the strengths of the interactions between spins and their environment. These interactions may be 'external' to the spins in the form of applied magnetic fields, such as the 'z'-field of the polarising magnet, or field pulses,[2, 3, 4, 5, 6] which are short periods of irradiation by oscillating electromagnetic fields at the frequency of transitions between spin angular momentum states. Spin interactions 'internal' to the spin system include couplings between nearby nuclei, shielding, and effects of molecular motion – including relaxation mechanisms.

The encoded density operator, after the evolution under $H(\{\omega_1, \omega_2 \ldots\}, t)$, may be denoted $\overline{\rho}(\{\omega_1, \omega_2 \ldots\}, t)$ regarding it as a function of the history in $\omega_i(t)$:

$$\overline{\rho}_{\mathrm{eq}} \xrightarrow{H(\{\omega_1, \omega_2 \ldots\}, t)} \overline{\rho}(\{\omega_1, \omega_2 \ldots\}, t) \;=\; \hat{U}(\{\omega_1, \omega_2 \ldots\}, (t; 0))\overline{\rho}_{\mathrm{eq}}. \tag{1.28}$$

The determinism of the spin evolution (seen in §1.2) is very powerful as it allows one to design any encoding in mind, for instance the encoding of nuclear positions in a sample, so as to later obtain an image of the spin density, or the transfer of magnetisation between different nuclei in the system. An excellent review is provided by Sørensen et al.[44] Control of spin dynamics also extends to compensating artifacts invariably present in experiment, such as pulse imperfections, undesired spin-spin couplings, quadrature images and magnetic field inhomogeneities.[3, 4, 5, 6]

- *Observation*

  The encoded density operator is conventionally detected through Faraday induction within a radiofrequency coil adjacent to the sample. Induction in the coil is proportional to the transverse magnetisations $M_x(t)$ and $M_y(t)$, giving a time-dependent signal that is recorded digitally and stored on a computer. The signal is recorded until the spins have fallen out of coherence or relaxed and the induction has decayed below a detectable level.

  The signals are then processed to unravel selected parts of the encoded information $\{\omega_1, \omega_2 \ldots\}$. This is done by Fourier transforming the time-oscillations to a frequency spectrum,[3, 4, 44] or by more elaborate methods into a two- or three-dimensional information scheme, such as an image, depending on the acquisition scheme.

1.4 NMR Sensitivity

1.4.1 Signal versus noise

The main challenge of NMR is regularly not how to retrieve desired information by encoding / decoding the spin ensemble, but how to fight the inherent low sensitivity of the experiment. The weakness of the observed signals, due to the weak nuclear magnetism, is a major issue. In a real experiment, the NMR signal will be accompanied by a certain

amount of random 'noise', the nature of which is usually assumed to be independent of the NMR pulse sequence and uncorrelated throughout time. Noise is usually caused within the experimental hardware; in the electronic circuitry, for example. Noise makes observation of the NMR signals more difficult and in extreme cases obscures the signal information content altogether.

One ultimately wishes to distinguish the signal from the noise as far as possible, obtaining maximum sensitivity. Better sensitivity opens the way to new NMR experiments and new regimes of study. Improved sensitivity in one area of the experiment may, for example, offset a reduction in signal strength upon using smaller samples (one may recall the NMR signal is proportional to the number of spins present), to the benefit of structural characterisation of precious or expensive samples by NMR. In MRI, where the spin density is measured from pixelised regions of a sample, this may enable higher spatial resolution.

1.4.2 Sensitivity improvement

NMR's unique role in science drives a large effort to improve sensitivity across all areas of the experiment:

- *Average several scans*

  If an experiment is repeated N times and the spectra summed together, the total signal is proportional to N. In contrast, the noise builds proportional to $\sqrt{N}$. Random noise is characterised by a root-mean-square amplitude, in this case denoted 'z'. The root-mean-square noise after a superposition of N repeated readouts is

  $$\sqrt{\sum_{j=1}^{N} z^2} \equiv z\sqrt{N}. \tag{1.29}$$

  This means when the experiment is repeated several times and the signals added together, the signal-to-noise improves as $\sqrt{N}$.

  Scan averaging is not always possible or desirable. Many NMR experiments may be 'single shot', particularly those that may monitor irreversible changes in a system through time, such as during an ongoing chemical reaction.

- *Detection advances*

  Signal-to-noise improvements can be made by better probe design for signal detection.

The Faraday induction can be improved by increasing the fraction of the coil volume filled with sample (coil filling factor). Cryogenically cooled probes are the most current advance,[45] which typically deliver 5- to 10-fold signal-to-noise improvements over standard probes. The receiver coils are cooled to 20 K using helium gas, which enormously reduces the thermal noise in the electronic circuitry.

- *Increase initial spin order*

  The polarisation of the nuclei can be improved vastly. Even at the largest available field strengths (≈20 T), the ensemble is very hot and the thermal equilibrium polarisation is very small. Larger initial polarisations are possible by thermalising at higher magnetic fields, or lower sample temperatures, though this comes at the expense of technical difficulty, and conditions may not be compatible with the system of interest.

  Some specialised techniques obtain large non-Boltzmann nuclear polarisations, potentially up to the order of unity (almost 100% nuclear alignment). These operate by transferring the much stronger polarisation of unpaired electron spins onto the nuclear spins. In the dynamic nuclear polarisation approach (DNP), the NMR sample is doped with a stable paramagnetic species to provide an electron source. It is cooled to a few Kelvin in a strong magnetic field where the electrons become polarised to unity order. Electron-nucleus polarisation transfer is then driven by microwave irradiation.[46] The recent dissolution-DNP method allows rapid melting of the cold sample by dissolving it with jet of hot liquid. This achieves hyperpolarised nuclear spins in a room temperature solution that can be used for liquid-state NMR.[47, 48, 49] An alternative route to polarised nuclear spins at ambient temperatures is to produce photoexcited electron states in a molecule or atom by LASER irradiation, whose emissive return back to the ground state drives spin-selective electron-nucleus transitions.[50, 51, 52] Similar effects can be produced by chemical reactions in which the intermediates contain unpaired electrons.[53]

  An unique route, without radicals, to hyperpolarised molecules is parahydrogen. The hydrogen diatomic (H_2) exists as two nuclear spin isomers: orthohydrogen (o-H_2), corresponding to a triplet state in which the two nuclear spins are parallel (total spin $I = 1$), and parahydrogen (p-H_2), a singlet state, where the two nuclear spins

are antiparallel (total spin $I = 0$). It is possible to enrich the lower-energy singlet spin-isomer by exposing H_2 to a paramagnetic catalyst at low temperatures.[54] Para enrichment persists after removing the catalyst and warming the hydrogen to room temperature, due to the relatively large energy difference between ortho and para forms. Spin order of enriched H_2 is thereafter transferred to other molecules through hydrogenation reactions, resulting in large nonequilibrium proton spin order in the product molecules.[55, 56, 57, 58, 59]

- *Efficient encoding*

  The period between the initialisation and detection steps is also important, as signal strength depends both on how efficiently the initial spin order is encoded and transferred into detectable magnetisation.

  Efficiency of the encoding step is generally constrained by a fixed information required of the spins in a given experiment. This does not mean sensitivity improvement is improbable, but may change one's focus somewhat: to recover sensitivity losses, rather than look for gains.

  A major if not the main source of signal loss is relaxation. Attempts to prolong spin order go back as far as Hahn's stimulated echo in the 1950s. To give a different example from biomolecular NMR, Wüthrich and co workers have shown that for selected observable coherences between ^{1}H–^{15}N spin pairs in proteins the dipolar (DD) and chemical shift anisotropy- (CSA-) induced relaxation rates can be arranged to partly cancel. The resulting extended coherence-lifetime gives enhanced intensity and resolution in the observed ^{1}H–^{15}N spectra compared to ordinary T_2 relaxation. This method, known under the acronym TROSY (Transverse Relaxation Optimised SpectroscopY), roughly triples the upper limit of molecular weight for which NMR can viably determine protein structure.[4, 12]

  Apart from relaxation, deviations from ideal spin evolution may arise from imperfections in applied pulses and static field inhomogeneity. These can be minimised using error-compensation strategies, by designing an evolution scheme with error terms taken into account. One of the best-known examples of this is composite pulses,[60] which are used to achieve near-ideal rotations of the spins despite flip angle miscalibration and off-resonance effects.

Ideally, one would like to combine all these methods together and generate *ultimate* NMR sensitivity, using the maximum feasible sample concentration at maximum initial polarisation, then with maximum carriage of spin order through the encoding sequence (efficient coherent spin dynamics, with minimal loss through relaxation) followed by detection on the most sensitive hardware available.

1.5 Boosting sensitivity using singlet states

Singlet NMR falls into the 'efficient encoding' category by prolonging spin lifetimes. This section introduces singlet states, their relaxation properties and gives an overview of their use in NMR.

1.5.1 Definition of singlet and triplet states

Singlet and triplet states are names given to the four eigenstates of the total angular momentum for two spins-1/2. Explicit form of the states is obtained using the angular momentum coupling series

$$|l,\, m\rangle^{jk} = \sum_{m_j m_k} C^{lm}_{l_j m_j l_k m_k}\, |l_j,\, m_j\rangle \otimes |l_k,\, m_k\rangle, \tag{1.30}$$

where each $C^{lm}_{l_j m_j l_k m_k}$ is a Clebsch-Gordan coefficient,[33, 34, 35] the quantum numbers $\{l, m\}$ are the eigenvalues of the total angular momentum and projection angular momentum operators of the composite system, respectively given by opertors ($I^2 = (I_x + I_y + I_z)^2$) and I_z, and the quantum numbers $\{l_j, m_j\}$ refer to the uncoupled nuclei, henceforth labelled 'j' and 'k'. The unique spin-zero ($l = 0$) configuration from destructive addition of the angular momenta is the *singlet state*. The singlet wavefunction is denoted

$$|S_0^{jk}\rangle \;=\; |0,0\rangle^{jk} \;=\; 2^{-1/2}(|\alpha_j\rangle \otimes |\beta_k\rangle - |\beta_j\rangle \otimes |\alpha_k\rangle) \tag{1.31}$$

$$\equiv\; 2^{-1/2}(|\alpha_j\beta_k\rangle - |\beta_j\alpha_k\rangle). \tag{1.32}$$

The *triplet* is the name given to the three states formed by constructive addition. These have total spin quantum number $l = 1$ and projections $m = -1, 0$ or $+1$. Notation $|T_m^{jk}\rangle$

is assigned to the states $|1,m\rangle^{jk}$ as follows

$$\begin{aligned} |T^{jk}_{+1}\rangle &= |1,+1\rangle^{jk} \equiv |\alpha_j\alpha_k\rangle \\ |T^{jk}_{0}\rangle &= |1,0\rangle^{jk} \equiv 2^{-1/2}(|\alpha_j\beta_k\rangle + |\beta_j\alpha_k\rangle) \\ |T^{jk}_{-1}\rangle &= |1,-1\rangle^{jk} \equiv |\beta_j\beta_k\rangle\,. \end{aligned} \tag{1.33}$$

1.5.2 Singlet relaxation basics

Relaxation and symmetry

Symmetry properties of singlet and triplet states favour long singlet relaxation times. As can be seen from the sign change under exchange of the nuclei, the singlet wavefunction is antisymmetric, while the triplet wavefunctions are all symmetric:

$$P(j,k)\,|S^{jk}_0\rangle = -\,|S^{jk}_0\rangle \tag{1.34}$$

$$P(j,k)\,|T^{jk}_m\rangle = +\,|T^{jk}_m\rangle\,. \tag{1.35}$$

The exchange operator $P(j,k)$ denotes swapping of the pair labels.

Fermi's golden rule (see eq. (1.24)) says that the relaxation rate between a pair of quantum states under a fluctuating Hamiltonian is proportional to the square of their transition dipole integral.[3, 41, 43] Exchange symmetry imposes a strong selection rule on the transition dipole between singlet and triplet states. For singlet-triplet transitions, a permutation-symmetric Hamiltonian gives a zero dipole, since the connected states have opposite symmetry:

$$\langle S^{jk}_0|H|T^{jk}_m\rangle = 0 \quad \text{if} \quad \hat{P}(j,k)H = +H. \tag{1.36}$$

Symmetric, correlated fluctuating fields at the nuclear sites therefore do not induce singlet-triplet transitions, and do not induce singlet relaxation. Singlet relaxation is only brought about by fluctuations that are uncorrelated (or anticorrelated) across the spin pair.

A similar selection rule exists for triplet-triplet transitions. A triplet-triplet transition dipole is zero if the fluctuating Hamiltonian is exchange-antisymmetric, for the triplet

states all have the same symmetry:

$$\langle T^{jk}_{m'}|H|T^{jk}_{m}\rangle = 0 \quad \text{if} \quad \hat{P}(j,k)H = -H. \tag{1.37}$$

Slow decoherence of the singlet state occurs when the relaxation involves a predominantly permutation-symmetric mechanism, so that the selection rule eq. (1.36) wins out over eq. (1.37). In the extreme case, when the relaxation mechanism is perfectly symmetric with respect to nuclear exchange the singlet is expected to be infinitely long-lived, and not decay at all.

Relaxation insensitivity of singlet states may be qualitatively interpreted from the total spin quantum number, which implies the singlet overall behaves as a nonmagnetic particle ($l = 0$), while the triplet exhibits nuclear paramagnetism ($l = 1$). A relaxation mechanism whose Hamiltonian is perfectly correlated across the nuclei will regard the spin-pair as nonmagnetic, and therefore leave the singlet state unperturbed.

Intra-pair dipole coupling

Many relaxation mechanisms in solution NMR are exchange-symmetric or near exchange-symmetric. A very important one for an isolated spin pair is the internuclear dipole coupling. This is the magnetic analogue of the coupling between two electric dipole moments. The magnetic dipole interaction between two nuclei with labels 'j' and 'k' in the principal axis frame of the internuclear vector is given by

$$H^{\mathrm{DD}}_{jk} = b_{jk}(2I_{jz}I_{kz} - I_{jx}I_{kx} - I_{jy}I_{ky}), \tag{1.38}$$

where the coefficient b_{jk} is the dipole-dipole coupling constant between the spins. This is proportional to the inverse-cube of the internuclear distance, d_{jk} and the gyromagnetic ratios of the two nuclei:

$$b_{jk} = -\frac{\mu_0 \hbar \gamma_j \gamma_k}{4\pi d^3_{jk}}. \tag{1.39}$$

It is clear that $H^{\mathrm{DD}}_{jk} \equiv \hat{P}(j,k)H^{\mathrm{DD}}_{jk} = +H^{\mathrm{DD}}_{jk}$. This means singlet-triplet transitions cannot be induced.

Dipole-dipole induced relaxation is often the strongest decay-causing mechanism in

solution NMR of coupled spins, especially protons; for two protons at a separation of 1.8 Å, the typical separation between two methylene (CH_2) protons, the coupling strength $|b_{jk}/2\pi|$ is approximately 20 kHz. Dipole-immune states were the subject of the very first demonstrations of singlet order with lifetimes longer than T_1.[18, 19]

Thermal stability of orthohydrogen and parahydrogen

Dipolar-forbidden transitions are the culprit of the very slow interconversion between ortho (triplet) and para (singlet) spin isomers of hydrogen gas.[54] To convert between the two forms, a paramagnetic catalyst must be added (*e.g.* ferric oxide, chromic oxide) because the ortho-para nuclear spin transitions are permitted only by pair-antisymmetric fields. The catalyst causes strong, unsymmetrical hyperfine shifts at the two hydrogen atoms. Without the catalyst the ortho and isomers persist as metastable species with lifetimes the order of several weeks.

1.5.3 Nomenclature of long-lived and singlet states

The term 'long-lived state' (LLS) has been used in the literature as a general term for spin order that relaxes slower than T_1, *in the same system*; in symbolic terms, decays with a time constant $T_{\mathrm{LLS}} > T_1$.

This comparison originates partly for historical reasons. Before the realisation that singlet states exhibit very slow relaxation – at some times altogether forbidden relaxation – it was thought that T_1 of a system presented a strict upper limit of spin lifetime. Initially this was because T_1 was found to be the upper lifetime predicted in observable spin order, namely the Cartesian components of bulk magnetisation, which relax with time constants T_1 and T_2. NMR-silent spin-0 states were ignored. It *is* true that T_1 provides the upper limit of spin lifetime in systems of isolated (uncoupled) nuclei, regardless of the spin quantum number I. A classical random-field model shows that in high magnetic field, longitudinal magnetisation can only be relaxed by fluctuating transverse fields, oscillating at the energy difference between the angular momentum states, not by fields along the symmetry axis. The transverse magnetisation does not lie along a symmetry axis in general, so is susceptible to field fluctuations along all three orthogonal axis, and therefore is faster relaxing.[14] In the absence of a symmetry axis, for example at zero field, then T_1

and T_2 are identical.

The slow singlet relaxation character was also 'missed' in the Liouvillian treatments of multinuclear systems by Bloch, Wangsness and Redfield.[14, 41] In that case, hasty approximations were made in deriving the relaxation superoperator, which obscured the existence of long-lived states.

As the term 'long-lived state' is relative, care in its use is advised. In most practical cases, one may want to know if such states provide the longest-available lifetimes. For instance: two carbon sites in a molecule may be isotopically enriched with ^{13}C ($I = 1/2$) giving a $^{13}C_2$ spin pair on which singlet order can be excited. The singlet decay constant, T_S, may well exceed T_1 in the same system, but does it exceed T_1 of either ^{13}C nucleus in the singly ^{13}C-labelled isotopologues? This possibility must be considered too.

Having said the above, comparison between T_S and T_1 of the same molecule is useful regardless of whether the singlet is long lived or not, since it gives information about the symmetry and likely nature of the dominant relaxation pathway in a molecule.[61, 62]

1.5.4 Symmetry switching concept in singlet NMR

A typical singlet NMR experiment involves 'switching' the spin-exchange symmetry of the nuclear spin Hamiltonian between exchange-symmetric and -unsymmetric forms. Preparation of singlet order from conventional magnetisation, (always a property of the triplet), such as equilibrium longitudinal order, requires nuclear inequivalence to facilitate coherent singlet-triplet transitions. Singlet storage, on the other hand, requires suppression of symmetry-breaking terms to enforce singlet-triplet isolation. Reconversion to observable magnetisation, as singlet order is nonmagnetic and cannot itself be observed directly, requires broken symmetry again.

A scheme for symmetry-switching is seen in fig. 1.5. In the case where parahydrogen is the initial source of spin order, singlet order may be released using asymmetry-inducing chemical reactions, where, for example, the protons in the products may end up in sites with different chemical shifts.[59, 63, 64]

For polyatomic molecules, where magnetisation is the initial spin order, it is necessary to start with inequivalent nuclei. Temporary magnetic equivalence may be brought about for periods of singlet storage in several ways: (i) by applying resonant rf irradiation to the sample,[18, 65] (ii) by removing the sample from the magnetic field[19] or applying

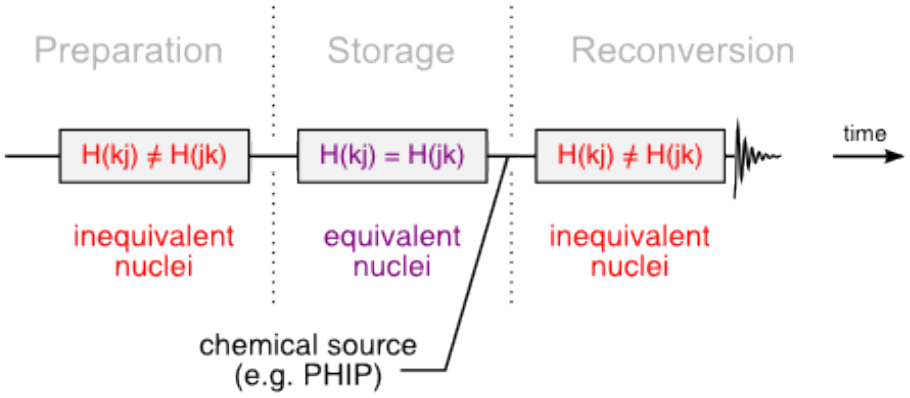

Figure 1.5: Symmetry switching sequence for a singlet NMR experiment

chemical reactions that render the two nuclear sites equivalent.[31] The resonant field brings the angular precession frequencies of the two spins into parallel, while transport of the sample into low magnetic field removes the symmetry-breaking interaction altogether as the chemical shift frequencies become vanishingly small.[17]

1.5.5 Singlet NMR at present

Singlet states open a new dimension in NMR by providing access to relaxation times far in excess of T_1. This has attracted growing attention over the last half-decade.

Applications of the long lifetime

On the application front, the most widespread use of long-lived singlet states has been to extend the detectable window of slow molecular dynamics phenomena. The typical scheme in these experiments involves encoding the spins with information on their state at some initial time point, then encoding again after a waiting time. Readout and post-processing separates these informations to capture what happens during the wait, on that condition that the wait is long enough to capture the process of interest. Slower timescales are made accessible by transforming the nonequilibrium spin order into a singlet-triplet population difference for the waiting time, so as to better preserve the ordered state against relaxation loss. Singlet-EXchange SpectroscopY (singlet-EXSY) has been demonstrated,[25, 66] which encodes the chemical environment of the nuclear spins for monitoring of slow chemical exchange, protein folding and other molecular dynamics. Slow translational diffusion in various contexts has been monitored by combining singlet

states with Diffusion Ordered SpectroscopY (singlet-DOSY), where molecular position is the encoded information.[24, 28, 29, 67]

A promising candidate for very long term polarisation storage is ^{15}N-labelled nitrous oxide, $^{15}N_2O$. The fast rotational correlation time of the triatomic molecule, in addition to the low gyromagnetic ratio of ^{15}N results in a singlet lifetime that may exceed tens of minutes.[22, 68, 69] Such long lifetimes exist for $^{15}N_2O$ dissolved in a wide range of solvents, including whole blood.[23] As N_2O is non-toxic and soluble in blood it has been suggested as a tracer in clinical MRI. Before this, however, a remaining challenge is to successfully hyperpolarise ^{15}N in $^{15}N_2O$, in order to overcome its intrinsically low magnetism.[22]

Understanding relaxation

The demonstrations of dipole-immune states made by Carravetta and co-workers initially drew curiosity not to the general relaxation properties of singlet states, but to long-lived states in general, with theoretical analyses made to determine whether such immune states can exist within systems containing more than two spins-1/2. In the early studies, exhaustive brute-force searches of the relaxation superoperator were made for its null (decoherence-free) space.[70, 71, 72, 73, 74, 75] More careful symmetry-based analyses for three- and four-spins-1/2 have since been made. In these, rules for exact dipole-immune states have been identified. For instance, such states may only exist if the geometry of nuclear spins possesses inversion symmetry.

Current opinion is that exact dipole-immune states are an overkill, and not widely useful since invariable presence other relaxation mechanisms causes their decay. A potential application, however, is NMR quantum computing, where generalised long-lived states in large spin systems may help one prepare entangled states.

Recently, efforts have taken the approach of rationalising T_S and T_1 lifetimes measured in real systems, to get a feel of the most significant relaxation mechanisms in practice. Theory has been developed to treat singlet relaxation in isolated spin-1/2 pair systems,[20] as well in presence of intra-[62, 76, 77, 78] and inter-molecular [79] neighbour spins.

In some cases it is possible to perform a 'reverse' analysis of singlet lifetimes. The relaxation of nuclear singlet states is very sensitive to the local magnetic environment of the spin pair. Studies have been made to determine the relative orientations between chemical shielding tensors from observed singlet relaxation constants,[61] Out-of-pair dipole

couplings have similarly been studied to give constraints on molecular geometry, including bond torsion angles.[62]

Methodology development

Storage of singlet order requires 'symmetry-switching' to bring the spin-1/2 pair into magnetic equivalence. Schemes for this must typically be tailored to the nature of magnetic symmetry-breaking interactions. As mentioned in the previous section, switching may be achieved by applying a resonant spin locking field,[65, 80, 81] by transporting the sample into a region of low field, where the chemical shift frequency difference is vanishingly small,[82] or by performing symmetry-switching chemical reactions.[31]

In the radio-frequency spin-lock type methods, the frequency and amplitude of the locking field is critical to enforcing magnetic equivalence. This has driven investigation of amplitude or phase-modulated decoupling schemes to find broadest bandwidths between the average chemical shift of the spins and the carrier that maintains singlet state isolation.[81] Shaped-pulse decoupling may sustain singlet order at resonance offsets that exceed both the difference in the chemical shifts and mean rf irradiation power.[25, 65, 81] For potential in-vivo singlet NMR, this may allow use of lower rf power, to avoid excessive SAR (Specific power Absorption Rate) in living tissues.

Another major area of methodology development is pulse sequences to make the conversions between magnetisation and singlet order. The magnitudes of the magnetic-equivalence-breaking interactions, which are also linked to the singlet storage requirements, are important for which sequence to use but in general these are not prohibitive to the efficiency of singlet-triplet conversion. Error-resistant preparation sequences have been developed that are broad-band with respect to variation in the chemical shifts and J couplings.[25] These also allow simultaneous singlet excitation on two or more spin pairs in a molecule. A more detailed discussion is reserved until chapter 2 of this thesis, where the current state of available methodology is reviewed.

Long-lived singlet-triplet coherences

The phenomenon of populations $|S_0\rangle\langle S_0|$ with lifetimes $T_S > T_1$ has led to the realisation of long-lived coherences (abbreviated LLCs) of the type $|S_0\rangle\langle T_0|$. The vanishing transition dipole between singlet and triplet states under a symmetric relaxation mechanism results

in enhanced lifetimes $T_{\mathrm{LLC}} > T_2$.[25] LLCs are not fully immune to the intra-pair dipolar relaxation, due to the nonequilibrium triplet component, though in theory may still relax up to 3 times slower than T_2 in small molecules, and up to 9 times more slowly in macromolecules.[83]

An application of LLCs is the precise determination of spin-spin couplings. The LLC of an homonuclear spin-1/2 pair oscillates at the singlet-triplet energy splitting, which equals the J coupling in isotropic solution phase, and the sum of J and the orientationally averaged 'residual' dipolar coupling in oriented media. The oscillatory dependence can be measured in either one-dimensional or two-dimensional fashion and Fourier transformed to an high-resolution spectrum yielding natural linewidths ($\propto 1/T_{\mathrm{LLC}}$) much narrower than the ordinary homogeneous resolution ($\propto 1/T_2$).[84, 85, 86] The LLC spectra also escape inhomogeneous line broadening. Linewidths as low as 10 millihertz have been observed. For an excellent review, see ref [87].

1.6 Scope of the present work

This thesis aims to communicate new methodology and theory for singlet NMR, while maintaining accessibility in the subject to a newcomer in the field. To achieve this I adopt a focus on broad concepts supplemented by specific experimental demonstrations. The following two chapters each start by introducing a general theoretical framework. This is used to explain existing features or techniques, present new methods and compare.

In chapter 2, ('Singlet nuclear magnetic resonance'), the introductory detail sketches out a Hilbert space evolution formalism for the singlet and triplet states of a spin-1/2 pair. Four ket states with well-defined exchange symmetries are easier to keep track of and appreciate than the sixteen spin operators of the Liouville space. This evolution formalism is applied to analyse pulse sequences that generate singlet spin order starting from longitudinal magnetisation, (and in reverse, vice versa, for singlet observation). 'Singlet polarisation' is used as an instrument to quantify how much singlet order is excited in any given experiment, how much is reconverted into observable signal, whether the excitation yielded is 'maximal' and make a comparison across the different sequences.

The most novel and extensively discussed sequence in chapter 2 is one that permits

access to singlet order in 'nearly equivalent' spin-1/2 pairs. These are systems where the singlet and triplet states are near-exact eigenstates of the free evolution and do not necessitate symmetry switching to redeem the long lifetime. Near-equivalence at a spin pair may be induced chemically, as demonstrated (i) by using symmetry-breaking function groups at remote sites in the molecule and (ii) by weak chemical shift perturbations caused by isotopic mass differences between neighbouring nuclei. A downside of near-equivalence is how the pulse sequence is rather sensitive to variation in the J coupling and chemical shift difference in the intramolecular Hamiltonian plus external magnetic field and rf pulse inhomogeneities. Error-compensating pulses and phase cycles are devised to in-part overcome these.

Access to singlet order is also examined in hetero-nuclear spin systems, where the homonuclear spin-1/2-pair may be coupled to nuclei of other magnetic isotopes. Heteronuclear J couplings provide a mechanism for symmetry switching that may facilitate excitation of singlet states in chemically equivalent pair systems. I give experimental demonstrations where the symmetry of a chemically equivalent ^{1}H pair is broken by differences in scalar couplings to a nearby ^{13}C nucleus. Spin locking on either the ^{13}C or ^{1}H nuclei, but not both, suppresses the heteronuclear ^{13}C-^{1}H couplings and the pair of protons 'switch' into magnetic equivalence, where the singlet is isolated.

Lastly in chapter 2 I discuss signal selection in singlet NMR. Singlet spin order is uniquely invariant to rotations of the spins quantisation axes, and therefore separable from other spin order under rotation quadrature. Efficient single-scan filtration of singlet-derived signals is the ultimate goal. Several approached are discussed in depth.

The focus of chapter 3, ('Nuclear singlet relaxation'), is the singlet's slow relaxation phenomenon. General tools for relaxation analysis are outlined starting with Redfield's relaxation formalism leading on to how rotation symmetries in the Liouvillian may impose strong selection rules on singlet relaxation pathways.

Some experimental case-studies are presented. These concentrate upon singlet relaxation caused by out-of-pair mechanisms (mechanisms involving spins other than just the spin pair). The dipolar contribution towards $1/T_S$ from individual passive spins within a molecule is shown to be determinable, within reasonable approximations, as the difference relaxation rates $1/T_S$ upon replacing the passive spin with a nonmagnetic, or effective

nonmagnetic isotope. This is examined using $^{13}C/^{12}C$ and $^{2}D/^{1}H$ isotopic replacement. Singlet lifetimes are more-sensitive to the out-of-pair dipole-dipole couplings than T_1, due to their immunity from the dominating intra-pair dipole-dipole mechanism. One may use this concept to determine reliable constraints on local molecular geometry, for example bond torsion angles.

Paramagnetic relaxation of singlet states is also studied, where the decay mechanism involves modulation of nucleus-electron hyperfine couplings. Singlet relaxation rates are measured versus concentration of paramagnetic transition metal ions in solution, and the data examined using an effective random-field relaxation model. Singlet lifetimes are found to be less-sensitive to paramagnet-induced relaxation than longitudinal polarisation lifetime, though the extent depends on the nature of the paramagnetic agent.

The conclusions section (4, 'Perspectives') highlights the new areas of study opened up by this work, as well as deficiencies that may be addressed in future.

2 Singlet nuclear magnetic resonance

This chapter focuses upon the methodology for excitation and readout of singlet population order. It addresses how to convert equilibrium longitudinal magnetisation into singlet order, and transfer singlet order back to detectable magnetisation. The maximum efficiency of these transformations is discussed, and the likely experimental achievement of this where invariable imperfections are present. Some extra considerations for hyperpolarised samples are also discussed.

Generally speaking, conversions between singlet and triplet spin order is only allowed if the participating spin-1/2 pair are magnetically inequivalent, due to the selection rule for crossing between the symmetric and antisymmetric spin states. Magnetic inequivalence is a frequent situation in polyatomic molecules, occurring where the nuclear pair sites are unrelated by molecular symmetry operations. In high symmetry molecules, the spin pair may be chemically equivalent but possess spin-spin couplings to other nuclei, which break magnetic symmetry.

The magnitude of the magnetic-equivalence-breaking interactions $|H_{\mathrm{asym}}|$ in the spin Hamiltonian is important for which method to use, but is not prohibitive to the efficiency of singlet-triplet conversion. All of the methods described here excite maximum available singlet order, so long as the conversion rate is fast compared to relaxation: that $|H_{\mathrm{asym}}|/2\pi \gg 1/T_1$ or $1/T_2$.

Also discussed are some techniques that produce singlet-'edited' NMR spectra, in which the observed signals derive exclusively from singlet order.

2.1 Dynamics of nuclear singlet and triplet states

This section introduces the basic concepts that will be required for understanding coherent interconversion between singlet and triplet states and how pulse sequences (plus certain other procedures) may in practice achieve this.

2.1.1 Angular momentum and magnetic equivalence symmetry

To recap on the introductory chapter, the nuclear spin wavefunction describing a spin-1/2 pair is a superposition of four orthogonal basis states. The *singlet-triplet* basis is the orthogonal set of states $|l,m\rangle$ possessing definite total ($l \equiv I$) and projection (m) angular momentum quantum numbers. These states are eigenfunctions of both the total I^2 and I_z spin angular momentum operators satisfying

$$I_{jk}^2 \,|l,m\rangle^{jk} \;\equiv\; (\boldsymbol{I}_j + \boldsymbol{I}_k)^2 \,|l,m\rangle^{jk} \;=\; l(l+1)\,|l,m\rangle^{jk} \tag{2.1}$$

$$I_z \,|l,m\rangle^{jk} \;\equiv\; (I_{jz} + I_{kz})\,|l,m\rangle^{jk} \;=\; m\,|l,m\rangle^{jk} \tag{2.2}$$

for explicit spin-1/2 nuclear labels 'j' and 'k', where $\boldsymbol{I}_j = (I_{jx}, I_{jy}, I_{jz})$ denotes the spin angular momentum vector. The overall nonmagnetic state $|0,0\rangle^{jk}$ is the singlet, otherwise symbolised $|S_0^{jk}\rangle$. The three total spin-1 states are the triplet, $|1,m\rangle^{jk} \equiv |T_m^{jk}\rangle$, where m can be -1, 0 or 1. In the Zeeman product basis the states appear as follows:

$$\begin{aligned} |S_0\rangle^{jk} &= (|\alpha_j\beta_k\rangle - |\beta_j\alpha_k\rangle)/\sqrt{2} \qquad & |T_{+1}\rangle^{jk} &= |\alpha_j\alpha_k\rangle \\ |T_0\rangle^{jk} &= (|\alpha_j\beta_k\rangle + |\beta_j\alpha_k\rangle)/\sqrt{2} \qquad & |T_{-1}\rangle^{jk} &= |\beta_j\beta_k\rangle\,. \end{aligned} \tag{2.3}$$

The angular momentum property is key to the problem of singlet-triplet conversion. An Hamiltonian that commutes with the total angular momentum operator I_{jk}^2 must preserve singlet and triplet eigenfunctions, since commuting operators have simultaneous eigenfunctions. Under such conditions, $|0,0\rangle^{jk}$ and $|1,m\rangle^{jk}$ are isolated from one another and do not interconvert. This is to say $|0,0\rangle^{jk}$ and $|1,m\rangle^{jk}$ states only interconvert only when the Hamiltonian does not commute with I_{jk}^2.

More often this commutation rule is referred by the concept of magnetic equivalence symmetry. Spins j and k are 'magnetically equivalent' when H is invariant to swapping

the pair indices. This is to say the relation $P(jk)H = HP(jk)$ holds, where $P(jk)$ is the permutation operator that swaps labels j and k. Connotations for the angular momentum states follow because $P(jk)$ commutes with I_{jk}^2. If H does not commute with $P(jk)$, the two spins are said to be 'magnetically inequivalent'.

Equivalence symmetry is a powerful concept for relaxation, not only coherent evolution. In §1.5.2 this has been applied to explain in basic terms the singlet's invariance to the intra-pair dipole-dipole Hamiltonian. Further details may be found later in §3.1.

2.1.2 Singlet-triplet inconversion during free evolution

Block-diagonal Hamiltonian in the singlet triplet basis

In the so-called 'high-field limit' where the Zeeman interaction dominates the spin Hamiltonian (for most practical purposes, when $B^0 > O(\mu\mathrm{T})$) and when time-dependent magnetic fields (in particular, fields resonant with the Larmor frequency) are absent, the secular part of the coherent Hamiltonian commutes with I_z. Under such conditions, states with different m quantum number do not mix. This means one can partition the quantum states into sets with different m and deal with their evolution separately.

For a spin-1/2 pair the secular Hamiltonian splits into two unit-dimensional subspaces, one for each of the $m = \pm 1$ states, plus one two-dimensional subspace for $m = 0$. This is to say the coherent Hamiltonian appears in the block-diagonal form

$$H = \begin{pmatrix} \langle T_{+1}|H|T_{+1}\rangle & 0 & 0 & 0 \\ 0 & \langle T_0|H|T_0\rangle & \langle T_0|H|S_0\rangle & 0 \\ 0 & \langle S_0|H|T_0\rangle & \langle S_0|H|S_0\rangle & 0 \\ 0 & 0 & 0 & \langle T_{-1}|H|T_{-1}\rangle \end{pmatrix} \begin{matrix} |T_{+1}\rangle \\ |T_0\rangle \\ |S_0\rangle \\ |T_{-1}\rangle \end{matrix} \tag{2.4}$$

or in the operator language, occupies the six-dimensional subspace of zero-quantum operators $|l,m\rangle\langle l',m'|\,\delta_{mm'}$, given by the sum

$$H = \sum_{l,l',m} \langle l',m|H|l,m\rangle\,|l',m\rangle\langle l,m|\,. \tag{2.5}$$

In this case, the operators $|l,m\rangle\langle l',m'|\,\delta_{mm'}$ comprise the population operators $|T_{+1}\rangle\langle T_{+1}|$, $|T_{-1}\rangle\langle T_{-1}|$ of the four basis states, $|T_0\rangle\langle T_0|$ and $|S_0\rangle\langle S_0|$ plus two zero-quantum coherences

$|T_0\rangle\langle S_0|$ and $|S_0\rangle\langle T_0|$ between the $m = 0$ states.

Evolution of $m = \pm 1$ states

Evolution of the one-dimensional m-subspaces is quite simple. The triplet states $|T_{+1}\rangle \equiv |\alpha_j\alpha_k\rangle$ and $|T_{-1}\rangle \equiv |\beta_j\beta_k\rangle$ evolve by acquiring a phase proportional to their energy:

$$|T_{+1}\rangle \xrightarrow{Ht} |T_{+1}\rangle \exp\Big(-\mathrm{i}\omega^{T(+1)}t\Big) \tag{2.6}$$

$$|T_{-1}\rangle \xrightarrow{Ht} |T_{-1}\rangle \exp\Big(-\mathrm{i}\omega^{T(-1)}t\Big), \tag{2.7}$$

for which frequencies are defined

$$\omega^{T(\pm 1)} \equiv \langle T_{\pm 1}|H|T_{\pm 1}\rangle = \mathrm{Tr}(|T_{\pm 1}\rangle\langle T_{\pm 1}|\, H). \tag{2.8}$$

Bloch sphere projection for $|S_0\rangle$ and $|T_0\rangle$

The 2×2 problem of $m = 0$ subspace evolution may be dealt within the 'fictitious spin-1/2' formalism by taking advantage of the properties of a Cartesian representation defined by the projection operator operators

$$I_x^{(S_0T_0)} = \big(|T_0\rangle\langle S_0| + |S_0\rangle\langle T_0|\big)/2 \tag{2.9}$$

$$I_y^{(S_0T_0)} = \big(|T_0\rangle\langle S_0| - |S_0\rangle\langle T_0|\big)/(2\mathrm{i}) \tag{2.10}$$

$$I_z^{(S_0T_0)} = \big(|T_0\rangle\langle T_0| - |S_0\rangle\langle S_0|\big)/2 \tag{2.11}$$

$$E^{(S_0T_0)} = \big(|T_0\rangle\langle T_0| + |S_0\rangle\langle S_0|\big), \tag{2.12}$$

which obey positive cyclic commutation of the form $[I_x^{(S_0T_0)}, I_y^{(S_0T_0)}] = -\mathrm{i}I_z^{(S_0T_0)}$ *etc.* and unity $[E^{(S_0T_0)}, I_x^{(S_0T_0)}] = [E^{(S_0T_0)}, I_y^{(S_0T_0)}] = [E^{(S_0T_0)}, I_z^{(S_0T_0)}] = 0$. In this basis, the total Hamiltonian is represented

$$H = \underbrace{\omega^{T(+1)}I_{j\alpha}I_{k\alpha}}_{m=+1} + \underbrace{\omega^{T(-1)}I_{j\beta}I_{k\beta}}_{m=-1} \underbrace{\omega_x^{(S_0T_0)}I_x^{(S_0T_0)} + \omega_y^{(S_0T_0)}I_y^{(S_0T_0)} + \omega_z^{(S_0T_0)}I_z^{(S_0T_0)} + \omega_E^{(S_0T_0)}E^{(S_0T_0)}}_{m=0\text{ subspace}}, \tag{2.13}$$

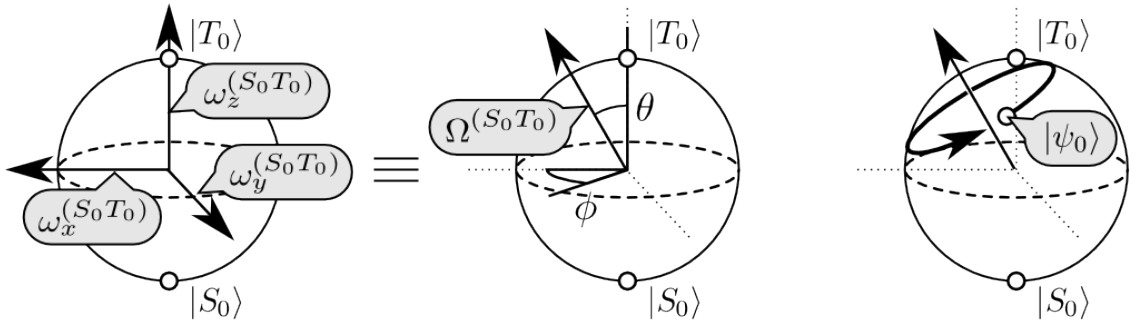

Figure 2.1: Bloch vector representation showing generalised $m = 0$ subspace evolution. The free-evolution trajectory is a rotation about the sum of the Cartesian x, y, z field axes.

where the zero-quantum frequencies of the Cartesian operators are determined through the projections

$$\omega_\xi^{(S_0T_0)} = \frac{\mathrm{Tr}(I_\xi^{(S_0T_0)\dagger} H)}{\mathrm{Tr}(I_\xi^{(S_0T_0)\dagger} I_\xi^{(S_0T_0)})}. \qquad \xi = x,\, y,\, z. \tag{2.14}$$

The Cartesian representation allows instructive geometric visualisation of the two-level subspace evolution using a Bloch sphere.[34, 88] To within a global phase factor, the $m = 0$ state vector, or qubit vector in this representation

$$|\psi_0\rangle = \cos(\vartheta/2)\,|T_0\rangle + \mathrm{e}^{\mathrm{i}\varphi} \sin(\vartheta/2)\,|S_0\rangle \tag{2.15}$$

maps to points $(\vartheta,\, \varphi)$ on the surface of a unit sphere. Fig. 2.1 illustrates that the free-evolution of this qubit vector corresponds to rotation in the Bloch sphere about the combined field axis $I_x^{(S_0T_0)}$, $I_y^{(S_0T_0)}$ and $I_z^{(S_0T_0)}$. The angular frequency of the rotation equals

$$\Omega^{(S_0T_0)} = \sqrt{\left(\omega_x^{(S_0T_0)}\right)^2 + \left(\omega_y^{(S_0T_0)}\right)^2 + \left(\omega_z^{(S_0T_0)}\right)^2} \tag{2.16}$$

and the rotation is oriented with polar angles determined by

$$\theta = \arctan\left(\frac{\sqrt{\left(\omega_x^{(S_0T_0)}\right)^2 + \left(\omega_y^{(S_0T_0)}\right)^2}}{\omega_z^{(S_0T_0)}}\right) \tag{2.17}$$

$$\phi = \arctan\left(\omega_x^{(S_0T_0)} / \omega_y^{(S_0T_0)}\right). \tag{2.18}$$

This geometric representation may be verified by exponentiating the $m = 0$ part of eq.

(2.13), as follows:

$$\begin{aligned} U^{(S_0T_0)}(t) &= \exp(-\mathrm{i}H^{(S_0T_0)}t) \\ &= \exp(-\mathrm{i}\,\omega_E^{(S_0T_0)}t)\exp\Big(-\mathrm{i}(\omega_x^{(S_0T_0)}I_x^{(S_0T_0)} + \omega_y^{(S_0T_0)}I_y^{(S_0T_0)} + \omega_z^{(S_0T_0)}I_z^{(S_0T_0)})t\Big) \\ &\equiv \exp(-\mathrm{i}\,\omega_E^{(S_0T_0)}t)R_{(\sin\theta\cos\phi,\,\sin\theta\sin\phi,\,\cos\theta)}(\Omega^{(S_0T_0)}t). \end{aligned} \tag{2.19}$$

It is important to be aware of the phase $(\omega_E^{(S_0T_0)}t)$ that accompanies the rotation of the Bloch vector. This term is not physically significant when dealing with spin order residing exclusively within the subspace $m = 0$, since the phase cancels when taking the outer product: for example, $[\exp(-\mathrm{i}\,\omega_E^{(S_0T_0)}t)\,|S_0\rangle] \otimes [\langle T_0|\exp(+\mathrm{i}\,\omega_E^{(S_0T_0)}t)]$ is equal simply to $|S_0\rangle \otimes \langle T_0|$, and as such $\omega_E^{(S_0T_0)}$ may be neglected. However, it is essential for observables concerning transitions between the $m = 0$ subspace and the external states $|T_{\pm1}\rangle$. Transverse magnetisation is an important example, the spin order involving triplet-triplet single-quantum coherences $|T_{\pm1}\rangle\langle T_0|$ and $|T_0\rangle\langle T_{\pm_1}|$.

The above formalism has outlined analytical behaviour of the Hilbert space during coherent evolution. For propagation in the Liouville space, one may simply take the ket-bra outer products of the states when required.[4]

2.1.3 Mechanisms for isolated spin-1/2 pair

If the spin pair has no neighbours through coupling, the free-evolution Hamiltonian comprises the Zeeman interaction of each nucleus and intra-pair spin-spin couplings. One may examine how each of these influence the singlet and triplet evolution:

- *Chemical shielding interaction*

  The Zeeman interaction is the splitting of states under the large B^0 static magnetic field, which dominates the total Hamiltonian of the spins. The interaction is written

  $$H_\delta = -\gamma_I B^0(1+\delta_j)I_{jz} - \gamma_I B^0(1+\delta_k)I_{kz} \tag{2.20}$$

  where δ_j and δ_k denote the isotropic chemical shielding for spins j and k. By projecting the above into the form of eq. (2.5), one can see that a difference in shieldings is required for singlet-triplet mixing. The difference induces a rotation about the $I_x^{(S_0T_0)}$-axis in the $m = 0$ Bloch sphere, since the part $(I_{jz} - I_{kz})$ does not commute

with I_{jk}^2. The sum Zeeman interaction, in contrast, evolves the $m = \pm 1$ triplet states:

$$\text{eq. (2.20)} \equiv -\frac{\gamma_I B^0}{2}(2+\delta_j+\delta_k)(\underbrace{I_{j\alpha}I_{k\alpha}}_{m=+1} - \underbrace{I_{j\beta}I_{k\beta}}_{m=-1}) - \underbrace{\gamma_I B^0(\delta_j-\delta_k)I_x^{(S_0T_0)}}_{\text{mixes } m=0 \text{ states}}. \quad (2.21)$$

- *Intra-pair scalar coupling*

  The scalar coupling, or so-called 'indirect dipole-dipole coupling' is the interaction between nuclear spins mediated via electrons in chemical bonds. The Hamiltonian for the scalar coupling is

$$H_J = 2\pi J_{jk}\boldsymbol{I}_j \cdot \boldsymbol{I}_k, \quad (2.22)$$

  where J_{jk} is the coupling constant. By convention this is quoted in Hz.

  Following the same treatment as above, one can see that H_J preserves $|l,m\rangle$ spin eigenfunctions since it is diagonal in both l and m:

$$\text{eq. (2.22)} = \frac{\pi J_{jk}}{2}(\underbrace{I_{j\alpha}I_{k\alpha}}_{m=+1} + \underbrace{I_{j\beta}I_{k\beta}}_{m=-1}) + \underbrace{2\pi J_{jk}I_z^{(S_0T_0)} - \frac{\pi J_{jk}}{2}E^{(S_0T_0)}}_{m=0}. \quad (2.23)$$

  This is consistent with the fact $I_j \cdot I_k$ commutes with the total angular momentum operator, and is invariant to nuclear permutation $\hat{P}(jk)$.

- *Residual dipolar coupling (RDC)*

  In liquid crystal solution or solutions within an external electric field there may exist a net orientational alignment of molecules, resulting in incomplete averaging of the anisotropic internuclear dipolar interaction (see eq. (1.38)):

$$H_{\text{RDC}} = \overline{H_{jk}^{\text{DD}}} = D_{jk}(I_{jx}I_{kx} + I_{jy}I_{ky} - 2I_{jz}I_{kz}) \quad (2.24)$$

  in which D_{jk} is known as the residual dipolar coupling constant. Like the J coupling,

RDC is permutation-symmetric and therefore preserves singlet-triplet eigenstates:

$$\text{eq. (2.24)} \quad \equiv \quad -\frac{D_{jk}}{2}\Big(\underbrace{I_{j\alpha}I_{k\alpha}}_{m=+1} + \underbrace{I_{j\beta}I_{k\beta}}_{m=-1}\Big) + \underbrace{D_{jk}I_z^{(S_0T_0)} + \frac{D_{jk}}{2}E^{(S_0T_0)}}_{m=0}. \quad (2.25)$$

2.1.4 Strongly and weakly coupled eigenstates

States $|T_{\pm 1}\rangle$ are always eigenstates of free evolution in the high field approximation. The $m = 0$ eigenstates on the other hand depend on the interactions present. These, however, are still straightforward to find. The eigenstates are invariant under unitary evolution (to within a phase factor) and therefore must be identified with the points in the Bloch sphere that are invariant to rotation about the field axis. These are clearly the points where the Bloch vector and field axis lie parallel to one another:

$$|\psi_0\rangle \quad = \quad \sin(\theta/2)\,|T_0\rangle + \cos(\theta/2)\,|S_0\rangle \quad (2.26)$$

$$\text{and} \quad |\psi_0\rangle \quad = \quad \cos(\theta/2)\,|T_0\rangle - \sin(\theta/2)\,|S_0\rangle\,. \quad (2.27)$$

with θ that defined in eq. (2.17).

The spin pair is said to be 'weakly coupled' in the regime $|\theta| \ll \pi/2$, where $|\omega_x^{(S_0T_0)}| \gg |\omega_z^{(S_0T_0)}|$. For chemically inequivalent nuclear sites in isotropic solution, the term refers to a spin-spin coupling J_{jk} that is weak compared to the chemical shielding difference $|\gamma B^0(\delta_j - \delta_k)|$. In this limit the spin eigenstates are the Zeeman product states. In the regime where $|\omega_x^{(S_0T_0)}|$ tends in magnitude to $|\omega_z^{(S_0T_0)}|$ we say the pair is 'strongly coupled'. This may occur when J_{jk} and $\gamma B^0(\delta_j - \delta_k)$ have similar magnitude: $|J| \approx |\gamma B^0(\delta_j - \delta_k)|$. In the extreme of perfect equivalence $\theta = 0$, ($\Omega^{(S_0T_0)} = \omega_z^{(S_0T_0)}$) and the singlet and triplet states are exact eigenstates.

2.1.5 Singlet-triplet conversion under applied rf fields

While in the spectrometer high field, transitions between spin states can be stimulated by passing a radio-frequency (rf) oscillating electrical current through an antenna coil next to the NMR sample, generating an oscillating magnetic field. The induced magnetic field may be expressed $\boldsymbol{B}_1(t) = B_1(\cos(\omega_{\rm rf}t + \phi_{\rm rf}),\, 0,\, 0)$, where $\omega_{\rm rf}$ is the alternation frequency, $\phi_{\rm rf}$ the phase and B_1 the peak field amplitude perpendicular to the B^0 axis. The corresponding

spin Hamiltonian, in the laboratory frame, is

$$H_{\rm rf}(t) = \omega_1 \cos(\omega_{\rm rf} t + \phi_{\rm rf}) I_x. \tag{2.28}$$

The prefactor $\omega_1 \equiv -\gamma B_1/2$ is called the *nutation frequency*, and relates the field strength to angular frequency units of the spins.

When $H_{\rm rf}$ is viewed from the reference frame of the coil, the combined Hamiltonian $([H_{\rm Zeeman}]^j + H_{\rm rf}) = (-\gamma B^0(1+\delta_j)I_z + H_{\rm rf})$ for spin j may be seen to approximate a time-independent superposition of I_x, I_y and I_z:

$$\begin{aligned} [\widetilde{H}_{\rm Zeeman}]^j + \widetilde{H}_{\rm rf}(t) &= \exp(-{\rm i}\omega_{\rm rf} t\, I_z)(-\gamma B^0(1+\delta_j)I_z + H_{\rm rf}) \exp(+{\rm i}\omega_{\rm rf} t\, I_z) \\ &\approx \underbrace{I_z(\omega_{\rm rf} - \gamma B^0(1+\delta_j))}_{\text{longitudinal field}} + \underbrace{\omega_1(I_x\cos(\phi_{\rm rf}) + I_y \sin(\phi_{\rm rf}))}_{\text{transverse field}} \end{aligned} \tag{2.29}$$

where tilde '~' denotes the new reference frame. The above is derived as detailed in ref. [4], in brief using the cyclic commutation $[A,\, B] = {\rm i}C$ of operators I_x, I_y and I_z,

$$\exp[-{\rm i}\omega t C] A \exp[+{\rm i}\omega t \hat{C}] = A\cos(\omega t) + B\sin(\omega t), \tag{2.30}$$

followed by ignoring 'nonresonant' or rapid time-oscillating terms.

Nonselective rf pulses

In the majority of cases $|\omega_1|$ (usually $10^0 - 10^2$ kHz order) greatly exceeds the magnitude of all spin-spin J couplings in the system (usually less than 100 Hz) and the spins evolution may be treated individually, *i.e.* by propagation under eq. (2.29) directly and ignoring J couplings. The exponential of eq. (2.29) in the tilde frame is a rotation of the spins polarisation within each $\{|\alpha_j\rangle\,,\, |\beta_j\rangle\}$ Bloch sphere at an angular velocity $\boldsymbol{\tilde{\omega}_j} = (\omega_1\cos(\phi_{\rm rf}),\, \omega_1\sin(\phi_{\rm rf}),\, (\omega_{\rm rf} - \gamma B^0(1+\delta_j)))$.

The rf field is said to be 'on-resonance' if the frequency offset magnitude $|\omega_{\rm rf} - \gamma B^0(1+\delta_j)|$ is much smaller than $|\omega_1|$. In this case the rf field induces transverse rotations in the Bloch sphere through angle $\omega_1 \tau_{\rm rf}$ about the unit axis $(\cos(\phi_{\rm rf}), \sin(\phi_{\rm rf}), 0)$, where $\tau_{\rm rf}$ is the duration the rf field is applied. Note this is a significant perturbation in view that the field

$|B_1| = |\omega_1/\gamma|$ is several orders of magnitude weaker than $|B^0|$:

$$U(\tau_{\rm rf}) = \exp(-{\rm i}[\text{ eq. (2.29) }]\tau_{\rm rf}) \tag{2.31}$$

$$= R_{(\cos(\phi_{\rm rf}),\sin(\phi_{\rm rf}),0)}(\omega_1\tau_{\rm rf}) \qquad \text{for } |\omega_{\rm rf} - \gamma B^0| \ll |\omega_1|. \tag{2.32}$$

For instance, $\phi_{\rm rf} = 0$ signifies the rotation operation is $R_x(\omega_{\rm rf}\tau_{\rm rf})$. For $\phi_{\rm rf} = 90°$, the rotation is $R_y(\omega_{\rm rf}\tau_{\rm rf})$.

The above is one way to solve evolution under rf pulses. Alternatively, the rf-induced transformations may be evaluated directly in the singlet-triplet basis using rules of angular momentum. An on-resonance, nonselective pulse equates to applying a uniform rotation to all spins. The singlet state is rotationally isotropic under these conditions, because the rotation commutes with the spin permutation operator for the pair. Nonselective rf pulses therefore only interchange the triplet states.

In formal terms the angular momentum eigenstates $|l,\, m\rangle$ are the defined irreducible representations of uniform rotations, and interconvert according to

$$R\,|l,m\rangle = \sum_{m'=-I}^{l} |l,m'\rangle\, D^l_{m'm}(R) \tag{2.33}$$

where $D^l_{m'm}(R)$ are elements of the so-called Wigner 'D' matrix.[33, 89] For a rotation $R(\alpha\beta\gamma) = R_z(\alpha)R_y(\beta)R_z(\gamma)$, in the Euler zyz convention,[89] the elements are expressed

$$D^l_{m'm}(\alpha\beta\gamma) = \langle l,m'|R_z(\alpha)R_y(\beta)R_z(\gamma)|l,m\rangle$$

$$= \exp(-{\rm i}(m'\alpha - m'\gamma))d^l_{m'm}(\beta) \tag{2.34}$$

$$d^l_{m'm}(\beta) = \langle l,m'|R_y(\beta)|l,m\rangle\,. \tag{2.35}$$

The reduced elements $d^l_{m'm}(\beta)$ on the lower line are in general rather complicated expressions, but may be derived from angular momentum commutation relations and the definition of the eigenfunctions in eqs. (2.1) and (2.2) and are easily computed. The matrix elements are block diagonal in the l quantum number, confirming the isolation between

the singlet and triplet. The triplet indices m interconvert according to

$$R_x(\xi) \equiv \begin{pmatrix} 1 & 0 & 0 & 0 \\ 0 & \cos^2\left(\frac{\xi}{2}\right) & -\frac{\mathrm{i}\mathrm{e}^{-\mathrm{i}\phi_{\mathrm{rf}}}\sin(\xi)}{\sqrt{2}} & -\mathrm{e}^{-2\mathrm{i}\phi_{\mathrm{rf}}}\sin^2\left(\frac{\xi}{2}\right) \\ 0 & -\frac{\mathrm{i}\mathrm{e}^{\mathrm{i}\phi_{\mathrm{rf}}}\sin(\xi)}{\sqrt{2}} & \cos(\xi) & -\frac{\mathrm{i}\mathrm{e}^{-\mathrm{i}\phi_{\mathrm{rf}}}\sin(\xi)}{\sqrt{2}} \\ 0 & -\mathrm{e}^{2\mathrm{i}\phi_{\mathrm{rf}}}\sin^2\left(\frac{\xi}{2}\right) & -\frac{\mathrm{i}\mathrm{e}^{\mathrm{i}\phi_{\mathrm{rf}}}\sin(\xi)}{\sqrt{2}} & \cos^2\left(\frac{\xi}{2}\right) \end{pmatrix} \begin{matrix} |S_0\rangle \\ |T_{+1}\rangle \\ |T_0\rangle \\ |T_{-1}\rangle \end{matrix} \tag{2.36}$$

where $\xi = \omega_1\tau_{\mathrm{rf}}$ abbreviates the rotation angle induced by the rf field.

Note that the resonant, nonselective rf spin Hamiltonian quenches coherent singlet-triplet transitions and acts as a means of symmetry switching to isolate and sustain long-lived order. Continuous rf irraditation of this type is called a 'spin lock', or sometimes a 'decoupling' field. In this thesis, little will be assumed about the details of spin locking other than this may be used to isolate singlet and triplet states from coherent interconversion. An extensive discussion has already been made in Sarkar's thesis [25] and papers by others. [18, 81, 65]

Transition-selective rf fields

If $|\omega_1|$ is small compared to both the magnitude of J and the Larmor frequency difference $|\gamma B^0(\delta_j - \delta_k)|$, the radiofrequency field may induce different rotations on the nuclei. Such 'spin-selective' rotation is precisely what is needed to induce singlet-triplet interconversion. The subject is considered in more detail in §2.2.4. Note that weak rf fields are unsuitable for singlet spin locking.

2.1.6 Singlet spin order

So far I have mentioned only singlet and triplet states. A formal definition of the corresponding *spin order* has not yet been made, in particular the potentially long-lived singlet spin order. Singlet order is now identified with the singlet-triplet population difference, given by the operator

$$|S_0\rangle\langle S_0| - \frac{1}{3}\Big(|T_{+1}\rangle\langle T_{+1}| + |T_0\rangle\langle T_0| + |T_{-1}\rangle\langle T_{-1}|\Big). \tag{2.37}$$

This operator may be identified because its relaxation involves transitions across the singlet-triplet states. There can be no relaxation between the triplet states, since these

have equal population.

The singlet order is sometimes called *isotropic spin order* due to its invariance under arbitrary global rotations of the spins. In analogy to eq. (1.30) one may use the Clebsch-Gordan series to determine the operators that have distinct rotational transformation properties, via the outer product

$$T_{\Lambda M} = \sum_{l,l',m,m'} |l,m\rangle \langle l',m'| \, C^{00}_{lml'm'} \tag{2.38}$$

such that they transform by

$$RT_{\Lambda M}R^{\dagger} = \sum_{M'=-\Lambda}^{\Lambda} T_{\Lambda M'} D^{\Lambda}_{M'M}(R). \tag{2.39}$$

One can show the set of operators $T_{\Lambda M}$, where $M = -\Lambda \ldots \Lambda$ and $0 \leq \Lambda \leq l + l'$, form an orthogonal operator basis. This basis is referred to as the spherical tensor operator basis, each basis operator $T_{\Lambda M}$ transforming as an irreducible representation of SO(3). The spherical tensor basis is very useful in NMR, especially in the coxtext of singlet NMR, though here is not the place to continue discussing its properties. Significance of $T_{\Lambda M}$ will be considered later in §2.5 for signal filtration, and in §3.1 for a more in-depth treatment of relaxation theory.

By evaluating the Clebsch-Gordan series for $\Lambda = M = 0$ one may show that the operator in eq. (2.37) equates to the totally-symmetric representation T_{00} as

$$\begin{aligned} T_{00} &= \sum_{l,l',m,m'} |l,m\rangle \langle l',m'| \, C^{00}_{lml'm'} \\ &= |0,0\rangle \langle 0,0| - \frac{1}{3}\Big(|1,-1\rangle \langle 1,-1| + |1,0\rangle \langle 1,0| + |1,1\rangle \langle 1,1|\Big) \qquad (2.40) \\ &\equiv |S_0\rangle \langle S_0| - \frac{1}{3}\Big(|T_{-1}\rangle \langle T_{-1}| + |T_0\rangle \langle T_0| + |T_{+1}\rangle \langle T_{+1}|\Big) \qquad (2.41) \end{aligned}$$

As a final comment, note the rotation isotropy is consistent with invariance of singlet order under a nonselective rf field.[65]

2.1.7 Singlet polarisation

For quantifying the level of singlet order in $\overline{\rho}_{\mathrm{eq}}$ it is useful to introduce the concept of 'singlet polarisation'. This is analogous to the more familiar concept of Zeeman polarisation, which quantifies the level of longitudinal spin order. The Zeeman polarisation (or just 'polarisation', more colloquially) of an ensemble of noninteracting spin-1/2 nuclei is defined by the population difference

$$p = n(\alpha) - n(\beta) \tag{2.42}$$

where $n(\alpha)$ and $n(\beta)$ are the normalised populations of the spin states with angular momentum parallel and antiparallel to the magnetic field: $n(\alpha) = \overline{\langle\alpha|\psi\rangle}/\langle\alpha|\alpha\rangle = (1+p)/2$ and $n(\beta) = \overline{\langle\beta|\psi\rangle}/\langle\beta|\beta\rangle = (1-p)/2$. The polarisation has extrema $p = \pm 1$, corresponding to which all molecules in the ensemble occupy $|\alpha\rangle$ or $|\beta\rangle$, respectively.

For an ensemble of coupled spin-1/2 pairs (of spins j and k) the populations of the Zeeman product basis are given by the products of the populations p_j and p_k on each spin:

$$\begin{aligned} n(\alpha_j\alpha_k) &= (1+p_j)(1+p_k)/4 \\ n(\alpha_j\beta_k) &= (1+p_j)(1-p_k)/4 \\ n(\beta_j\alpha_k) &= (1-p_j)(1+p_k)/4 \\ n(\beta_j\beta_k) &= (1-p_j)(1-p_k)/4. \end{aligned} \tag{2.43}$$

Longitudinal polarisation is in this case defined as the difference $n(\alpha_1\alpha_2) - n(\beta_1\beta_2) \equiv p$, or more prosaically, the population difference between the states $|T_{+1}\rangle \equiv |\alpha\alpha\rangle$ and $|T_{-1}\rangle \equiv |\beta\beta\rangle$. In terms of operators, p is the projection of the density operator onto the sum $I_z = I_{jz} + I_{kz}$: $\quad p = \mathrm{Tr}(I_z|\overline{\rho})/\mathrm{Tr}(I_z|I_z)$. Extrema $p = \pm 1$ correspond in this case to all ensemble members in states $|T_{\pm 1}\rangle$, respectively.

Singlet polarisation p_S is defined as the mean singlet-triplet population difference

$$p_S = n(S_0) - \frac{1}{3}\big(n(T_{+1}) + n(T_0) + n(T_{-1})\big), \tag{2.44}$$

such that $p_S = \mathrm{Tr}(T_{00}|\overline{\rho})/\mathrm{Tr}(T_{00}|T_{00})$. The normalisation with T_{00} is purely coincidental; the above convention is chosen so that the maximum singlet-triplet population difference

is $p_S = +1$. In this limit the density operator corresponds to unity population of $|S_0\rangle$, and zero population of $|T_m\rangle$. Note that in contrast to p, the singlet polarisation ranges between $p_S = -1/3$ and $p_S = +1$ and is unsymmetrical about zero polarisation. This comes into significance when working with hyperpolarised ensembles, which are discussed later in §2.4. For the rest of the material in thesis, only ordinary thermal polarisation levels (of order 10^{-4} or 10^{-5}) will be considered.

2.1.8 Magnetisation-singlet conversion efficiency

While the limits of p and p_S are determined by maximum population asymmetry in the density operator a more careful analysis remains to see the allowed limits to the transfer of spin order between the two forms. The maximum transfer amplitude between two operators can be worked out without difficulty, and is done using a general formula derived for this problem by Sørensen,[90] and further discussed by Levitt.[16, 91] If an initial operator Q_A is assumed, the maximum allowed transformation onto an operator Q_B under a unitary tranformation $\hat{U}$ is given by

$$\left|\frac{\mathrm{Tr}(Q_B^\dagger \hat{U} Q_A)}{\mathrm{Tr}(Q_B^\dagger Q_B)}\right|_{\max} = \frac{\mathbf{\Lambda}_B \cdot \mathbf{\Lambda}_A}{\mathbf{\Lambda}_B \cdot \mathbf{\Lambda}_B}, \tag{2.45}$$

in which $\mathbf{\Lambda}_A$ and $\mathbf{\Lambda}_B$ are ordered lists of the eigenvalues of the operators Q_A and Q_B.

In the current case, the two operators correspond to $I_z = (I_{jz} + I_{kz})$ and T_{00}^{jk} for magnetisation-to-singlet conversion. The eigenvalue spectra are already known because both operators are diagonal in the $|l, m\rangle$ basis. For the longitudinal polarisation one has:

$$(I_{jz} + I_{kz}) \equiv \begin{pmatrix} 1 & 0 & 0 & 0 \\ 0 & 0 & 0 & 0 \\ 0 & 0 & 0 & 0 \\ 0 & 0 & 0 & -1 \end{pmatrix} \begin{matrix} |T_{+1}\rangle \\ |T_0\rangle \\ |S_0\rangle \\ |T_{-1}\rangle \end{matrix} \quad \Rightarrow \quad \mathbf{\Lambda} = \begin{pmatrix} -1 \\ 0 \\ 0 \\ 1 \end{pmatrix}, \tag{2.46}$$

and for the singlet order,

$$T_{00}^{jk} \equiv \begin{pmatrix} -1/3 & 0 & 0 & 0 \\ 0 & -1/3 & 0 & 0 \\ 0 & 0 & 1 & 0 \\ 0 & 0 & 0 & -1/3 \end{pmatrix} \begin{matrix} |T_{+1}^{jk}\rangle \\ |T_{0}^{jk}\rangle \\ |S_{0}^{jk}\rangle \\ |T_{-1}^{jk}\rangle \end{matrix} \quad \Rightarrow \quad \mathbf{\Lambda} = \begin{pmatrix} -1/3 \\ -1/3 \\ -1/3 \\ 1 \end{pmatrix}. \tag{2.47}$$

Using eq. (2.45) with $Q_A = I_z$ and $Q_B = T_{00}^{jk}$ one obtains a maximum conversion amplitude of 1 between starting longitudinal polarisation and singlet order. This means the maximum singlet polarisation starting from pI_z is equal to $p_S = p$.

Now consider the reverse transformation (singlet order into magnetisation I_z), with $Q_A = T_{00}^{jk}$ and $Q_B = I_z$. Eq. (2.45) evaluates to $2/3$ in this case, meaning that the maximum longitudinal polarisation obtained from $p_S T_{00}$ is equal to $p = 2p_S/3$.

These limits highlight an important fact in considering the use of singlet spin order. The conversion of longitudinal polarisation into singlet order, and back again, generates at most $2/3$ of the starting polarisation. So while one may exploit the sensitivity gain from long lifetimes, there is a cost of 33% against the initial magnetisation. For singlet order to provide a net sensitivity gain, the lifetime ratio T_S/T_1 must compensate this loss.

2.2 Singlet NMR of two isolated spins-1/2

This section covers singlet preparation and readout methods for both high and low magnetic fields for a spin-1/2 pair with no coupled neighbours, *i.e.* an isolated system of chemically inequivalent spins-1/2. The choice of method depends upon whether the spin pair is weakly or strongly coupled.

2.2.1 Adiabatic field cycling

This method operates by transferring a population difference between the nuclear Zeeman eigenstates of the pair in high magnetic field into a population difference between singlet-triplet eigenstates at a low magnetic field. Recall from §2.1.4 the pair eigenstates are

$$\begin{pmatrix} |\phi_1\rangle \\ |\phi_2\rangle \\ |\phi_3\rangle \\ |\phi_4\rangle \end{pmatrix} = \begin{pmatrix} 1 & 0 & 0 & 0 \\ 0 & \cos(\theta/2) & \sin(\theta/2) & 0 \\ 0 & -\sin(\theta/2) & \cos(\theta/2) & 0 \\ 0 & 0 & 0 & 1 \end{pmatrix} \begin{pmatrix} |T_{+1}\rangle \\ |T_0\rangle \\ |S_0\rangle \\ |T_{-1}\rangle \end{pmatrix} \tag{2.48}$$

where $\theta = \arctan(-\gamma B^0(\delta_j - \delta_k)/2\pi J)$. On reducing the B^0 field strength the mixing angle θ tends to zero, such that at low magnetic fields the spins become more strongly coupled and closer to equivalence. In the limit we have singlet and triplet eigenstates

$$\lim_{|\theta|\to 0} |\phi_2\rangle = |T_0\rangle \tag{2.49}$$

$$\lim_{|\theta|\to 0} |\phi_3\rangle = |S_0\rangle \tag{2.50}$$

At higher fields where $|B^0| \gg |J/\gamma(\delta_j - \delta_k)|$ the angle θ tends to $\pm\pi/2$ and the eigenstates are the Zeeman product states. For an homonuclear pair with positive scalar coupling constant J, gyromagnetic ratio γ, and isotropic chemical shielding difference $(\delta_j - \delta_k)$, the angle θ tends to $-\pi/2$ into a static field $B^0 > 0$, resulting in eigenstates

$$\lim_{|\theta|\to 0} |\phi_2\rangle = |\beta_j\alpha_k\rangle \tag{2.51}$$

$$\lim_{|\theta|\to 0} |\phi_3\rangle = |\alpha_j\beta_k\rangle \tag{2.52}$$

The low-field and high-field eigenstates correlate in this case as [19]

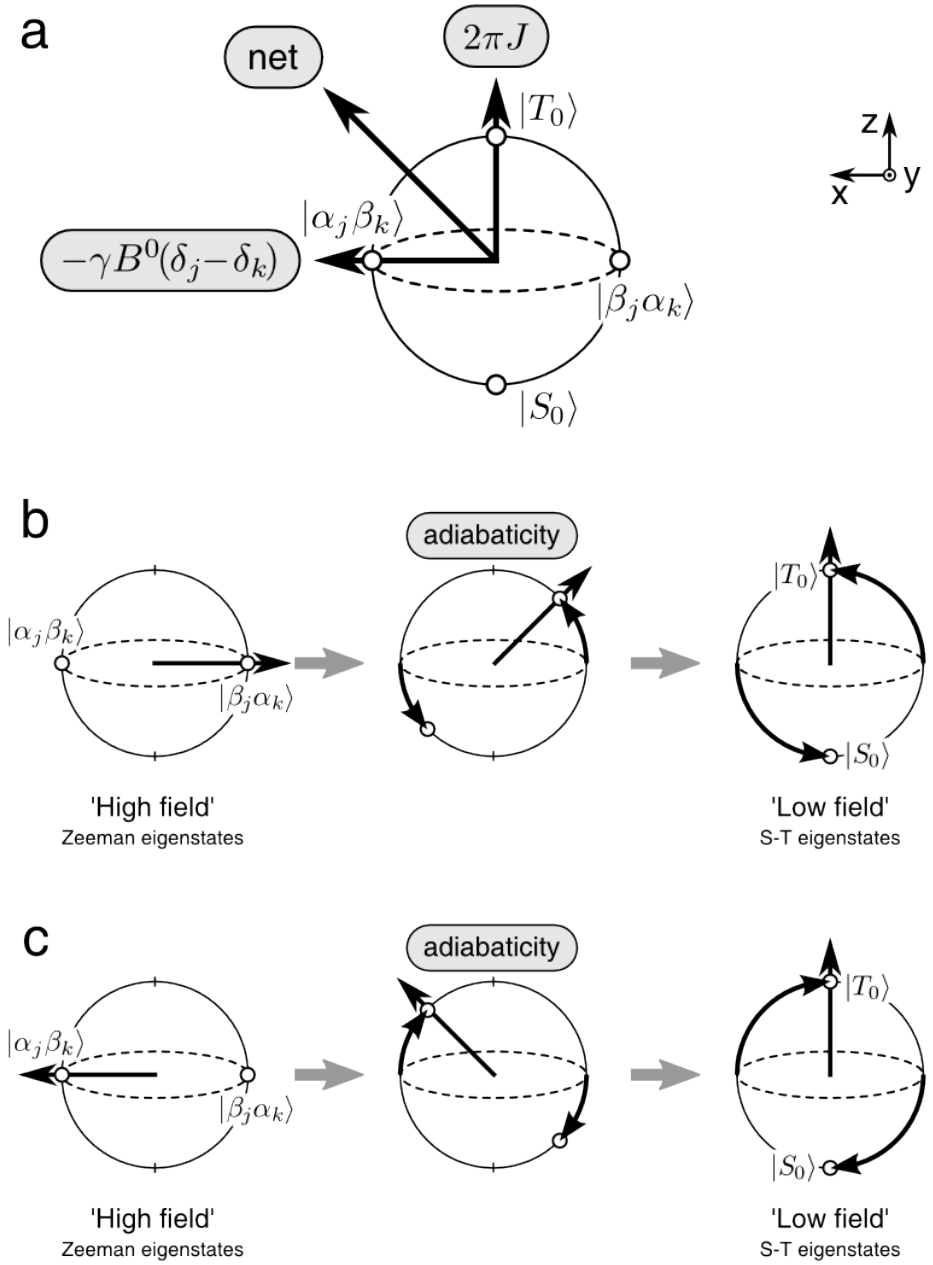

Figure 2.2: Illustration of state correlation on the $m = 0$ Bloch sphere during adiabatic field cycling. The arrows in (a) mark the rotation axes about which the quantum state evolves. The $m = 0$ eigenstates occur at the two points where the net field axis intersects the sphere's surface. During adiabatic transfer, the eigenstates follow the movement of the rotation axis, such that their populations are 'dragged across' the sphere. The trajectory in (b) shows the trajectory taken between weakly coupled spin eigenstates in high magnetic field and strongly coupled eigenstates in low field for $\text{sign}(\gamma B^0(\delta_j - \delta_k)) = \text{sign}(J) = +1$. If the relative sign changes, states must correlate the other way around; in (c), the trajectory is that for negative $\gamma B^0(\delta_j - \delta_k)$, with J positive.

$$|\alpha_j\beta_k\rangle \leftrightarrow |S_0\rangle \qquad |\beta_j\alpha_k\rangle \leftrightarrow |T_0\rangle \tag{2.53}$$
$$|\alpha_j\alpha_k\rangle \leftrightarrow |T_{+1}\rangle \qquad |\beta_j\beta_k\rangle \leftrightarrow |T_{-1}\rangle\,.$$

For opposite sign in $(\gamma B^0(\delta_j - \delta_k)/J)$, the states $|T_0\rangle$ and $|S_0\rangle$ will correlate the other way around. These rotations are summarised graphically in fig. 2.2.

The above transformations permit populations of the high-field Zeeman states to be smoothly transferred into the low-field singlet and triplet by adiabatic transport of the sample between different field strengths. Transport is adiabatic so long as the change in the spin Hamiltonian remain slower than the smallest difference in energy eigenvalues of the system. The velocity of the Hamiltonian during field cycling is the time derivative of the Larmor frequency: $(2\pi)^{-1}\gamma \mathrm{d}B^0/\mathrm{d}t$. The smallest eigenvalue difference is the zero-quantum frequency, given by $|\,\langle\phi_2|H|\phi_2\rangle - \langle\phi_3|H|\phi_3\rangle\,| = \sqrt{(\gamma B^0(\delta_j - \delta_k))^2 + (2\pi J)^2}$, which tends to J in the low-field limit. The adiabatic condition is therefore satisfied if the transport time is slow compared to $|1/J|$.

Invariable presence of relaxation means field cycling must also take place fast compared to the nuclear T_1. This may not be so easily achieved for protons, where T_1 is often the order of seconds and comparable to $1/|J|$. Field cycling best favours lower-gamma nuclei, (*e.g.* ^{13}C and ^{15}N), since at moderate field strengths the T_1s are usually much longer than $1/|J|$. Also, in general, the relaxation mechanisms for low-gamma nuclei are less potent than those for protons, meaning T_S is also longer.

Magnetisation-singlet conversion

Conversion of longitudinal magnetisation into singlet order was demonstrated using the field cycling method by Carravetta and co workers in 2004.[19] A DMSO solution containing 2,3-dibromothiophene (a system containing two isolated and weakly coupled protons) was pre-polarised to thermal magnetisation at $B^0 \approx 9.4$ T. A spin-selective 180° pulse was applied, followed by adiabatic sample transport into low magnetic field.

To run through the sequence of transformations analytically, a selective 180° rotation exchanges the populations of outer and inner Zeeman states:

$$\text{invert spin } j\text{:} \qquad |\alpha_j\alpha_k\rangle \leftrightarrow |\beta_j\alpha_k\rangle\,; \qquad |\alpha_j\beta_k\rangle \leftrightarrow |\beta_j\beta_k\rangle \tag{2.54}$$
$$\text{invert spin } k\text{:} \qquad |\alpha_j\alpha_k\rangle \leftrightarrow |\alpha_j\beta_k\rangle\,; \qquad |\beta_j\alpha_k\rangle \leftrightarrow |\beta_j\beta_k\rangle\,. \tag{2.55}$$

This converts longitudinal polarisation

$$pI_z \;=\; p\Big(|T_{+1}\rangle\langle T_{+1}| - |T_{-1}\rangle\langle T_{-1}|\Big) \tag{2.56}$$

$$\equiv\; p\Big(|\alpha_j\alpha_k\rangle\langle\alpha_j\alpha_k| - |\beta_j\beta_k\rangle\langle\beta_j\beta_k|\Big) \tag{2.57}$$

into a 'precursor' [19] to singlet order that contains a population difference across the $m = 0$ Zeeman states, namely the $I_x^{(S_0T_0)}$ spin operator:

$$\text{eq. (2.57)} \xrightarrow{\text{invert } j} p\Big(|\beta_j\alpha_k\rangle\langle\beta_j\alpha_k| - |\alpha_j\beta_k\rangle\langle\alpha_j\beta_k|\Big) \tag{2.58}$$

$$= \quad -2pI_x^{(S_0T_0)}$$

$$\text{eq. (2.57)} \xrightarrow{\text{invert } k} p\Big(|\alpha_j\beta_k\rangle\langle\alpha_j\beta_k| - |\beta_j\alpha_k\rangle\langle\beta_j\alpha_k|\Big) \tag{2.59}$$

$$= \quad +2pI_x^{(S_0T_0)}.$$

Selective inversion may be executed as illustrated in fig. 2.3(a)i by applying a pair of nonselective 90° pulses resonant with the mean Larmor frequency of the spin pair, which are separated by a free evolution delay $\tau_\Delta = \pi/|\gamma B^0(\delta_j - \delta_k)|$. The relative phase between the two pulses governs the spin selectivity. For $\gamma B^0(\delta_j - \delta_k) > 0$,

$$p(I_{jz} + I_{kz}) \xrightarrow{90_0 - \tau_\Delta - 90_{\pm 90}} \pm p(I_{jz} - I_{kz}). \tag{2.60}$$

Alternatively, a weak rf field on-resonance may be applied on resonance with either nucleus, as illustrated in fig. 2.3(a)ii.

Adiabatic transport of the precursor $I_x^{(S_0T_0)}$ into low field $|B^0| \ll |2\pi J/\gamma(\delta_j - \delta_k)|$ generates a population difference across $|S_0\rangle$ and $|T_0\rangle$:

$$pI_x^{(S_0T_0)} \xrightarrow{|\theta| \to 0} \pm 2pI_z^{(S_0T_0)} \;\equiv\; \pm p(|T_0\rangle\langle T_0| - |S_0\rangle\langle S_0|). \tag{2.61}$$

This transformation can be verified with the aid of fig. 2.2. The resulting singlet polarisation is

$$p_S \;=\; 2p\frac{\mathrm{Tr}(T_{00}^\dagger I_z^{(S_0T_0)})}{\mathrm{Tr}(T_{00}^\dagger T_{00})} = p. \tag{2.62}$$

This polarisation equals the value predicted by Sørensen for the maximum conversion

between I_z and T_{00}, as discussed in §2.1.8.

Once in low field $|B^0| \ll |2\pi J/\gamma(\delta_j - \delta_k)|$ the singlet order is an eigenoperator and relaxes monoexponentially with time constant T_S (fig. 2.3(b)).

Detection of singlet order after adiabatic reinsertion

The singlet order is overall nonmagnetic (total spin $I = 0$) and in the absence of symmetry-breaking spin interactions at low magnetic field remains undetectable. Conversion of singlet order to detectable magnetisation is done by adiabatically transporting the sample back to high field, for observation. The state immediately after reinsertion is referred to as the adiabatic 'postcursor' to T_{00}.[19] The nature of spin populations in the postcursor depends on the final sign of θ:

$$p_S T_{00} \xrightarrow{\theta \to -\pi/2} p_S \left|\alpha_j\beta_k\right\rangle\left\langle\alpha_j\beta_k\right| - \frac{p_S}{3}\Big(\left|\beta_j\alpha_k\right\rangle\left\langle\beta_j\alpha_k\right| + \left|\alpha_j\alpha_k\right\rangle\left\langle\alpha_j\alpha_k\right| + \left|\beta_j\beta_k\right\rangle\left\langle\beta_j\beta_k\right|\Big) \tag{2.63}$$

$$p_S T_{00} \xrightarrow{\theta \to +\pi/2} p_S \left|\beta_j\alpha_k\right\rangle\left\langle\beta_j\alpha_k\right| - \frac{p_S}{3}\Big(\left|\alpha_j\beta_k\right\rangle\left\langle\alpha_j\beta_k\right| + \left|\alpha_j\alpha_k\right\rangle\left\langle\alpha_j\alpha_k\right| + \left|\beta_j\beta_k\right\rangle\left\langle\beta_j\beta_k\right|\Big). \tag{2.64}$$

The postcursor may be converted into observable magnetisation in a multitude of ways. The most common ones are summarised graphically in fig. 2.3(c)i-iv. The simplest method, to start with, is a single rf pulse (fig. 2.3(c)i). Assuming weakly coupled spins in high field, a strong, nonselective radiofrequency pulse with flip angle ξ generates an NMR signal that comprises the outer J-doublet peaks with opposite amplitudes

$$\pm p_S \times \cos^2(\xi/2)\sin(\xi)/2, \tag{2.65}$$

and inner doublet peaks with opposite amplitudes

$$\pm p_S \times \sin^2(\xi/2)\sin(\xi)/2. \tag{2.66}$$

Fig. 2.3(d)i illustrates spectra in the case of a 90° read pulse ($\xi = \pi/2$) and a small flip angle pulse ($|\xi| \ll \pi/2$). The small flip angle gives peak intensities proportional to the population differences across the states. In this case, the two outer peaks occur with

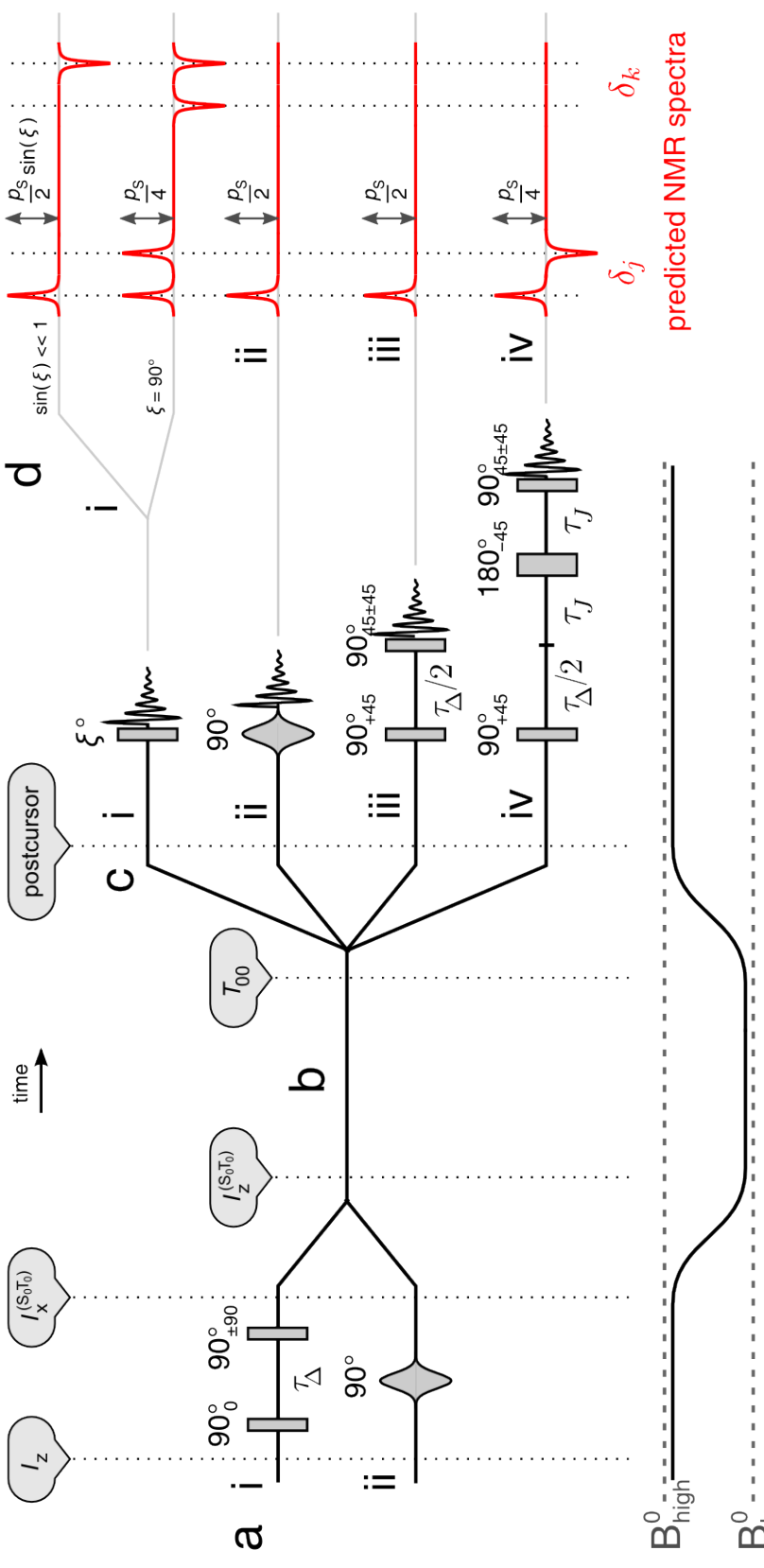

Figure 2.3: Overview of the field cycling procedures for singlet preparation and observation. The high and low magnetic fields are indicated by $B^0_{\text{high}} \gg 2\pi J/\gamma(\delta_j - \delta_k)$ and $B^0_{\text{low}} \ll 2\pi J/\gamma(\delta_j - \delta_k)$.

opposite amplitudes $\propto p_S$. The inner transitions are absent, since the adiabatic postcursor contains equal populations in the connected states. The 90° pulse generates a characteristic 'up-down' spectrum pattern.

These intensities are similar to those obtained applying a nonselective pulse to pure longitudinal order pI_z in a weakly coupled pair. A pulse of flip angle ξ excites all four transitions with equal amplitude

$$p \times \sin(\xi)/4. \tag{2.67}$$

Comparing with the sum of eqs. (2.65) and (2.66), one may confirm that for the same pulse flip angle, the area under each J-doublet is (p_S/p) times that from the longitudinal polarisation. The maximum singlet-derived NMR signal is therefore 2/3 the intensity obtainable from the same starting angle pulse on the same initial longitudinal order.

Alternatively one may apply a spin-selective 90° pulse to the singlet postcursor (fig. 2.3(c)ii).[22] A selective 90° rotation of spin j results in a double-intensity peak for the outermost transition of spin j (twice the intensity of that from a nonselective 90° read pulse) and no signal at all for site k (fig. 2.3(d)ii). Fig. 2.3(c)iii shows a sequence that mimics selective 90° rotation while using nonselective pulses. The rf carrier frequency is positioned at the mean chemical shift frequency, whereat the chemical shift difference induces opposite 45° rotations on the spins. Spin selectivity depends on the relative pulse phase:[22]

$$\left(90^\circ_{+45}\right) - \left(\tau_\Delta/2\right) - \left(90^\circ_{90}\right) \equiv \left(90^{\circ(j)}_{0} 180^{\circ(k)}\right); \tag{2.68}$$

$$\left(90^\circ_{+45}\right) - \left(\tau_\Delta/2\right) - \left(90^\circ_{0}\right) \equiv \left(180^{\circ(j)} 90^{\circ(k)}_{90}\right), \tag{2.69}$$

where, as before, $\tau_\Delta = \pi/|\gamma B^0(\delta_j - \delta_k)|$.

In fig. 2.3(c)iv a fourth readout sequence is illustrated. This is the same as fig. 2.3(c)iii, but into which a spin echo element

$$\left(\frac{1}{|4J|}\right) - \left(180^\circ_{-45}\right) - \left(\frac{1}{|4J|}\right) \tag{2.70}$$

is absorbed. The spin echo preserves the transformation of the adiabatic postcursor, whilst suppressing signals from longitudinal magnetisation that may build up during cycling back

to high field. In brief, un-coupled single-quantum coherences are converted into antiphase coherences through evolution under the J coupling.

$$I_{jz} \xrightarrow{90^\circ_{45}} \frac{1}{\sqrt{2}}(I_{jx} - I_{jy}) \xrightarrow{\text{eq. (2.70)}} \sqrt{2}(I_{jx} + I_{jy})I_{kz}. \tag{2.71}$$

The final 90° pulse converts these to non-observable double- and zero-quantum coherence:

$$\text{eq. (2.71)} \xrightarrow{\pi/|2\gamma B^0(\delta_j - \delta_k)|} 2I_{jy}I_{kz} \xrightarrow{90^\circ_{90}} \underbrace{\sqrt{2}I_{jy}I_{kx}.}_{\text{unobservable}} \tag{2.72}$$

The coupled spin order of the adiabatic postcursor commutes with $(I_j \cdot I_k)$, and therefore passes unperturbed through the spin echo.

ALTADENA

Adiabatic population transfer between singlet-triplet and Zeeman eigenstates is well known in the field of parahydrogen-enhanced NMR. In the experiment known as ALTADENA (*Adiabatic Longitudinal Transport After Dissociation Engenders Nuclear Alignment*),[56] an unsaturated substrate is hydrogenated with parahydrogen in 'low' magnetic field $|B^0| \ll |2\pi J/\gamma B^0 \Delta\delta|$, *e.g.* at the laboratory magnetic field. The singlet spin order of parahydrogen correlates directly into singlet-hydrogenated product as indicated in fig. 2.4(a). For readout, the high-field adiabatic *postcursor* corresponds to a population excess in $|\alpha_j\beta_k\rangle$ and zero population in the other states (assuming $\theta \to -\pi/2$, see fig. 2.4(b)).

'Direct' singlet hyperpolarisation

Singlet order is available immediately from an hyperpolarised spin-1/2-pair ensemble, without need for pulse sequences.[32] This phenomenon is demonstrated for the ^{13}C spin-pair in [1,2-$^{13}C_2$]-labelled pyruvic acid, ($CH_3{}^{13}CO{}^{13}COOH$, or [1,2-$^{13}C_2$] 2-oxopropanoic acid) in a solution of D_2O using the dissolution-DNP hyperpolarisation procedure.[47, 49]

The experiments were made as part of a collaboration with Kevin Brindle's laboratory (Cambridge University Biochemistry Department) as an initial step to explore hyperpolarised singlet NMR in vivo. Hyperpolarised NMR of [^{13}C]-pyruvate sits in a prominent position in metabolism and oncology studies due to the slow T_1 relaxation relative to uptake and metabolism in cells, and the relative ease of ^{13}C polarisation.[92, 93, 94] Simul-

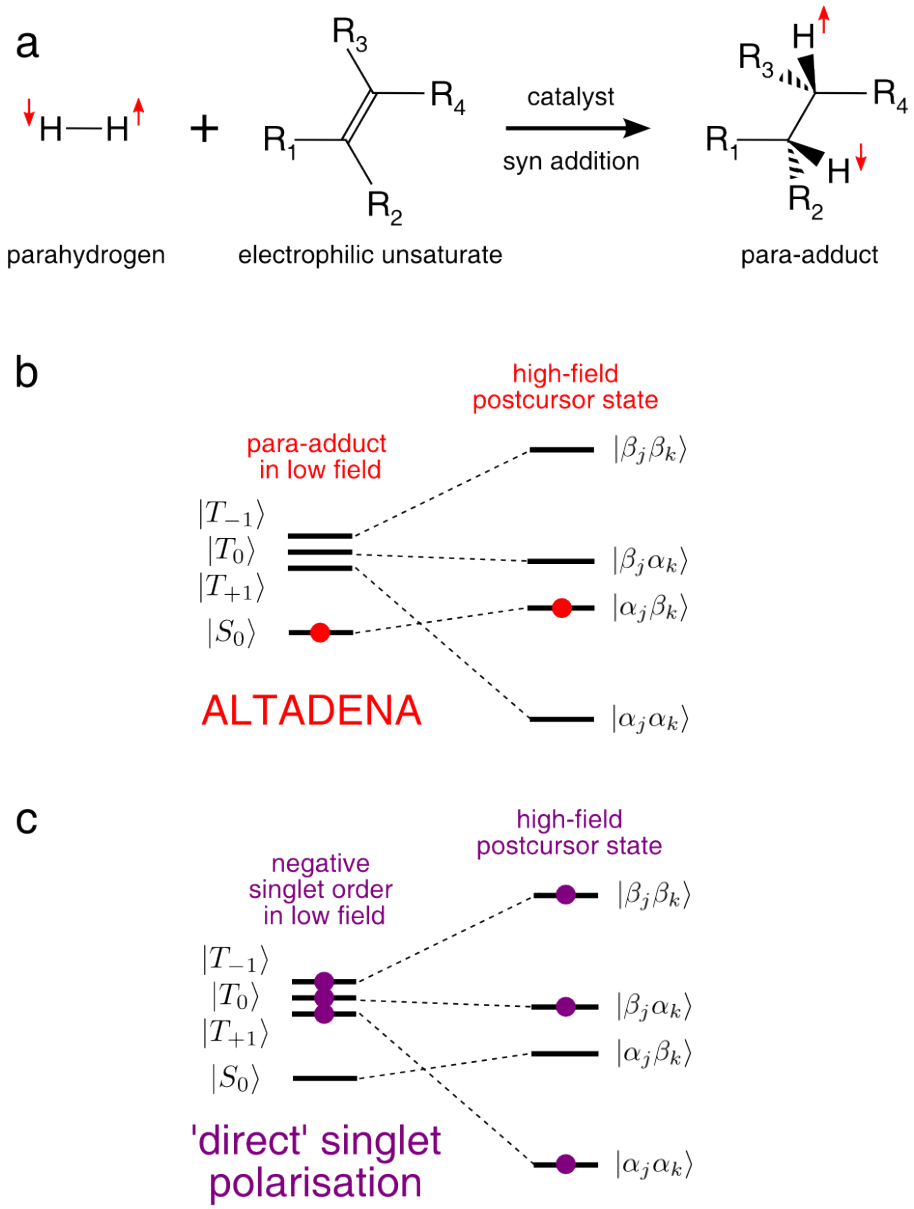

Figure 2.4: Examples of adiabatic field cycling in singlet NMR: (a) one of the many possible reaction schemes for parahydrogen-induced hyperpolarisation (PHIP); (b) low to high-field correlation between hyperpolarised singlet order of a parahydrogenated substance and the adiabatic postcursor state on which NMR readout is performed. This is the ALTADENA experiment. For simplicity a polarisation $p_S = +1$ is assumed in the adduct; (c) the analogue of ALTADENA for singlet depletion order in an hyperpolarised sample, for simplicity assuming a pure singlet polarisation $p_S = -1/3$. Labels apply to the case $2\pi J/\gamma B^0(\delta_j - \delta_k) > 0$.

taneous real-time monitoring of pyruvate dehydrogenase and Krebs cycle metabolism in heart has been demonstrated using hyperpolarised [1,2-$^{13}C_2$]-pyruvate.[95] Metabolic flux between hyperpolarised [1-^{13}C]-pyruvate and lactate has been used to grade tumours and their response to treatment.[92, 96]

Labelled pyruvic acid was polarised in an alpha-prototype hyperpolariser (GE Healthcare, Amersham, UK) working at 3.35 T according to the procedure given in ref. [96]. A mixture containing 35 mg [1,2-$^{13}C_2$] pyruvic acid (95% purum, Sigma-Aldrich UK), 0.7 mg of the trityl radical OX063 (GE Healthcare, Little Chalfont, UK) and 1.2 mg of 0.1 μM gadolinium chelate solution (Gadoteric acid, Dotarem®; Guerbet, Roissy, France) was cooled to 1.2 K in liquid He and irradiated close to the electron Larmor frequency at ≈ 94 GHz, using a 100 mW microwave source. The build-up of ^{13}C polarisation was monitored via the solid-state NMR signal.

DNP of [1,2-$^{13}C_2$]-pyruvate creates a significant population imbalance between $m = 0$ states ($n_{\alpha_1\beta_2} + n_{\beta_1\alpha_2}$) and $m = \pm 1$ states ($n_{\alpha_1\alpha_2} + n_{\beta_1\beta_2}$) of the ^{13}C spin pair. Assuming both spins are equally polarised during the process ($p_j = p_k = p$), these populations are given using eq. (2.43) as

$$n(\alpha_j\alpha_k) = (1+p)(1+p)/4 = (1+2p+p^2)/4 \quad (2.73)$$

$$n(\alpha_j\beta_k) = (1+p)(1-p)/4 = (1-p^2)/4 \quad (2.74)$$

$$n(\beta_j\alpha_k) = (1-p)(1+p)/4 = (1-p^2)/4 \quad (2.75)$$

$$n(\beta_j\beta_k) = (1-p)(1-p)/4 = (1-2p+p^2)/4. \quad (2.76)$$

After approximately 1 hour of microwave irradiation the frozen material was dissolved with a jet of hot buffer solution (6 ml, heated to 180 °C, containing 100 mg/L EDTA, 30 mM NaCl, 94 mM NaOH and 40 mM 4-(2-hydroxyethyl)-1-piperazineethanesulfonic acid (HEPES)) and the solution collected in a vial located in a region of low magnetic field ($\approx$ 0.5 mT) outside the polariser magnet. During transport, the high-field eigenstates are transformed adiabatically into the nuclear singlet and triplet eigenstates. Ignoring

relaxation losses during sample melting and transport, the low-field populations are

$$n(T_{+1}) = (1 + 2p + p^2)/4 \tag{2.77}$$

$$n(T_0) = (1 - p^2)/4 \tag{2.78}$$

$$n(S_0) = (1 - p^2)/4 \tag{2.79}$$

$$n(T_{-1}) = (1 - 2p + p^2)/4. \tag{2.80}$$

The mean singlet-triplet population difference in the low field is therefore

$$p_S = n(S_0) - \frac{1}{3}(n(T_{+1}) + n(T_0) + n(T_{-1})) = -p^2/3. \tag{2.81}$$

Note the negative sign of p_S, which arises since strong nuclear polarisation depletes the $m = 0$ states, leading to population deficit in the singlet. Although this singlet polarisation is significantly lower than the longitudinal order, it may nevertheless be substantial compared to $p_{\text{thermal}} = \tanh(\gamma_C \hbar B^0/2k_B T)$, which is the order of 8 ppm for ^{13}C in [^{13}C]-pyruvate at 9.4 T and room temperature. A 30%-polarised ensemble, ($p = 0.3$), for instance, yields 3% negative singlet order ($p_S = -0.03$). This is still 3 orders of magnitude larger than thermal polarisation.

Amplitudes of p and p_S were estimated by sharing the hyperpolarised solution between two identical 10 mm o.d. NMR sample tubes, each already containing 2.0 ml D_2O, resulting in a final pyruvate concentration ≈ 10 mM. The first tube was inserted immediately into a 9.4 T, Varian Inova NMR spectrometer and the ^{13}C NMR spectrum recorded after a $\approx 6°$ flip angle pulse. The spectrum is shown in fig. 2.5(a) and is characteristic of the predominant longitudinal spin order, with all peaks having the same sign.

In the intervening time, the second tube was inserted into a mu-metal cylinder (15 mm tube diameter, 0.5 mm wall thickness) and shaken for ≈ 5 seconds. This sample was then removed from the cylinder, inserted in the NMR spectrometer in place of the first tube, and the spectrum recorded after applying the same $\approx 6°$ flip angle pulse.

As explained in §2.5.7, shaking of the sample in the weak and sharply inhomogeneous magnetic field of the cylinder's edge induces spatially random rotations on the spins. This has the effect of rapidly equalising the nuclear triplet populations and erasing triplet-triplet

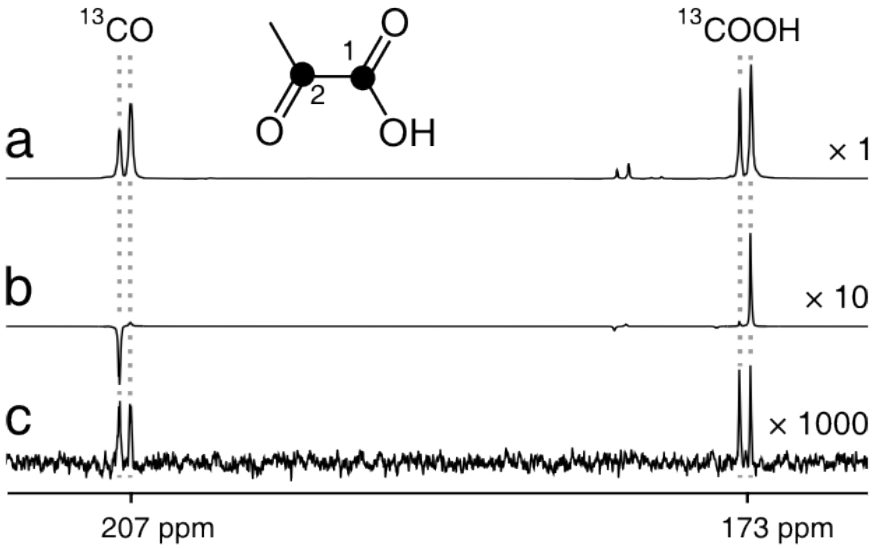

Figure 2.5: ^{13}C NMR spectra at 9.4 T using a 6° flip angle for detection recorded (a) on hyperpolarised [1,2-$^{13}C_2$] pyruvate (single scan); (b) after erasing magnetisation by shaking inside a mu-metal chamber, followed by transfer into high field (single scan); (c) later on the same sample in (a), thermally polarised (16 scans).

order. Singlet order survives intact, on the other hand, since it is rotation-invariant. After shaking in the mu-shield the sample therefore contains only a population asymmetry $p_S T_{00}$, in the laboratory magnetic field (≈ 0.5 mT). As shown in fig. 2.4(c) this situation is similar to low-field singlet order in ALTADENA (see fig. 2.4(b)), albeit with opposite sign in the polarisation.

Fig. 2.5(b) shows the 6° flip angle spectrum recorded after adiabatic transport into the 9.4 T magnet. This displays the same pattern predicted by fig. 2.3d(i), thereby proving the presence of singlet order in low magnetic field. The singlet order is also indicated through the asymmetry in the doublet peak components in fig. 2.5(a). The absolute signs of the peaks in the singlet-derived spectrum fig. 2.5(b) are consistent with the sign of θ on adiabatic transformation into high field, bearing in mind the negative singlet polarisation.

The integral across the ^{13}COO doublet at 173 ppm in both tubes are consistent with the hyperpolarised singlet order being $|p_S/p| = |p|/3$ times the amplitude of longitudinal magnetisation. A longitudinal polarisation $p = (0.26 \pm 0.01) = (26 \pm 1)\%$ was estimated by comparing the integrals between fig. 2.5(a) and the spectrum of the same sample at thermal equilibrium (see fig. 2.5(c)). This value of p corresponds to the sample polarisation at the time of arrival in the detection magnet (≈ 15 s after dissolution). The expected value of p_S from this polarisation, neglecting sample relaxation, is $p_S = 0.023 = 2.3\%$ such

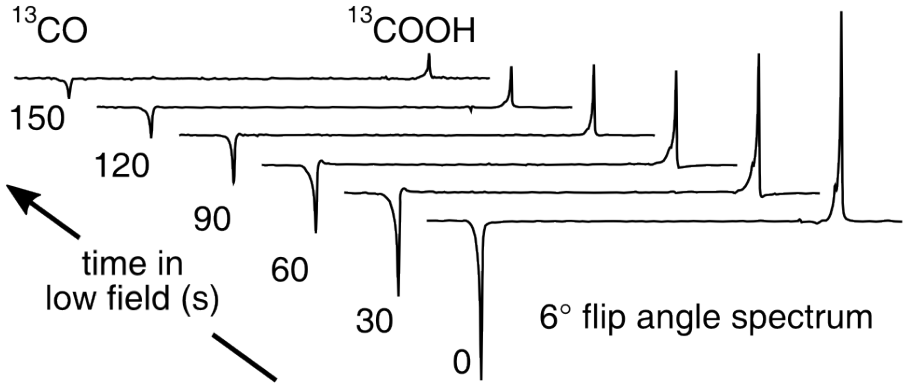

Figure 2.6: Decay of hyperpolarised singlet order on [1,2-$^{13}C_2$]-pyruvic acid in the laboratory magnetic field. The fitted singlet lifetime is $T_S = (70 \pm 2)$ seconds.

that the ratio $p : p_S$ is approximately 12:1. The experimental ratio between the integrals of fig. 2.5(a) and (b), which ignoring relaxation equals the ratio $p : p_S$, is approximately 20:1. These ratios agree to within a factor of 2. The discrepancy may be attributed to sample relaxation during the additional low-field manipulations involved in the singlet experiment.

A separate experiment was performed to estimate the singlet decay constant T_S for the [1,2-$^{13}C_2$] pyruvate in the low field. This time upon exiting the hyperpolariser, the entire solution was shaken in the mu-metal cylinder. The solution was then added into a vial containing 15 ml D_2O. The dilute solution was pipetted equally into six 10 mm o.d. NMR tubes.

The tubes were inserted at 30 second intervals from low field into the 9.4 T spectrometer magnet, where a $\approx 6°$ flip angle spectrum was recorded. Spectra for the different waiting times in the low field are displayed in fig. 2.6. The peak integrals were fit to a monoexponential decay $\exp(-t/T_S)$ yielding a singlet decay constant T_S of (70 ± 2) seconds.

This observed singlet decay constant is approximately twice the T_1 of the ^{13}C pair. The longitudinal relaxation time was later measured using a field-cycled experiment on the thermally polarised sample. The sample was polarised in the high field spectrometer magnet to $p = p_{\text{thermal}}$, then shuttled outside the magnet to rest for a time in low field, for relaxation. After reinsertion into the magnet a 90° pulse was applied, and the NMR spectrum recorded. Peak integrals for different low-field waiting times were fit by the monoexponential decay $\exp(-t/T_1)$, yielding a time constant T_1 for both carbons of (36±1)

seconds.

The ratio T_S/T_1 of only $\approx$ 2 for [1,2-$^{13}C_2$]-pyruvate in D_2O is slightly disappointing. The relatively short singlet lifetime suggests the presence of strong singlet relaxation mechanisms. Spin rotation is a possible candidate. The nature of the mechanism currently remains under investigation.

As a final point, the 'direct' preparation method is independent of spin-spin couplings and chemical shifts, allowing access to hyperpolarised singlet order even in magnetically equivalent spins-1/2 pairs. This cannot be done by pulse sequence methods. Singlet order in these systems may later be released via spin-symmetry-breaking chemical reactions, akin to ALTADENA.

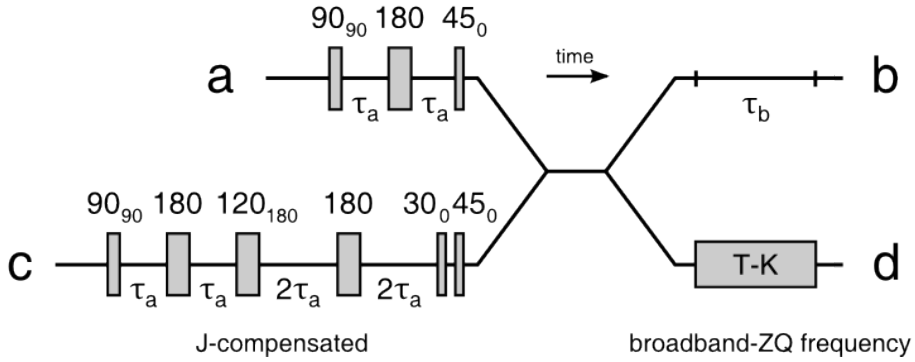

Figure 2.7: Sarkar's sequences for singlet preparation in the regime $|\omega_x^{(S_0T_0)}| \gg |\omega_z^{(S_0T_0)}|$: (a) preparation of anti-phase triplet-triplet coherences; (b) zero quantum evolution period; (c) compensatory sequence for broad-band excitation with respect to $|\omega_z^{(S_0T_0)}|$; (d) Zero-quantum equalisation by the Thrippleton-Keeler technique gives broad-band excitation with respect to chemical shifts.

2.2.2 Sarkar's sequence for weakly coupled spins

Singlet excitation at fixed magnetic field (without field cycling) has been extensively discussed for the regime $|(\delta_j - \delta_k)\gamma B^0| \gg |J|$ in thesis work by Sarkar.[25]

The basic pulse sequence used by Sarkar (*al. et*) is shown in fig. 2.7(a)+(b). The first part of the sequence involves a 90° rf pulse followed by a spin echo ($\tau_a - 180° - \tau_a$). The first pulse generates in-phase single-quantum coherence between the triplet states. Spin echo evolution under a half-echo duration $\tau_a = 1/|4J|$ converts these into anti-phase:

$$
\begin{aligned}
p(I_{jz} + I_{kz}) \quad &= \quad p\Big(|T_{+1}\rangle\langle T_{+1}| - |T_{-1}\rangle\langle T_{-1}|\Big) && (2.82)\\
&\xrightarrow{90^\circ_{90}} \quad \frac{p}{\sqrt{2}}\Big((|T_{+1}\rangle + |T_{-1}\rangle)\langle T_0| + |T_0\rangle(\langle T_{+1}| + \langle T_{-1}|)\Big) && (2.83)\\
&\xrightarrow{\tau_a - 180^\circ_0 - \tau_a} \quad \frac{p}{\sqrt{2}}\Big(\mathrm{e}^{-\mathrm{i}\pi J\tau_a}(|T_{+1}\rangle + |T_{-1}\rangle)\langle T_0| + \mathrm{e}^{+\mathrm{i}\pi J\tau_a}|T_0\rangle(\langle T_{+1}| + \langle T_{-1}|)\Big)\\
&= \quad \frac{p}{\sqrt{2}}\Big(-\mathrm{i}(|T_{+1}\rangle + |T_{-1}\rangle)\langle T_0| + \mathrm{i}|T_0\rangle(\langle T_{+1}| + \langle T_{-1}|)\Big). && (2.84)
\end{aligned}
$$

On applying a 45° rf pulse, phase shifted by 90° from the starting pulse, these become converted into double-quantum coherence and a triplet population imbalance

$$
\begin{aligned}
\text{eq. (2.84)} \quad &\xrightarrow{45^\circ_0} \quad \frac{p}{2}\Big((|T_{+1}\rangle + |T_{-1}\rangle)(\langle T_{+1}| + \langle T_{-1}|) - 2|T_0\rangle\langle T_0|\Big) && (2.85)\\
&\equiv \quad \frac{p}{2}\Big(|T_{+1}\rangle\langle T_{+1}| + |T_{-1}\rangle\langle T_{-1}| - 2|T_0\rangle\langle T_0|) && (2.86)\\
&\qquad\qquad +(|T_{-1}\rangle\langle T_{+1}| + |T_{+1}\rangle\langle T_{-1}|)\Big).
\end{aligned}
$$

At this point there is no net singlet-triplet population imbalance. However, this is now simple to arrange. The excited triplet population $|T_0\rangle\langle T_0|$ may be transferred into $|S_0\rangle\langle S_0|$ by a free evolution period $\tau_b = \pi/2\omega_x^{(S_0T_0)}$ (see fig. 2.7(b)). This executes a 180° rotation about the x-axis of the $m = 0$ Bloch sphere. In the case of inequivalent spins-1/2 a delay $\tau_b = |\pi/\gamma B^0(\delta_j - \delta_k)|$ swaps the identities of $|S_0\rangle$ and $|T_0\rangle$ generating the density operator

$$\text{eq. (2.85)} \quad \xrightarrow{\text{ZQ only}} \quad \frac{p}{2}\Big(|T_{+1}\rangle\langle T_{+1}| + |T_{-1}\rangle\langle T_{-1}| - 2\,|T_0\rangle\langle T_0|\Big); \tag{2.87}$$

$$\text{eq. (2.87)} \quad \xrightarrow{\tau_b} \quad \frac{p}{2}\Big(|T_{+1}\rangle\langle T_{+1}| + |T_{-1}\rangle\langle T_{-1}| - 2\,|S_0\rangle\langle S_0|\Big). \tag{2.88}$$

Signals from the double-quantum coherence in eq. (2.85) are unimportant and may be suppressed by a magnetic field gradient pulse during τ_b.

The final density operator corresponds to the maximum singlet polarisation $p_S = p$, neglecting relaxation effects. Note the delay τ_b depends only on the difference in chemical shifts and therefore imposes no constraint on the rf carrier frequency. The pulse sequence therefore maintains good performance even in inhomogeneous magnetic field.

Sarkar has demonstrated some options for improving singlet excitation if nominal values of τ_a and τ_b cannot be used (see fig. 2.7(c) and fig. 2.7(d)):

- *J-compensation*

  The efficiency of singlet excitation with respect to J, $p_S \propto \sin(2\pi J\tau_a)$, (fig. 2.7(a)) can be broadened to $p_S \propto \sin(2\pi J\tau_a)[1 + \cos^2(2\pi J\tau_a)/2]$ by replacing the spin echo with the composite-pulse-inspired [60] preparation illustrated in fig. 2.7(c).[97] This method gives improved singlet excitation over a wider range of J couplings to help generate singlet order simultaneously in systems containing more than one distinct pair of spins-1/2. The price of this method is the tripling of the single-quantum evolution time. This may be unfeasible, however, if the transverse relaxation rate $1/T_2$ is fast relative to J, which may be the case in large molecules such as proteins.

- *True chemical-shift-broadbandness*

  Dependence of p_S on $\omega_x^{(S_0T_0)}$ is eliminated completely using Thrippleton and Keeler's zero-quantum dephasing technique in stead of the evolution delay τ_b.[66, 24, 97] The Thrippleton-Keeler filter, (or T-K filter), as the event is known, is a swept-frequency inversion pulse applied in the presence of a static field gradient.[98, 99] The T-K filter

saturates sets of quantum states with the same m projection quantum number. In this case, the T-K filter equalises the population imbalance of $|S_0\rangle$ and $|T_0\rangle$ resulting in net spin order between $|S_0\rangle$ and $|T_{\pm 1}\rangle$. The 'saturation time' of the filter is proportional to the zero-quantum evolution period $1/|\omega_x^{(S_0T_0)}|$. After this time the density operator is

$$\text{eq. (2.85)} \quad \xrightarrow{\text{ZQ only}} \quad \frac{p}{2}\Big(|T_{+1}\rangle\langle T_{+1}| + |T_{-1}\rangle\langle T_{-1}| - 2\,|T_0\rangle\langle T_0|\Big) \tag{2.89}$$

$$\xrightarrow{\text{T-K filter}} \quad \frac{p}{2}\Big(|T_{+1}\rangle\langle T_{+1}| + |T_{-1}\rangle\langle T_{-1}| - |T_0\rangle\langle T_0| - |S_0\rangle\langle S_0|\Big). \tag{2.90}$$

This final state corresponds to a singlet polarisation $p_S = p/2$. True broadband excitation therefore comes at a cost of 50% in the obtainable singlet polarisation, or 25% combined across excitation and reconversion steps of the experiment. While rather severe, this expense may be worthwhile in some contexts. One application is EXchange SpectroscopY (EXSY), where the chemical shift asymmetry of a spin pair is time-dependent as a result of ongoing chemical reactions.[24]

2.2.3 Multiple-echo pulse sequence for strongly coupled spin pairs

Sarkar's sequence excites singlet order efficiently in the regime $|\omega_x^{(S_0T_0)}| \gg |\omega_z^{(S_0T_0)}|$, where the spins are weakly coupled. However, outside this limit the sequence performs increasingly inefficiently because the states $m = 0$ do not mix to any great extent under free evolution (apply small θ to fig. 2.1). In the following a different method for conversion $I_z \leftrightarrow I_z^{(S_0T_0)}$ is evaluated, which works efficiently even when the spins are strongly coupled. The protocol involves 'trains' of spin echoes that accumulate $|T_0\rangle \leftrightarrow |S_0\rangle$ mixing when applied in synchrony with the zero-quantum frequency $\Omega^{(S_0T_0)}$.[69, 68, 88]

J-synchronised spin echo trains

In discussing this sequence an emphasis is placed on magnetisation-singlet conversion in the limit $|\omega_x^{(S_0T_0)}| \ll |\omega_z^{(S_0T_0)}|$, where the spins are 'extremely strongly coupled'. Here $|T_0\rangle$ and $|S_0\rangle$ are very close to the $m = 0$ eigenstates and as a result do not appreciably mix during free evolution. Near-equivalence is a favourable target of singlet NMR since no symmetry-switching interventions, such as field cycling,[19] spin locking,[18, 65] or chemical reactions [31] are required to sustain a singlet-triplet population difference. The price, however, is the more difficult excitation of singlet order.

Singlet-triplet transitions may be stimulated in nearly equivalent pairs over the course of a spin echo ($\tau - 180° - \tau$). After one echo, the $m = 0$ Bloch vector is determined by the product $U^{(S_0T_0)}(\tau)R_z(\pi)U^{(S_0T_0)}(\tau)$, where $U^{(S_0T_0)}$ is the propagator given in eq. (2.19) and $R_z(\pi)$ signifies a 180° rotation about the z axis of the $m = 0$ Bloch sphere that corresponds to the 180° rf pulse inverting the sign of $|T_0\rangle$ while leaving $|S_0\rangle$ unchanged. It is found that the half-period $\tau = \pi/|2\Omega^{(S_0T_0)}| \approx 1/|4J|$ gives maximum polar displacement of the Bloch vector at the end of the spin echo. The overall propagator is in this case

$$U^{(S_0T_0)}(\tau)\underbrace{\begin{pmatrix} -1 & 0 \\ 0 & 1 \end{pmatrix}}_{\equiv R_z(\pi)} U^{(S_0T_0)}(\tau) \;=\; \mathrm{e}^{-2\mathrm{i}\,\omega_E^{(S_0T_0)}2\tau} R_{(\cos\theta,\,0,\,-\sin\theta)}(2\theta), \tag{2.91}$$

which in the limit $|\theta| \ll 1$ approximates a rotation about the x-axis, through angle 2θ.

It follows that after N successive back-to-back echoes the propagator approximates an x-rotation $2N\theta$, giving a mixing amplitude $|\sin(2N\theta)|$. This allows one to overcome the

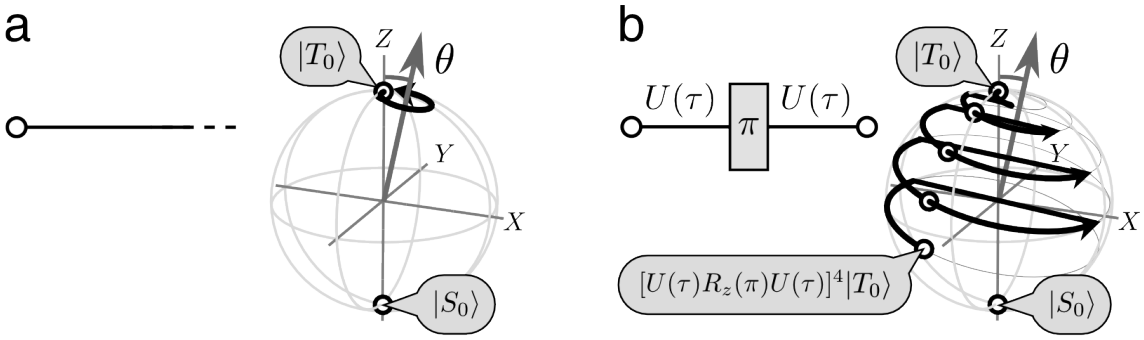

Figure 2.8: Singlet and triplet mixing in the extreme strong coupling regime $|\omega_z^{(S_0T_0)}| \gg |\omega_x^{(S_0T_0)}|$ in the $m = 0$ Bloch sphere. The example trajectory in (a) shows the two states do not significantly interconvert under free evolution. The low-amplitude of mixing may be arranged to accumulate, however, over the course of several spin echoes. The example trajectory in (b) indicates cumulative conversion between $|T_0\rangle$ and $|S_0\rangle$ through a mixing angle of 8θ, as the result of four spin echoes with half-period $\tau = \pi/|2\Omega^{(S_0T_0)}|$.

rather limited maximum singlet-triplet conversion amplitude $|\sin(2\theta)| \ll 1$ under normal free evolution. Fig. 2.8 provides a visualisation of these two trajectories.

Complete interchange $|T_0\rangle \leftrightarrow |S_0\rangle$ requires a train of N_{180} echoes, where N_{180} is the integer that best satisfies $|2N_{180}\theta| \approx \pi$. Note that the total conversion time, in the near-equivalence limit, depends only on the value of $\omega_x^{(S_0T_0)}$. For a 180° rotation about the x axis, the time taken is approximately:

$$2\tau \times N_{180} \quad = \quad \frac{\pi}{\Omega^{(S_0T_0)}} \times \text{round}\Big(\frac{\pi}{2\theta}\Big). \tag{2.92}$$

For $|\theta| \ll \pi/2$, this expression reduces to

$$\text{eq. (2.92)} \quad \approx \quad \omega_z^{(S_0T_0)} \frac{\pi\omega_z^{(S_0T_0)}}{2\omega_x^{(S_0T_0)}} \quad = \quad \pi^2/|2\omega_x^{(S_0T_0)}|. \tag{2.93}$$

'M2S' pulse sequence

Synchronised spin echo trains combine together with rf pulses to give the magnetisation-to-singlet pulse sequence illustrated in fig. 2.9, which is abbreviated 'M2S'.[69, 88] The sequence proceeds as follows. First, a 90° rf pulse is applied, to generate in-phase triplet-triplet single quantum coherences. These are converted into singlet-triplet single-quantum

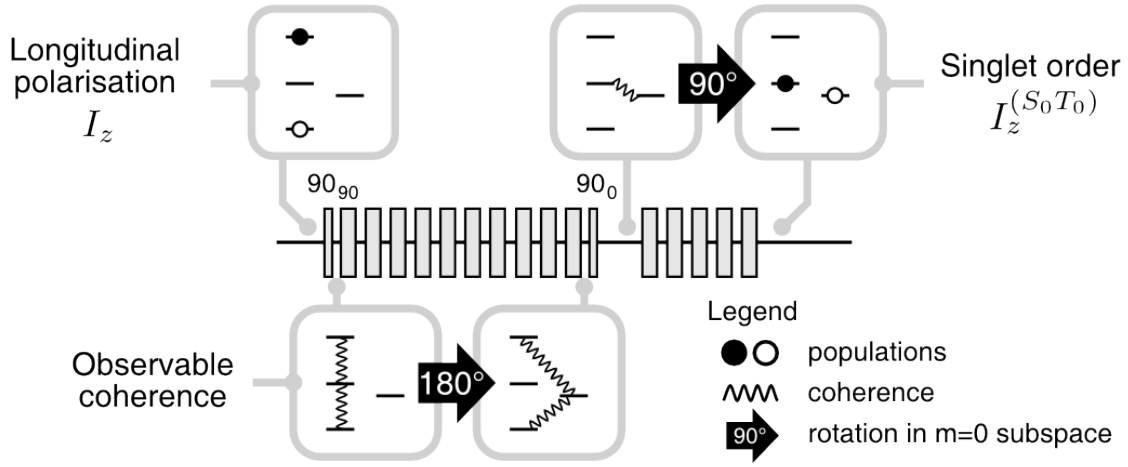

Figure 2.9: The magnetisation-to-singlet conversion sequence for strongly coupled spins, using J-synchronised spin echo trains.

coherence via a synchronised echo train, which swaps the $m = 0$ states:

$$p(I_{jz} + I_{kz}) \quad = \quad p\Big(|T_{+1}\rangle\langle T_{+1}| - |T_{-1}\rangle\langle T_{-1}|\Big) \tag{2.94}$$

$$\xrightarrow{90^\circ_{90}} \quad \frac{p}{\sqrt{2}}\Big(|T_{+1}\rangle + |T_{-1}\rangle)\langle T_0| + |T_0\rangle(\langle T_{+1}| + \langle T_{-1}|)\Big) \tag{2.95}$$

$$\xrightarrow{180^{\circ(S_0T_0)}_0} \quad \frac{p}{\sqrt{2}}\Big(\mathrm{e}^{+\mathrm{i}\xi}(|T_{+1}\rangle + |T_{-1}\rangle)\langle S_0| + \mathrm{e}^{-\mathrm{i}\xi}|S_0\rangle(\langle T_{+1}| + \langle T_{-1}|)\Big) \tag{2.96}$$

A 90° rf pulse is then applied, phase-shifted 90° from the starting pulse. This converts the single-quantum coherence into singlet-triplet zero-quantum coherences:

$$\text{eq. (2.96)} \quad \xrightarrow{90^\circ_0} \quad -\mathrm{i} \times p\Big(\mathrm{e}^{+\mathrm{i}\xi}|T_0\rangle\langle S_0| + \mathrm{e}^{-\mathrm{i}\xi}|S_0\rangle\langle T_0|\Big) \tag{2.97}$$

$$\equiv \quad -\mathrm{i} \times 2p\Big(I_x^{(S_0T_0)}\cos(\xi) + I_y^{(S_0T_0)}\sin(\xi)\Big). \tag{2.98}$$

The phase ξ in these equations is equal to $\xi = 4\omega_E^{(S_0T_0)}N_{180}\tau$ from the singlet-triplet energy difference. For extremely strongly coupled spin pairs ξ is a multiple of π and may be ignored, such that the density operator after the second 90° pulse is proportional to $I_x^{(S_0T_0)}$. In less strongly coupled pairs, or where a large number of echoes is performed (see '*J-broadband spin echo trains*', page 82), this phase may be need to be taken into careful consideration.

The transverse (S_0T_0) coherence is rotated finally into the singlet-triplet population difference $I_z^{(S_0T_0)}$ using a second synchronised spin-echo train. A train of $N_{90} = \mathrm{round}(\frac{\pi}{4\theta})$

spin echoes induces a 90° rotation about the axis $I_x^{(S_0T_0)}$. This requires that the spin order from eq. (2.98) must first be transferred onto $I_y^{(S_0T_0)}$, which may be achieved by leaving a short evolution delay which I call τ_{shift}, to rotate approximately about the z axis under the strong J coupling:

$$\text{eq. (2.98)} \quad \xrightarrow{\tau_{\text{shift}}} \quad p\left(\mathrm{i}\,|T_0\rangle\langle S_0| - \mathrm{i}\,|S_0\rangle\langle T_0|\right) \;\equiv\; 2pI_y^{(S_0T_0)}. \tag{2.99}$$

The delay τ_{shift} must be chosen to ensure $(2\pi J\tau_{\text{shift}} + \xi)$ is an odd multiple of $\pi/2$. In the limit of extremely strongly coupled spins, this reduces to $\tau_{\text{shift}} = 1/|4J|$.[69, 88]

From eq. (2.99) the final transformation is

$$\text{eq. (2.99)} \quad \xrightarrow{90_0^{\circ}(S_0T_0)} \quad p\left(|T_0\rangle\langle T_0| - |S_0\rangle\langle S_0|\right) \;\equiv\; 2pI_z^{(S_0T_0)}. \tag{2.100}$$

The resulting singlet polarisation p_S equals $(T_{00}|2pI_z^{(S_0T_0)})/(T_{00}|T_{00}) = p$. The total time for $I_z \rightarrow 2I_z^{(S_0T_0)}$ conversion by M2S is $3\pi^2/|4\omega_x^{(S_0T_0)}|$, in the near-equivalence limit.

Reconversion and observation

When applied in reverse chronological order the M2S sequence converts the population difference $I_z^{(S_0T_0)}$ into observable single-quantum coherences. Ignoring relaxation, the intensity of the resulting signal is again two-thirds that which may be obtained from the starting polarisation. This is determined from the following operator transformations:

$$pI_z \xrightarrow{\text{M2S}} 2pI_z^{(S_0T_0)} \xrightarrow{\text{project } T_{00}} pT_{00} \xrightarrow{\text{project } I_z^{(S_0T_0)}} \frac{4p}{3}I_z^{(S_0T_0)} \xrightarrow{\text{S2M}} \frac{2p}{3}I_x. \tag{2.101}$$

The recoverable signal is therefore the same as that following both Sarkar's sequences and the field cycling methods and, once again, the maximum obtainable overall.

Sequence performance, robustness and resistance to errors

The J-synchronous echo method may appear to operate effectively in inhomogeneous B^0 fields since the ideal evolution is insensitive the to rf offset. In practice, however, the off-resonance efficiency is limited by a deteriorating performance of the inversion pulses. For 180° pulses that are not sufficiently accurate, states $m = 0$ and $m = \pm 1$ come into

contact with one another and the interconversion $|T_0\rangle \leftrightarrow |S_0\rangle$ is interrupted. Rf pulses may deliver a different rotation from nominal 180° in two ways: (i) when rf irradiation is applied off-resonance from the nuclear Larmor frequency; (ii) when rf amplitude is not calibrated properly. Situation (ii) may apply to rf fields that are not homogeneous across the sample volume.

Composite rf pulses, such as $(90^\circ_0)(180^\circ_{90})(90^\circ_0)$, offer improved inversion with respect to rf inhomogeneity and offset.[60] Another method is compensation of errors by phase cycling the 180° pulses throughout the train. By analysing the average Hamiltonian (AH)[100] for the pulse train we have determined that the phase cycle $[0°, 0°, 180°, 180°, \ldots]$ compensates both rf amplitude and frequency errors. Below is a summary of the AH outcome with supporting numerical simulations performed using SpinDynamica.[101] The details of the AH analysis are rather complicated so shall be skipped for now and published elsewhere.

- *Model*

  The plots in fig. 2.10 and fig. 2.11 show the variation in the singlet-triplet mixing amplitude $\langle S_0|U_{\text{train}}|T_0\rangle$ for a pair of very strongly coupled spins with $|\gamma B^0 \Delta\delta/2\pi| =$ 10 Hz and $|J| = 100$ Hz ($\theta \approx 5.7°$). The propagator U_{train} is evolution across a train of 16 J-synchronised spin echoes, which corresponds to a nominal 180°_x rotation in the $m = 0$ Bloch sphere. Under nominal conditions the integral is equal to 1, which corresponds to a complete swapping of the states.

- *Rf amplitude error*

  The upper plot in fig. 2.10 shows variation in $\langle S_0|U_{\text{train}}|T_0\rangle$ against the dimensionless rf amplitude $\omega_{\text{rf}}/\omega^0_{\text{rf}}$, where ω^0_{rf} is the nominal rf amplitude for the pulse length, chosen arbitrarily as $\omega^0_{\text{rf}}/2\pi = 500$ Hz. All pulses are on resonance.

  The black curve show the conversion efficiency in the absence of error correction, using basic 180° pulses and no phase cycling. Singlet-triplet conversion is narrowband and only efficient within $1 - 2\%$ of the nominal rf amplitude. This behaviour occurs because the amplitude error disrupts the AH at first order perturbation level.

  Blue and red curves show that cycling the 180° pulses phases through $[0°, 180°, \ldots]$ or $[0°, 0°, 180°, 180°, \ldots]$ the excitation profile becomes much wider. These cycles average out rf amplitude errors for all perturbation orders of the AH and give the best possible error compensation. For example, at a $\pm 40\%$ error in rf amplitude the

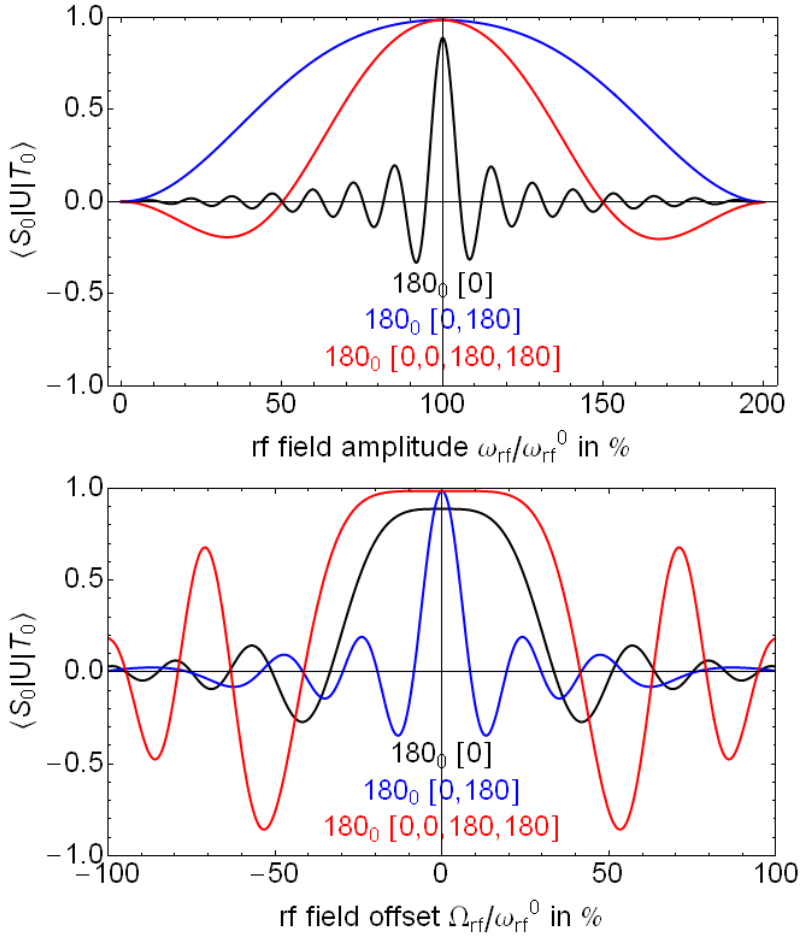

Figure 2.10: Phases of the 180° pulses may compensate for rf amplitude and frequency offset errors during the spin echo trains. The plots show conversion amplitude of $|T_0\rangle$ into $|S_0\rangle$ following a spin echo train where: in (a), 180° pulses are applied on resonance, but rf amplitude ω_{rf} is mis-set by a percentage of the nominal value ω_{rf}^0; in (b), 180° pulses are applied with nominal rf amplitude ω_{rf}^0, but off-resonance from the nuclei by frequency ω_{off}. The phase cycle $[0°, 0°, 180°, 180°]$ compensates well against both types of error, as seen from the widened excitation profiles. The transformation amplitudes were calculated numerically using the SpinDynamica software for Mathematica 8.[101]

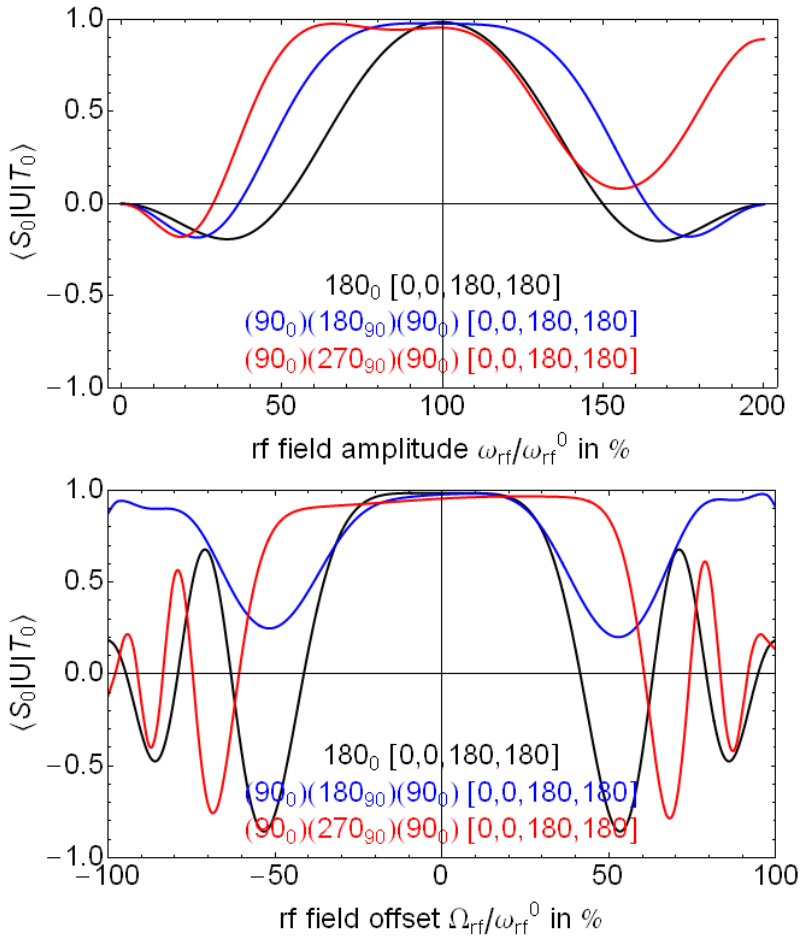

Figure 2.11: Broadband excitation is improved with respect to amplitude and frequency offset errors if composite-pulses and phase-cycling are applied together within the spin echo train. The profiles were calculated using the SpinDynamica software for Mathematica 8.[101]

cycle $[0°, 180°]$ results in a 70% conversion efficiency between $|S_0\rangle$ and $|T_0\rangle$. Without the phase cycling, there is almost no conversion.

- *Offset rf frequency*

  The lower part of Fig. 2.10 shows $\langle S_0|U_{\text{train}}|T_0\rangle$ versus a dimensionless rf offset $\omega_{\text{off}}/\omega_{\text{rf}}^0$. Pulse amplitudes are kept nominal.

  The curves show that while the phase cycle $[0°, 180°, \ldots]$ gives excellent compensation of rf amplitude errors it exacerbates the inefficiency due to resonance offset. The width of the band $\langle S_0|U_{\text{train}}|T_0\rangle > 99\%$ is much wider when constant-phase pulses are used. In terms of the AH, first-order error terms vanish across pairs of echoes $[0°, 0°]$, but are compounded across pairs $[0°, 180°]$. Improved compensation is provided by the four-step cycle $[0°, 0°, 180°, 180°]$ as shown in red. This phase cycle averages the offset dependence in both the first- and second-order levels of the AH.

It is clear that the phase cycle $[0°, 0°, 180°, 180°, \ldots]$ is the shortest one that compensates both types of error. We have not investigated the average Hamiltonian in detail beyond second order, since the higher orders are quickly diminishing in strength.

Additional compensation may be arranged by combining the phase cycle with inversion through composite pulses, as shown in fig. 2.11. The most effective method is the one using $[(90_0^\circ)(180_{90}^\circ)(90_0^\circ)]_{\phi_{\text{rf}}}$ for inversion, applied with the cycle $\phi_{\text{rf}} = [0°, 0°, 180°, 180°]$, still this strictly only provides an *error-compensated* sequence, not a completely broadband one.

Near-equivalence induced by a remote stereocenter

Near equivalence may occur as a result of remote molecular asymmetry. In ref. [88] we studied the persistent singlet order of geminal protons in the tripeptide L-alanyl-glycyl-glycine (AGG), both in presence and absence of rf locking.

Fig. 2.12 shows the locations of two isolated CH_2 units in AGG. Each proton pair is *diastereotopic*, by virtue of the alanine chiral centre that destroys global mirror symmetry across the plane of the peptide chain. The terminal pair has only a small chemical asymmetry, however, due to its remoteness and local symmetry. The terminal protons reside six sigma bonds from the chiral centre and are hence 'nearly equivalent'. While the one-dimensional NMR spectrum shows the 'central' glycine protons as a strongly roofed pair, only three atom centres from the chiral centre with $|^2J_{\text{HH}}| = 18$ Hz and $|\Delta\delta| = 0.035$

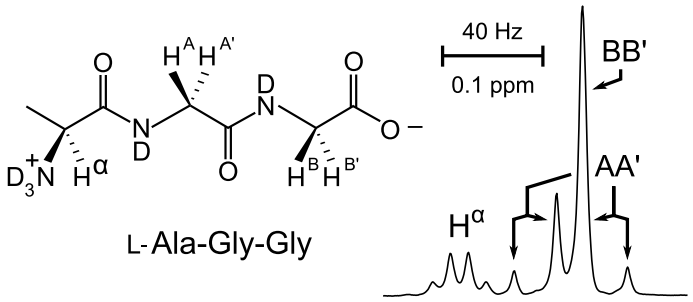

Figure 2.12: Proton NMR spectrum of AGG (20mM in D_2O), 9.4 T.

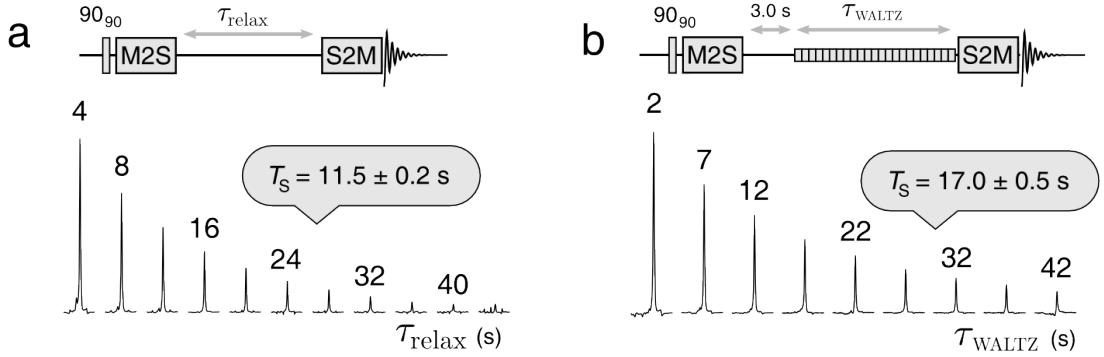

Figure 2.13: Singlet relaxation of the nearly equivalent terminal glycine protons in AGG: (a) when no rf locking is applied; (b) during forced magnetic equivalence under an rf field. The delay $4T_1 \approx 3$ seconds is provided in (b) to allow equilibration of the triplet populations before applying 3.0 kHz resonant WALTZ decoupling. Blocks 'M2S' and 'S2M' each abbreviate the forward and reverse $I_x \leftrightarrow I_z^{(S_0T_0)}$ transformations.

ppm ($|\gamma_H B^0 \Delta\delta/2\pi| = 14$ Hz at 9.4 T), the terminal pair appears as just a single peak with the chemical shifts of the nuclei unresolved.

Singlet order on the terminal glycine protons was excited using the pulse sequences shown in fig. 2.13(a) and fig. 2.13(b). At a field of 9.4 T, thermal longitudinal polarisation was converted using M2S. Following excitation, the state was left for a time for relaxation, after which remanent T_{00} singlet order was converted to in-phase magnetisation (S2M) and estimated through the spectral intensity. A two-step phase cycle [0°, 180°] on both the starting 90° pulse and on the receiver was used to eliminate signals arising from longitudinal recovery prior to the S2M step.

The fitted exponential time constants was $T_S = (11.5 \pm 0.2)$ seconds for the terminal glycine protons, which is approximately 15 times T_1 (fig. 2.13(b)). The decay constant T_S in the presence of rf locking was measured as $T_S = (17.0 \pm 0.5)$ seconds (23 times T_1, see fig. 2.13(b)). We used a WALTZ-16 modulation of the applied irradiation at a nutation frequency of 2.0 kHz, which is sufficiently strong to isolate the coherent singlet-triplet

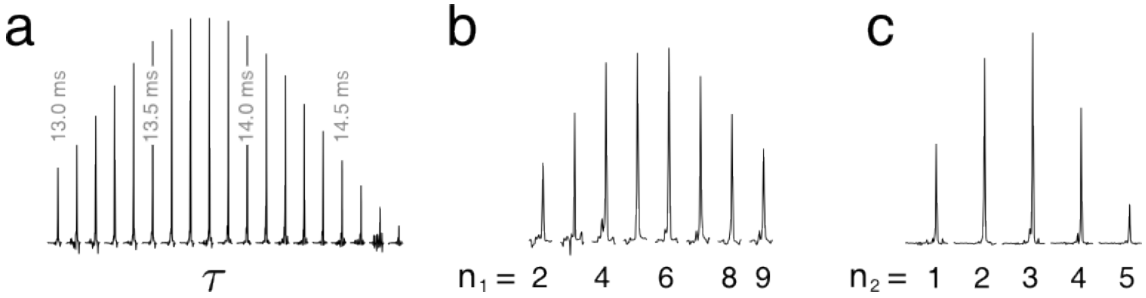

Figure 2.14: Efficiency of Magnetisation-to-Singlet transfer. Shown are the amplitudes of the NMR signal from the sequence in fig. 2.13(a) following variation of: (a) the echo delay $\tau = \pi/|2\Omega|$; (b) the number of echoes N_{180} performed in the first train of M2S and (c) the number of echoes N_{90} performed in the second train of M2S. Each displayed spectral region has width 100 Hz.

conversion.[65] A delay of $4T_1 \approx 3.0$ seconds was left before applying the spin lock to allow the equilibration of triplet populations. These results confirm it is not necessary, in the nearly-equivalent case, to force coherent isolation of the singlet state using rf locking. Coherent evolution between singlet and triplet states is already suppressed by the internuclear J coupling, as predicted by the theory of ref. [65]

The spin echo train parameters used in these experiments were $\tau = \pi/|2\Omega| = 13.9$ ms and $N_{180} \approx \pi/|2\theta| = 6$, $N_{90} \approx \pi/|4\theta| = 3$, which were found empirically to maximise M2S and S2M transfer. Variation of excitation through adjusting each parameter about the maximum is shown in fig. 2.14. The adjustments are made for both the M2S *and* S2M parts of the experimental sequence. The optimum values allow precise determination of the previously unresolved chemical shift separation of the pair, $|\gamma_H B^0 \Delta\delta/2\pi| = (5.0 \pm 0.1)$ Hz ($\Delta\delta \approx 12$ ppb), at 9.4 T and the coupling constant $^2J_{\mathrm{HH}} = (18.0 \pm 0.05)$ Hz.

Isotope symmetry breaking via ^{18}O enrichment

Nearly equivalent spin pairs may be induced by substituting close atoms with a different spin-zero isotope of the same element.[102] The change in the atomic mass modifies the vibronic motion of the molecular environment, and causes small isotope shifts which are usually of the order of parts-per-billion (ppb).[103] These small shifts are sufficient to provide access to singlet order through the M2S and S2M pulse sequences.

Here we demonstrate that isotope-shift-induced symmetry breaking allows access to singlet order in the oxalate anion, $[(\mathrm{COO})_2]^{2-}$. Oxalate contains two carbon atoms, each bonded to two oxygen atoms. In the absence of isotope effects the two carbons

are chemically identical due to inversion symmetry of the whole molecule. Symmetry may be lost, however, in unsymmetrical isotopologues[104] with the spin-0 isotopes ^{16}O and ^{18}O.[105, 106]

Isotope shifts induced at ^{13}C by ^{18}O are illustrated in fig. 2.15(a). This shows ^{13}C NMR spectra of natural-abundance oxalic acid dissolved in 1:1 $D_2{}^{18}O$:$D_2{}^{16}O$ at room temperature. Initially a single ^{13}C NMR line is observed in the spectrum at chemical shift $\delta_C \approx 162$ ppm. The natural isotopic abundance of oxygen is *c.* 99.8% ^{16}O, 0.2% ^{18}O, and therefore all oxalate starts as the $^{16}O_4$ isotopologue. At later times in ^{18}O-enriched water, peaks at lower chemical shift appear, as acid-catalysed ^{18}O / ^{16}O exchange populates the other isotopologues.[107]

The NMR spectrum at equilibrium (after 12 hours) contains nine peaks. These are consistent with the nine distinct permutations of ^{16}O and ^{18}O around [$^{13}C_1$]-oxalate, each isotopologue being resolved through the isotope shift between ^{16}O and ^{18}O,[105, 108, 106] and that isotope shifts induced at ^{13}C are different depending on whether ^{18}O is substituted one or two chemical bonds away.

The 'triplet of triplets' intensity pattern indicates the shifts are additive,[103, 106] to within measurement error. As demonstrated by fig. 2.16(a), ^{18}O isotopic substitution over the ^{13}C–O single bond at a 1:1 ratio between ^{16}O and ^{18}O, generates isotopologues [1,1-$^{16}O_2$]-, [1,1-$^{16}O^{18}O$]- and [1,1-$^{18}O_2$]-oxalate in the ratio 1:2:1. The ^{13}C chemical shifts of these are respectively 0, 1 and 2 times the one-bond-induced isotope shift from δ_C in [$^{16}O_4$]-oxalic acid, giving a triplet multiplet pattern. The possibility of $^{16}O_2$, $^{16}O^{18}O$ and $^{18}O_2$ substitution at the second carbon site splits this 'triplet' pattern a second time, this time by the two-bond isotope shift.

Isotope shifts fitted to the spectrum in fig. 2.15(a) are $^1\Delta C(^{18}O) = -32$ ppb across the ^{13}C–O bond and $^2\Delta C(^{18}O) = -7$ ppb across the ^{13}C–C–O bond. The isotope shift follows the convention as the chemical shift change upon substituting the heavier nucleus: $^n\Delta C(^{18}O) = \delta_C(^{18}O) - \delta_C(^{16}O)$, where n denotes the number of chemical bonds between ^{18}O and ^{13}C.[103]

Fig. 2.15(b) shows the similar isotopic equilibration of [$^{13}C_2$]-oxalic acid in 50% ^{18}O-water. In this case the equilibrium spectrum displays five peaks with intensity ratio 1:4:6:4:1, separated by the mean isotope shift across one and two bonds ($^1\Delta C(^{18}O) + {}^2\Delta C(^{18}O))/2$. This pattern confirms the $^{13}C_2$ spin pairs remain nearly equivalent, despite

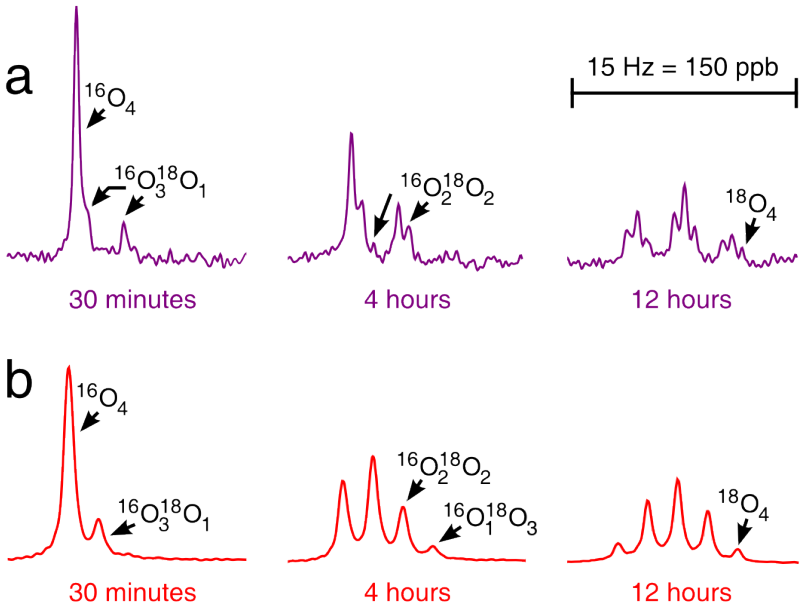

Figure 2.15: ^{13}C NMR spectra recorded following dissolution of [$^{16}O_4$]-oxalic acid in 1:1 $D_2{}^{18}O$:$D_2{}^{16}O$ at 30°C, 9.4 T (^{13}C Larmor frequency 100 MHz). The ^{18}O isotopologues formed during acid-catalysed ^{18}O / ^{16}O exchange resolve as separate peaks, due to ^{18}O isotope shifts. The width of each region shown is 0.15 ppm (15 Hz) and centred at 162.02 ppm.

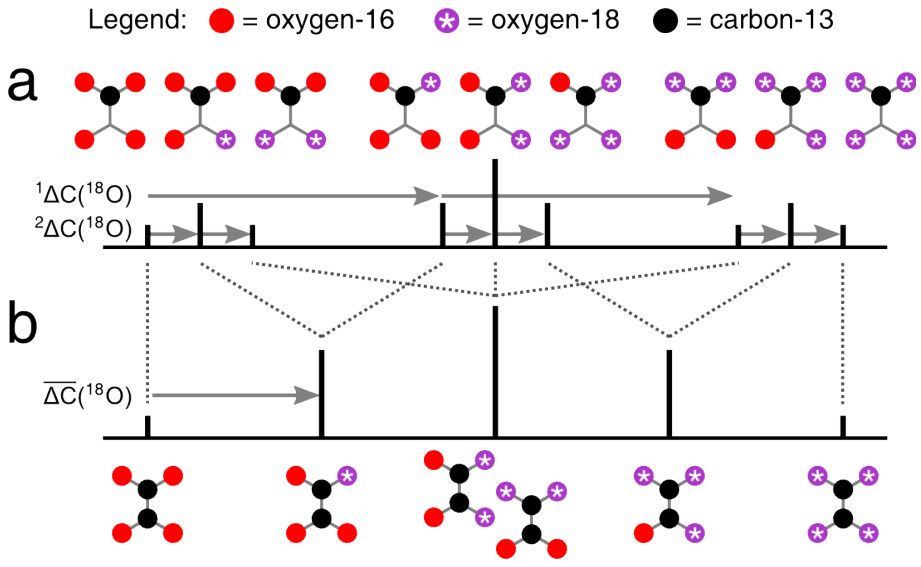

Figure 2.16: Isotope splitting patterns in the ^{13}C NMR spectra of [$^{13}C_1$]- and [$^{13}C_2$]-oxalic acid. The dotted lines show the correlation of ^{18}O isotopomers between the singly and doubly ^{13}C-labelled forms.

the isotope-induced chemical inequivalence, and that differences in chemical shift between the nuclear sites are always smaller than $^1J_{CC}$. The NMR spectrum of each isotopologue contains a single line at the average chemical shift of the spin pair. For instance in [1-^{18}O^{13}C$_2$]-oxalic acid one of the carbons is shifted by $^1\Delta$C(^{18}O) relative to [^{16}O$_4$,^{13}C$_2$]-oxalic acid, while the other is shifted by $^2\Delta$C(^{18}O). The average chemical shift is ($^1\Delta$C(^{18}O) + $^2\Delta$C(^{18}O))/2. The peaks in fig. 2.15(b) and fig. 2.16(b) thereby correspond to isotopomers with 0, 1, 2, 3 and 4 atoms of ^{18}O, reading from left to right.

Fig. 2.16(b) indicates three of the six ^{18}O isotopologues of ^{13}C$_2$-oxalate exhibit asymmetric substitution patterns, and therefore are suitable for singlet NMR. These are [^{16}O$_3$, ^{18}O$_1$; ^{13}C$_2$]-oxalate and [^{16}O$_1$ ^{18}O$_3$; ^{13}C$_2$]-oxalate, both of which have a ^{13}C chemical shift difference $|\Delta\delta_C| = |^1\Delta C(^{18}O) -^2 \Delta C(^{18}O)| = 25$ ppb, plus the [1,1-^{16}O$_2$;2,2-^{18}O$_2$;^{13}C$_2$]-oxalate, which has $|\Delta\delta_C| = 2|^1\Delta C(^{18}O) -^2 \Delta C(^{18}O)| = 50$ ppb. As shown by fig. 2.16(b), however, the ^{13}C peak of the latter isotopologue coincides with that of the symmetric [1,2-^{16}O$_2$;1,2-^{18}O$_2$;^{13}C$_2$] isotopologue, which makes it more difficult to observe cleanly.

In order to apply the M2S sequence both $\tau \approx 1/|4^1J_{CC}|$ and $\Delta\delta_C$ must be accurately known. Above, we have determined the chemical shift differences. The value of $^1J_{CC}$, however, is unavailable from the 90°-acquire spectrum due to the extreme strong coupling. To find $^1J_{CC}$, experiment was performed consisting of a 90° radiofrequency pulse followed by a train of spin echoes, as shown in fig. 2.17(a).

The number of echoes was chosen so as to approximate a 360° rotation in the zero-quantum singlet-triplet subspace for a 'guess' value of $^1J_{CC} = 100$ Hz, which is the measured value of the scalar coupling in the chemically similar, but weakly coupled molecule of methyl-ethyl-[1,2,^{13}C$_2$]-oxalic acid diester. At 9.4 T, this number of echoes corresponds to $N_{360} = \text{round}(|2\pi/2\theta|) = 100$ echoes.

The data in figure fig. 2.17(b) show the signals obtained for $N_{\text{echo}} = 100$ against different values of τ. The initial 90° pulse in this experiment creates transverse coherences $|T_{\pm1}\rangle\langle T_0|$ and $|T_0\rangle\langle T_{\pm1}|$ from starting longitudinal polarisation. For nominal τ_{echo}, the train of echoes is expected to invert the sign of both coherences, resulting in an inverted amplitude during signal acquisition. The peak intensities of [^{16}O$_3$,^{18}O$_1$,^{13}C$_2$]- and [^{16}O$_1$,^{18}O$_3$,^{13}C$_2$]-oxalate, highlighted in red, are most negative for $\tau = (2.85 \pm 0.005)$ ms (composite pulse duration $\tau_p = 44$ μs). From this resonant value of τ, the magnitude of $^1J_{CC}$ is determined through the back-calculation as (87.7 ± 0.2) Hz. Note that the resonance is extremely narrow, due

to the large number of echoes performed.

The spectra in fig. 2.17(c) were recorded using $\tau = 2.85$ ms (and $\tau_p = 44$ μs) and incrementing the number of echoes performed. This stack shows the resonant mixing induced in the zero-quantum subspaces of [$^{16}O_3$,$^{18}O_1$,$^{13}C_2$]- and [$^{16}O_1$,$^{18}O_3$,$^{13}C_2$]-oxalate. The inverted spectrum at $N = 110$ echoes corresponds 360° rotation in the subspace, where observable triplet-triplet coherence is restored with negative sign. Zero intensity at $N_{\text{echo}} \approx 55$ echoes and $N \approx 170$ echoes corresponds respectively to 180° and 540° rotations in the subspace. At these points all of the starting triplet-triplet coherence is converted into non-observable singlet-triplet coherence.

With $^1J_{\text{CC}}$ and $\Delta\delta$ both known the M2S-S2M pulse sequence as shown in fig. 2.18(a)i–iv was attempted. Immediately before the experiment, dissolved paramagnetic oxygen (O_2 gas) was removed from the sample by bubbling oxygen-free nitrogen through the solution for 15 minutes, followed by degassing under vacuum with the solution in a Young valved glass tube.

Singlet order $I_z^{(S_0T_0)}$ was excited using $N_{180} = 55$ and $N_{90} = 27$ spin echoes and spin echo delay $\tau = 2.85$ ms corresponding to nominal 180° and 90° rotations in $m = 0$ subspace of the singly asymmetric isotopomers [$^{16}O_3{}^{18}O_1$]- and [$^{16}O_1{}^{18}O_3$]-oxalate, taking an overall time of 0.42 seconds (fig. 2.18(a)i). Singlet order was left undisturbed in high field for a time T_{HF}, for relaxation (fig. 2.18(a)ii). At the end of this waiting time a sequence $(G_1) - (90_{54.7°}) - (G_2) - (90_{54.7°}) - (90_{180°}) - (G_3)$ was applied, (fig. 2.18(a)iii), where G_1, G_2 and G_3 are sine-bell pulsed-field z gradients with respective strengths +0.8 G cm^{-1}, −0.8 G cm^{-1} and −0.8 G cm^{-1} and durations 4.4 ms, 2.4 ms and 2.0 ms. As explained later, in §2.5.5, the gradients induce a z rotation of the nuclear spin polarisation through an angle that depends on position within the sample volume. The radiofrequency pulses sample the rotation angle so as to cause destructive interference of rank-1 and rank-2 spin order,[109] while leaving singlet nuclear spin order undisturbed, since it has rank zero. This procedure is a more general version of the Only Parahydrogen SpectroscopY (OPSY) technique used frequently in parahydrogen NMR (see §2.5.5).[110] After this 'filtration', the 'pure' singlet-triplet population difference order was reconverted into observable triplet-triplet single quantum coherences, applying the M2S sequence in reverse (fig. 2.18(a)iv). The experiment was performed for several values of T_{HF} as shown in fig. 2.18(a)v and the resulting spectrum integrals were fit by a monoexponential decay curve $\exp(-T_{\text{HF}}/T_S)$ to

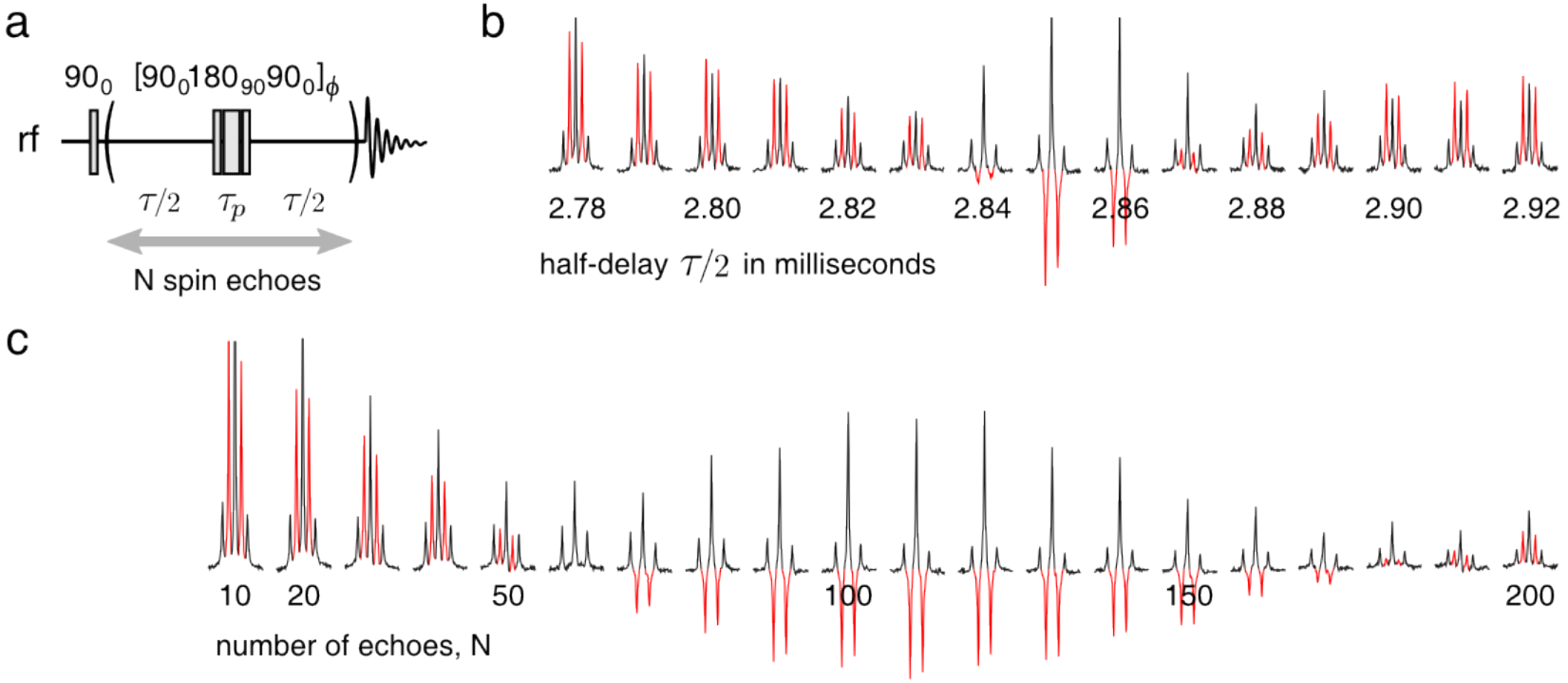

Figure 2.17: Demonstration of zero-quantum singlet-triplet subspace transitions in unsymmetrical [$^{16}O_3$,$^{18}O_1$,$^{13}C_2$]- and [$^{16}O_1$,$^{18}O_3$,$^{13}C_2$]-oxalic acid isotopologues (shown in red). The pulse sequence in (a) converts between observable triplet-triplet coherence and non-observable singlet-triplet coherence. Stacked ^{13}C NMR spectra in (b) show the signal obtained after $N = 100$ spin echoes against different values of the spin echo half-delay τ, using constant composite pulse duration $\tau_p = 44$ μs. In (c) the length N of the spin echo train is varied, while keeping fixed the echo duration $\tau_{\text{echo}} = (2\tau + \tau_p) = 5.75$ ms.

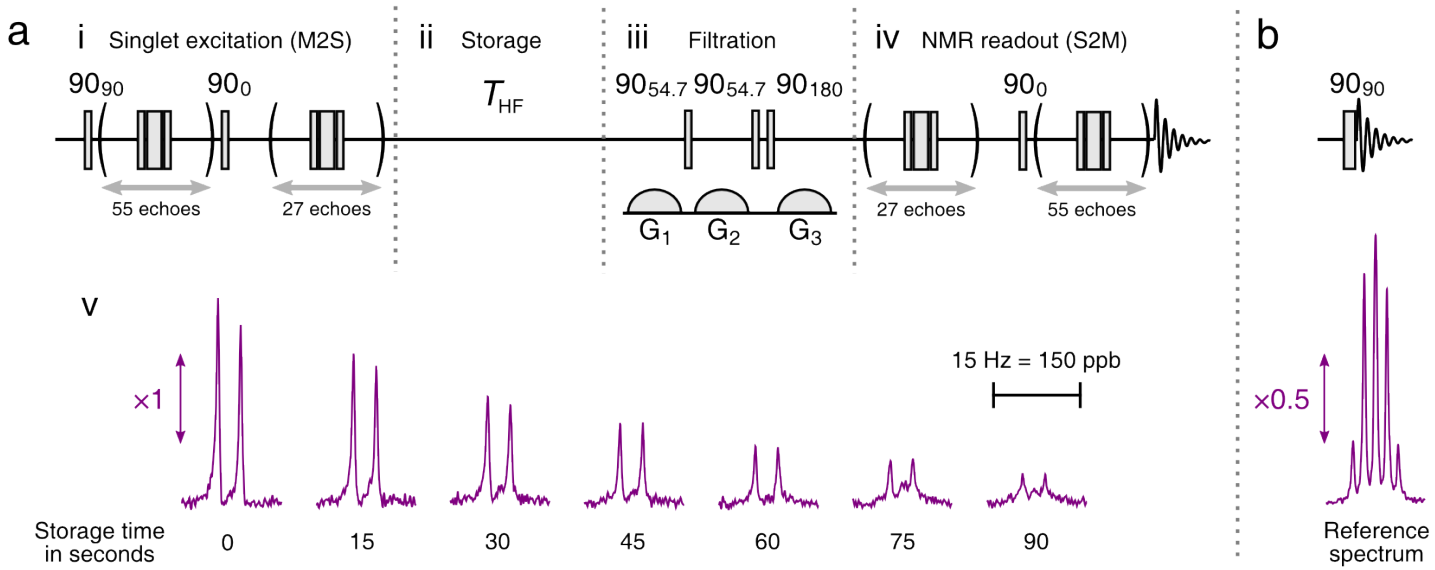

Figure 2.18: Experimental singlet decay in [$^{16}O_3$,$^{18}O_1$,$^{13}C_2$]-oxalate and [$^{16}O_1$,$^{18}O_3$,$^{13}C_2$]-oxalate at 30°, 9.4 T. Parts (a)i-iv show detail of the M2S-S2M pulse sequence used; (a)iii shows the details of the filter used to rid of non-singlet spin order. The stack of spectra in (a)v show the signals obtained at different singlet storage times in the high field. In (b) the regular 90°-acquire ^{13}C spectrum is given for comparison. All radiofrequency pulses are applied on-resonance. For all the spectra, the regions displayed are centred at 162.02 ppm relative to tetramethylsilane, and are the processed result of a single scan.

yield the singlet decay constant $T_S = (55 \pm 5)$ seconds.

The singlet lifetime is approximately three times T_1, measured later as (21 ± 0.2) seconds on the same sample at 9.4 T by inversion recovery. The ratio of only 2-3 times T_1 is slightly disappointing, however, in view of the degassing precautions taken to eliminate dissolved paramagnetic oxygen.[111] This may suggest that oxalate relaxes under a strong spin-rotation mechanism, due to the molecule's low moment of inertia. Intramolecular dipole-dipole or scalar relaxation may also be possible, since oxalic acid dissolved in water exists mainly as the monoanion $[C_2DO_4]^-$ owing to high acidic strength; $pK_a = 1.5$ for the diprotic species, 4.5 for the dianion. CSA-CSA correlations may also be significant. A study of decay rates versus B^0 may help determine the likely singlet relaxation mechanism.

The spectra in fig. 2.18(a)v do not show any evidence of singlet order from the unsymmetrical [1,1-$^{16}O_2$;2,2-$^{18}O_2$;$^{13}C_2$]-oxalate. This is because the chemical shift difference is twice that for [$^{16}O_3{}^{18}O$] and [$^{16}O^{18}O_3$]-oxalate, therefore the rotation angles θ in the zero-quantum subspace are doubled also. During the first spin echo train this results in 360° refocusing of the triplet-triplet coherence. As a result, no singlet order is produced.

To summarise: asymmetric induction is possible in $^{13}C_2$ oxalate by exploiting $^{18}O/^{18}O$ isotope shifts. Despite the induced asymmetry being ≈ 30 times weaker than the carbon-carbon J coupling, it still permits efficient coherent access to the nuclear singlet order. Isotope-induced symmetry breaking is expected to be useful in singlet NMR of other molecules, plus multiple-quantum spectroscopy of strongly coupled spin pairs in general. Apart from ^{16}O and ^{18}O, useful shifts may be generated by other isotopic pairs, for instance ^{32}S and ^{34}S (both spin-0), plus ^{35}Cl and ^{37}Cl (both spin 3/2, but with rapid self-decoupling due to quadrupolar relaxation).

Strongly coupled pairs in low magnetic field

Conversion between $|T_0\rangle$ and $|S_0\rangle$ may be accomplished completely outside the spectrometer field via synchronised echo trains with pulses applied at audio frequency. This has been demonstrated by Pileio and co-workers by pre-polarisation of $^{15}N_2O$ at 7 T, followed by transfer to the 2.2 mT fringe field, at which: the Larmor frequency $|\gamma_N B^0|$ is of order 10 kHz; the chemical shift frequency difference (82 ppm)$\times|\gamma_N B^0| \approx 0.8$ Hz is an order of magnitude smaller than the $^1J_{NN} = 8$ Hz scalar coupling.[69]

In a separate work on $^{15}N_2O$, the authors demonstrated the conversion between $|S_0\rangle$

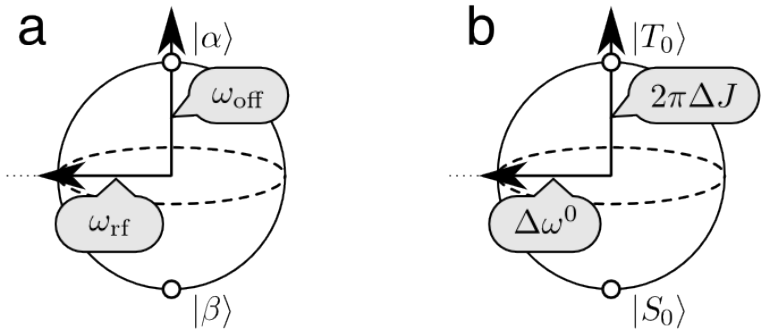

Figure 2.19: Bloch spheres for: (a) a single spin-1/2, showing fields present when an rf field $\omega_{\rm rf}(I_x\cos(\phi_{\rm rf}) + I_y\sin(\phi_{\rm rf}))$ is applied in the presence of a carrier frequency offset $\omega_{\rm off}I_z$; (b) the $m = 0$ singlet-triplet subspace of a nearly equivalent spin-1/2 pair, showing the effective field of a J-synchronous spin echo train and an error ΔJ in the spin-spin scalar coupling.

and $|T_0\rangle$ is also possible by applying a z magnetic field at the $|T_0\rangle \leftrightarrow |S_0\rangle$ transition frequency.[68] Storage and retrieval of longitudinal magnetisation using these techniques paves a way for singlet NMR entirely outside high-resolution magnets. This gives a promising outlook for low-field (*e.g.* SQUID [112]) detection, imaging and remote sensing using singlet NMR.

J-broadband spin echo trains

In its current form, the synchronised-echo pulse sequence is extremely narrowband with respect to variation in Ω, (J, in the extreme strong coupling limit *c.f.* fig. 2.14(a) and fig. 2.17(a)). One may ask whether more broadband excitation is possible. Both the J coupling and chemical shift difference, hence Ω, may change subtly, for instance on changing the temperature or solvent environment around the spins.

Inspiration for a 'J-broadband' magnetisation-singlet conversion procedure in near-equivalence pairs is sought from Shaka, who has addressed the problem of ultrawideband spin-1/2 inversion.[113, 114] For an isolated spin-1/2, an rf field induces the following rotation in the $\{|\alpha\rangle, |\beta\rangle\}$ Bloch sphere:

- a transverse rotation with angular velocity $\omega_{\rm rf}(\cos(\phi_{\rm rf}), \sin(\phi_{\rm rf}), 0)$, induced by the nominal rf field $\omega_{\rm rf}(I_x\cos(\phi_{\rm rf}) + I_y\sin(\phi_{\rm rf}))$;
- a longitudinal rotation with angular velocity $\omega_{\rm off}(0, 0, 1)$ due to the offset $\omega_{\rm off}I_z$.

As illustrated in fig. 2.19(a), the transverse rotation mediates the point-to-point transformation I_z into $-I_z$, while rotation about the longitudinal axis acts as a suppressant.

Using a nonlinear-optimisation algorithm on a computer, Shaka developed 'phase-alternating' composite pulses to counteract the longitudinal component and obtain uniform, broadband inversion of the spin-1/2. 'Phase-alternating' refers to the confinement of radiofrequency phase to a single axis $\phi_{\rm rf} = \pm 180°$, which was done both for simplicity of computation and for ease of implementation on the spectrometer. The shortest phase-alternating pulse found was $(34.2_0)(123_{180})(197.6_0)(288.8_{180})$, which gave $> 99\%$ longitudinal inversion $I_z \rightarrow -I_z$ up to dimensionless rf offset $\omega_{\rm off}/|\omega_{\rm rf}| = \pm 1.0$. In contrast, the constant-phase rf pulse only inverts efficiently at exact resonance.

Shaka's phase-alternating pulses are amenable to the point-to-point inversion $I_z^{(S_0T_0)} \rightarrow -I_z^{(S_0T_0)}$, in view that J-asynchronous spin-echo trains induce similar rotations in the $\{|T_0\rangle, |S_0\rangle\}$ subspace.

- a transverse rotation with angular velocity $\Delta\omega^0(1,0,0)$ from nominal J-synchronised spin echo trains ($\Delta\omega^0 = \gamma B^0 \Delta\delta$);
- a longitudinal rotation with angular velocity $2\pi\Delta J(0,0,1)$, due to an error ΔJ in the J coupling.

These rotations are indicated in fig. 2.19(b).

A J-broadband sequence analogous to $(34.2_0)(123_{180})(197.6_0)(288.8_{180})$ is shown in fig. 2.20. Approximate transverse rotations β_0° in the $m = 0$ Bloch sphere are obtainable via $N_\beta = \text{round}(\pi(\beta°/360°)/\theta)$ spin echoes. Phase alternation of these rotations can be applied by inserting 180° rf pulses between trains of spin echoes. The latter can be verified using the identity $R_z(180°)\beta_0 R_z(180°) \equiv \beta_{180}^\circ$.

Computer simulations show that the J-broadband echo sequence performs roughly as expected. By analogy with Shaka's single spin inversion, the 99% inversion bandwidth of $I_z^{(S_0T_0)}$ for $(34.2_0)(123_{180})(197.6_0)(288.8_{180})$ is a dimensionless error in J equal to $|2\pi\Delta J/(\Delta\omega^0/2)| < 1$. The plot in fig. 2.21 shows the calculated amplitude of $I_z^{(S_0T_0)}$ against $2\pi\Delta J/(\Delta\omega^0)$ after applying (black curve) the non-compensated and (red curve) J-compensated spin echo sequences. Calculations were performed in SpinDynamica [101] using $J = 100$ Hz and $\Delta\omega^0/2\pi = 25$ Hz for the nominal interaction parameters of the spin pair. One can confirm the much-widened inversion profile. Explicit $|T_0\rangle$ and $|S_0\rangle$ trajectories during the two pulse sequences are compared in fig. 2.22(a) to (d) for instances of $\Delta J = 0$ and $\Delta J = +\Delta\omega^0/2$.

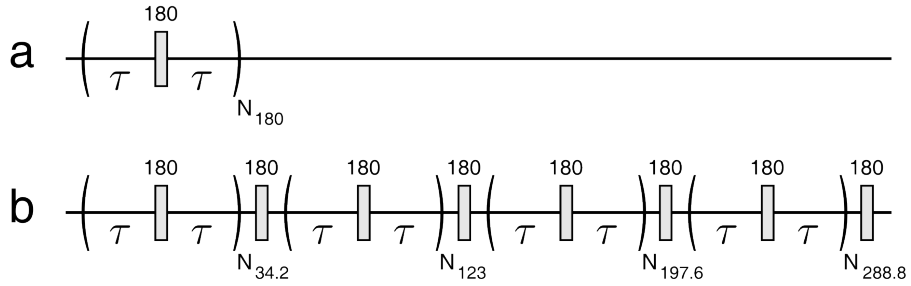

Figure 2.20: Pulse sequences for point-to-point inversion $I_z^{(S_0T_0)} \rightarrow -I_z^{(S_0T_0)}$: (a) the nominal 'constant rotation' spin echo train, where the sum of spin echo delays τ and the 180° pulse length is equal to $(2\tau+\tau_p) = \pi/\sqrt{(2\pi J)^2 + (\Delta\omega/2)^2}$; (b) phase-alternate sequence, which involves spin echo trains interleaved with 180° rf pulses. The length of each train is determined by the discretisation formula $N_\beta = \mathrm{round}(\pi(\beta°/360°)/\theta)$.

Phase-alternating rotations are also available for point-to-point 90° rotations. The shortest available sequences are $(59_0)(149_{180})$ and $(58_0)(140_{180})(172_0)$.[115] These may be useful for transforming $I_y^{(S_0T_0)} \leftrightarrow I_z^{(S_0T_0)}$ during the second spin echo train of the 'M2S' sequence.

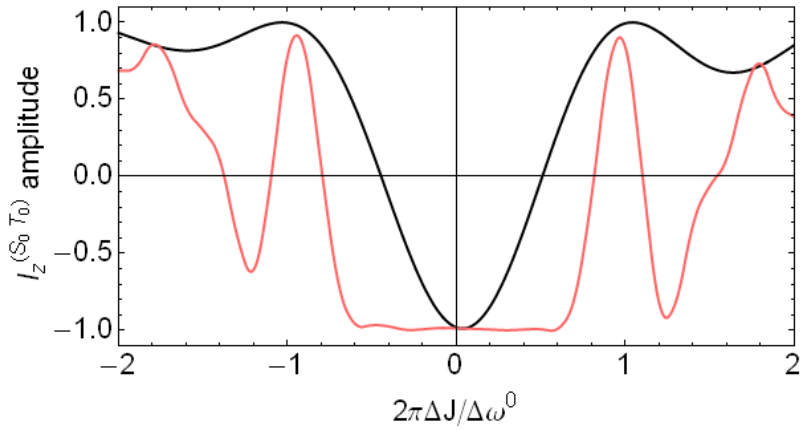

Figure 2.21: Calculated performance $I_z^{(S_0T_0)}/I_z^{(S_0T_0)}(0)$ versus an error ΔJ in the nominal spin-spin J coupling during the sequences shown in fig. 2.20(a) and (b): (black curve) a nominal (180_0) rotation in the Bloch sphere; (red curve) phase-alternate rotations $(34.2_0)(123_{180})(197.6_0)(288.8_{180})$. $J = 100$ Hz and $\Delta\omega^0/2\pi = 25$ Hz are the nominal interactions between the spin pair.

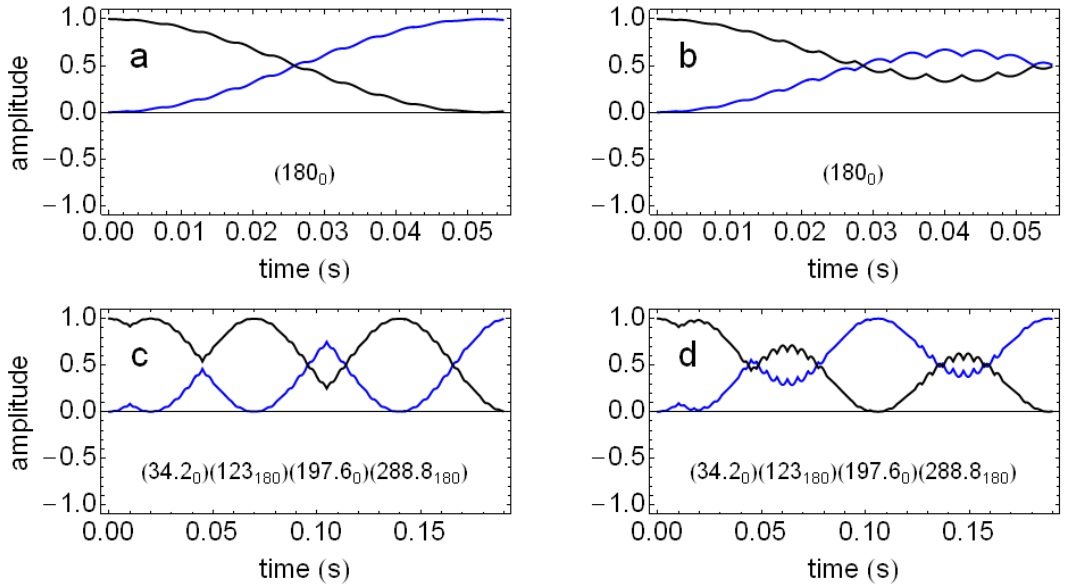

Figure 2.22: Simulated trajectories of (blue) $|S_0\rangle$ and (black) $|T_0\rangle$ states starting from an initial wavefunction $|\psi\rangle(0) = |T_0\rangle$. Interaction parameters were $J = 100$ Hz and $\Delta\omega^0/2\pi = 25$ Hz. The plots show: (a) complete interchange of the states during the sequence fig. 2.20(a) with $\Delta J = 0$; (a) incomplete conversion for the same sequence using $\Delta J = +\Delta\omega^0/2$; (c) trajectory under the phase-alternating echo sequence $(34.2_0)(123_{180})(197.6_0)(288.8_{180})$ in fig. 2.20(b) at $\Delta J = 0$ and (d) trajectory for the same sequence at $\Delta J = +\Delta\omega^0/2$. In (d) there is full inversion even under the large J offset, albeit at the cost of trebling the length of the pulse sequence.

2.2.4 Singlet excitation using transition-selective rf fields

Selective rotation in the single-quantum subspaces $\{|T_{\pm1}^{jk}\rangle\,,\,|S_0^{jk}\rangle\}$ can be induced on applying narrowband rf fields. This was demonstrated almost 20 years ago by Chandrakumar and Velan for production of two-spin longitudinal order (product order $I_{jz}I_{kz}$).[116] Here a more detailed theoretical treatment is provided for the specific conversion between I_z and T_{00}, in particular in the near-equivalence regime.

Consider, for simplicity, two isolated and chemically inequivalent spins-1/2. Under free evolution the field experienced by the $m = 0$ states is given by the magnitude $\Omega^{(S_0T_0)} = \sqrt{(2\pi J)^2 + (\gamma B^0(\delta_j - \delta_k))^2}$ and orientation $\theta = \arctan(-\gamma B^0(\delta_j - \delta_k)/2\pi J)$. The eigenstates of the Hamiltonian are defined

$$\begin{array}{c} |\phi_1\rangle \\ |\phi_2\rangle \\ |\phi_3\rangle \\ |\phi_4\rangle \end{array} = \begin{pmatrix} 1 & 0 & 0 & 0 \\ 0 & 1 & 0 & 0 \\ 0 & 0 & \cos(\theta/2) & \sin(\theta/2) \\ 0 & 0 & -\sin(\theta/2) & \cos(\theta/2) \end{pmatrix} \begin{array}{c} |\alpha_j\alpha_k\rangle \\ |\beta_j\beta_k\rangle \\ (|\alpha_j\beta_k\rangle + |\beta_j\alpha_k\rangle)2^{-1/2} \\ (|\alpha_j\beta_k\rangle - |\beta_j\alpha_k\rangle)2^{-1/2} \end{array}. \tag{2.102}$$

In this bases, the diagonal matrix representation of the Hamiltonian appears as

$$H = \frac{1}{2}\begin{pmatrix} \pi J + \omega_j^0 + \omega_k^0 & 0 & 0 & 0 \\ 0 & \pi J - \omega_j^0 - \omega_k^0 & 0 & 0 \\ 0 & 0 & \Omega - \pi J & 0 \\ 0 & 0 & 0 & -\Omega - \pi J \end{pmatrix}, \tag{2.103}$$

where $\omega_j^0 = -\gamma_j B^0(1 + \delta_j)$ are the Larmor frequencies of the nuclei.

Single-quantum transitions between eigenstates occur at frequencies equal to the difference in energy eigenvalues. The list below orders the transitions from low to high frequency, assuming positive J:

$$(\phi_4 \leftarrow \phi_2): \quad (\omega_j^0 + \omega_k^0 - 2\pi J - \Omega)/2 \tag{2.104}$$

$$(\phi_1 \leftarrow \phi_3): \quad (\omega_j^0 + \omega_k^0 + 2\pi J - \Omega)/2 \tag{2.105}$$

$$(\phi_3 \leftarrow \phi_2): \quad (\omega_j^0 + \omega_k^0 - 2\pi J + \Omega)/2 \tag{2.106}$$

$$(\phi_1 \leftarrow \phi_4): \quad (\omega_j^0 + \omega_k^0 + 2\pi J + \Omega)/2. \tag{2.107}$$

The main feature of this treatment is that the 'outermost' transitions denoted in eqs. (2.104) and (2.107) connect $|T_{\pm 1}\rangle$ with the eigenstate $|\phi_4\rangle$ that has largest singlet component. The transitions eqs. (2.105) and (2.106) connect $|T_{\pm 1}\rangle$ with the minimum singlet component. Selective exciting of these manifolds may therefore allow net transfer of triplet population into singlet population, and vice versa.

Subspace restriction

Consider shifting the carrier frequency to $+(2\pi J + \Omega)$ above the mean single-quantum frequency. This places the transition $\phi_1 \leftarrow \phi_4$ on resonance. The Hamiltonian in this new frame (denoted by prime) is represented by the matrix

$$H' = \frac{1}{2}\begin{pmatrix} -\Omega - \pi J & 0 & 0 & 0 \\ 0 & \Omega + 3\pi J & 0 & 0 \\ 0 & 0 & \Omega - \pi J & 0 \\ 0 & 0 & 0 & -\Omega - \pi J \end{pmatrix}. \tag{2.108}$$

The spectrum shift is confirmed by consulting the eigenvalue differences:

$$(\phi_4 \leftarrow \phi_2)' : \quad -2\pi J - \Omega \tag{2.109}$$

$$(\phi_1 \leftarrow \phi_3)' : \quad -\Omega \tag{2.110}$$

$$(\phi_3 \leftarrow \phi_2)' : \quad -2\pi J \tag{2.111}$$

$$(\phi_1 \leftarrow \phi_4)' : \quad 0. \tag{2.112}$$

A constant-amplitude rf field is applied at the frequency of this new frame. The Hamiltonian for the rf field $H'_{\mathrm{rf}} = \omega_{\mathrm{rf}} I_x$ is represented by

$$H'_{\mathrm{rf}} = \frac{\omega_{\mathrm{rf}}}{\sqrt{2}}\begin{pmatrix} 0 & 0 & \cos(\theta/2) & \sin(\theta/2) \\ 0 & 0 & \cos(\theta/2) & \sin(\theta/2) \\ \cos(\theta/2) & \cos(\theta/2) & 0 & 0 \\ \sin(\theta/2) & \sin(\theta/2) & 0 & 0 \end{pmatrix}. \tag{2.113}$$

The sine and cosine factors in eq. (2.113) can be interpreted by the fact that the rf field does not bridge the homonuclear spin symmetry, as $\langle T_M | H'_{\mathrm{rf}} | S_0 \rangle = 0$. The effective rf

field experienced by each transition is thus proportional to the triplet amplitude of the connected states. Outer transitions $\phi_4 \leftarrow \phi_2$ and $\phi_1 \leftarrow \phi_4$ experience an rf amplitude scaled by $\sin(\theta/2)$ whilst the inner ones $\phi_1 \leftarrow \phi_3$ and $\phi_3 \leftarrow \phi_2$ scale by $\cos(\theta/2)$. This is the familiar 'roofing' phenomenon,[4] where inner J-doublet transitions of a strongly coupled spin-1/2 pair are more intense in the 90°-acquire spectrum than the outer ones.

For single-transition selectivity the rf field strength must be weak to satisfy $|\omega_{\mathrm{rf}}/2\pi| \ll |J|$. Under this condition the off-diagonal elements of H'_{rf} leave nonresonant transitions unperturbed. The Hamiltonian is secular and perturbs only the resonant two-level system:

$$H'_{\mathrm{rf}} + H' = \frac{1}{2}\begin{pmatrix} -\Omega - \pi J & \square & \square & \omega_{\mathrm{rf}}\sin(\theta/2)\sqrt{2} \\ \square & \square & \square & \square \\ \square & \square & \square & \square \\ \omega_{\mathrm{rf}}\sin(\theta/2)\sqrt{2} & \square & \square & -\Omega - \pi J \end{pmatrix}. \tag{2.114}$$

On exponentiation of eq. (2.114) one may see the propagator corresponds to a rotation in the $\{|\phi_1\rangle, |\phi_4\rangle\}$ subspace:

$$\exp[-\mathrm{i}(H'_{\mathrm{rf}} + H')t] = \mathrm{e}^{\mathrm{i}At}\begin{pmatrix} \cos(Bt) & \square & \square & -\mathrm{i}\sin(Bt) \\ \square & \square & \square & \square \\ \square & \square & \square & \square \\ -\mathrm{i}\sin(Bt) & \square & \square & \cos(Bt) \end{pmatrix}. \tag{2.115}$$

where $A = (\Omega + \pi J)/2$ and $B = \omega_{\mathrm{rf}}\sin(\theta/2)/\sqrt{2}$. This result is exact, provided the rf field is weak compared to J.

Magnetisation-singlet conversion

The off-diagonal elements in eq. (2.115) is maximised for rf duration $\tau_{\mathrm{rf}} = |\pi/2B|$. This swaps identities of the connected states, meaning that if one starts with a longitudinal polarisation

$$p(I_{jz} + I_{kz}) = p(|T_{+1}\rangle\langle T_{+1}| - |T_{-1}\rangle\langle T_{-1}|), \tag{2.116}$$

the application of the weak rf field leads to a singlet-excess given by

$$\text{eq. (2.116)} \xrightarrow{H_{\text{rf}} \times \tau_{\text{rf}}} p(|\phi_4\rangle\langle\phi_4| - |T_{-1}\rangle\langle T_{-1}|) \tag{2.117}$$

$$\begin{aligned} = \quad & p\Big[\cos^2(\theta/2)\,|S_0\rangle\langle S_0| + \sin^2(\theta/2)\,|T_0\rangle\langle T_0| \\ & - \sin(\theta/2)\cos(\theta/2)\Big(|T_0\rangle\langle S_0| + |S_0\rangle\langle T_0|\Big) \\ & - |T_{-1}\rangle\langle T_{-1}|\Big]. \end{aligned} \tag{2.118}$$

The singlet polarisation is determined by projection onto T_{00} which gives

$$p_S = p \times \frac{(T_{00}\,|\,|\phi_4\rangle\langle\phi_4| - |\phi_2\rangle\langle\phi_2|\,)}{(T_{00}|T_{00})} = \frac{p}{2} \times (1 + \cos(\theta)). \tag{2.119}$$

It is clear that p_S increases as the spins become more strongly coupled for the target eigenket $|\phi_4\rangle$ becomes richer in $|S_0\rangle$. Yet while there is potentially twice the singlet polarisation available for near-equivalent spins than those weakly coupled, this polarisation builds up much more slowly. In the weakly coupled limit $|\theta| \to \pi/2$, the duration τ_{rf} tends to $\pi/|\omega_{\text{rf}}|$, (N.B. equivalent to a spin-selective 180° rf pulse). For near-equivalence spin pairs, (small $|\theta|$), τ_{rf} tends to

$$\tau_{\text{rf}} \approx \frac{\pi\sqrt{2}}{\omega_{\text{rf}}\theta} + O(\theta^3). \tag{2.120}$$

The conversion time is inversely proportional to θ, so approaches infinity as $\theta \to 0$.

Simulations

Trajectories for I_z and T_{00} during weak rf irradiation are demonstrated in fig. 2.23 for two very strongly coupled spin-1/2 pairs (see fig. 2.23(a) and fig. 2.23(b)) and a weakly coupled pair (see fig. 2.23(c)). Trajectories are plotted from time $t = 0$, where starting spin order is defined as I_z, until time $t = 2\tau_{\text{rf}} = \pi\sqrt{2}/|\omega_{\text{rf}} \sin(\theta/2)|$, such that in each case the width of the plot corresponds to a 360° rotation of the resonant transition. Midway time points therefore correspond to where maximum singlet excitation is expected. These maxima occur as predicted, and the singlet amplitude agrees with the values of p_S predicted by eq. (2.119) (grey lines). The plots (a) and (b) confirm half the starting I_z remains at this time, in accordance with eq. (2.117).

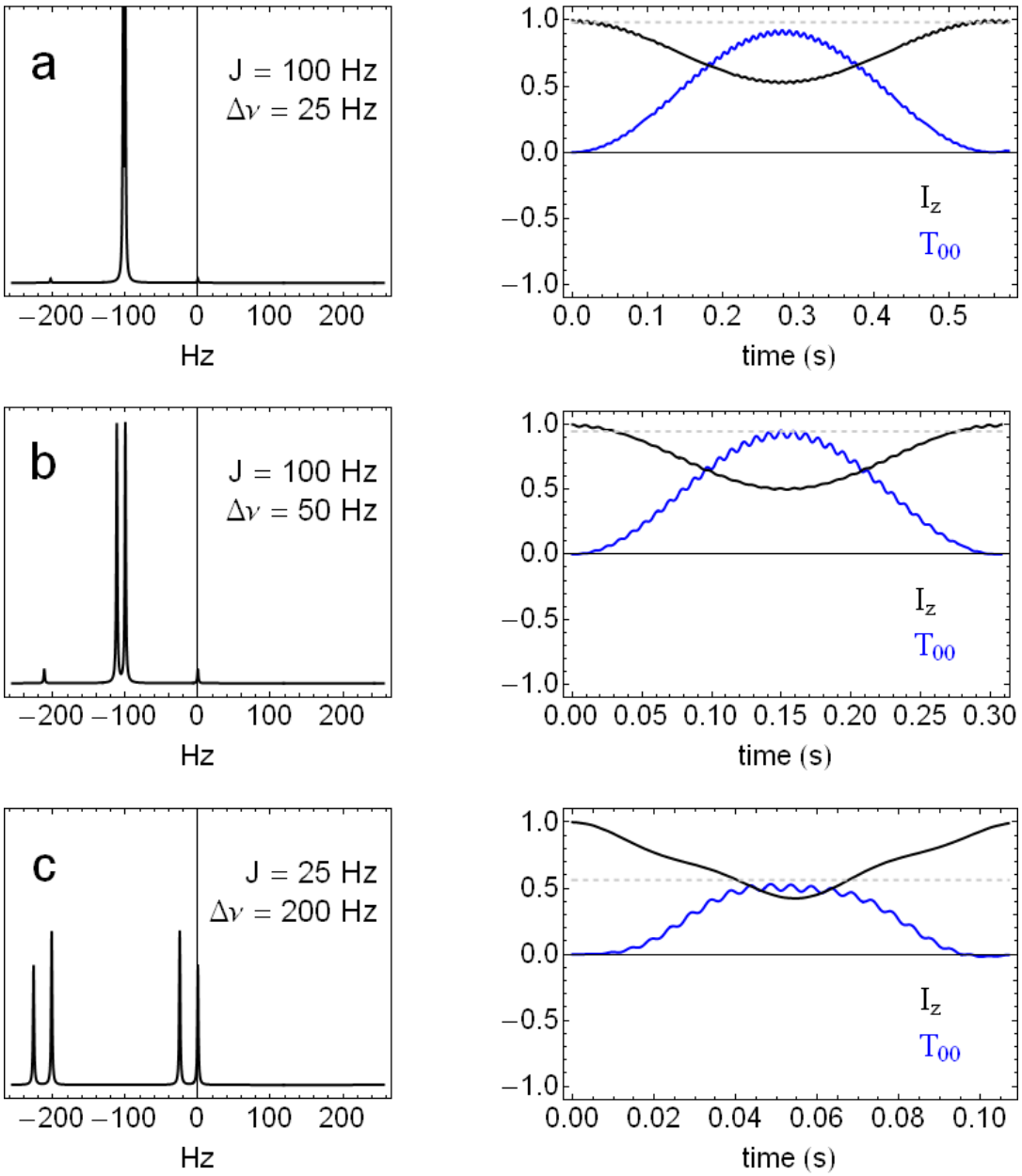

Figure 2.23: Simulated magnetisation-singlet order interconversion during irradiation under a weak rf field. The field is centred upon the rightmost transition in the multiplets of spin pairs with: (a) $J = 100$ Hz, $\gamma B^0 \Delta\delta/2\pi = 25$ Hz ($\theta = 14°$); (b) $J = 100$ Hz, $|\gamma B^0 \Delta\delta/2\pi| = 50$ Hz ($\theta = 26.5°$); (c) $J = 25$ Hz, $|\gamma B^0 \Delta\delta/2\pi| = 200$ Hz ($\theta = 83°$). The trajectories on each right-hand side show amplitudes of I_z (black) and T_{00} (blue) through a 360° excitation of the selected transition, in each case using an rf amplitude $|\omega_{\mathrm{rf}}/2\pi| = 10$ Hz. The dashed grey lines indicate the theoretical maximum conversion amplitude predicted by eq. (2.119).

Comparison with spin echo method

In the limit of small $|\theta|$, singlet excitation by the transition-selective rf method is competitive with the spin echo method described in §2.2.3. Both methods excite singlet order to the same efficiency $p_S = p$, and do so within similar timescales.

The duration of each method is proportional to $1/|\Delta\delta|$. For the spin echo method, echoes $(\tau - 180° - \tau)$ are arranged with $\tau = \pi/\Omega$ with approximately $|3\pi/4\theta|$ echoes required for optimum $I_z \rightarrow T_{00}$ conversion. For small $|\theta|$, the total conversion time is

$$\tau_{\text{echoes}} \approx \frac{3\pi^2}{4} \frac{1}{|\gamma B^0 \Delta\delta|}. \tag{2.121}$$

A weak rf pulse excites maximum T_{00} over the timescale τ_{rf} from eq. (2.120). Assuming the rf amplitude as multiple $|K| \ll 1$ of the J coupling, *i.e.* $\omega_{\text{rf}} = 2\pi J \times K$, this is expressible in the form

$$\tau_{\text{rf}} \approx \frac{\pi\sqrt{2}}{K} \frac{1}{|\gamma B^0 \Delta\delta|}. \tag{2.122}$$

Typically, one would expect to use a value $K \approx 0.1$ to 0.2, to ensure narrowband excitation about the Larmor frequency. Eqs. (2.121) and (2.122) are therefore comparable in magnitude, though the former (eq. (2.121)) is usually shorter

In regards to errors, the synchronised echo train method is superior. Phase cycling of successive spin echoes guards exceptionally well against both frequency offsets and amplitude inhomogeneity in the rf pulses, as seen in §2.2.3. In the weak-rf method, rf compensation is more of a problem since the subspace-specific rotation is induced only near exact resonance. As an illustration, consider fig. 2.24(a) where the conversion amplitude p_S/p of I_z into T_{00} is plotted versus a dimensionless rf frequency offset $\omega_{\text{off}}/\omega_{\text{rf}}^0$ and amplitude $\omega_{\text{rf}}/\omega_{\text{rf}}^0$. The spin system assumed is an isolated spin-1/2 pair with parameters $J = 100$ Hz, $|\gamma B^0 \Delta\delta| = 25$ Hz ($\theta = 14°$), and the nominal rf field strength chosen as $\omega_{\text{rf}}^0 = 10$ Hz. It is clear that the excitation performance diminishes rapidly versus rf offset. The singlet excitation becomes extremely inefficient at offsets $|\omega_{\text{off}}/\omega_{\text{rf}}^0|$ as low as 10% (± 2 Hz in this example).

The secularity of weak nonresonant rf fields suggests that shaped pulses and other engineered pulses,[117] including composite pulses,[60] are unable to compensate for frequency

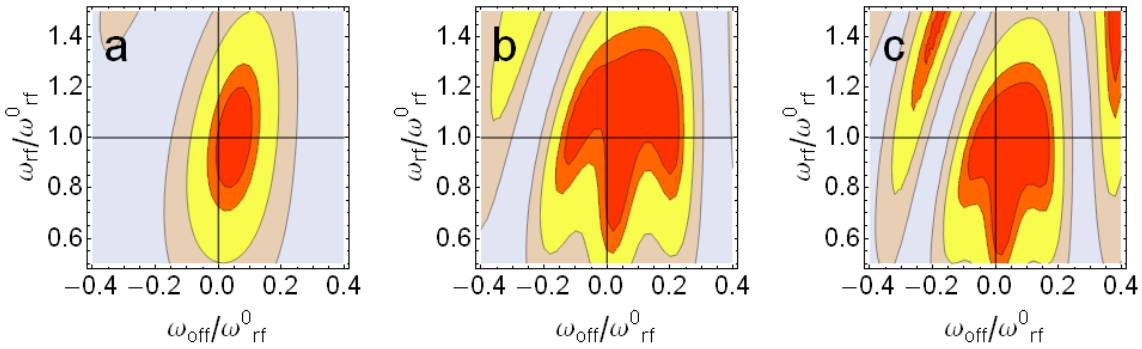

Figure 2.24: Singlet excitation via weak rf-irradiation is narrowband with respect to rf parameters. The plot in (a) shows calculated values of p_S/p after irradiation for nominal time $\tau_{rf} = \pi/2|\sqrt{2}\omega_{rf^0}\sin(\theta/2)|$ under conditions of a dimensionless offset $\omega_{off}/\omega^0_{rf}$ (horizontal scale) and dimensionless rf amplitude $\omega_{rf}/\omega^0_{rf}$ (vertical scale). Parameters for the system are $J = 100$ Hz, $|\gamma B^0 \Delta\delta| = 25$ Hz, and the nominal rf field strength is chosen arbitrarily as $\omega^0_{rf} = 10$ Hz. In (b) the excitation sequence comprises a sandwich of pulses $(\tau_{rf}/2)(\tau_{rf})(\tau_{rf}/2)$, where the central pulse is phase-shifted by 90°; this can be thought as a $(90^\circ_0)(180^\circ_{90})(90^\circ_0)$ composite rotation. In (c) the analogous rotation $(90^\circ_0)(240^\circ_{90})(90^\circ_0)$ is applied. Colours of the shaded regions denote singlet excitation $p_S/p > 0.5$ (yellow), $p_S/p > 0.8$ (orange), $p_S/p > 0.9$ (red) and $p_S/p < 0.2$ (blue region).

offsets. Fig. 2.24(b) and fig. 2.24(c) show singlet amplitudes after weak rf $(90^\circ_0)(180^\circ_{90})(90^\circ_0)$ and $(90^\circ_0)(240^\circ_{90})(90^\circ_0)$ composite weak-rf pulses. The 'flip angle' in each of these pulse is understood as that induced the Bloch sphere of the resonant single-transition subspace (*e.g.* $180^\circ_0 \equiv \tau_{rf} I_x$, $90^\circ_{90} \equiv 0.5\tau_{rf} I_y$). Comparison with fig. 2.24(a) shows that excitation may be protected to a small extent using composite pulses, although not beyond offsets $\omega_{off}/\omega^0_{rf} \approx 1$. According to these results, the J-sychronised-echo sequence (2.2.3) performs better against unstable and inhomogeneous rf at low power. Note that the multiple spin-echo sequence has its resonance condition on the zero-quantum frequency, not the single-quantum frequency. This falls to setting the spin echo timing accurately, which is vastly less prone to error.

2.3 Heteronuclear-mediated singlet NMR

The transfer of singlet spin order to neighbouring heteronuclei has extensive history within parahydrogen-enhanced NMR (PHIP). It is a natural wish in PHIP to hyperpolarise nuclei other than just the protons and extend the scope for signal enhancement.[118] Cross-polarisation of this kind is useful not only for NMR observation at other chemical sites, but also because low-gamma nuclei may relax more slowly than the protons and can provide a storage haven for the hyperpolarised spin order.[119]

First experiments to excite ^{13}C spin order from antisymmetric parahydrogen order used pulse sequences based upon INEPT.[120] Later, midway through the 2000's, Goldman and Jóhanesson demonstrated a range of other methods including diabatic field cycling and pulse sequences for both low and high B^0 magnetic fields.[121, 122, 123] These methods sparked parahydrogen-induced hyperpolarisation an immediate prominence in biomedical MRI, in particular of ^{13}C in metabolites in vivo, including succinic acid,[124] a participant in the Krebs cycle. More elaborate pulse sequences have since been developed,[58, 63] including some designed for time-optimal polarisation transfer.[125]

In general, successful heteronuclear transfer of spin order from parahydrogen requires magnetic inequivalence at the two proton sites, either or both that: (i) the two proton sites occupy chemically inequivalent sites, and have different chemical shifts;[30] (ii) the proton pair has unequal J couplings to a heteronucleus contained within the molecule. Recently, a demonstration was made showing that (ii) suffices for PHIP-NMR in a zero magnetic field environment.[126]

The present section applies the idea of heteronuclear-induced symmetry-breaking to the problem of homonuclear magnetisation-to-singlet conversion. Chemically and magnetically equivalent spin pairs in high-symmetry molecules may become unsymmetrical on substitution with a magnetic heteronucleus, for instance a nearby ^{13}C or ^{15}N. We have used this approach to obtain singlet relaxation data in otherwise-equivalent spin pairs. This provides useful information to help understand the singlet relaxation phenomenon.

2.3.1 Heteronucleus-induced symmetry breaking

The following analysis takes the same approach as §2.1, where heteronuclear spin interactions are decomposed into a singlet-triplet operator basis. The spin system is assumed to

contain two homonuclear spins-1/2, denoted 'I', plus heteronuclei 'S', where $\gamma_S \neq \gamma_I$.

The basis for decomposing the Hamiltonian is chosen as the ket-bra product operator basis $(|l_I, m_I\rangle \otimes |l_S, m_S\rangle)(\langle l'_I, m_I| \otimes \langle l'_S, m_S|)$. For all practical field strengths $|B^0| > \mu$T, the secular approximation partitions the free-evolution Hamiltonian into block-diagonals in the m_I and m_S quantum numbers. For simplicity, and in consideration of the likely heteronuclear abundance, the 'S' nuclei are chosen to be spin-1/2 (includes ^{13}H, ^{13}C, ^{15}N, ^{19}F and ^{31}P), but in general the approach applies to heteronuclei with spin quantum number greater than 1/2.

For a single 'S'-spin, singlet-triplet transitions are allowed under a difference in J_{I_jS} and J_{I_kS}. The Hamiltonian may be written

$$\begin{aligned} H_J &= 2\pi J_{I_jS} I_{jz} S_z + 2\pi J_{I_kS} I_{kz} S_z & (2.123) \\ &= \pi(J_{I_jS} + J_{I_kS})(I_{j\alpha} I_{k\alpha} - I_{j\beta} I_{k\beta}) + \underbrace{\pi(J_{I_jS} - J_{I_kS}) I_x^{(S_0T_0)} (S_\alpha - S_\beta)}_{m_I = 0,\, m_S = 0}. & (2.124) \end{aligned}$$

The nondiagonal part is proportional to $I_x^{(S_0T_0)}$ and indicates zero-quantum singlet-triplet transitions of the 'I' spins at the rate $\pi\Delta J_{IS}$. Geometrical representation of this off-diagonal field is shown in fig. 2.25(b) along with the homonuclear II coupling, which as seen previously (§2.1) behaves as a z rotation in the Bloch sphere. Comparing with §2.1, it can be seen that as far as the homonuclei are concerned, IS couplings behave in an identical way to chemical shifts. This confirms singlet order is accessible in chemically equivalent homonuclear pairs ($AA'X$ systems), provided $\Delta J_{IS} \neq 0$.

If there is more than one heteronucleus the situation is more complicated, but in general homonuclear singlet-triplet conversion still requires unsymmetrical J couplings. A case worth considering in detail is that of two chemically equivalent I spins plus two chemically equivalent S spins where $J_{IS} = J_{I'S'}$ and $J_{I'S} \equiv J_{IS'}$ ($AA'XX'$ system, see fig. 2.25(c) inset). This 'rectangular' topology exists in quite a few high-symmetry molecules including [1,2-^{13}C$_2$] ethyne and [1,4-^{13}C$_2$] or [2,3-^{13}C$_2$] fumaric and maleic acids. The heteronuclear

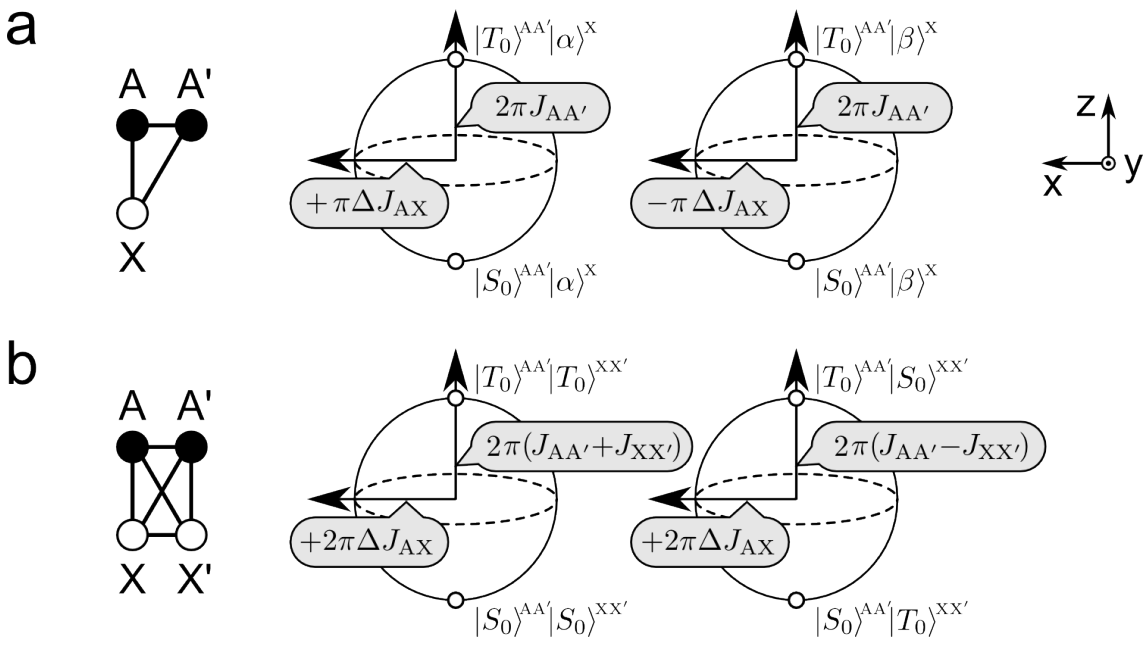

Figure 2.25: Illustration of fields induced in the non-diagonal subspaces of the J Hamiltonian: (a) for two chemically equivalent homonuclei, plus one heteronucleus; (b) for two homo and heteronuclear pairs, both chemically equivalent.

J Hamiltonian decomposes in the four-spin operator basis decomposes into

$$\begin{aligned} H_J &= 2\pi\Big(J_{AX}I_{Az}S_{Xz} + J_{AX'}I_{Az}S_{X'z} + J_{A'X}I_{A'z}S_{Xz} + J_{A'X'}I_{A'z}S_{X'z}\Big) \qquad (2.125)\\ &\equiv \pi(I_{Az}+I_{A'z})(J_{AX}+J_{A'X})(S_{Xz}+S_{X'z}) \\ &\qquad +\pi(I_{Az}-I_{A'z})(J_{AX}-J_{A'X})(S_{Xz}-S_{X'z}) \\ &= \underbrace{\pi(J_{AX}-J_{A'X})I_x^{(S_0T_0)}S_x^{(S_0T_0)}}_{m_I=0,\,|m_S|=1} + \pi(J_{AX}+J_{A'X})I_zS_z, \qquad (2.126) \end{aligned}$$

where $J_{AX} = J_{IS} \equiv J_{I'S'} = J_{A'X'}$ and $J_{A'X} = J_{I'S} \equiv J_{IS'} = J_{AX'}$.

This example stresses the magnetic equivalence symmetry refers completely to the symmetry of the spin Hamiltonian, not the molecular symmetry. Singlet-triplet conversion is mediated by the scalar coupling difference $(J_{AX} - J_{A'X})$. The difference in heteronuclear couplings induces rotations in the triplet-triplet and singlet-triplet product spaces of the two spin pairs, as is represented in fig. 2.25(c). For completeness, the Bloch spheres in fig. 2.25(c) show also the field axes of the homonuclear J couplings, whose sum $J_{AA'} + J_{XX'}$ acts to preserve singlet-singlet and triplet-triplet product states.

2.3.2 Experimental demonstrations

The analysis of heteronucleus-induced symmetry-breaking suggests that existing pulse sequences for magnetisation-singlet conversion, for instance Sarkar's sequence, may be used simply by replacing all dependences of the chemical shift differential with the relevant heteronuclear J difference. A scheme for heteronuclear singlet NMR is thereby summarised in fig. 2.26. These sequences are explained through the experimental demonstrations below.

Sarkar's sequence for 'strong' heteronuclear couplings

Sarkar's sequence (see §2.2.2 and fig. 2.26(a)i) was used unmodified to excite singlet order on the protons in the molecule 2,5-dibromothiophene, hereafter abbreviated 2,5-DBT. Fig. 2.27(a) shows the proton sites in 2,5-DBT are interchangeable by a C_{2v} mirror symmetry operation on the molecule and therefore chemically equivalent. Ordinarily the molecular symmetry precludes excitation of singlet order on the protons. Heteronuclear symmetry-breaking, however, is possible where the ring sites C2($\equiv$ C5) or C3($\equiv$ C4) are occupied by ^{13}C. Both carbon sites are situated outside the mirror plane bisecting the two protons and may therefore generate a J-coupling differential.

Values of $^3J_{\mathrm{HH}}$ and the J_{CH} couplings for [^{13}C$_1$]2,5-dibromothiophene are displayed in fig. 2.27(b) and fig. 2.27(c). These were determined by fitting the multiplets of the 90°-acquire ^{13}C NMR spectra for a sample containing 0.2 M 2,5-dibromothiophene dissolved in d_6-DMSO, recording at 9.4 T and room temperature. Naturally abundant [2-^{13}C] and [3-^{13}C] isotopologues were each present at 4.4 mM concentration, due to the approximate 1.1% ^{13}C abundance.

The couplings in 2,5-DBT satisfy $|\omega_x^{(S_0T_0)}| \gg |\omega_z^{(S_0T_0)}|$, *i.e.* that $|\pi\Delta J_{\mathrm{CH}}| \gg |\pi J_{\mathrm{HH}}|$, which is the regime that Sarkar's sequence is applicable (fig. 2.26(a)i). An initial 90° pulse on the I spins rotates the equilibrium longitudinal polarisation into transverse coherences. The ensuing spin echo, denoted $(\tau_a - 180° - \tau_a)$ where $\tau_a = 1/|4J_{\mathrm{HH}}|$, transforms these into antiphase coherences, where the 180° ^{1}H pulse refocuses the proton chemical shifts

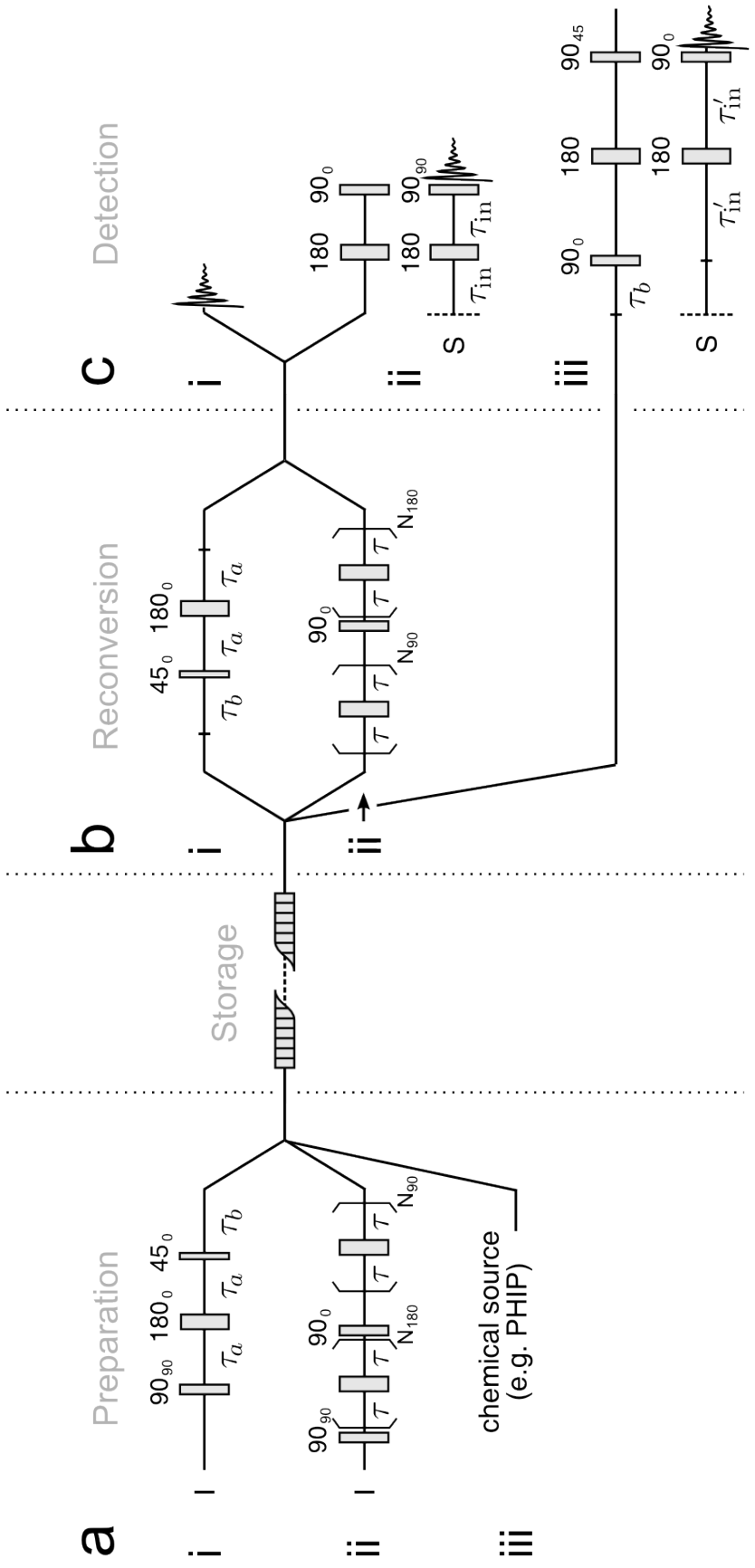

Figure 2.26: Summary of magnetisation-singlet conversion methods, for both homo- and hetero-nuclear singlet NMR.

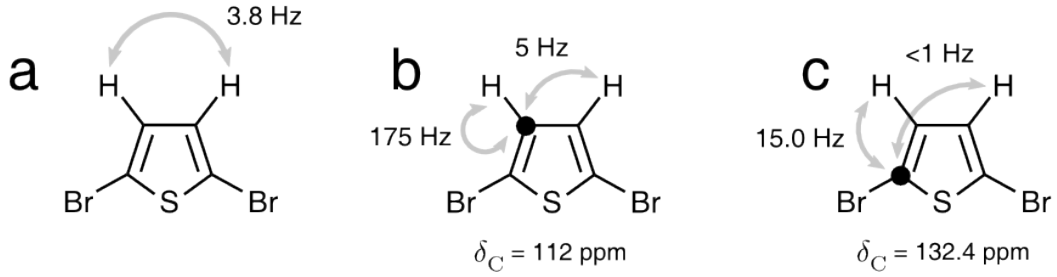

Figure 2.27: Scalar couplings and isotropic chemical shifts obtained from ^{13}C NMR spectra of the $^{13}C_1$-containing isotopologues of 2,5-dibromothiophene, measured at 9.4 T on a 0.2 M solution in degassed d_6-DMSO. The black dot in (b) and (c) denotes the position of ^{13}C.

and the heteronuclear couplings:

$$p_I I_z \quad \equiv \quad p_I \Big(|T_{+1}\rangle^I \langle T_{+1}|^I - |T_{-1}\rangle^I \langle T_{-1}|^I \Big) \Big(|\alpha\rangle^S \langle\alpha|^S + |\beta\rangle^S \langle\beta|^S \Big) \quad (2.127)$$

$$\xrightarrow{90^\circ_{90}} \xrightarrow{\text{echo}} \quad \frac{p_I}{\sqrt{2}} \Big(-\mathrm{i}(|T_{+1}\rangle^I + |T_{-1}\rangle^I) \langle T_0|^I + \mathrm{i}\,|T_0\rangle^I (\langle T_{+1}|^I + \langle T_{-1}|^I) \Big) \Big(|\alpha\rangle^S \langle\alpha|^S + |\beta\rangle^S \langle\beta|^S \Big). \quad (2.128)$$

The antiphase coherences are then converted into zero-quantum triplet-triplet coherences by the 45° pulse:

$$\text{eq. (2.128)} \quad \xrightarrow{45^\circ_0} \quad \frac{p_I}{2} \Big((|T_{+1}\rangle^I + |T_{-1}\rangle^I)(\langle T_{+1}|^I + \langle T_{-1}|^I) - 2\,|T_0\rangle^I \langle T_0|^I \Big) \Big(|\alpha\rangle^S \langle\alpha|^S + |\beta\rangle^S \langle\beta|^S \Big) \quad (2.129)$$

$$\xrightarrow{\text{ZQ only}} \quad \frac{p_I}{2} \Big(I_\alpha + I_\beta - 2(|T_0\rangle^I |\alpha\rangle^S)(\langle T_0|^I \langle\alpha|^S) - 2(|T_0\rangle^I |\beta\rangle^S)(\langle T_0|^I \langle\beta|^S) \Big). \quad (2.130)$$

Free evolution for time $\tau_b = 1/|\Delta J_{IS}|$ converts the products of the form $|T_0\rangle^I |\alpha\rangle^S$ into $|S_0\rangle^I |\alpha\rangle^S$ via a 180° rotation about $I_x^{(S_0T_0)}$, as indicated by fig. 2.25(a). The experimental values of τ_b found to give optimum singlet excitation agree with this formula. These were found to be $\tau_b = 60$ ms for [2-^{13}C]-2,5-DBT and $\tau_b = 6.0$ ms for [3-^{13}C]-2,5-DBT.

The zero-quantum density operator after time τ_b is given finally by

$$\text{eq. (2.130)} \quad \xrightarrow{\tau_b} \quad \frac{p_I}{2} \Big(I_\alpha + I_\beta - 2(|S_0\rangle^I |\alpha\rangle^S)(\langle S_0|^I \langle\alpha|^S) - 2(|S_0\rangle^I |\beta\rangle^S)(\langle S_0|^I \langle\beta|^S) \Big) \quad (2.131)$$

$$\equiv \quad \frac{p_I}{2} \Big(I_\alpha + I_\beta - 2\,|S_0\rangle^I \langle S_0|^I \Big), \quad (2.132)$$

The last line indicates a singlet polarisation p_S (on the 'I' spins) equal to p_I. As only the I spin states are transformed in this sequence, Sarkar's zero-quantum dephasing and J-broadband techniques may be used if desired (2.2.2).

Singlet order on 2,5-DBT was isolated (with the sample residing in high field) by applying a 3 kHz WALTZ-16 modulated rf field at the proton Larmor frequency. The resonant field has the effect of 'switching' the AA'X spin configuration into A_2X by suppressing all CH couplings. The locking is applied for the entire duration of the storage time.

For detection, singlet order was converted into to antiphase carbon magnetisation I_zS_x by removing the spin decoupling field, executing Sarkar's sequence in reverse chronological order back to in-phase coherence on the I spins, I_x, (fig. 2.26(b)i) and performing INEPT (fig. 2.26(c)ii). Observation on the carbon channel, as opposed to the proton channel (fig. 2.26(c)i) guarantees ^{13}C site resolution, plus avoids the large proton background resulting from the all-^{12}C isotopologues, which contain magnetically equivalent proton pairs. An INEPT half-echo delay $\tau_{\mathrm{IN}} = 16$ ms was used to give optimal cross-polarisation under the 15 Hz J_{CH} coupling in [2-^{13}C]2,5-dibromothiphene. For [3-^{13}C]2,5-dibromothiphene the delay used was $\tau_{\mathrm{IN}} = 50$ ms, optimal for the 5 Hz $^2J_{\mathrm{CH}}$ coupling. To distinguish signals coming from the starting spin order a phase cycle $\{0°, 180°\}$ was used on both the initial 90° pulse and receiver phases.

Experimental decay profiles for the proton singlet order are displayed in fig. 2.28. These show the singlet-derived spectra against incremented spin locking times. A fitted decay constant $T_S \approx 2.2$ seconds is obtained for the near ^{13}C-containing isotopologue [3-^{13}C]-DBT. This is similar in magnitude to the experimental proton $T_1 = 2.2$ seconds of the same molecule, which we measured by proton inversion-recovery followed by INEPT. Singlet order in the more remote isotopologue exhibits a much longer decay time $T_S = (68 \pm 5)$ seconds. This is an order of magnitude longer than the proton T_1 of the same molecule, which was measured to be (5.4 ± 0.1) seconds. To within fitting error, the values of T_S were the same when measured under carbon decoupling (3 kHz WALTZ, on-resonance).

These results prove that the ratio of lifetimes T_S/T_1 is strongly dependent on the geometry between the spins. The fast singlet decay when ^{13}C at short distances conforms to a relaxation mechanism involving the ^{1}H-^{13}C dipole interaction. Further discussion of this is made in §3.2.2.

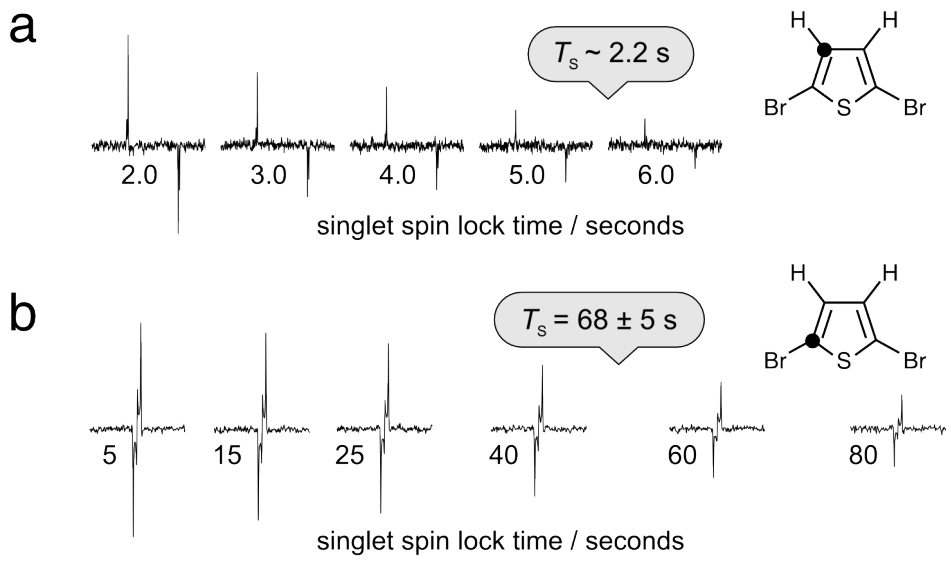

Figure 2.28: Singlet relaxation measurements in 2,5-DBT. The spectra show antiphase ^{13}C coherences obtained after different values of the singlet locking time. Singlet order was stored at 9.4 T under a 3 kHz WALTZ rf field resonant with the proton Larmor frequency ($\delta_{\mathrm{H}} = 7.1$ ppm, relative to TMS). The displayed regions show: (a) fast singlet decay in [3-^{13}C]-DBT, spectrum centred at $\delta_{\mathrm{C}} = 112$ ppm, width of displayed region = 400 Hz; (b) decay of singlet order in [2-^{13}C]-DBT, spectrum centred at $\delta_{\mathrm{C}} = 132.4$ ppm, width of displayed region = 400 Hz. Fitted monoexponential time constants T_S are given above.

Strongly coupled heteronuclear systems

Heteronuclear-mediated singlet NMR is now demonstrated using synchronised spin-echo trains (2.2.3). This is the method appropriate to low values of the singlet-triplet mixing angle θ, in this case $\theta = \arctan(\Delta J_{\mathrm{IS}}/2J_{II})$, *i.e.* for $|\Delta J_{IS}| \ll |2J_{II}|$. The study is made upon the [1-^{13}C$_1$] and [2-^{13}C$_1$] isotopologues of 1,2,3,4-tetrachlorobenzene, hereafter abbreviated as 1,2,3,4-TCB. Like 2,5-TCB, the molecule contains two chemically equivalent protons and an unsymmetrically placed ^{13}C.

A 90°-acquire ^{13}C spectrum was recorded at 9.4 T for a sample containing 35 mM natural-abundance 1,2,3,4-TCB dissolved in d$_4$-methanol. The region between 133 and 134 ppm is displayed in fig. 2.29(a), where the resonances for [1-^{13}C]-1,2,3,4-TCB and [2-^{13}C]-1,2,3,4-TCB can both be seen. It was possible to fit the J-couplings to the resolved multiplet frequencies, despite the accidental overlap of the carbon resonances. The following values were obtained by fitting single-quantum eigenfrequencies of the J Hamiltonian to each multiplet. The small values of θ confer that both [1-^{13}C]- and [2-^{13}C]-1,2,3,4-TCB contain strongly coupled protons:

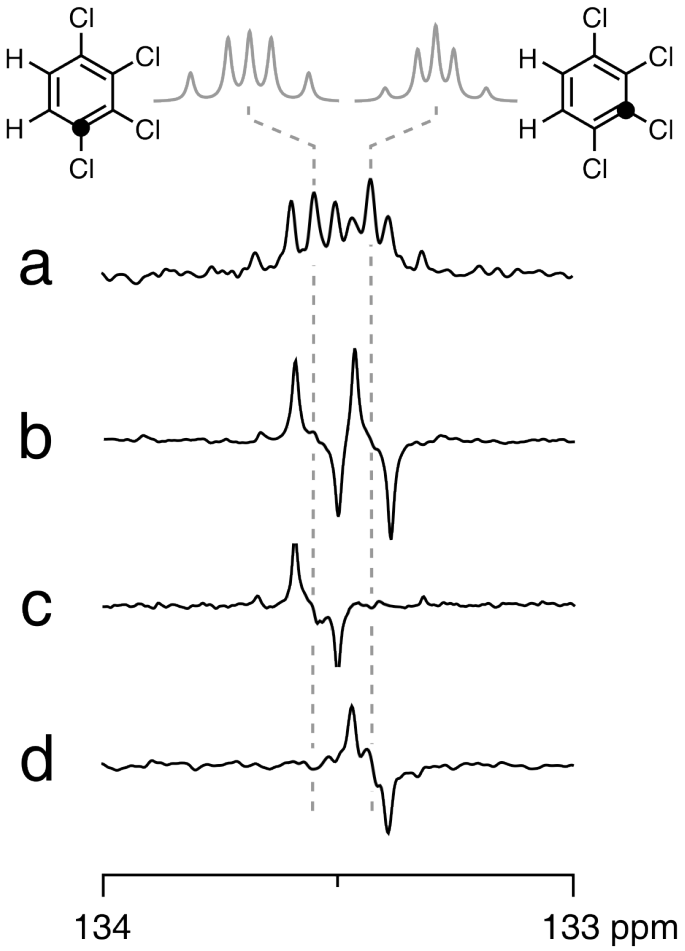

Figure 2.29: ^{13}C NMR spectra of [1-^{13}C]- and [2-^{13}C]-1,2,3,4-tetrachlorobenzene (1,2,3,4-TCB) at 9.4 T on a degassed, room-temperature solution of d_4-methanol containing 35 mM 1,2,3,4-TCB. The displayed region is between 133.0 and 134.0 ppm, referenced to tetramethylsilane. Experiments as follows: (a) ^{13}C 90°-acquire, sum of 100 transients; (b) ^{1}H-^{13}C INEPT to antiphase single-quantum coherences on ^{13}C, with INEPT delay $\tau_{\mathrm{in}} = 50$ ms; (c) and (d) the ^{13}C spectrum acquired after M2S-(τ_{lock})-S2M applied on the proton channel followed by HC-INEPT, where the element (τ_{lock}) indicates 3.0 kHz WALTZ irradiation on the protons for a duration τ_{lock}. M2S and S2M parameters used in (c) were $N_{180} = 2, N_{90} = 1$ spin echoes, synchronised-echo half-delay $\tau = 41.6$ ms, which gives optimum singlet excitation in the [1-^{13}C] isotopologue. Parameters used in (d) are $N_{180} = 4, N_{90} = 2$ spin echoes, synchronised-echo half-delay $\tau = 48.0$ ms, optimum for [2-^{13}C]-1,2,3,4-TCB.

- [1-^{13}C]-1,2,3,4-TCB: $J_{\mathrm{HH'}} = 8.9$ Hz; $J_{\mathrm{CH}} = 12.6$ Hz; $J_{\mathrm{CH'}} = -3.5$ Hz; ($\theta \approx 42°$)
- [2-^{13}C]-1,2,3,4-TCB: $J_{\mathrm{HH'}} = 8.9$ Hz; $J_{\mathrm{CH}} = 8.9$ Hz; $J_{\mathrm{CH'}} = -1.7$ Hz; ($\theta = 22°$).

While the one-dimensional spectra of [1-^{13}C]- and [2-^{13}C]-1,2,3,4-TCB partially overlap, as shown by fig. 2.29(a), there is no significant overlap in the antiphase lineshapes, as seen from the HC-INEPT-acquire spectra in fig. 2.29(b). Singlet-derived NMR signals, detected through carbon antiphase coherences, are therefore resolved unambiguously.

Singlet order was generated by applying synchronised echo trains of the form displayed in fig. 2.26(a)ii, locked for a short period of time (4-5 seconds) by applying a 3.0 kHz WALTZ decoupling field at the proton Larmor frequency and then converted into observable ^{13}C magnetisation by the S2M-INEPT combination of sequences shown in fig. 2.26(b)ii and fig. 2.26(c)ii. Spin locking was necessary in this case to successfully isolate the singlet order, for while the protons in 1,2,3,4-TCB are strongly coupled, they are not sufficiently near to magnetic equivalence to avoid rf irradiation.

The maximum signal intensity after excitation by M2S-S2M-INEPT was found to be using the parameters $N_{180} = 2, N_{90} = 1$, echo timing $\tau = 41.6$ ms for [1-^{13}C]-1,2,3,4-TCB and $N_{180} = 4, N_{90} = 2$ echoes, $\tau = 48.0$ ms for [1-^{13}C]-1,2,3,4-TCB. These values agree very closely with those predicted from theory of rotations in the $|T_0\rangle^I$ and $|S_0\rangle^I$ subspaces. The expected spin echo half-delays are

$$\tau \;=\; \frac{\pi}{2\Omega} \;=\; \frac{1}{(2\sqrt{4J_{II}^2 + \Delta J_{IS}^2})}. \tag{2.133}$$

The length of each spin echo trains is determined by

$$N_{\beta°} = \mathrm{round}\Big(\frac{\beta°}{360} \times \Big|\frac{\pi}{\theta}\Big|\Big) = \mathrm{round}\Big(\frac{\beta°}{360} \times \Big|\frac{\pi}{\arctan(\Delta J_{\mathrm{IS}}/2J_{II})}\Big|\Big), \tag{2.134}$$

where β is the nominal rotation angle required between the $m_I = 0$ states. Spectra recorded using the optimal τ and N parameters are displayed in fig. 2.29(c) and (d). Singlet order can be excited independently on the two isotopologues, it can be seen, due to the narrow synchronisation on τ. Again this helps distinguish the signals and avoid ambiguities.

The singlet decay constants were determined by measuring the spectral intensity for a series of different singlet storage times τ_{storage} and fitting to the monoexponential decay

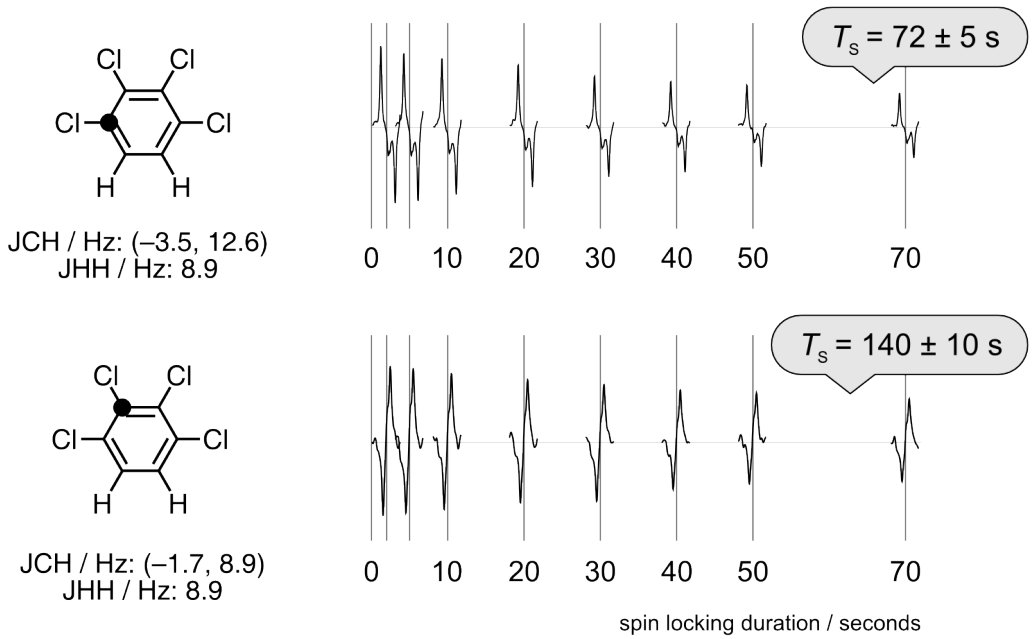

Figure 2.30: Proton singlet decay profiles for [1-^{13}C]- and [2-^{13}C]-1,2,3,4-TCB. For maximum detail, the stacked regions display only the regions of the spectrum where the signals are observed, as expansions of the regions in fig. 2.29.

$\exp(-\tau_{\text{storage}}/T_S)$. Decay profiles are displayed in fig. 2.30(a) and (b).

The yielded decays constants were $T_S = (72 \pm 5)$ seconds for [1-^{13}C]-1,2,3,4-TCB and $T_S = (140 \pm 10)$ seconds for [2-^{13}C]-1,2,3,4-TCB. These values are 8 and 15 times larger than the respective longitudinal relaxation constants of the protons: in [1-^{13}C]-1,2,3,4-TCB the measured value of T_1 was (8.7 ± 0.1) seconds; for [2-^{13}C]-1,2,3,4-TCB T_1 was (9.0 ± 0.1) seconds. Singlet order is long-lived for both isotopologues, but like 2,5-DBT, the decay constant T_S of the protons depends on location of the ^{13}C. The large disparity in T_S between [1-^{13}C]-1,2,3,4-TCB and [2-^{13}C]-1,2,3,4-TCB is consistent again with a dominant relaxation mechanism in [1-^{13}C]-1,2,3,4-TCB involving modulation of heteronuclear dipolar interactions. A quantitative discussion of these lifetimes is given in §3.2.2.

Extensions in future

Singlet order in 2,5-DBT and 1,2,3,4-TCB may be read out using the pulse sequences that were originally developed for parahydrogen, such as the 45-INEPT sequence displayed in fig. 2.26(c)iii.[58, 120, 125] These methods are likely to be very useful in singlet NMR of heteronuclear systems and the exploration of their relaxation properties, and their use is

encouraged.

2.4 Excitation of hyperpolarised singlet order

In outlining procedures for magnetisation-singlet conversion I have so far dealt exclusively with conversion between pure longitudinal magnetisation of coupled spins (or pure transverse magnetisation) and singlet order. At high polarisation levels, however, the initial density operator tends not to be dominant longitudinal polarisation, but contains other forms of spin order too.

Conversion of hyperpolarised longitudinal order into singlet order requires some care due to the nature of the singlet-triplet population difference. To illustrate this, consider an ensemble of two spins-1/2 in the extreme of unity population in $|\alpha\alpha\rangle$, corresponding to maximum longitudinal polarisation $p = +1$. Suppose a pulse sequence is applied that transfers population of $|\alpha\alpha\rangle$ into $|S_0\rangle$. The final state comprises unity singlet population, therefore corresponds to a singlet polarisation $p_S = +1$.

Now suppose the same pulse sequence is applied to the opposite extreme of negative unit polarisation, $p = -1$, corresponding to zero population in $|\alpha\alpha\rangle$. The resulting density operator must have zero population in $|S_0\rangle$. The singlet-triplet population asymmetry is at most $p_S = -1/3$, which is only a third of the polarisation above. This illustrates that p_S changes according to the sign of the starting hyperpolarisation. It suggests that to ensure the greater singlet polarisation is obtained, the pulse sequence must be carefully considered in relation to the initial ensemble state.

Fig. 2.31(a) illustrates the above for the adiabatic field cycling method. In order to obtain the maximum singlet polarisation in an hyperpolarised sample, one must apply selective inversion so as to transfer maximum $|T_{\pm 1}\rangle$ population into the singlet precursor state. This will depend on the relative signs of p, $\gamma B^0 \Delta\delta$ and J.

A similar rule applies to selective irradiation of the weak singlet-triplet transitions in a strongly coupled spin pair (2.2.4), where the population of states $|T_{\pm 1}\rangle$ and $|S_0\rangle$ can be interchanged while leaving states $|T_{\mp 1}\rangle$ and $|T_0\rangle$ unperturbed. To generate maximum singlet polarisation, one must irradiate the transition with the largest singlet-triplet population difference, as shown in fig. 2.31(b). Similar considerations apply also to Sarkar's pulse sequence and the J-sychronised spin echo sequences.

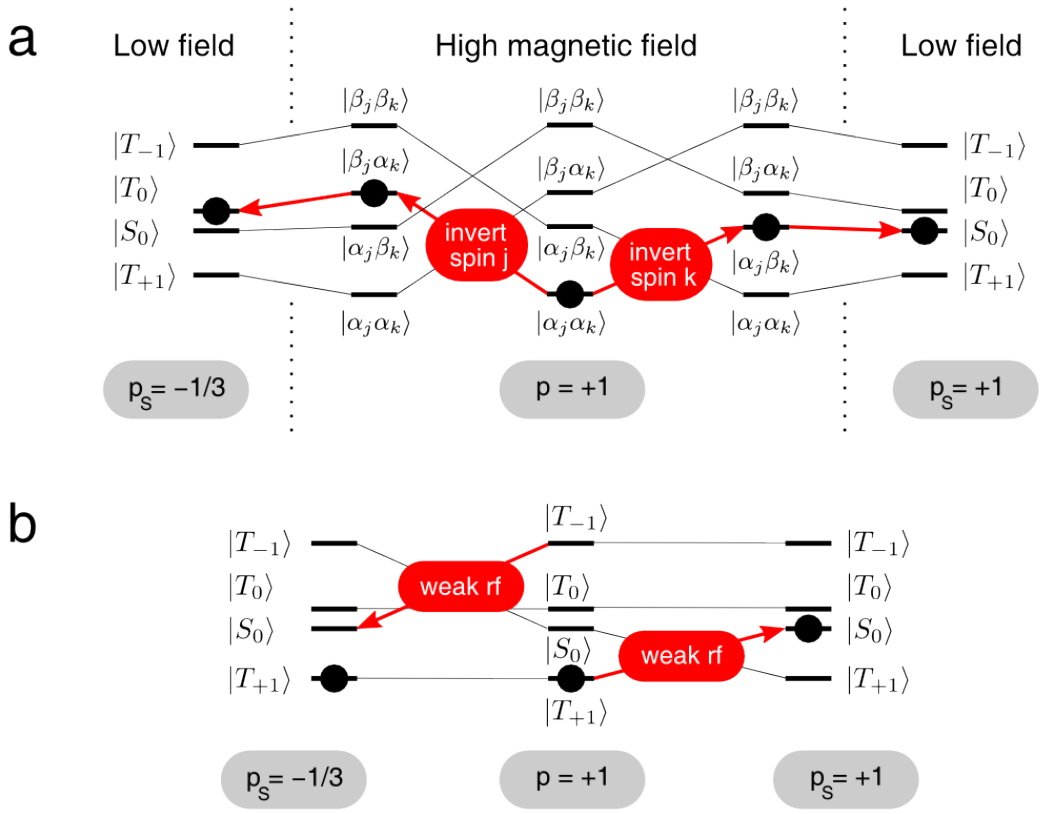

Figure 2.31: Preparation of singlet order in hyperpolarised ensembles. The centre of the above diagrams represent a spin-1/2 pair ensemble that is 100% polarised ($p = 1$), for the case $\gamma B^0(\delta_j - \delta_k)/J > 0$. Diagram (a) indicates the singlet order that results after (left) inverting spin j and (right) nucleus k, followed by adiabatic transfer to low field. Inversion of spin k transfers the population of $|\alpha_j\alpha_k\rangle$ into $|S_0\rangle$, creating maximal singlet polarisation $p_S \to 1$. Inversion of j results in a lesser singlet polarisation $p_S = -1/3$. The diagram in (b) indicates similar transformations for the selective outer-peak irradiation method (see 2.2.4).

To illustrate more generally, consider an initial hyperpolarised ensemble state comprising populations $n(\alpha\alpha) = (1+p)^2/4$ for the $m = +1$ state, $n(\beta\beta) = (1-p)^2/4$ for the $m = -1$ state and $n(\alpha\beta) = n(\beta\alpha) = (1-p)(1+p)/4$ for both states $m = 0$, where p is the nuclear polarisation. The singlet polarisation obtainable from this state, neglecting relaxation effects, can be shown equal to

$$p_S = \frac{(2p \pm p^2)}{3} \tag{2.135}$$

where the positive sign applies to when the magnetisation-singlet converting pulse sequence transfers the larger of the $T_{\pm 1}$ populations into the singlet state, and the negative sign to when the minimum is transferred. The square term indicated there is only a significant difference in p_S at polarisations $p > O(10^{-1})$, though this is nevertheless worth taking into account. If the initial polarisation p is $0.5 = 50\%$ then the expected singlet order is either $p_S = 41.7\%$ if the pulse sequence is correctly 'matched' to the initial state, but only $p_S = 25\%$ if 'mismatched'. At $p = 0.2 = 20\%$ the difference is less pronounced; the values are $p_S = 0.15$ (matched) and $p_S = 0.12$ (mismatched). At much lower starting polarisations, such as thermal polarisation, the square term is negligible and p_S is equal to $2p/3$ regardless of the spin selectivity and initial sign of p, as determined earlier.

2.5 Signal selection and filtering

This section reviews some techniques that 'filter' or 'pick out' the singlet order component of the density operator during an NMR experiment. Their purpose is to eliminate non-singlet spin order, leaving only singlet-derived NMR signals surviving to the acquisition.

Removal of non-singlet order results in NMR spectra that are quantitative of the singlet-triplet population difference at the given time point. This allows accurate measurement of singlet lifetimes despite the presence of non-singlet order within the system. As seen earlier in this work, magnetisation-to-singlet pulse sequences invariably produce other forms of spin order as a by-product to singlet order. Filtration removes these potentially contaminating terms, which may be helpful in situations where the T_S, T_1 and T_2 relaxation constants are all of similar magnitude.

On a more qualitative level, filtering allows diagnosis of whether singlet order has been excited between two spins-1/2, or has not. This helps avoid misidentification of signals by distinguishing singlet-derived signal from other spin order and artefacts.

2.5.1 Basic theory and concept

Erasure of non-singlet spin order is readily achieved by exploiting the behaviour of nuclear spin under rotations. This lies in the fundamental interplay between nuclear spin angular momentum and the rotation group.

We recall from earlier that the irreducible basis of the Liouville space under global rotations of the spins (the rotation group SO(3)), and hence the irreducible basis of spin order, is the spherical tensor operator basis.[33] Each tensor operator $\boldsymbol{T}^{\Lambda}$ is an entity with $(2\Lambda+1)$ components, $T_{\Lambda M}$ ($\Lambda \geq 0$ and $M = -\Lambda \ldots \Lambda$) whose indices Λ and M distinguish the unique way each behaves under a rotation. On applying a rotation $R \in \mathrm{SO}(3)$, the 'rank' Λ of the tensor is preserved. The components of each tensor interconvert according to the Wigner matrix:

$$RT_{\Lambda M}R^{\dagger} = \sum_{M'=-\Lambda}^{\Lambda} T_{\Lambda M'} \underbrace{D^{\Lambda}_{M'M}(R)}_{\text{(Wigner)}}. \tag{2.136}$$

The Wigner matrix is the rotation operator represented in the eigenket basis, such that

the block $\boldsymbol{D}^l(\Omega)$ connects the $(2l+1)$ eigenstates $|lm\rangle$ as

$$R\,|l,m\rangle = \sum_{m'=-l}^{l} |l,m'\rangle\, D^l_{m'm}(R). \tag{2.137}$$

The irreducible tensor indices Λ and M are each related to the total angular momentum quantum and coherence order quantum numbers of the spin states involved. The Clebsch-Gordan series defines a ket-bra operator basis of the $|l,m\rangle$ that states obeys eq. (2.136):

$$T_{\Lambda M} = \sum_{l,m}\sum_{l',m'} \Big[|lm\rangle\,\langle l'm'|\Big] C^{\Lambda M}_{lml'm'} \tag{2.138}$$

where from the Clebsch-Gordan indices it is clear that spin operators with definite 'angular momenta' are arranged. The coefficients $C^{\Lambda M}_{\lambda m\lambda' m'}$ are zero, unless $(m-m') = M$, confirming in eq. (2.138) that M represents the coherence order. One may also evaluate the commutators

$$[I_\pm,\, T_{\Lambda M}] \;=\; \sqrt{\Lambda(\Lambda+1) - M(M\pm 1)}\; T_{\Lambda(M\pm 1)}, \tag{2.139}$$

$$[I_z,\, T_{\Lambda M}] \;=\; (m-m')\; T_{\Lambda M}. \tag{2.140}$$

The second equation states that an infinitesimal rotation about the z axis yields the character $(m-m') \equiv M$. This again validates M as the coherence order.

Singlet order of a spin-1/2 pair is distinguishable because the singlet-triplet population difference operator is identified uniquely with the invariant spherical tensor operator $\boldsymbol{T}^0$. T_{00} is the only nontrivial rank-zero tensor in a system of two spins-1/2. From the four angular momentum states, the resulting sixteen $(= (2(\frac{1}{2})+1)^2 \times (2(\frac{1}{2})+1)^2)$ ket-bra product operators reduce into *five* rank-2, *nine* rank-1, and *two* rank-0 spherical tensor operators $(5+9+2=16)$. One of the invariant tensors must the unity operator,

$$E \propto |S_0\rangle\langle S_0| + |T_{-1}\rangle\langle T_{-1}| + |T_0\rangle\langle T_0| + |T_{+1}\rangle\langle T_{+1}|\,. \tag{2.141}$$

which represents the sum of all populations. There is hence one nontrivial invariant.

To summarise this section, singlet order corresponds to the rank-zero spherical tensor $\boldsymbol{T}^0 \equiv T_{00}$. The signature of $\boldsymbol{T}^0$, like all spin-0 objects, is invariance to arbitrary rotation of

the system's quantisation axes. In the current context this translates to distinguishability from other types of spin order, which is required for the separation of resulting NMR signals.

2.5.2 Isotropic filtration superoperator

Mathematically speaking, the problem of singlet filtering is to find a *projection superoperator*, which we call $\hat{P}(T_{00})$, that sieves all rank-0 operators from the density operator

$$\hat{P}(T_{00})T_{\Lambda M} \;=\; \begin{cases} T_{\Lambda M} & \text{for } \Lambda = 0 \\ 0 & \text{otherwise.} \end{cases} \tag{2.142}$$

By expressing $\overline{\rho}$ in the spherical tensor operator basis,

$$\overline{\rho}(t) = \sum_i \sum_{\Lambda,\, M} c^i_{\Lambda M}(t) T^i_{\Lambda M} \tag{2.143}$$

it is clear $\hat{P}(T_{00})$ acts to preserve isotropic tensors, and eliminate all the others:

$$\hat{P}(T_{00})\,\overline{\rho}(t) = \sum_i c^i_{00}(t) T^i_{00}. \tag{2.144}$$

The exact projection superoperator is unique, and is given by the isotropic projector of the SO(3) rotation group, which is the integral over all orientational space:

$$\hat{P}(T_{00}) \;\equiv\; \frac{1}{8\pi^2} \int_{\mathrm{SO(3)}} \hat{R}\, \mathrm{d}R. \tag{2.145}$$

Solutions in practice to attempt to approximate this integral by *quadrature*, the premise of approximation by a finite sum of rotations.

Rotation quadrature is the same approach used in coherence-pathway selection in NMR. Coherence pathways are the chronologies of coherence order in an NMR signal.[127] These pathways are discriminated in how spin operators with different coherence order (the quantum number M) rotate about the z quantisation axis at different rates. Filtration of T_{00} falls into a more general classification called Spherical Tensor Analysis (STA),[109, 128] where the chronologies of both Λ and M are selected. The specific situation of T_{00} is called isotropic filtration, as the goal is to select the rotation-invariant spin order.

Below is a description of isotropic filtration in practice. This leads to some new methods, which are demonstrated in the later sections.

2.5.3 Quadrature method for isotropic filtration

The 'traditional' approach to $\hat{P}(T_{00})$ is to select a finite set of rotations. This is called the *sampling set*, which is denoted by $\mathcal{S} = \{R_1^{\mathcal{S}}, R_2^{\mathcal{S}}, \ldots, R_{N_{\mathcal{S}}}^{\mathcal{S}}\}$. One of these rotations is inserted into the NMR pulse sequence at the point where isotropic selection is desired, and the signal acquired. The sequence is then repeated for the other rotations in turn, so there are $N_{\mathcal{S}}$ signals recorded in total. The rotations are chosen such that upon summing the NMR signals together the singlet-derived components add constructively, while the undesired components interfere destructively and cancel.[129]

As shown in fig. 2.32a, there are three main events in the pulse sequence as far as signal selection is concerned. These are (i) a common initial propagation from equilibrium spin order, which is denoted by the superoperator $\hat{U}_a$; (ii) a rotation of the spins, by one of the rotation elements $R_i^{\mathcal{S}} \in \mathcal{S}$; (iii) a common propagation until acquisition, under a superoperator denoted $\hat{U}_{\mathrm{b}}$.

A rotation $R_i^{\mathcal{S}}$ may be applied through a pair of strong 90° radiofrequency pulses with carefully chosen phases. To determine the phases one may use the fact that an arbitrary rotation, in the Euler zyz convention,

$$\hat{R}_i^{\mathcal{S}} = \hat{R}(\alpha_i^{\mathcal{S}}\beta_i^{\mathcal{S}}\gamma_i^{\mathcal{S}}) \equiv \hat{R}_z(\alpha_i^{\mathcal{S}})\hat{R}_y(\beta_i^{\mathcal{S}})\hat{R}_z(\gamma_i^{\mathcal{S}}), \tag{2.146}$$

may be effected through: (i) a 90° pulse with phase $(\alpha^{\mathcal{S}} + \beta^{\mathcal{S}})$, followed by (ii) a 90° pulse with phase $(\alpha^{\mathcal{S}} + 180°)$, then (iii) phase shifting all preceding elements of the pulse sequence by $(\alpha^{\mathcal{S}} + \beta^{\mathcal{S}} + \gamma^{\mathcal{S}})$.[109] This sequence is illustrated in fig. 2.32b, and verified

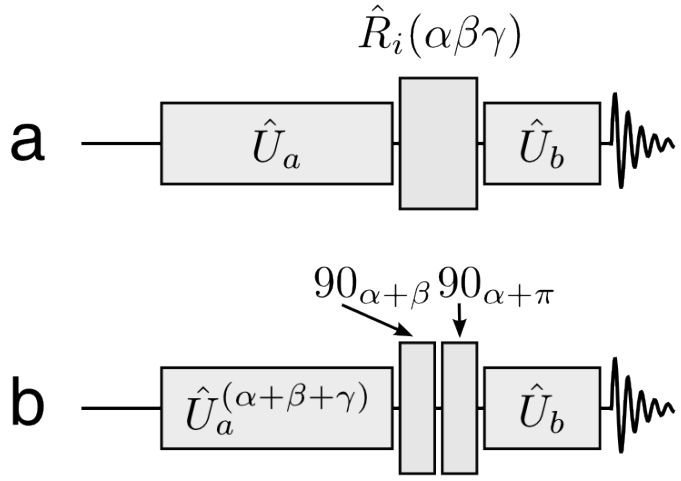

Figure 2.32: Implementation of a general Euler rotation on the spins using two 90° rf pulses.[109]

below using rotation identities about the Cartesian xyz axes:

$$\overbrace{\hat{R}_z(\alpha+\pi)\hat{R}_x(\pi/2)\hat{R}_z(-\alpha-\pi)}^{(\pi/2)_{\alpha+\pi}\text{ rf pulse}}\overbrace{\hat{R}_z(\alpha+\beta)\hat{R}_x(\pi/2)\hat{R}_z(-\alpha-\beta)}^{(\pi/2)_{\alpha+\beta}\text{ rf pulse}}\hat{U}_a^{(\alpha+\beta+\gamma)}\overline{\rho}_{\rm eq}$$

$$= \hat{R}_z(\alpha)\underbrace{\hat{R}_x(-\pi/2)\hat{R}_z(\beta)\hat{R}_x(\pi/2)}_{\text{rotation }\hat{R}_y(\beta)}\hat{R}_z(-\alpha-\beta)\hat{U}_a^{(\alpha+\beta+\gamma)}\overline{\rho}_{\rm eq} \tag{2.147}$$

$$= \Big[\hat{R}_z(\alpha)\hat{R}_y(\beta)\hat{R}_z(\gamma)\Big]\hat{U}_a\hat{R}_z(-\alpha-\beta-\gamma)\overline{\rho}_{\rm eq} \tag{2.148}$$

$$\equiv \Big[\hat{R}_z(\alpha)\hat{R}_y(\beta)\hat{R}_z(\gamma)\Big]\hat{U}_a\overline{\rho}_{\rm eq}. \tag{2.149}$$

To reach the penultimate line, one applies the fact $\overline{\rho}_{\rm eq}$ is invariant under with $\hat{R}_z$.

The NMR signals are summed together afterwards on a computer. To maintain generality, a weighted average is assumed, where each signal is multiplied by a weighting factor $w_i^{\mathcal{S}}$ before superposition. As the algebra of Liouville space is linear, the average NMR signal after superposition is equivalent to the signal after a single experiment using the weighted-average rotation superoperator:

$$\frac{1}{N_{\mathcal{S}}}\sum_{i=1}^{N_{\mathcal{S}}} w_i^{\mathcal{S}}\Big[\hat{U}_{\rm b}\hat{R}_i^{\mathcal{S}}\hat{U}_a\overline{\rho}_{\rm eq}\Big] \equiv \Big[\hat{U}_{\rm b}\Big(\frac{1}{N_{\mathcal{S}}}\sum_{i=1}^{N_{\mathcal{S}}} w_i^{\mathcal{S}}\hat{R}_i^{\mathcal{S}}\Big)\hat{U}_a\overline{\rho}_{\rm eq}\Big]. \tag{2.150}$$

The goal is to approximate the term in round brackets to $\hat{P}(T_{00})$.

Finite sampling constraint

Isotropic filtration requires $R_i^{\mathcal{S}}$ and $w_i^{\mathcal{S}}$ to satisfy

$$\Big(\frac{1}{N_{\mathcal{S}}}\sum_{i=1}^{N_{\mathcal{S}}} w_i^{\mathcal{S}}\hat{R}_i^{\mathcal{S}}\Big)T_{\Lambda M} \;=\; \frac{1}{N_{\mathcal{S}}}\sum_{i=1}^{N_{\mathcal{S}}} w_i^{\mathcal{S}} D^{\Lambda}_{M'M}(R_i^{\mathcal{S}}) \;=\; \begin{cases} 1 & \text{for } \Lambda = 0, \\ 0 & \text{for } 0 < \Lambda \leq \Lambda_{\max} \end{cases} \tag{2.151}$$

where $\Lambda_{\max}$ is the maximum rank of spin order of the spin system. The maximum rank equals the sum of $(2I{+}1)$ over all nuclei in the spin system. Spin order between two coupled spins-1/2, for instance, cannot exceed past rank two: $\Lambda_{\max} = [(2\frac{1}{2}+1)+(2\frac{1}{2}+1)] = 2$.

A preferred sampling scheme has one with minimal possible dimension while retaining the ability to average accessible ranks $0 < \Lambda \leq \Lambda_{\max}$, or at least ranks Λ that are likely to be excited.

2.5.4 Polyhedral sampling schemes

Pileio and Levitt have demonstrated that low ranks are suppressed by sampling the three poly-axial rotation subgroups of SO(3), $\mathcal{G} \in \mathrm{SO}(3)$. These are the groups of the regular polyhedra, [129]

- $\mathcal{T}$, the *tetrahedral* group, (12 rotation elements),
- $\mathcal{O}$, the *octahedral* group (24 rotation elements),
- $\mathcal{I}$, the *icosahedral* group, (60 rotation elements).

Low rank spin order has high orientational symmetry, so may be averaged successfully by relatively small sampling sets. The isotropic projector of these sub-groups maintains the same averaging properties as SO(3) for selected low spin ranks.

$$\frac{1}{|\mathcal{G}|}\sum_{R\in\mathcal{G}}\hat{R} \;\approx\; \frac{1}{8\pi^2}\int_{\mathrm{SO}(3)}\hat{R}\,\mathrm{d}R \;\equiv\; \hat{P}(T_{00}). \tag{2.152}$$

The above equation, amounts to eq. (2.151) with unit weights $w_i^{\mathcal{S}} = 1$.

Isotropic filtration under $\mathcal{T}$, $\mathcal{O}$ and $\mathcal{I}$ is determined by reducing the Wigner matrix blocks D^{Λ} in each subgroup. In any *group* of operations, in this case rotations, there is always *one* irreducible representation preserved by all operations *i.e.* is 'totally symmetric'. All other irreducible representations are anisotropic, and averaged by the subgroup $\mathcal{G}$.

Rank-Λ spin order is therefore successfully averaged if D^Λ does not reduce into the totally symmetric irreducible representation in the subgroup.

The multiplicity of the rank-zero tensor D^0 in each block D^Λ under the rotation subgroup is denoted $a_{0,\Lambda}$, and is given by the character of D^Λ averaged over all rotations in the group:

$$a_{0,\Lambda} = \frac{1}{|\mathcal{G}|} \sum_{R \in \mathcal{G}} \chi^\Lambda(R_\mathcal{G}). \tag{2.153}$$

The character under rotation, $\chi^\Lambda(R)$, equals the trace of D^Λ and is involved since tracing is independent of operator basis. The trace of the Wigner matrix evaluates as follows, where ζ is the angular displacement around the rotation axis of R: [89]

$$\chi^\Lambda(R) = \sum_{M=-\Lambda}^{\Lambda} D^\Lambda_{MM}(R) = \frac{\sin\left((2\Lambda+1)\zeta/2\right)}{\sin\left(\zeta/2\right)}, \tag{2.154}$$

The angle ζ relates to the Euler angles of $R = R(\alpha, \beta, \gamma)$ through

$$\cos(\zeta/2) \equiv \cos(\beta/2)\cos((\alpha+\gamma)/2). \tag{2.155}$$

Eq. (2.153) is briefly derived by considering irreducible representations of the subgroup, denoted $D^k_\mathcal{G}$, where k is an index, so that the reducible representation D^Λ is expressed by a sum

$$D^\Lambda(R_\mathcal{G}) \;\; = \;\; \sum_k D^k_\mathcal{G}(R_\mathcal{G}) a_{k,\Lambda}, \tag{2.156}$$

where coefficients $a_{k,\Lambda}$ are the multiplicities of $D^k_\mathcal{G}$ in D^Λ. Tracing both sides and then averaging over all rotations in $\mathcal{G}$ leads immediately to

$$\frac{1}{|\mathcal{G}|} \sum_\mathcal{G} \chi^\Lambda(R_\mathcal{G}) \;\; = \;\; \sum_k \Big[\frac{1}{|\mathcal{G}|} \sum_\mathcal{G} \chi^k_\mathcal{G}(R_\mathcal{G})\Big] a_{k,\Lambda} \;\; = \;\; a_{0,\Lambda}, \tag{2.157}$$

The second equality follows because $\sum_\mathcal{G} \chi^k_\mathcal{G}(R_\mathcal{G})$ is zero except for the totally symmetric representation ($k = 0$), where it is equal to the group order $|\mathcal{G}|$.

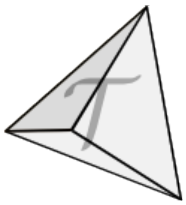

tetrahedral group

$\mathcal{T}$	E	$4C_3$	$4C_3^2$	$3C_2$	
	$\zeta = 0$	120°	240°	180°	
Λ					$a_{0,\Lambda}$
0	**1**	**1**	**1**	**1**	**1**
1	3	0	0	−1	0
2	5	−1	−1	1	0
3	**7**	**1**	**1**	**−1**	**1**
4	**9**	**0**	**0**	**1**	**1**
5	11	−1	−1	−1	0
6	**13**	**1**	**1**	**1**	**2**
⋮	⋮	⋮	⋮	⋮	⋮

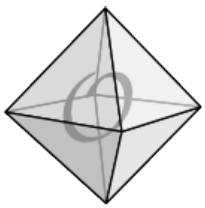

octahedral group

$\mathcal{O}$	E	$8C_3$	$3C_4^2$	$6C_4$	$6C_2$	
	$\zeta = 0$	120°	180°	90°	180°	
Λ						$a_{0,\Lambda}$
0	**1**	**1**	**1**	**1**	**1**	**1**
1	3	0	−1	1	−1	0
2	5	−1	1	−1	1	0
3	7	1	−1	−1	−1	0
4	**9**	**0**	**1**	**1**	**1**	**1**
5	11	−1	−1	1	−1	0
6	**13**	**1**	**1**	**−1**	**1**	**1**
⋮	⋮	⋮	⋮	⋮	⋮	⋮

icosahedral group

$\mathcal{I}$	E	$12C_5$	$12C_5^2$	$20C_3$	$15C_2$	
	$\zeta = 0$	72°	144°	120°	180°	
Λ						$a_{0,\Lambda}$
0	**1**	**1**	**1**	**1**	**1**	**1**
1	3	s	s’	0	−1	0
2	5	0	0	−1	1	0
3	7	−s	−s’	1	−1	0
4	9	−1	−1	0	1	0
5	11	1	1	−1	−1	0
6	**13**	**s**	**s’**	**1**	**1**	**1**
⋮	⋮	⋮	⋮	⋮	⋮	⋮

Figure 2.33: Character tables for the ‘polyhedron’ rotation groups. The rightmost column $a_{0,\Lambda}$ gives the isotropic projections (see text for detail). Representations D^Λ are averaged more effectively by the large, high symmetry rotation groups. Under the tetrahedral group, for instance, only ranks $\Lambda = 1$, 2 and 5 are averaged, while under the icosahedral group, out of the first 6 ranks, all but $\Lambda = 6$ are averaged.

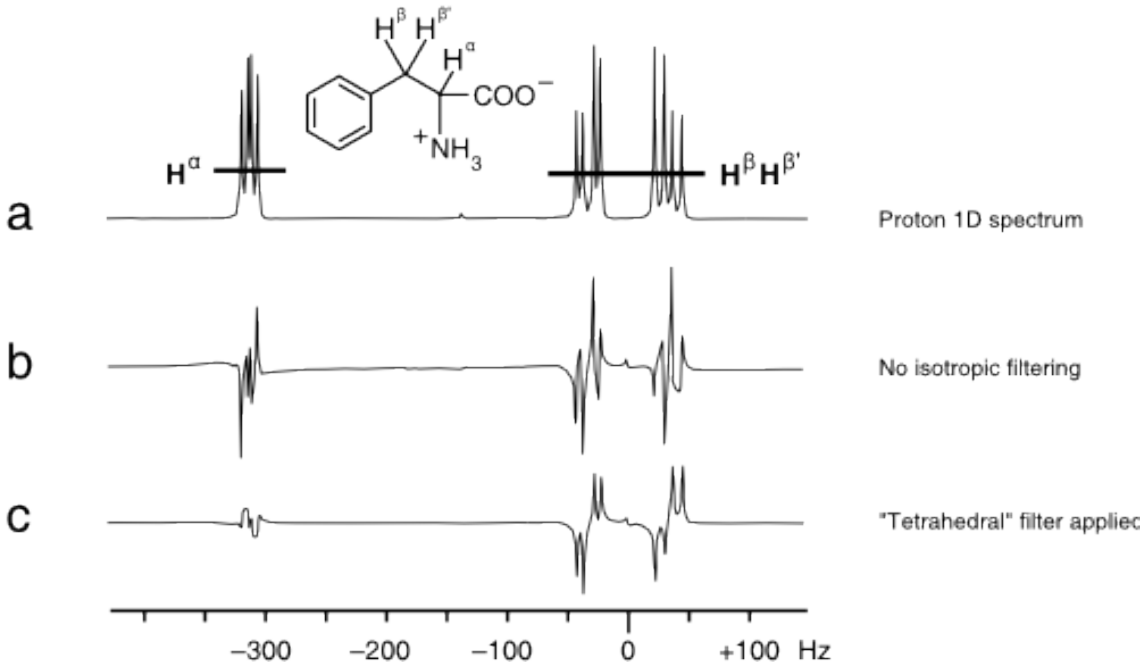

Figure 2.34: Isotropic filtration was performed on a sample containing 50 mM phenylalanine in D_2O at 9.4 T. The spectra show (a) proton 1D spectrum, single-scan; (b) proton singlet NMR spectrum, using Sarkar's sequence with delays $\tau_a = 17.1$ ms and $tau_b = 14.9$ ms, single scan; (c) as (b), but projecting out T_{00} by applying tetrahedral sampling (12 scans) at the end of the spin locking period.[129] The spectrum in (c) is scaled down by a factor of 12 to allow comparison of intensities with (a) and (b) spectra. The chemical shift at the spectrum centre is +3.60 ppm relative to tetramethylsilane.

Multiplicities $a_{0,\Lambda}$ between $\Lambda = 0$ and $\Lambda = 6$ and the characters for $\mathcal{T}$, $\mathcal{O}$ and $\mathcal{I}$ are tabulated in fig. 2.33. The multiplicities show the $\mathcal{T}$ subgroup averages spin ranks up to a maximum of $\Lambda_{\max} = 2$; the $\mathcal{O}$ subgroup averages ranks up to and including $\Lambda_{\max} = 3$ and the $\mathcal{I}$ subgroup averages up to and including $\Lambda_{\max} = 5$.

For most high-field applications of singlet NMR, tetrahedral sampling tends to be sufficient. Spin order with rank $\Lambda > 2$ is usually not strongly excited during magnetisation-to-singlet pulse sequences, plus higher ranks are in general much faster relaxing and may itself decay to zero long before acquisition.

As an experimental example, fig. 2.34 shows the aliphatic region of ^{1}H-NMR spectra recorded at 9.4 T for a solution of 50 mM L-phenylalanine dissolved in D_2O. Fig. 2.34(a) is the 90°-acquire spectrum, showing an ABX peak pattern corresponding to the α- and two β-proton resonances. The two β-protons are a target for singlet NMR because they are diastereotopic, due to the adjacent chiral centre, and because their intra-pair J coupling exceeds the difference in J couplings to the α-proton.[77] Fig. 2.34(b) is the single-scan

spectrum recorded after using Sarkar's basic sequence to prepare, store and retrieve singlet order (see fig. 2.7). Delays $\tau_a = 17.1$ ms and $tau_b = 14.9$ ms were determined to generate maximum singlet order on the β-protons. The singlet order was locked for 0.5 seconds under a 3 kHz WALTZ-16 modulated rf field applied at the average chemical shift frequency of the β-protons, before reconversion to antiphase coherences, and acquisition. Due to the short spin locking time, which is about half the T_1 lifetime of the β-protons, the peaks are contaminated with a large contamination of unwanted terms, which obscure the expected antiphase pattern.

The spectrum in fig. 2.34(c) is the result after the same experiment in fig. 2.34(b), but applying the tetrahedral quadrature (12 scans) at the end of the decoupling period. The sum spectrum is normalised to the amplitude of the single scan in fig. 2.34(a). The antiphase spectrum is much clearer and easier to integrate than that in fig. 2.34(b) due to the removal of spin ranks 1 and 2. There is no evidence of third-rank spin order potentially carried through by $\mathcal{T}$.

2.5.5 'Targeted' sampling sets

A problem with using the polyhedral groups is their great time-expense, because the angle sets are very large. In this section a different approach is considered: freedom to choose both orientations and weights in a sampling set suggests a *minimal* set is available whose number of angles equals the number of constraints imposed by eq. (2.151). This idea is attractive when a small subset of spin ranks must be averaged, to which the polyhedral sampling sets may be overkill. Polyhedral orientation sets, as well as other rotation group angle sets, have a capacity to project out *all* irreducible components $T_{\Lambda M}$ for which the quadrature is exact.[109] This indicates a large redundancy present if one simply wants suppression of ranks $\Lambda \neq 0$.

Below I consider some approaches that target the quadrature constraint directly and use the smallest-possible number of angles.

Pulse field gradients

Most modern NMR spectrometers are capable of producing *field-gradient pulses* (PFGs) – pulses of a purposely inhomogeneous magnetic field parallel to the direction of the static

B^0 field. PFGs induce a z-axis rotation on the spins through an angle that depends on molecular position in the sample.[4]

Using gradients it is possible to sample rotations

$$\hat{R}_{zyz}(\alpha\beta\gamma) \equiv \hat{R}_z(\alpha)\hat{R}_y(\beta)\hat{R}_z(\gamma) \tag{2.158}$$

in parallel using the sequence (PFG1)-(β_{90°)-(PFG2), (see fig. 2.35(a)), which comprises two pulsed gradients and an rf y-pulse. The gradients induce the Euler angles α and γ (not to be confused with the gyromagnetic ratio) that are functions of spatial displacement $\boldsymbol{r} = (x, y, z)$ from the gradient origin. The rotation angles are determined by $\alpha(r) = (\int_0^\tau \mathrm{d}t' \, \boldsymbol{G}^{(\mathrm{PFG2})}(t') \cdot \boldsymbol{r})$ and $\gamma(r) = (\int_0^\tau \mathrm{d}t' \, \boldsymbol{G}^{(\mathrm{PFG1})}(t') \cdot \boldsymbol{r})$ where the gradients varies along the axis $\boldsymbol{G}^{(\mathrm{PFG1})} = (G_x^{(\mathrm{PFG1})}, G_y^{(\mathrm{PFG1})}, G_z^{(\mathrm{PFG1})})$, the PFG durations are τ_{PFG1} and τ_{PFG2} and where t' is the local time variable of each pulse. From the theory of composite rotations,[109] the central (β_{90°) rotation may in practice be replaced by a pair of 90° pulses (90°_β)-$(90^\circ_{180^\circ})$, for greater accuracy in the β angle (fig. 2.35(b)).

Strong gradients produce an uniformly distributed set of rotations over the α and γ orientational space via the relation

$$\frac{1}{V}\int_V \hat{R}(\boldsymbol{r})\,\mathrm{d}r \;\approx\; \frac{1}{4\pi^2}\int_{\alpha\gamma} \hat{R}_{zyz}(\alpha\beta\gamma)\mathrm{d}\alpha\mathrm{d}\gamma, \tag{2.159}$$

which holds provided the gradients vary linearly along orthogonal spatial axes and the density of excited spins is uniform across the sample volume. Modern NMR and MRI hardware can produce linearly varying z gradients independently along each of the x, y and z axes ('triple gradients'). A single z-gradient G_z is more common on older hardware in which case the integrals over α and γ are coupled, though with suitable choice of the gradient strengths $G_z^{(1)}$ and $G_z^{(2)}$, such that $M'\alpha =\neq M\gamma$, improper averaging may be avoided. Depending on the gradient strengths, *i.e.* the spatial resolution of the gradients, (ii) may preclude in-vivo spectroscopy.

If the gradients satisfy eq. (2.159), the sampling constraint reduces to

$$\frac{1}{N_{\mathcal{S}}}\sum_{i=1}^{N_{\mathcal{S}}} w_i^{\mathcal{S}} d_{00}^{\Lambda}(R_y(\beta_i^{\mathcal{S}})) = \begin{cases} 1 & \text{for } \Lambda = 0 \\ 0 & \text{for } 0 < \Lambda \leq \Lambda_{\max} \end{cases}. \tag{2.160}$$

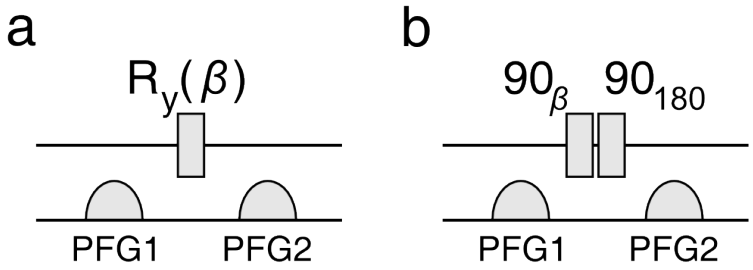

Figure 2.35: Schematic pulse sequence for uniform sampling over α and γ Euler angles.

This shows a rather striking decrease from $(2\Lambda+1)^2$ constraints per rank to one per rank.

Gauss-Legendre quadrature

There are several ways to proceed from the above. For a maximum rank $\Lambda_{\max}$ there are $((\sum_{\Lambda=1}^{\Lambda_{\max}}) - 1)$ equations to satisfy:

$$\begin{pmatrix} d^1_{00}(R_y(\beta_1)) & \dots & d^1_{00}(R_y(\beta_N)) \\ d^2_{00}(R_y(\beta_1)) & \dots & d^2_{00}(R_y(\beta_N)) \\ \vdots & & \vdots \\ d^{\Lambda_{\max}}_{00}(R_y(\beta_1)) & \dots & d^{\Lambda_{\max}}_{00}(R_y(\beta_N)) \end{pmatrix} \begin{pmatrix} w_1 \\ w_2 \\ \vdots \\ w_N \end{pmatrix} = \begin{pmatrix} 1 \\ 0 \\ \vdots \\ 0 \end{pmatrix} \tag{2.161}$$

and therefore at most $(\Lambda_{\max}-1)$ orientations are needed for quadrature (the first equation always holds, provided $\sum_i w_i = 1$). By comparison, the eq. (2.151) requires at least $\sum_{\Lambda=1}^{\Lambda_{\max}} (2\Lambda+1)^2 \approx O(\Lambda^3_{\max})$ orientations.

One may solve eq. (2.161) numerically for a predefined set of angles or weights. More expediently, one may recognise these matrix equations as the Gauss-Legendre quadrature.[130, 131] By recognising equality of the Wigner matrix elements d^Λ_{00} with Legendre polynomials, $P_\Lambda(\cos(\beta^{\mathcal{S}}_i)) = d^\Lambda_{00}(R_y(\beta^{\mathcal{S}}_i))$, eq. (2.161) reads

$$\text{eq. (2.160)} \quad \rightarrow \quad \frac{1}{N_{\mathcal{S}}} \sum_{i=1}^{N_{\mathcal{S}}} w^{\mathcal{S}}_i P_\Lambda(\cos(\beta^{\mathcal{S}}_i)). \tag{2.162}$$

Hence the solution of

$$\begin{pmatrix} P_0(\cos(\beta_1)) & \dots & P_0(\cos(\beta_N)) \\ P_1(\cos(\beta_1)) & \dots & P_1(\cos(\beta_N)) \\ \vdots & & \vdots \\ P_{\Lambda_{\max}}(\cos(\beta_1)) & \dots & P_{\Lambda_{\max}}(\cos(\beta_N)) \end{pmatrix} \begin{pmatrix} w_1 \\ w_2 \\ \vdots \\ w_N \end{pmatrix} = \begin{pmatrix} 1 \\ 0 \\ \vdots \\ 0 \end{pmatrix}. \tag{2.163}$$

An analytical solution of this equation is known. The derivation is beyond the scope of this work, but involves using the recurrence relations between $P_n(\cos(\beta))$ and $P_{n\pm2}(\cos(\beta))$. Abscissas β_i are given by the zeroes of $P_N(\cos(\beta))$, [131]

$$P_N(\cos(\beta_i)) \quad = \quad 0, \tag{2.164}$$

and the corresponding weights by the formula

$$w_i^N \quad = \quad \frac{\sin\beta_i}{\sum_j \sin(\beta_j)}. \tag{2.165}$$

The value $\Lambda_{\max}$ up to which the zeroes of N average is not $(N-1)$ in this case, but in fact $(2N-1)$. The Legendre zeroes come in pairs β and $(180^\circ - \beta)$, or singly at $\cos(\beta_i) = 0$. Due to the symmetry $P_\Lambda(\cos(\beta_i)) = (-)^\Lambda P_\Lambda(\cos(180^\circ - \beta_i))$ this means all odd ranks vanish automatically. This leaves only half the number of original constraints – namely those left on the even ranks – to satisfy by the absolute angles and weights.

Angles β_i and weights w_i are given in fig. 2.36 for sets $N = 1$ to $N = 5$. These achieve isotropic selection up to maximum ranks $\Lambda_{\max} = 1$ to $\Lambda_{\max} = 9$. As an example of the gains achievable, spin order up to and including rank $\Lambda_{\max} = 3$ can be eliminated by averaging just two equal-weighted scans ($N = 2$). This sampling scheme is 24 times smaller than the octahedral set, which requires 48 scans to average third-rank spin order.

2.5.6 Single-shot filtration

The sequences shown in fig. 2.35(a) and (b) eliminate rank-Λ spin order in entirety if the angle β is a zero of d_{00}^Λ. Furthermore, note that if the angle β is 90°, spin order of *all* odd ranks is eliminated.

The latter case is the well-known Only Parahydrogen SpectroscopY (OPSY) method,

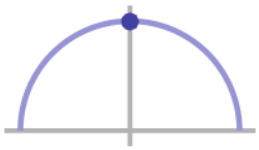

$\Lambda_{max}= 1$

i	$\beta_i/^\circ$	w_i
1	90.00	1.000

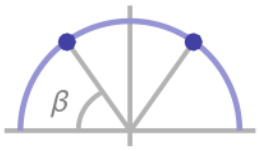

$\Lambda_{max}= 3$

i	$\beta_i/^\circ$	w_i
1	54.74	0.500
2	125.26	0.500

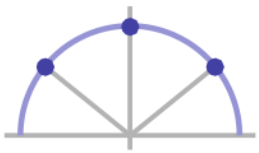

$\Lambda_{max}= 5$

i	$\beta_i/^\circ$	w_i
1	39.23	$0.27\dot{7}$
2	90.00	$0.44\dot{4}$
3	140.77	$0.27\dot{7}$

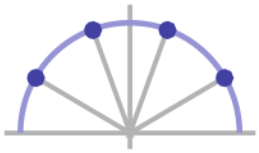

$\Lambda_{max}= 7$

i	$\beta_i/^\circ$	w_i
1	30.56	0.174
2	70.12	0.326
3	109.88	0.326
4	149.44	0.174

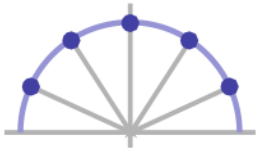

$\Lambda_{max}= 9$

i	$\beta_i/^\circ$	w_i
1	25.02	0.118
2	57.42	0.239
3	90.00	0.284
4	122.58	0.239
5	154.98	0.118

Figure 2.36: Orientational sampling sets for the Gauss-Legendre quadrature.[131] (Left), graphical representation of the angle sets on a polar plot. The polar angle of each 'node' is equal to β_i and the corresponding ordinate is proportional to the w_i; (Right), tabular representation of the sampling schemes.

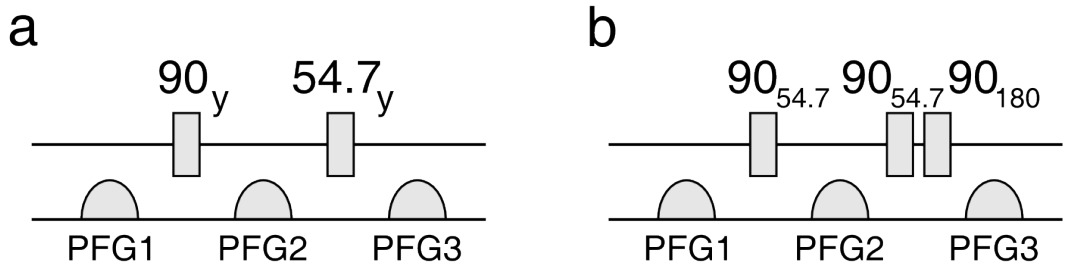

Figure 2.37: Schematic pulse sequence for suppression of non-isotropic spin order up to and including rank 3 ($\Lambda_{\max} = 3$).

used for signal filtering in parahydrogen-enhanced NMR.[110, 59] The purpose of OPSY is to remove rank-1 components of the density operator, which includes the strong magnetisation of the solvent and the magnetisation of orthohydrogen, so that only the parahydrogen addition products are observed in the NMR spectrum.

One may generalise OPSY by chaining several filters together. The sequence shown in fig. 2.37(a) and (b) consists of an odd-rank filter followed by a rank-2 filter. This achieves suppression of spin order up to and including rank-3, providing there is no mixing between ranks between the filters, *i.e.* during the PFG2 gradient pulse duration. In practice, this limits application to strongly coupled spin pairs, though the suppression of rank-interconversion is not ruled out by other means, for example by refocusing.

Single-shot filtration may be useful in hyperpolarised NMR, where initial polarisation levels cannot be guaranteed the same (at odds with quadrature that rely on averaging several scans) and other single-scan NMR experiments, such as reaction monitoring, where signal averaging is not feasible.

Experimental demonstration of single-shot selection

The single-shot filter in fig. 2.37(b) was tested upon the singlet NMR of perdeuterated [1,2-$^{13}C_2$]-isopropyl-cyclohexyl oxalate diester, whose molecular structure is shown in fig. 2.38(a). This molecule was synthesised by Lynda Brown (Southampton University) and investigated in collaboration with Chris Laustsen (Aarhus University, Denmark) and Jan-Henrik Ardenkjær Larsen as an early candidate for long-lived hyperpolarised singlet order in a nearly equivalent spin pair.[132] Dissolved in d_4-methanol at room temperature the two ^{13}C nuclei in the molecule have close chemical shifts in the region of 158.6 ppm, where the chemical shift difference is a small 0.13 ppm due to the weak four-bond asymmetric

induction by the ester groups. The chemical shift difference translates at the 5 T of a small-animal MRI magnet to a frequency of 6.6 Hz, which is much less than the and one-bond coupling $^1J_{\mathrm{CC}}$ measured as 100.1 Hz. Singlet order survives in high magnetic field without resort to spin locking interventions.[132]

The filter in fig. 2.38(b) was applied to the singlet NMR of a methanol-d_4 solution of the oxalate diester on a 9.4 T NMR spectrometer (100 MHz ^{13}C Larmor frequency) in Southampton. To determine the parameters required to suppress non-singlet order, the isotropic filter was applied to the sample at thermal equilibrium polarisation, followed immediately by a 90° rf pulse and spectrum acquisition. Sine-bell shaped pulsed-field z-gradients (PFG1), (PFG2), (PFG3) were applied with respective durations 4.4 ms, 2.4 ms and 2.0 ms and relative strengths $+g$, $-g$ and $-g$. The area under these gradients sums to zero to avoid eddy currents that may otherwise disturb the spectrum acquisition. The gradient strength g was incremented until the 90°-acquire spectrum showed negligible signal, at which point that the filter successfully suppresses rank-1 spin order. Fig. 2.38(c) shows the ^{13}C NMR spectrum (left) in the absence of the filter and (right) using the filter with z-gradient amplitude $g = 0.8$ G cm^{-1}, which is approximately 8% of the maximum available on the hardware.

Having calibrated the filtering element, measurements of the singlet decay constant T_S were performed using the J-synchronised echo pulse sequence displayed in fig. 2.38(d). The optimum parameters for the oxalate ester were $N_{180} = 12$ and $N_{90} = 6$ spin echoes and spin echo delay $\tau = 2.48$ ms for nominal 180° and 90° x-rotations in $m = 0$ subspace of the carbon pair. The singlet order was left undisturbed in high field for a time T_{HF}, then the filter applied, and finally singlet order was reconverted to in-phase transverse magnetisation for detection, by performing the J-synchronised echo sequence in reverse.

The experiment was repeated for several different values of the initial pulse flip angle $\xi = 90°$, 45° and 30° to mimic a varying degree of inefficiency in exciting the singlet order. The longitudinal order remaining after the first pulse is proportional to $p\cos(\xi)$ while the singlet order is proportional to $p\sin(\xi)$. In the absence of the filter, the longitudinal component carries through until the final signal. As shown in fig. 2.38(d), in the presence of the filter the spectrum integral against the high-field waiting time T_{HF} were fitted to monoexponential decay curves $\exp(-T_{\mathrm{HF}}/T_S)$. Singlet decay constants T_S for all three initial flip angles $\xi = 90°$, 45° and 30° were fit to the same value of $T_S = (55 \pm 5)$ seconds.

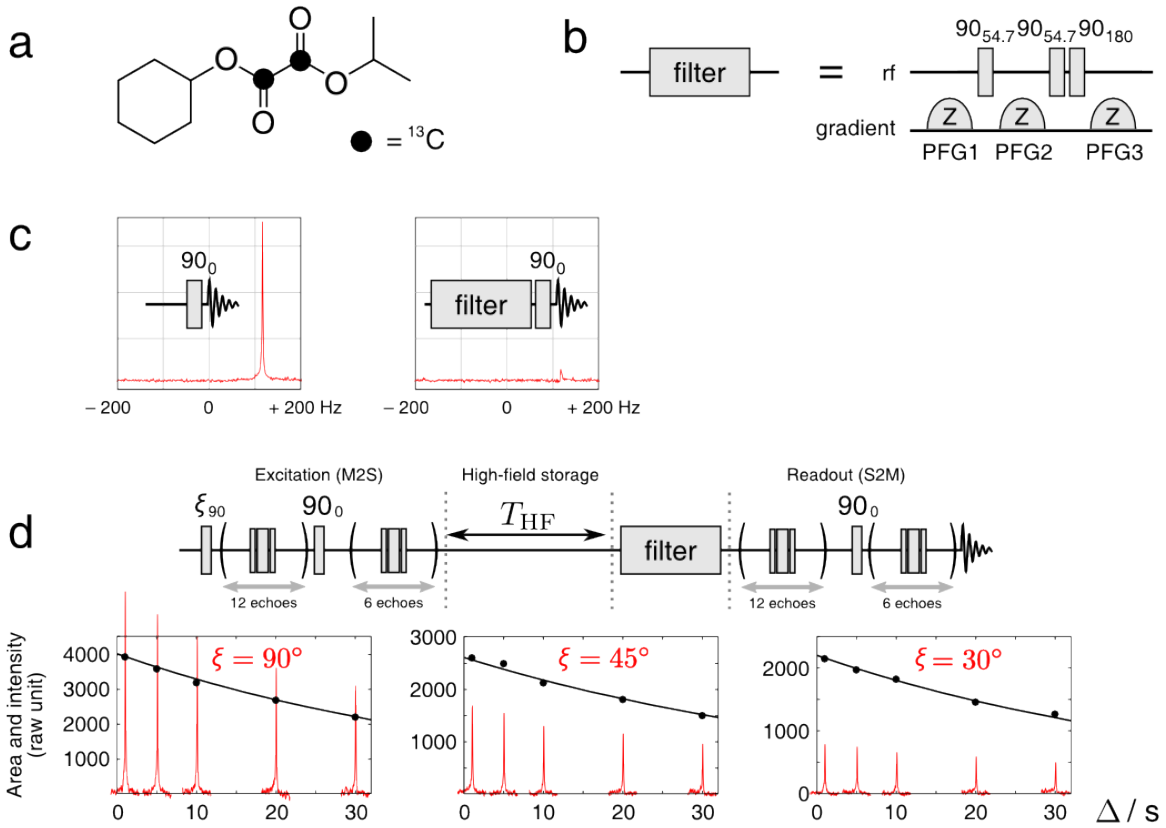

Figure 2.38: Single-shot isotropic filter optimisation and application for d_{18}-[1,2-$^{13}C_2$]-isopropyl-cyclohexyl oxalate diester: (a) molecular structure of the doubly ^{13}C-labelled oxalate diester; (b) pulse sequence for isotropic filtration up to and including maximum spin rank $\Lambda_{\max} = 3$; (c, left) single-scan 90°-acquire ^{13}C spectrum at 9.4 T of the region around 158 ppm, showing the singly resolved peak of the strongly coupled carboxyl resonances; (c, right) 90°-acquire ^{13}C spectrum recorded immediately after applying the isotropic filter, with gradient durations and strengths as described in the main text, indicating suppression of rank-1 spin order by the filter; (d) singlet relaxation profiles recorded at 9.4 T for initial pulse flip angles ξ. All three decays are fit to the monoexponential function $\propto \exp(-T_{\mathrm{HF}}/T_S)$ with the same time constant $T_S = (55 \pm 5)$ seconds, indicating that due to the isotropic filter, all spectra are contaminant-free.

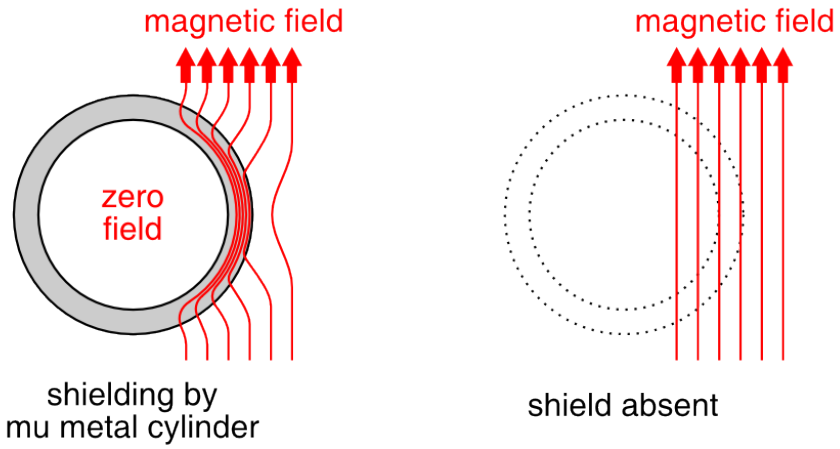

Figure 2.39: External magnetic field distortion by a mu-metal cylinder.

This proves reliable elimination of signals from non-singlet spin order contaminants.

2.5.7 Filtration in low magnetic field

The above methods all involve rotations induced by applying radio-frequency pulses while the sample sits in the spectrometer magnetic field. In principle, similar manipulations are possible outside the magnet, for example by applying audio-frequency pulses in earth's field.

A more crude, yet equally effective means of isotropic filtration at low field is simply to place the sample in a very inhomogeneous, rapidly fluctuating magnetic field. Field fluctuations occurring near the Larmor frequency appear as randomly sampled rotations, when seen from the rotating frame, thereby realising a good approximation to eq. (2.145).

In ref. [32] we used a mu-metal cylinder to filter hyperpolarised singlet order after dissolution DNP of sodium pyruvate (§2.2.1). Mu-metal is a material with extremely high magnetic permeability, typically $\mu/\mu_0 = 10^5$ (in comparison, μ/μ_0 for steel is less than 10^3). It is primarily used for shielding objects from a background magnetic field by distorting flux into the surface of the metal, leaving a near-zero magnetic field in enclosed regions (see fig. 2.39). At the edges of the mu-metal, however, the background field is distorted very sharply. Shaking the sample in this inhomogeneous magnetic field rapidly equilibrates the nuclear triplet populations while leaving the rotation-invariant singlet order intact.[32]

2.5.8 Filtration by spin decoupling in high field

Random rotations may be induced with the sample residing at high field due to inhomogeneity in applied rf fields. This may be useful in filtering the singlet order of weakly coupled spin pairs under spin locking, where singlet-triplet transitions must forcibly be suppressed by resonant rf irradiation.[65]

Singha Roy and Mahesh have identified that WALTZ-16 and similar phase-modulated irradiation schemes that sustain nuclear singlet order in high field, while simultaneously ensuring the rapidly destruction of other spin order by rf inhomogeneity.[133, 134] They have used the resulting long-lived, high-fidelity entangled state of the filtered singlet order for NMR quantum computation.

2.5.9 Summary of signal filtration methods

Isotropic filtration relies on ability to apply a uniform sampling the rotation group onto the nuclear spin ensemble, under which non-singlet spin order averages to zero. A summary of the techniques reviewed in the section is displayed graphically in fig. 2.40. The chart shows which methods are appropriate to high and low instances of singlet NMR where one may wish to filter singlet order. In all of these instances, there is a method to achieve selection in a single scan.

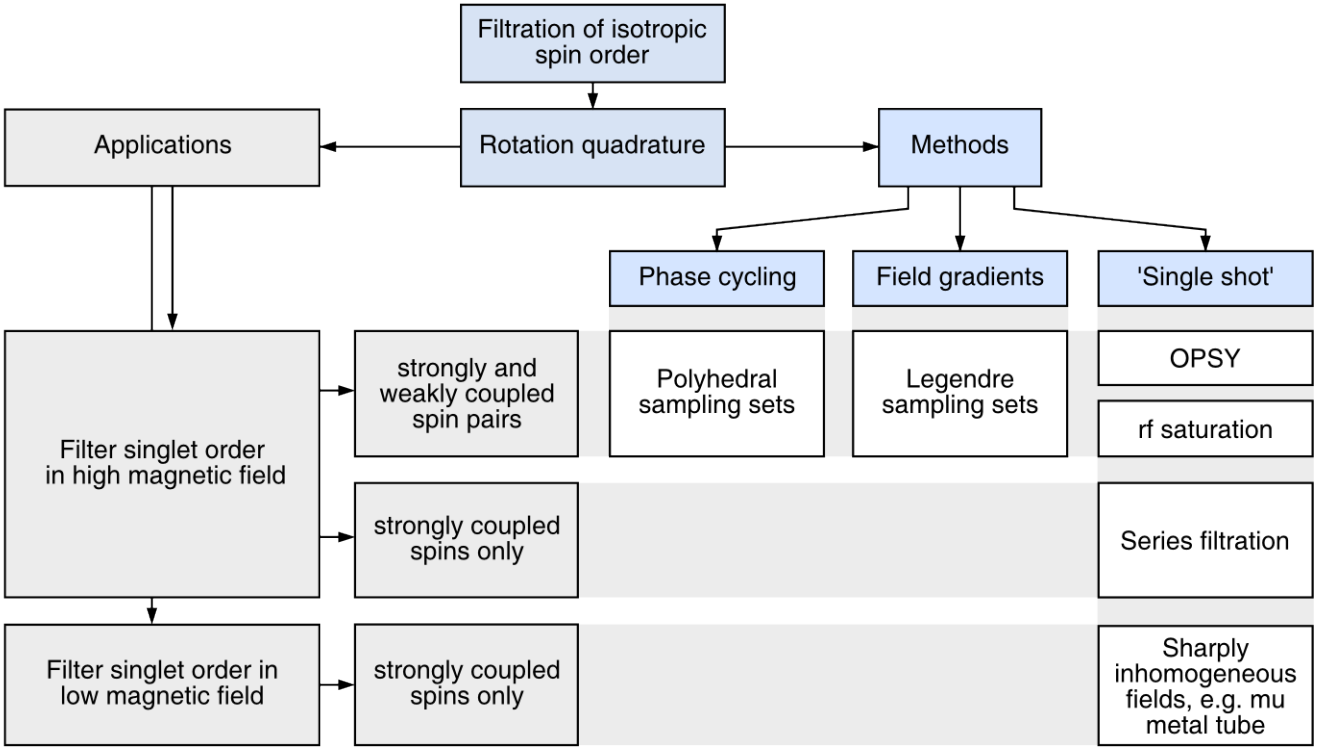

Figure 2.40: Isotropic filtration applied in singlet NMR, a summary.

3 Nuclear singlet relaxation

Whereas the previous chapter has dealt with coherent evolution between singlet and triplet states, the following chapter concerns incoherent evolution phenomena, or relaxation.

First in this chapter I overview the Liouvillian formalism for relaxation, the foundation of which is the very successful theory derived by Wangsness, Bloch, and Redfield, abbreviated 'WBR' theory, or sometimes referred as just 'Redfield' relaxation theory. The WBR theory approaches relaxation through second-order time-dependent perturbation theory of the density operator.

Spherical tensors operators are the natural language of relaxation in solution NMR due to rotational modulation of the intramolecular Hamiltonian by random molecular tumbling. This leads to pointing out several useful concepts for singlet relaxation analysis. If molecular rotation is much faster than the Larmor frequency, the relaxation of nuclear spin states is invariant to their orientation with respect to the $\boldsymbol{B^0}$ magnetic field. In this case relaxation superoperator behaves as a scalar, where it is shown that there can be no relaxation between spin order of different rank. This allows simple, well justified analytical formulae to be derived for singlet relaxation rates.

Several experimental studies are then reported. These are focused towards the goal of 'relaxometry', which is to obtaining information on the singlet relaxation mechanisms by analysing experimental relaxation rates. Examples covered include both homonuclear and heteronuclear intramolecular dipole-dipole relaxation and the influence of dissolved paramagnetic species.

3.1 Tools for singlet relaxation analysis

3.1.1 Introduction to WBR theory

WBR theory considers the relaxation phenomenon for an ensemble of the spin system of interest diluted within a classical 'lattice' surrounding, the latter being of no particular interest in general. Spin decoherence is treated by dividing the Hamiltonian H for each ensemble member into two parts, an uniform, coherent part, $H_0 \equiv \overline{H}$, responsible for bulk evolution, plus a stochastic counter-part $H_1 = (\overline{H} - H_0)$ that fluctuates through time due to interactions with the lattice. Intermolecular interactions are usually ignored at a basic level, due to their often short-range, random nature and the relatively dilute concentration of spins within the bulk.

In this microscopic view the Liouvillian equation of motion for pure states reads

$$\frac{\mathrm{d}}{\mathrm{d}t}\rho(t) \quad = \quad -\mathrm{i}\hat{H}_0(t)\rho(t) - \mathrm{i}\hat{H}_1(t)\rho(t) \tag{3.1}$$

where the hat, ('$\hat{}$'), in this case denotes commutation superoperator.[37] This equation is to be solved in the interaction representation of the static magnetic field (Larmor representation, denoted by 'tilde') *i.e.* as

$$\frac{\mathrm{d}}{\mathrm{d}t}\tilde{\rho}(t) \quad = \quad -\mathrm{i}\hat{\tilde{H}}_0(t)\tilde{\rho}(t) - \mathrm{i}\hat{\tilde{H}}_1(t)\tilde{\rho}(t) \tag{3.2}$$

where $\tilde{H}(t) = \exp(-\mathrm{i}\int_0^t \omega^0 I_z \mathrm{d}t')H(0)\exp(+\mathrm{i}\int_0^t \omega^0 I_z \mathrm{d}t') \equiv \hat{R}_z(\omega^0 t)H(0)$. Integration of eq. (3.2) from a starting time point t_0, up to a future time t gives

$$\rho(t) = \rho(t_0) - \mathrm{i}\int_{t_0}^{t} \mathrm{d}t'\, \hat{H}(t')\rho(t'). \tag{3.3}$$

Recursive substitution to second-order in the Dyson series in H leads to

$$\tilde{\rho}(t) = \tilde{\rho}(0) - \mathrm{i}\int_{t_0}^{t} \mathrm{d}t'\, \hat{\tilde{H}}(t')\tilde{\rho}(t_0) - \int_{t_0}^{t} \mathrm{d}t' \int_{t_0}^{t'} \mathrm{d}t''\, \hat{\tilde{H}}(t')\hat{\tilde{H}}(t'')\rho(t'') + \ldots \tag{3.4}$$

where it is acceptable to truncate the iteration after only the second term. The interaction frame transformation justifies truncation as it ensures successive iterative terms rapidly diminish in size.

Following the integral truncation the view reverts immediately to a time-derivative formulation. One may differentiate with respect to t using the well-known formula

$$\frac{\mathrm{d}}{\mathrm{d}t}\Big[\int_{a(t)}^{b(t)} \mathrm{d}t'\, f[t,\, t']\Big] = f[t,\, b(t)] - f[t,\, a(t)] + \int_{a(t)}^{b(t)} \mathrm{d}t'\, \frac{\mathrm{d}}{\mathrm{d}t} f[t,\, t'] \tag{3.5}$$

where $a(t)$, $b(t)$ and $f(t)$ denote explicit functions of time. The equation of motion after the differentiation is

$$\text{eq. (3.4)} \;\Rightarrow\; \frac{\mathrm{d}}{\mathrm{d}t}\rho(t) \;=\; -\mathrm{i}\hat{H}(t)\rho(t) - \int_{t_0}^{t} \mathrm{d}t''\, \hat{H}(t)\hat{H}(t'')\rho(t''). \tag{3.6}$$

In the next step the density operators $\rho(t'')$ and $\rho(t_0)$ are replaced by $\rho(t)$ under assumption that the perturbations in ρ are weak compared to the Larmor frequency and smoothly fluctuating across the interval t_0 to t. Finally, an ensemble average is taken to reach

$$\frac{\mathrm{d}}{\mathrm{d}t}\overline{\rho}(t) \;=\; -\mathrm{i}\hat{\bar{H}}_0(t)\overline{\rho}(t) - \overline{\int_{t_0}^{t} \mathrm{d}t''\, \hat{\bar{H}}_1(t)\hat{\bar{H}}_1(t'')\overline{\rho}(t)}, \tag{3.7}$$

where independent averaging is allowed between uncorrelated quantities H_1 and $\rho(t)$. From this form one may identify the commutation superoperators of the right-hand side as the pure coherent Liouvillian evolution superoperator that contains only coherent terms H_0

$$\hat{L}_0(t) \;=\; -\mathrm{i}\hat{\bar{H}}_0(t), \tag{3.8}$$

and the relaxation superoperator, which contains only H_1:

$$\hat{\Gamma}(t) \;=\; -\overline{\int_{t_0}^{t} \mathrm{d}t''\, \hat{\bar{H}}_1(t)\hat{\bar{H}}_1(t'')}. \tag{3.9}$$

Last steps in WBR theory modify the integral to a form that is more ready for computation. One assumes the anisotropic Hamiltonian H_1 is Markovian, meaning it averages to zero over long periods of time. This justifies extending the upper time limit to infinity in the future: $(t - t'') \to \infty$. Doing this, and changing the integration variable to $\tau = (t' - t)$,

the relaxation superoperator is transformed into the form

$$\hat{\Gamma}(t) \;=\; -\overline{\int_{-\infty}^{0} \mathrm{d}\tau\, \hat{\tilde{H}}_1(t+\tau)\hat{\tilde{H}}_1(t)}. \tag{3.10}$$

3.1.2 Spherical tensor formalism

Incoherent Hamiltonian

The explicit calculation of relaxation superoperators requires a knowledge of (i) the relaxation causing interactions in H_1 and (ii) the nature of the spin-lattice interaction (relative time-dependence in eq. (3.10)). For solution NMR the model adopted is to assume the field fluctuations are due to molecular rotations, and that the incoherent spin interactions comprise those which are anisotropic with respect to molecular orientation. It is convenient to formulate $\hat{\Gamma}$ by expanding H_1 in a set of rotational symmetry-adapted basis functions. H_1 is generally expressible as products between (i) time-dependent spherical tensor functions in orientational space, here denoted A^p_{lm}, and (ii) spherical tensor spin operators, T^p_{lm}, where labels p indicate the identity of the specific relaxation mechanism. These functions are defined through

$$\hat{\mathcal{R}}(\Omega)A^p_{lm} \;=\; A^p_{lm'}D^l_{m'm}(\Omega) \tag{3.11}$$

$$\hat{R}(\Omega)T^p_{lm} \;=\; T^p_{lm'}D^l_{m'm}(\Omega), \tag{3.12}$$

wher $\mathcal{R}$ and R are used here to denote space and spin rotations, respectively. The Hamiltonian is expressible as a scalar product between A and T as follows:

$$H^L_1(t) \;=\; \sum_p [H^p_1]^L(t); \tag{3.13}$$

$$[H^p_1]^L(t) \;=\; \sum_l \sum_{m=-l}^{l} (-)^m [A^p_{lm}]^L(t)[T^p_{l-m}]^L, \tag{3.14}$$

which conforms to invariance upon simultaneous spin-space rotations:

$$\hat{\mathcal{R}}(\Omega)\hat{R}(\Omega)[H^p_1]^L(t) \;=\; [H^p_1]^L(t). \tag{3.15}$$

The superscript 'L' in this equation denotes that the Hamiltonian is written in the laboratory frame, which is the reference frame in which we observers reside.

The laboratory-frame spatial components $[A^p_{lm}]^L$ are determined by rotating the principal axis components $[A^p_{lm}]^P$ of each spin interaction into the L frame. This is done in two stages. The axes systems of each interaction tensors within each molecule is synchronised to a molecule-fixed frame, M,

$$[A^p_{lm}]^M(t) = \hat{\mathcal{R}}(\Omega^{(P\to M)}(t))[A^p_{lm}]^P = \sum_{m'=-l}^{l} [A^p_{lm'}]^P D^l_{m'm}(\Omega^{(P\to M)}(t)), \tag{3.16}$$

where $(P \to M)$ indicates the direction of the frame transformation and $\Omega^{(P\to M)}$ the relevant Euler angle. The molecular frame is then rotated into the laboratory frame:

$$[A^p_{lm}]^L(t) = \hat{\mathcal{R}}(\Omega^{(M\to L)}(t))[A^p_{lm}]^M = \sum_{m'=-l}^{l} [A^p_{lm'}]^M D^l_{m'm}(\Omega^{(M\to L)}(t)). \tag{3.17}$$

This form is very convenient since it separates intramolecular motion from overall molecular rotation, which will be discussed shortly. Together with the transformation of the spin tensors into the Larmor frame, one can now write $\tilde{H_1}^L$ in a form ready for substituting into eq. (3.10):

$$\begin{aligned} \tilde{H_1}^L(t) \;=\; \sum_p \sum_l \sum_{m,m',m''=-l}^{l} & (-)^m [A^p_{lm''}]^P [T^p_{l-m}]^L \\ & \times D^l_{m''m'}(\Omega^{(P\to M)}(t)) D^l_{m'm}(\Omega^{(M\to L)}(t)) \mathrm{e}^{\mathrm{i}m\omega^0 t}. \end{aligned} \tag{3.18}$$

The relaxation Hamiltonian invariably involves second-rank space tensors ($l = 2$) due to the pairwise, symmetric nature of the interactions. This includes dipole-dipole couplings between nuclear pairs, the anisotropic chemical shielding (CSA) interaction between nuclei and the B^0 field, and spin- rotational-angular-momentum coupling.[14] Principal axis components for the dipole-dipole and the CSA tensors are listed in 3.1.

	Mechanism	
	Dipole-dipole coupling (p = DD, $l = 2$)	Chemical shielding anisotropy (p = CSA, $l = 2$)
Space tensor (in principal-axes frame, P)		
$[A^p_{20}]^P$	$\sqrt{6}\,b_{jk}$	$\sqrt{3/2}\,\Delta\delta^{(j)}_{zz}$
$[A^p_{2\pm1}]^P$	0	0
$[A^p_{2\pm2}]^P$	0	$-\frac{1}{2}\Delta\delta^{(j)}_{zz}\eta^{(j)}$
Spin-field tensor (in laboratory frame, L)		
$[T^p_{20}]^L$	$\frac{1}{\sqrt{6}}(2I_{jz}I_{kz} - I_{jx}I_{kx} - I_{jy}I_{ky})$	$\sqrt{2/3}\,\gamma_j B^0 I_{jz}$
$[T^p_{2\pm1}]^L$	$\mp\frac{1}{2}(I_{j\pm}I_{kz} + I_{jz}I_{k\pm})$	$\mp\frac{1}{2}\gamma_j B^0 I_{j\pm}$
$[T^p_{2\pm2}]^L$	$\mp\frac{1}{2}I_{j\pm}I_{k\pm}$	0

Table 3.1: Principal axis components of the dipole-dipole ('DD') Hamiltonian between two spins 'jk' (where $b_{jk} = -\hbar\mu_0\gamma_j\gamma_k/(4\pi d^3_{jk})$) and anisotropic chemical shielding ('CSA') Hamiltonian of a spin-1/2 'j'. ($\Delta\delta^{(j)}_{zz} = (\delta^{(j)}_{zz} - \delta^{(j)}_{\rm iso})$; $\delta^{(j)}_{\rm iso} = (\delta^{(j)}_{xx} + \delta^{(j)}_{yy} + \delta^{(j)}_{zz})/3$; $\eta^{(j)} = (\delta^{(j)}_{xx} - \delta^{(j)}_{yy})/\Delta\delta^{(j)}_{zz}$ for spin j are given in terms of the principal components $\delta^{(j)}_{xx}$, $\delta^{(j)}_{yy}$, $\delta^{(j)}_{zz}$ of the chemical shielding tensor). Both interactions are second-rank ($l = 2$) with respect to spatial rotations.

Relaxation superoperator

The spherical tensor formulation generates a rather monstrous looking expression for $\hat{\Gamma}$, particularly if there is more than one relaxation mechanism in operation where it involves a superposition of self or auto time-correlated ($\hat{\Gamma}^{pp}(t)$) and cross time-correlated ($\hat{\Gamma}^{pq}(t)$, $p \neq q$) products:

$$\hat{\Gamma}(t) = \sum_{p,q} \hat{\Gamma}^{pq}(t), \tag{3.19}$$

where the general correlation is given by

$$\begin{aligned}\hat{\Gamma}^{pq}(t) = -\sum_{l} \sum_{m,m',m''=-l}^{l} \sum_{\lambda} \sum_{\mu,\mu',\mu''=-\lambda}^{\lambda} (-)^{m+\mu} [\hat{T}^{p}_{l-m}]^{L} [\hat{T}^{q}_{\lambda-\mu}]^{L} \\ \times [A^{p}_{lm''}]^{P} [A^{q}_{\lambda\mu''}]^{P} D^{l}_{m''m'}(\Omega^{(P\to M)}) D^{\lambda}_{\mu''\mu'}(\Omega^{(P\to M)}) \mathrm{e}^{\mathrm{i}(m+\mu)\omega^{0}t} \\ \times \overline{\int_{-\infty}^{0} \mathrm{d}\tau \, D^{l}_{m'm}(\Omega^{(M\to L)}(t+\tau)) D^{\lambda}_{\mu'\mu}(\Omega^{(M\to L)}(t)) \mathrm{e}^{\mathrm{i}m\omega^{0}\tau}}.\end{aligned} \tag{3.20}$$

However, by bringing out detail of the molecular motion in solution this can be compacted into the form

$$\begin{aligned}\hat{\Gamma}^{pq}(t) = -\sum_{l} \frac{1}{2l+1} \sum_{m',m'',\mu''} [A^{p}_{lm''}]^{P} [A^{q}_{l\mu''}]^{P} \\ \times D^{l}_{m''m'}(\Omega^{(P\to M)}) D^{l}_{\mu''-m'}(\Omega^{(P\to M)}) \\ \times \sum_{m} (-)^{m} j(m\omega^{0}) [\hat{T}^{p}_{l-m}]^{L} [\hat{T}^{q}_{\lambda m}]^{L}.\end{aligned} \tag{3.21}$$

Eq. (3.20) connects to eq. (3.21) on two reasonable assumptions for small molecules in isotropic solution. Firstly, that the frame transformations $(P \to M)$ and $(M \to L)$ are uncorrelated, so can be averaged separately. Such assumption holds when the intramolecular motions are either much faster or much slower than overall molecular reorientation. This includes rigid molecules where intramolecular motion is absent altogether. The second assumption is that molecular reorientations across the interval t to $(t+\tau)$ are quantifiable

by a probability function, $G(\tau)$ (usually called the 'correlation function'), defined

$$\overline{D^l_{m'm}(\Omega^{(M\to L)}(t+\tau))D^\lambda_{\mu'\mu}(\Omega^{(M\to L)}(t))} = \overline{D^l_{m'm}(\Omega^{(M\to L)}(t))D^\lambda_{\mu'\mu}(\Omega^{(M\to L)}(t))}G(\tau), \tag{3.22}$$

where $G(0) = 1$ and $\lim_{\tau\to\infty} G(\tau) = 0$. In isotropic solution $G(\tau)$ is independent of both Ω and t so one can further identify

$$\text{eq. (3.22)} = \frac{(-)^{m-m'}}{2l+1}\delta_{l\lambda}\delta_{\mu-m}\delta_{\mu'-m'}G(\tau). \tag{3.23}$$

Ranks (l, λ) and the projection indices are not explicitly involved in G since they are taken care of by ensemble averaging. Working in this regime, the relaxation superoperator appears

$$\begin{aligned}\hat{\Gamma}^{pq}(t) = -\sum_l \frac{1}{2l+1} \sum_{m',m'',\mu''} & [A^p_{lm''}]^P[A^q_{l\mu''}]^P \\ & \times D^l_{m''m'}(\Omega^{(P\to M)})D^l_{\mu''-m'}(\Omega^{(P\to M)}) \\ & \times \sum_m (-)^m[\hat{T}^p_{l-m}]^L[\hat{T}^q_{\lambda m}]^L \int_{-\infty}^{0} \mathrm{d}\tau\, G(\tau)\mathrm{e}^{\mathrm{i}m\omega^0\tau}.\end{aligned} \tag{3.24}$$

For final relation to eq. (3.21), integration over τ translates the time-correlation function $G(\tau)$ into a spectral density function $j(\omega)$, which is sampled at integer multiples of the Larmor frequency:

$$\int_{-\infty}^{0} \mathrm{d}\tau\, G(\tau)\mathrm{e}^{\mathrm{i}m\omega^0\tau} = j(m\omega^0). \tag{3.25}$$

Note that by virtue of the Fourier transform that the spectral density essentially 'pick out' the amplitude of molecular tumbling at frequencies resonant with nuclear spin transitions (the latter separated by multiples of ω^0, under the earlier-assumed B^0 field dominance). This is consistent with the idea that in order to have transitions between spin states, one requires a fluctuating Hamiltonian at the corresponding energy difference.

In this work, like many others have done previously,[14] I assume an exponentially decaying correlation function $G(\tau) = \exp(-\tau/\tau_c)$ quantified by the memory time constant of random molecular tumbling, or 'correlation time', τ_c. This function satisfies

$\lim_{\tau\to\infty} G(\tau) = 0$ and $G(0) = 1$, and independence to the global time coordinate. The corresponding spectral density is

$$j(m\omega^0) = \frac{\tau_c}{1 + (m\omega^0\tau_c)^2}. \tag{3.26}$$

Quick-reference to relaxation superoperators

We are finished with outlining the assumptions and considerations involved in setting up the Redfield relaxation problem and are ready to solve it. To consolidate the material presented so far, and give a reference point for later, I list explicit relaxation superoperators for the most common mechanisms expected in solution:

- *Dipole-dipole relaxation superoperator*

  Using the notation given in table 3.1, the explicit cross-correlation between two nucleus-nucleus dipole-dipole couplings is

$$\begin{aligned}\hat{\Gamma}^{(\mathrm{DD}_{jk,uv})} &= -\frac{6b_{jk}b_{uv}}{5}\sum_{m'=-2}^{2} D^2_{m'0}(\Omega^{(P_{jk}\to M)})D^2_{0-m'}(\Omega^{(P_{uv}\to M)}) \\ &\quad\times\sum_m (-)^m j(m\omega^0)[\hat{T}^{\mathrm{DD}_{jk}}_{2-m}]^L[\hat{T}^{\mathrm{DD}_{uv}}_{2m}]^L.\end{aligned} \tag{3.27}$$

  Indices jk and uv denote the nuclear labels of homonuclear spins-1/2, each of which may be different (but this is only the case if four or more spins-1/2 are present).

  Note the above may be simplified by compounding Wigner matrices into

$$\hat{\Gamma}^{(\mathrm{DD}_{jk,uv})} = -\frac{6b_{jk}b_{uv}}{5}d^2_{00}(\beta^{(P_{jk}\to P_{uv})})\sum_m (-)^m j(m\omega^0)[\hat{T}^{\mathrm{DD}_{jk}}_{2-m}]^L[\hat{T}^{\mathrm{DD}_{uv}}_{2m}]^L \tag{3.28}$$

  where $\beta^{(P_{jk}\to P_{uv})}$ is angle formed between the internuclear vectors of spin pairs jk and uv. This leads to a very simple expression for auto-correlated dipolar relaxation superoperator where $\beta^{(P_{jk}\to P_{jk})} = 0$ within the constant principal axes frame:

$$\hat{\Gamma}^{(\mathrm{DD}_{jk,jk})} = -\frac{6b^2_{jk}}{5}\sum_m (-)^m j(m\omega^0)[\hat{T}^{\mathrm{DD}_{jk}}_{2-m}]^L[\hat{T}^{\mathrm{DD}_{jk}}_{2m}]^L. \tag{3.29}$$

- *CSA-dipole relaxation superoperator*

  The cross-correlation between a dipole coupling involving nuclei jk and the anisotropic

chemical shielding on nucleus u is derived from the quantities in table 3.1 as

$$\hat{\Gamma}^{(\mathrm{DD}_{jk}\mathrm{CSA}_u)} = -\frac{\sqrt{6}\,b_{jk}}{5}\sum_{m'=-2}^{2}[A_{2m'}^{\mathrm{CSA}_u}]^P D^2_{m'0}(\Omega^{(P_{jk}\to P_u)}) \times\sum_m(-)^m j(m\omega^0)[\hat{T}^{\mathrm{DD}_{jk}}_{2-m}]^L[\hat{T}^{\mathrm{CSA}_u}_{2m}]^L. \tag{3.30}$$

- *Pure CSA relaxation superoperator*

  The general form of the superoperator describing correlated anisotropic chemical shieldings between a nucleus j and nucleus k is

$$\hat{\Gamma}^{(\mathrm{CSA}_{j,k})} = -\frac{1}{5}\sum_{m',m''=-2}^{2}[A_{2m'}^{\mathrm{CSA}_j}]^P[A_{2m''}^{\mathrm{CSA}_k}]^P D^2_{m'm''}(\Omega^{(P_j\to P_k)}) \times\sum_m(-)^m j(m\omega^0)[\hat{T}^{\mathrm{CSA}_j}_{2-m}]^L[\hat{T}^{\mathrm{CSA}_k}_{2m}]^L. \tag{3.31}$$

3.1.3 Liouvillian eigenvalue analysis

A complete view over the progress of spin order under simultaneous coherent and incoherent evolutions is obtainable by tackling eq. (3.7) as an eigenvector-eigenvalue problem. By diagonalising the matrix representation of the total Liouvillian $(\hat{L}_0+\hat{\Gamma})$, one obtains eigenvectors as stationary combinations of spin order. Eigenoperators Q_i evolve as

$$\mathrm{d}Q_i/\mathrm{d}t = (\hat{L}_0+\hat{\Gamma})Q_i = +\lambda_i Q_i, \tag{3.32}$$

where the eigenvalues λ_i describe the oscillatory behaviour and relaxation. The eigenvalues may be split as $\lambda_i = (-\mathrm{i}\omega_i - k_i)$, where ω and k are real, such that the parts $\mathrm{Re}(\lambda_i) = k_i \geq 0$ correspond to monoexponential decay rates in eigenoperator amplitudes and $\mathrm{Im}(\lambda_i) = \omega_i$ corresponds to a single-frequency phase modulation. This becomes more apparent on integrating the eigenvalue differential equation with respect to time:

$$\text{eq. (3.32)} \xrightarrow{\text{integrate}} \begin{aligned} Q_i(t_0+\tau) &= \exp(+\lambda_i\tau)Q_i(t_0) \\ &= \exp(-\mathrm{i}\omega_i\tau)\exp(-k_i\tau)Q_i(t_0). \end{aligned} \tag{3.33}$$

One cannot understate the power of eigenvalue analysis. Firstly it allows one to deter-

mine multiexponential relaxation of arbitrary spin order:

$$\overline{\rho}(t_0+\tau)=\sum_i (Q_i|\overline{\rho}(t_0))\exp(-\mathrm{i}\omega_i\tau)\exp(-k_i\tau)Q_i. \tag{3.34}$$

In a more specific context to this work, the eigenspectrum answers many important questions about long-lived spin order. The longest-lived order in the system corresponds to the eigenoperators with eigenvalues k_i nearest to zero. Under a given coherent environment and set of relaxation mechanisms, is singlet order close to a long-lived eigenoperator? The answer is a matter of diagonalising the relaxation matrix.

3.1.4 Thermalisation

Although it makes for a simple derivation, the classical lattice surrounding in WBR theory is perhaps an oversimplification, and a potentially serious caveat. As WBR theory stands $\hat{\Gamma}$ describes equalisation of spin populations, rather than a tendence of the ensemble to a Boltzmann equilibrium state (see *e.g.* eq. (1.25)). Formally, eq. (3.10), and hence eq. (3.21), holds valid only for infinite spin temperature.

The thermal defect in $\hat{\Gamma}$ can be fixed 'ad hoc' by acting $\hat{\Gamma}$ on the deviation from thermal equilibrium $\overline{\rho}-\overline{\rho}_{\mathrm{eq}}$. This ensures a steady state $\mathrm{d}\overline{\rho}/\mathrm{d}t=0$ for $\overline{\rho}=\overline{\rho}_{\mathrm{eq}}$:

$$\mathrm{d}\overline{\rho}/\mathrm{d}t \;=\; \hat{L}_0\overline{\rho}+\hat{\Gamma}(\overline{\rho}-\overline{\rho}_{\mathrm{eq}}). \tag{3.35}$$

The correction can be absorbed into a 'thermalised' relaxation superoperator $\hat{\Gamma}_{\mathrm{thermalised}}=\hat{\Gamma}\hat{\Theta}$, where the superoperator $\hat{\Theta}$ is defined through [101]

$$\hat{\Theta}^{-1}=\hat{E}-\left(\frac{E}{|E|^2}-\overline{\rho}_{\mathrm{eq}}\right)\otimes E, \tag{3.36}$$

such that the correct equilibrium is restored at long evolution times by

$$\mathrm{d}\overline{\rho}/\mathrm{d}t \;=\; (\hat{L}_0+\hat{\Gamma}_{\mathrm{thermalised}})\overline{\rho}. \tag{3.37}$$

One can show $\hat{\Theta}$ satisfies the required properties in $\hat{\Gamma}\hat{\Theta}$ via

$$\hat{\Theta}^{-1}E = |E|^2\overline{\rho}_{\mathrm{eq}} \quad \Rightarrow \quad \hat{\Gamma}\hat{\Theta}\overline{\rho}_{\mathrm{eq}} \propto \hat{\Gamma}E = 0, \tag{3.38}$$

$$\hat{\Theta}^{-1}\Big(\overline{\rho} - \frac{(E|\rho)}{(E|E)}E\Big) = \Big(\overline{\rho} - \frac{(E|\rho)}{(E|E)}E\Big) \quad \Rightarrow \quad \hat{\Gamma}\hat{\Theta}\overline{\rho} \equiv \hat{\Gamma}(\overline{\rho} - \overline{\rho}_{\mathrm{eq}}). \tag{3.39}$$

It is important to state that while alone $\hat{\Gamma}$ is thermally deficient, it still predicts the relaxation rates correct for tendence to thermal equilibrium. Relaxation eigenvalues are preserved between $\hat{\Gamma}\hat{\Theta}$ and $\hat{\Gamma}$, seeing that the eigenvectors are mixed with only the null (zero-eigenvalue) space. Eigenvalue analysis is therefore valid without explicit thermalisation in $\hat{\Gamma}$. This shortcut is used heavily in the remaining part of this chapter.

3.1.5 Scalar superoperators in relaxation analyses

A superoperator that is unaffected by arbitrary rotations of the spins is called a *scalar superoperator*, $\hat{\Xi}$, where

$$\hat{R}(\Omega)\hat{\Xi}\hat{R}^{-1}(\Omega) = \hat{\Xi}. \tag{3.40}$$

A scalar superoperator imposes strict selection rules on the evolution of spin order within the spherical tensor operator basis, rather similar to the restricted evolution of the angular momentum functions $|l, m\rangle$ under a scalar spin operator (spin tensor rank-0). Consider the superoperator matrix element $(T_{pq}|\hat{\Xi}T_{rs})$ of $\hat{\Xi}$ between two spherical tensor spin operators T_{pq} and T_{rs}. The scalar property dictates

$$(T_{pq}|\hat{\Xi}T_{rs}) \equiv \mathrm{Tr}(T_{pq}^{\dagger}\hat{R}^{-1}(\Omega)\hat{R}(\Omega)\hat{\Xi}\hat{R}^{-1}(\Omega)\hat{R}(\Omega)T_{rs}) \tag{3.41}$$

$$= \mathrm{Tr}(T_{pq}^{\dagger}\hat{R}^{-1}(\Omega)\hat{\Xi}\hat{R}(\Omega)T_{rs}) \tag{3.42}$$

$$= \sum_{q',s'} D_{qq'}^{p}(\Omega)^{*} D_{ss'}^{r}(\Omega) \times \mathrm{Tr}(T_{pq'}^{\dagger}\hat{\Xi}T_{rs'}). \tag{3.43}$$

The relation holds for all orientations, so one may average over orientations Ω. This gives

$$\frac{1}{8\pi^2}\int_\Omega \mathrm{d}\Omega[\text{ eq. (3.43)}] = \frac{1}{8\pi^2}\sum_{q',s'}\Big[\int_\Omega \mathrm{d}\Omega D^p_{qq'}(\Omega)^* D^r_{ss'}(\Omega)\Big]\mathrm{Tr}(T^\dagger_{pq'}\hat{\Xi}T_{rs'}) \quad (3.44)$$

$$= \frac{\delta_{pr}\delta_{qs}}{2p+1}\sum_{q',s'}\delta_{q's'}\mathrm{Tr}(T^\dagger_{pq'}\hat{\Xi}T_{rs'}) \quad (3.45)$$

$$= \delta_{pr}\delta_{qs}(T_{pq}|\hat{\Xi}T_{rs}). \quad (3.46)$$

The last line reveals that the matrix element is zero unless both rank and coherence order indices are the same in the connected operators, or in other words that $\hat{\Xi}$ is block-diagonal in the spherical tensor operator basis.

Scalar superoperator allow one to calculate analytical $1/T_S$ and $1/T_1$ relaxation rates, as spin order for T_S and T_1 is each described by a single spherical tensor operator. For a spin-1/2 pair jk the determination of T_S is simple; The Liouville space comprises only two rank-0 operators. One is the singlet order $T^{jk}_{00} = I_j \cdot I_k = |S_0\rangle\langle S_0| - \frac{1}{3}[|T_{-1}\rangle\langle T_{-1}| + |T_0\rangle\langle T_0| + |T_{+1}\rangle\langle T_{+1}|]$ and the other the trivial unit operator $E \propto |S_0\rangle\langle S_0| + |T_{-1}\rangle\langle T_{-1}| + |T_0\rangle\langle T_0| + |T_{+1}\rangle\langle T_{+1}|$ that commutes with all operators. If $\hat{\Gamma}$ is a scalar superoperator, then T_{00} must be an eigenoperator with relaxation rate given by the diagonal matrix element

$$\frac{1}{T_S^{(jk)}} \approx -(T^{(jk)}_{00}|\hat{\Gamma}T^{(jk)}_{00})/(T^{(jk)}_{00}|T^{(jk)}_{00}). \quad (3.47)$$

For T_1 the situation is more complex but analytical solutions remain accessible. For a spin-1/2 pair jk there are a total of three rank-1 projection-0 tensor operators, these being longitudinal order on each nucleus, $T^j_{10} = I_{jz}$ and $T^k_{10} = I_{kz}$, (where $T^k_{10} + T^k_{10} \equiv (|T_{+1}\rangle\langle T_{+1}| - |T_{-1}\rangle\langle T_{-1}|)$) and multispin rank-1 order $T^{jk}_{10} = -(I_{j+}I_{k-} - I_{j-}I_{k+})/\sqrt{2} \equiv (|S_0\rangle\langle T_0| - |T_0\rangle\langle S_0|)/\sqrt{2}$. It turns out that the coupled order T^{jk}_{10} is disconnected from the single-spin longitudinal operators and may be neglected, leaving the following biexponential matrix problem for T_1:

$$\frac{\mathrm{d}}{\mathrm{d}t}\begin{pmatrix} I_{jz} \\ I_{kz}\,. \end{pmatrix} = \begin{pmatrix} (T^{(j)}_{10}|\hat{\Gamma}T^{(j)}_{10}) & (T^{(j)}_{10}|\hat{\Gamma}T^{(k)}_{10}) \\ (T^{(k)}_{10}|\hat{\Gamma}T^{(j)}_{10}) & (T^{(k)}_{10}|\hat{\Gamma}T^{(k)}_{10}) \end{pmatrix}\begin{pmatrix} I_{jz} \\ I_{kz} \end{pmatrix}. \quad (3.48)$$

This 2×2 problem for T_1 is simplified when $\hat{\Gamma}$ is approximately symmetric with respect to exchange of the nuclei, which incidentally is the regime most of interest to singlet NMR,

where longest singlet lifetimes are predicted. Approximate permutation symmetry in the relaxation problem dictates eigenoperators approximately equal to the sum and difference order $(I_{jz} \pm I_{kz})$, giving a monoexponential decay rate for longitudinal relaxation

$$\frac{1}{T_1^{(jk)}} \approx -\frac{((T_{10}^{(j)} + T_{10}^{(k)})|\hat{\Gamma}(T_{10}^{(j)} + T_{10}^{(k)}))}{((T_{10}^{(j)} + T_{10}^{(k)})|(T_{10}^{(j)} + T_{10}^{(k)}))}. \tag{3.49}$$

Dipole-dipole scalar relaxation superoperator

Scalar relaxation superoperators $\hat{\Gamma} = \hat{R}(\Omega)\hat{\Gamma}\hat{R}^{-1}(\Omega)$ (not to be confused with superoperators for scalar relaxation) arise commonly in so-called 'extreme-narrowing' motion limit where molecular tumbling is fast compared to the Larmor frequency, at which $|\omega^0\tau_c| \ll 1$, and the spectral density across all transitions thereby uniformly sampled; $j(m\omega^0) \Rightarrow \tau_c$. The most frequent example is the general dipole-dipole cross-correlation superoperator derived earlier in eq. (3.27). In extreme narrowing

$$\text{eq. (3.27)} \xrightarrow{|\omega^0\tau_c|\ll 1} -\frac{6b_{jk}b_{uv}\tau_c}{5} d_{00}^2(\beta^{(P_{jk}\to P_{uv})}) \sum_m (-)^m [\hat{T}_{2-m}^{\mathrm{DD}_{jk}}]^L [\hat{T}_{2m}^{\mathrm{DD}_{uv}}]^L. \tag{3.50}$$

The double commutator part

$$\sum_m (-)^m [\hat{T}_{2-m}^{\mathrm{DD}_{jk}}]^L [\hat{T}_{2m}^{\mathrm{DD}_{uv}}]^L \tag{3.51}$$

is a scalar product between two rank-2 spin tensors, and therefore invariant under arbitrary global rotation of spins. For small molecules, the 'extreme-narrowing' limit usually holds very well in fields up to several tesla since τ_c is of order 10 to 100 picoseconds (1 ps $= 10^{-12}$ s). For larger molecules (MW > 500) this may not always be the case but is always more likely at lower B^0 field.

Anisotropic relaxation superoperators

Outside extreme narrowing the relaxation superoperator is generally not diagonal in spin operator rank l and therefore a full Liouvillian diagonalisation may be needed.

For an example consider the dipolar relaxation superoperator within the very high field or macromolecular limit $|\omega^0\tau_c| \gg 1$. This is the opposite regime to extreme narrowing in which molecular tumbling is too slow to cause transitions at the Larmor frequency. In this

situation the relaxation superoperator is limited to the zero-frequency fluctuation

$$\text{eq. (3.27)} \quad \xrightarrow{|\omega^0\tau_c|\gg 1} \quad -\frac{6b_{jk}b_{uv}\tau_c}{5}d^2_{00}(\beta^{(P_{jk}\to P_{uv})})[\hat{T}^{\mathrm{DD}_{jk}}_{20}]^L[\hat{T}^{\mathrm{DD}_{uv}}_{20}]^L. \tag{3.52}$$

It can be shown via the Clebsch-Gordan series that $\hat{\Gamma}$ connects spin operators T_{pq} and $T_{(p+\Delta p)q}$ up to a change in spin rank $0 \leq |\Delta p| \leq 4$. This rule follows because $[\hat{T}^{\mathrm{DD}_{jk}}_{20}]^L[\hat{T}^{\mathrm{DD}_{uv}}_{20}]^L$ spans a tensor superoperator space between spin ranks $|2-2| = 0$ and $(2+2) = 4$.

3.1.6 Spherical tensor commutation

Basic shortcuts must not be overlooked. While the latter sections have discussed spherical symmetry properties of the Liouvillian superoperator as a whole, some answers are available by examination of commutations between operators.

As an example, it can easily be shown that the commutator

$$[T^{uv}_{2m}, T^{jk}_{00}] \equiv \hat{T}^{uv}_{2m}T^{jk}_{00} \tag{3.53}$$

between a rank-2 spin tensor T^{uv}_{2m} and a rank-0 spin tensor T^{jk}_{00} is zero when spin pair indices jk and uv: (i) are the same; (ii) have no common label. This fact alone establishes singlet order is a null eigenoperator of (i) the auto-correlation intra-pair dipolar relaxation superoperator eq. (3.29), and (ii) dipole-dipole relaxation between external spins, regardless of whether extreme narrowing holds.

3.1.7 Liouvillian perturbation theory

In cases where the Liouvillian the superoperator is not scalar it may be difficult to obtain analytical formulae for singlet relaxation rates. If the Liouvillian is 'nearly scalar', however, approximate analytical formulae for T_1 and T_S may be derived using perturbation theory.

The starting point of perturbation theory is centered around the 'localised-singlet' hypothesis introduced in refs. [76] and [80]. An isolated spin pair is initially assumed, which is characterised by a reference Liouvillian superoperator

$$\hat{L}^{(0)} = \hat{L}^{(0)}_0 + \hat{\Gamma}^{(0)}. \tag{3.54}$$

The reference Liouvillian is scalar, obeying $\hat{R}(\Omega)\hat{L}^{(0)}\hat{R}^{-1}(\Omega) = \hat{L}^{(0)}$. The matrix represen-

tation of $\hat{L}^{(0)}$ is rank-diagonal in the spherical tensor operator basis. The singlet relaxation rate $1/T_S$ is given therefore by the diagonal matrix element eq. (3.47). Speaking in general, the reference eigensystem is known completely:

$$\hat{L}^{(0)}Q_i^{(0)} = \lambda_i^{(0)}Q_i^{(0)} \tag{3.55}$$

where $Q_i^{(0)}$ is equal to a spherical tensor operator and $\lambda_i^{(0)}$ its eigenvalue counterpart.

This reference system is related to the true Liouvillian superoperator by a term $\hat{L}^{(1)}$, which may or may not be scalar. The true eigensystem is defined such that

$$(\hat{L}^{(0)} + \hat{L}^{(1)})Q_i = \lambda_i Q_i, \tag{3.56}$$

where λ_i and Q_i are the exact eigenvalues and eigenoperators of the problem. Through the recipe of perturbation theory for normal matrices,[34] these are expressible from $Q_i^{(0)}$ and $\lambda_i^{(0)}$ by power series in $\hat{L}^{(1)}$:

$$\lambda_i = \sum_{n=0} \lambda_i^{(n)}, \tag{3.57}$$

$$Q_i = \sum_{n=0} Q_i^{(n)}, \tag{3.58}$$

where the lowest-order corrections are given by

$$\lambda_i^{(0)} = (Q_i^{(0)}|\hat{L}^{(0)}Q_i^{(0)}) \tag{3.59}$$

$$\lambda_i^{(1)} = (Q_i^{(0)}|\hat{L}^{(1)}Q_i^{(0)}) \tag{3.60}$$

$$\lambda_i^{(2)} = -\sum_{j\neq i} \frac{|(Q_i^{(0)}|\hat{L}^{(1)}Q_j^{(0)})|^2}{\lambda_j^{(0)} - \lambda_i^{(0)}}. \tag{3.61}$$

The perturbation theory method allows one to determine approximate analytical formulae for T_1 and T_S under a rotationally anisotropic Liouvillian. The series expansion rapidly converges when the perturbation induced by $\hat{L}^{(1)}$ on an eigenoperator $Q_i^{(0)}$ is much less than the difference in eigenvalues between $Q_i^{(0)}$ and other reference states; namely that $|\lambda_i - \lambda_i^{(0)}| \ll |\lambda_i^{(0)} - \lambda_j^{(0)}|$ for any j.

To date, eigenvalue perturbation theory has been used in several analyses of singlet relaxation. Dipole-induced relaxation for inequivalent spin pairs at low field has been

examined with reference to the zero-field relaxation rates, by treating the Zeeman interaction as a perturbation.[82] This approach applies also to evaluating the singlet leakage due to chemical shift frequency differences $|\gamma B^0 \Delta\delta/2\pi| \ll |J|$ of nearly equivalent spin-1/2 pairs in high field.[88] Gopalakrishnan and Bodenhausen used Liouvillian perturbation theory to derive a formula for T_S during off-resonance spin locking.[80] As described in the next section, perturbation analysis has also been used to examine T_S under weak relaxation mechanisms external to the spin pair, which may include out-of-pair dipole-dipole couplings.[62]

3.2 Singlet relaxometry

This section presents some case studies where experimental measurements of singlet relaxation rates are compared with predictions made using Redfield theory. Such a process is termed *singlet relaxometry*, where the aim is to back-calculate various information on singlet relaxation mechanisms from measured relaxation rates. This can take two forms, either (i) to quantify parameters in some pre-assumed relaxation-causing Hamiltonian such as the strengths of dipole-dipole couplings,[62] CSA,[61] or other parameters, or (ii) the reverse, to determine whether or not a given singlet relaxation mechanism is consistent with experimental data. Both of these are useful towards rationalising singlet relaxation times from a perspective of molecular functional groups, the knowledge of which may help in predicting molecules that have extremely long lifetimes.

In total *three* illustrative studies are reported. In the first I discuss singlet relaxation a of CH_2 proton pair caused by neighbouring protons in the molecule, entertaining a possibility of conformational analysis from the geometry-dependence of T_S predicted by Redfield theory. This is followed by analysis of the singlet lifetimes in heteronuclear systems, as prepared in earlier in §2.3. Finally, I analyse singlet relaxation in solutions doped with paramagnetic agents.[111]

3.2.1 Singlet relaxation of methylene protons

Introduction

The proton spin pair of an inequivalent CH_2 group (a methylene group) is both an interesting system for quantitative study of singlet relaxation. The internuclear magnetic dipole-dipole coupling $|b_{12}|$, assuming indices '1' and '2' to indicate the nuclei of the pair, is approximately $\hbar\mu_0\gamma_{\mathrm{H}}^2/4\pi d_{12}^3 \approx 21$ kHz in strength for the typical proton-proton distance $d_{12} \approx 1.8$ Åand by far exceeds dipolar couplings to nearby nuclei, and th CSA of the protons due to their low nuclear shielding. The T_1 relaxation mechanism is consequently well-determined, and the rate $1/T_1$ therefore provides an effective calibration of the molecular rotational correlation time in Redfield theory. For small molecules in extreme-narrowing

$$\text{eq. (3.49)} \quad \Rightarrow \quad \frac{1}{T_1} \quad = \quad \frac{3\tau_c}{2}|b_{12}|^2. \tag{3.62}$$

The singlet state between the protons does not relax under the strong dipole-dipole auto-correlation. This means the relaxation rate $1/T_S$ relative to $1/T_1$, or in other words the ratio of rates T_S/T_1, depends to good approximation only on the variables of out-of-pair spin interactions, and can be used as a probe of molecular environment local to CH_2.

Determination of molecular conformations using singlet relaxation

Nuclei in the vicinity of the methylene protons may induce relaxation through the dipole-dipole mechanism, the rate at which depends on the relative geometry between the CH_2 protons and neighbouring spins according to the superoperator eq. (3.27). This opens a possibility of determining molecular conformation from the ratio T_S/T_1. Relaxation ratios for all accessible molecular conformations can be calculated via Redfield theory, compared against the actual T_S/T_1 of the system measured by experiment, and the most likely conformations thereby determined.[62]

In the case where there is one proton external to the CH_2 (a system of three protons overall) the overall dipole-dipole relaxation superoperator contains $3 \times 3 = 9$ correlation terms:

$$\begin{aligned} \hat{\Gamma}^{(\mathrm{DD_{total}})} \;=\; & \underbrace{\hat{\Gamma}^{(\mathrm{DD_{12,12}})} + \hat{\Gamma}^{(\mathrm{DD_{13,13}})} + \hat{\Gamma}^{(\mathrm{DD_{23,23}})}}_{\text{auto-correlation}} + \\ & \underbrace{(\hat{\Gamma}^{(\mathrm{DD_{12,13}})} + \hat{\Gamma}^{(\mathrm{DD_{13,12}})}) + (\hat{\Gamma}^{(\mathrm{DD_{12,23}})} + \hat{\Gamma}^{(\mathrm{DD_{23,12}})}) + (\hat{\Gamma}^{(\mathrm{DD_{13,23}})} + \hat{\Gamma}^{(\mathrm{DD_{23,13}})})}_{\text{cross-correlation}}, \end{aligned} \tag{3.63}$$

where label 3 denotes the passive spin. If the CH_2 protons have no significant J-couplings to the nucleus 3,[77] the relaxation constant T_S evaluates to a good approximation the first-order perturbation estimate

$$\frac{1}{T_S} \;\approx\; (T_{00}^{12}|\hat{\Gamma}^{(\mathrm{DD_{total}})}T_{00}^{12}) \;=\; (b_{13}^2 + b_{23}^2 - 2b_{13}b_{23}d_{00}^2(\beta_{132}))\tau_c. \tag{3.64}$$

Here β_{1j2} symbolises the angle between the two vectors joining spins 1 and 2 with spin 3. Within the first-order perturbation approximation the contributions from additional spins are additive, so for more than three spins

$$\frac{T_1}{T_S} \;\approx\; \frac{2}{3b_{12}^2}\sum_{i>2}\Big(b_{1\mathrm{i}}^2 + b_{2\mathrm{i}}^2 - 2b_{1\mathrm{i}}b_{2\mathrm{i}}d_{00}^2(\beta_{1i2})\Big). \tag{3.65}$$

These above formulae are valid for distances d_{1i}, d_{2i} and $d_{ii'}(i > 2)$ all greater than d_{12}, to justify the perturbation approximation. In this limit, the rate constant decays with the inverse eighth power of the distance between each spin j and the centre of the spin pair '12'.[72] Magnetic nuclei at longer range therefore have a negligible effect even if they are present in large numbers, for instance the solvent bulk. The comparison of T_S and T_1 may hence be used to set confident geometric restraints on the immediate molecular environment of the CH_2 group.

Measurements on phenylalanine-derived compounds

To test this concept and eq. (3.65) a series of isotopically substituted phenylalanine analogues were prepared in which some of the hydrogens of the molecule were replaced with deuterium. Deuteration 'quenches' the selected proton-proton dipole couplings owing to (i) the effective downscaling of the dipole-dipole coupling constant by a factor of $(\gamma_D/\gamma_H) \approx 1/6$, and (ii) rapid self-decoupling of deuterium from the proton spin system due to its fast quadrupolar relaxation. The difference in rate constants between isotopologues is to a good approximation the rate induced by the proton difference.

Four isotopomers were studied as indicated in fig. 3.1 with proton/deuterium substitutions made synthetically (i) at the alpha-proton (referred as d_1-Phe), (ii) on only the proton sites of the phenyl ring (d_5), and (iii) both of these environments (d_6-Phe). Methyl ester and N-phthalimido groups, both non-deuterated, were also added with the aim of eliminating solvent-induced relaxation at the carboxyl and amino groups. Detail of the preparations can be found in the supporting information of ref. [62]. Each sample was dissolved to approximately 60 mmol concentration in 0.5 mL 99.99 % d_4-methanol. The solutions were gently warmed to assist dissolution, then transferred into 5 mm outer-diameter NMR tubes equipped with Young values and thoroughly degassed to remove dissolved paramagnetic molecular oxygen, O_2 (freeze-pump-thaw), and finally sealed.

Singlet order was excited on the diastereotopic methylene protons by applying Sarkar's sequence (§2.2.2, fig. 2.7) at an external B^0 field of 9.4 T. Optimum delays were $\tau_a = 1/4|^2J_{HH}| = 17.2$ ms ($^2J_{HH} = 14.5$ Hz between the CH_2 pair) and $\tau_b = \pi/|2\gamma B^0 \Delta\delta| = 14.9$ ms. An on-resonance CW decoupling field of strength 3.0 kHz was applied for time τ_{lock}, before reconversion to antiphase signals and detection. Non-singlet spin order was suppressed by applying a 12-step tetrahedral phase cycle (see §2.5.4) at the end of the

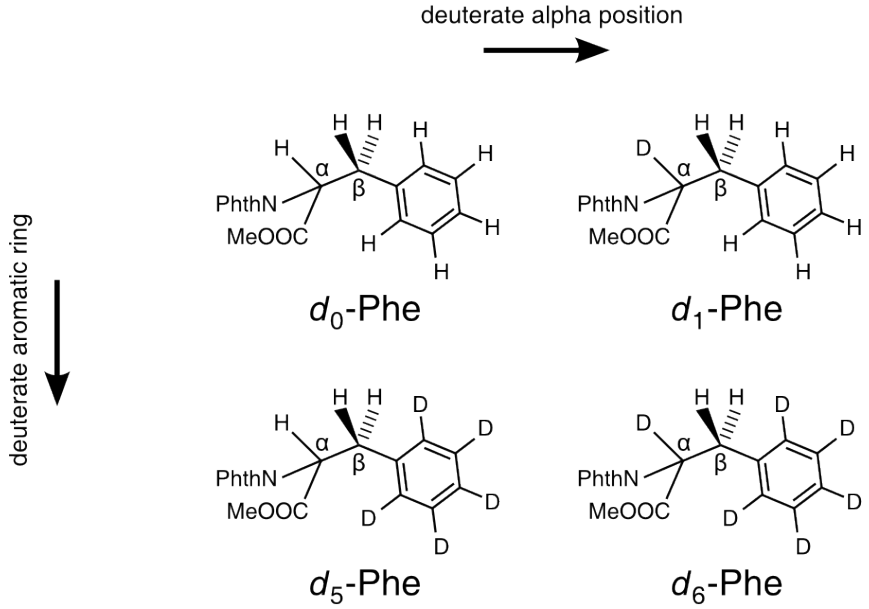

Figure 3.1: Series of isotopically substituted phenylalanines, denoted d_n-Phe where n is the number of deuterium nuclei present. Methyl ester and N-phthalimido blocking groups were added to suppress solvent-induced relaxation at the carboxyl and amino groups, respectively.

spin locking time.[129] The sequence was repeated for several values of τ_{lock} and the signal intensity on the β-protons fitted to a monoexponential decay $\exp(-\tau_{\text{lock}}/T_S)$ yielding the singlet lifetimes. These lifetimes are displayed in table 3.2 alongside which are given the conventional T_1 lifetimes for the methylene protons, measured by inversion recovery on the same samples.

	T_S (s)	T_1 (s)	T_S/T_1	$[T_S^{-1} - T_S^{-1}(d_6)]$ $(\text{s})^{-1}$
d_0	7.4	1.15	6.4	0.13
d_1	8.0	1.17	6.8	0.12
d_5	16.0	1.33	16	0.04
d_6	51	1.38	37	0

Table 3.2: Experimental T_S and T_1 relaxation times for the doubly protected phenylalanine analogues (see fig. 3.1) an external field B^0 of 9.4 T in degassed d_4-methanol. The singlet lifetimes were measured using Sarkar's sequence under 3.0 kHz WALTZ-16 proton decoupling. The T_1 lifetimes were measured by inversion recovery.

Static conformational analysis

The CH_2 singlet lifetimes are longest in the d_5 and d_6 ring-deuterated isotopologues. For d_6-Phe, the lifetime was $T_S = (51 \pm 2)$ seconds, which is approximately 37 times longer than $T_1 = (1.38 \pm 0.05)$ seconds. The decay time of d_1-Phe was $T_S = (8.0 \pm 0.1)$ seconds or only 6.8 times longer than $T_1 = (1.17 \pm 0.04)$ seconds. The rate constants $(1/T_S - 1/T_S(d_6))$ in the far-right column of 3.2 show that the alpha-proton contributes $(16^{-1} - 51^{-1})$ $s^{-1} = 0.04$ s^{-1} to the singlet relaxation rate, while the phenyl protons contribute $(8.0^{-1} - 51)$ $s^{-1} = 0.12$ s^{-1}, *i.e.* about 3 times more. The rate for d_0-Phe looks consistent with these two contributions being additive.

Why do the phenyl protons contribute 0.12 s^{-1} and what constraints does this put on the orientation of the aromatic ring? To determine the answers, eq. (3.65) was used to analyse the dependence of the singlet relaxation rate constant upon the torsional angle $\varphi_{\beta\gamma}$ around the C^{β}–C^{γ} sigma bond. Eq. (3.65) is assumed to be valid for the phenyl protons, since: (i) CH_2 protons do not have significant J-couplings with the ring protons; (ii) molecular rotation is within the extreme narrowing limit, as verified from the T_1 value of (1.38 ± 0.05) seconds, which corresponds to a rotational correlation time of $\tau_c = 24$ ps; (iii) the 51 second singlet lifetime in the d_6 compound indicates that CSA and the contributions of the protonated blocking groups make a negligible contribution to the singlet relaxation. It was assumed the ortho protons make the dominant contribution the relaxation, so that the meta and para ring protons can be omitted from the calculation.

Internuclear vectors between the two ortho protons of the ring and the methylene protons were calculated as a function of the coordinate $\varphi_{\beta\gamma}$ using standard bond lengths and bond angles. The derived dipole-dipole couplings $\propto |\boldsymbol{r}_{jk}|^{-3}$ and angles $\cos(\beta_{1j2}) = (\boldsymbol{r}_{1j} \cdot \boldsymbol{r}_{j2})/(|\boldsymbol{r}_{1j}||\boldsymbol{r}_{j2})$ are then used with Eq. (3.65) to determine T_S/T_1 versus $\varphi_{\beta\gamma}$. The calculation was performed using SpinDynamica.[101] The dependence is shown by the solid line plotted in fig. 3.2, defining the convention $\varphi_{\beta\gamma} = 0$ where the midpoint of the vector joining the two CH_2-protons lies in the plane of the aromatic ring (see also fig. 3.2).

The calculated values of T_S/T_1 show a variation between ≈ 14 near $\varphi_{\beta\gamma} = 0°$ and ≈ 6 in the vicinity of $\varphi_{\beta\gamma} = 90°$. Experimentally, the ratio for d_1-Phe is $T_S/T_1 = (6.8 \pm 0.2)$, indicating an angle between $\varphi_{\beta\gamma} = 45°$ and $135°$. This range of orientations is consistent with the known crystal structure of L-phenylalanine.[135]

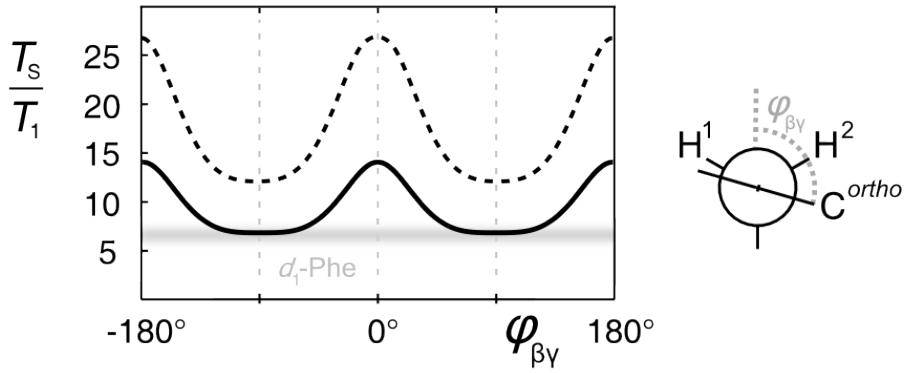

Figure 3.2: Variation of T_S/T_1 in d_1-Phe against the $C^\beta C^\gamma$ torsional angle of the aromatic ring $\varphi_{\beta\gamma}$. The ratio plotted is that predicted by eq. (3.65) assuming pure dipole-dipole relaxation in the system containing the two ortho ring protons and the methylene protons: (solid line) for a single, static ring orientation; (dashed line) for rapid 180° rotational jumps between ring orientations $\varphi_{\beta\gamma}$ and $(\varphi_{\beta\gamma} + 180°)$. The horizontal grey band indicates the experimental value of T_S/T_1 for d_1-Phe, the height indicating the error margin.

Molecular dynamics

The aromatic ring in phenylalanine, as well as in other aromatic amino acids, is known to execute 180° 'hops' between conformations with torsion angles $\varphi_{\beta\gamma}$ and $(\varphi_{\beta\gamma} + 180°)$.[136] This may have strong consequences on the CH_2 singlet relaxation. For ring flips that are slow relative to the rotational correlation time, but fast compared to the Larmor frequency, Redfield theory says the rate constants $1/T_1$ and $1/T_S$ are each given by the conformationally averaged rate.

Fig. 3.2 (dashed curve) shows the predicted $\varphi_{\beta\gamma}$-dependence of the resulting T_S/T_1 ratio for rapid jumps of the ring. The model predicts much longer singlet relaxation times due to averaging of dipolar couplings between the two geometries of the CH_2 and each ortho ring proton, with T_S/T_1 varying between ≈ 13 and ≈ 26. The experimental value of $T_S/T_1 = 6.8$, however, does not at all agree with this range. This proves either ring flips are slow compared to the Larmor frequency, or nonexistent altogether.

This apparent immobility of the phenyl ring is confirmed by singlet and longitudinal relaxation measurements made on samples of α-deuterated tyrosines (9.4 T, D_2O, see fig. 3.3). Lifetimes $T_S = (3.1 \pm 0.2)$ seconds and $T_1 = 0.5$ seconds were measured for the methylene group of α-deuterated tyrosine. These remained unchanged upon adding a nitro group (NO_2) meta on the ring, the large mass and bulk of which quenches ring-hopping. The ratio $T_S/T_1 \approx 6$ further suggests a near-90° equilibrium torsion angle $\varphi_{\beta\gamma}$ of the ring.

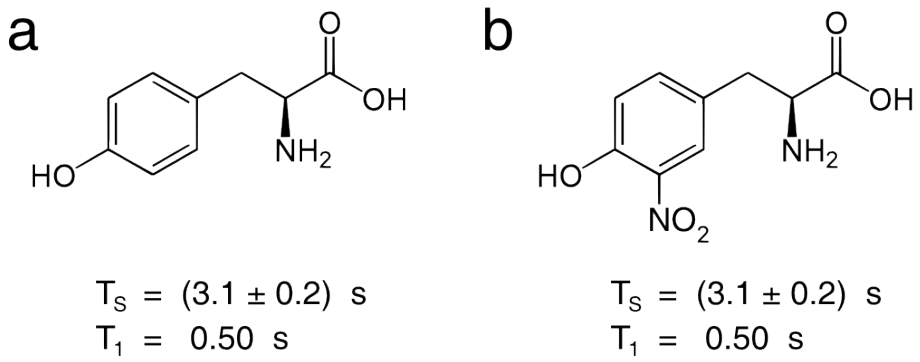

Figure 3.3: Experimental relaxation time constants for α-deuterated tyrosine at 9.4 T in D_2O: (left) free amino acid; (right) hindered meta nitro analogue. The similar lifetimes suggest a non-rotating phenyl group in ordinary tyrosine.

Presence of J-couplings

Due to the relaxation induced by the α proton, T_S/T_1 in the d_5-Phe isotopologue is dependent on the torsion angle between C^β and C^α, $\varphi_{\alpha\beta}$. In this case, however, eq. (3.65) cannot determine conformation restraints since the relaxation is accompanied by evolution under the vicinal ${}^3J_{\alpha\beta}$ couplings. In this case, T_S/T_1 was determined by resorting to full Liouvillian eigenvalue analysis of the zero quantum subspace, using the Karplus relationship to treat the conformationally dependent ${}^3J_{\alpha\beta}$ couplings, ${}^3J_{13}$ and ${}^3J_{23}$. Parameterisations for ${}^3J_{\alpha\beta}$ were chosen according to the $C^\beta H_2 C^\alpha H$ vicinal couplings expected for amino acids in a random-coil peptide chain.[137] In units of Hz, these are

$$ {}^3J_{13} = 9.4\cos(\varphi_{\alpha\beta}+60^\circ) - 1.6\cos^2(\varphi_{\alpha\beta}+60^\circ) + 1.8, \tag{3.66} $$

$$ {}^3J_{23} = 9.4\cos(\varphi_{\alpha\beta}-60^\circ) - 1.6\cos^2(\varphi_{\alpha\beta}-60^\circ) + 1.8. \tag{3.67} $$

These relationships have been plotted in fig. 3.4(b).

The $T_S(\varphi_{\alpha\beta})/T_1$ curve resulting from eigenvalue analysis is shown in fig. 3.4(a). Minima in T_S/T_1 occur in the vicinity of the eclipsed syn conformations where the α-proton lies nearest to one of the methylene protons ($\varphi_{\alpha\beta} \approx 60^\circ$). The maximum lifetime occurs at the anti configuration ($\varphi_{\alpha\beta} = 140^\circ$ to 180°). The experimental ratio T_S/T_1 supports a torsion angle $\varphi_{\alpha\beta} \approx 100^\circ$ for a static conformation of the amino acid, which according to fig. 3.4(b) agrees approximately with the angle inferred from the two experimental J-couplings ${}^3J_{\alpha\beta} = 4.9$ Hz and 12.0 Hz.

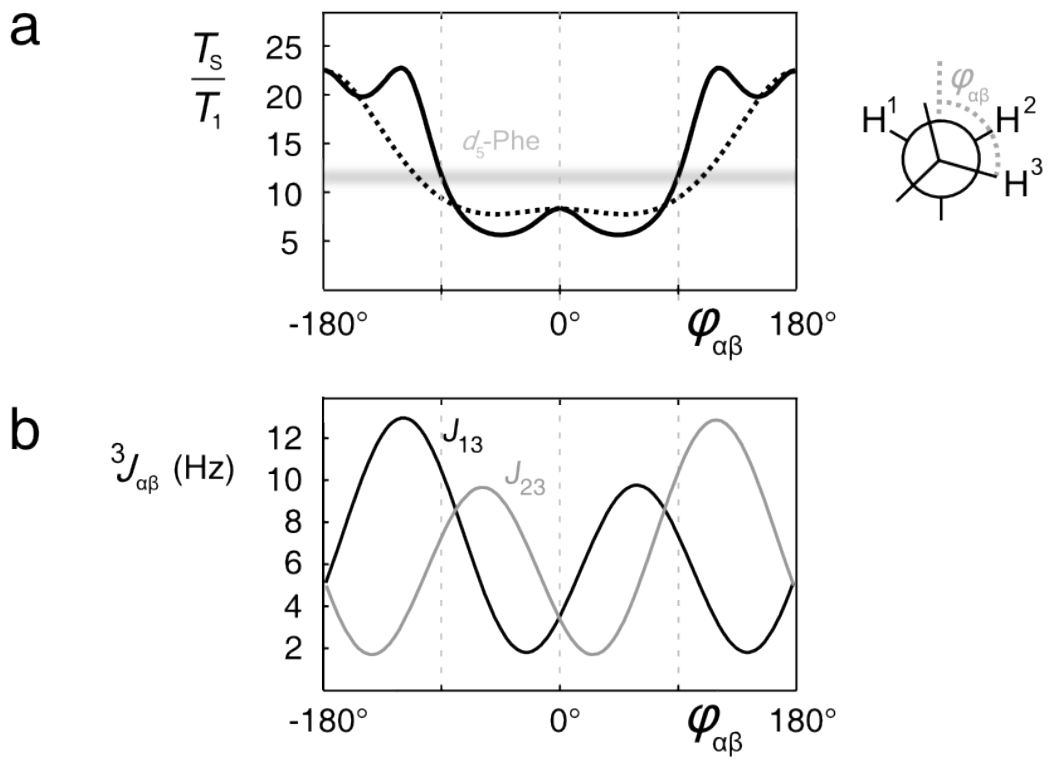

Figure 3.4: Dependence of T_S/T_1 for relaxation caused by the α-proton in d_5-Phe. The solid line in (a) shows the variation in T_S/T_1 against the torsion angle $\varphi_{\alpha\beta}$ as calculated by Liouvillian eigenvalue analysis, taking into account the vicinal $^3J_{\alpha\beta}$ couplings that are themselves dependent on $\varphi_{\alpha\beta}$ according to the Karplus relations, which are plotted in (b).[137] The dotted line in (a) shows the variation in T_S/T_1 against the first-order matrix element $(T_{00}^{12}|\hat{\Gamma}^{(\mathrm{DD_{total}})}T_{00}^{12})$. The solid curve is the more correct approach; note, however, the dotted and solid lines coincide at the torsion angles where $|^3J_{13} -^3 J_{23}| \ll^2 J_{12}$. This behaviour is in accordance with ref. [77].

This analysis shows that T_S/T_1 provides information that difficult to obtain using the Karplus relationships alone. The ratio T_S/T_1 shows a large contrast between the $\varphi_{\alpha\beta} = 0°$ and $\varphi_{\alpha\beta} = 180°$ conformations of the molecule, while the J-couplings according to fig. 3.4(b) are roughly similar. In this particular demonstration it is unlikely that nuclear Overhauser effect (nOe) measurements can resolve the ambiguity, since these are dominated by the strong intra-pair coupling b_{12} and relatively insensitive to the position of the vicinal proton.

To summarise, the ratio T_S/T_1 of a CH_2 group, within the stated approximations, is insensitive to overall molecular rotation and depends only on spatial positions and dynamics of neighbouring nuclei. Singlet relaxometry of methylene groups may complement other NMR methods, such as J-coupling analysis and the nOe, both as a support of structure-determination outcomes obtained from the existing methods, or resolving answers that are otherwise difficult to obtain.

3.2.2 Heteronuclear singlet relaxation

In §2.3 a demonstration was made of singlet excitation on a pair of chemically equivalent protons by exploiting J-couplings to a nearby ^{13}C nucleus. As well as being another means to excite singlet order, and access lifetimes extended beyond T_1, heteronuclear singlet NMR provides interesting opportunities for singlet relaxometry.

To illustrate this, the molecule 1,2,3,4-tetrachlorobenzene (1,2,3,4-TCB) is returned to, which contains two equivalent aromatic protons and three distinguishable aromatic carbon sites. Singlet relaxation times T_S and longitudinal relaxation times T_1 were recorded for all of the natural-abundance $^{13}C_1$ isotopomers. These experimental data are summarised in table 3.3, which confer the longest singlet lifetimes are when the ^{13}C nucleus is furthest from the proton pair. Qualitatively, this agrees with the reduction in the strength of ^1H-^{13}C dipole couplings, which are proportional to $1/d_{CH}^3$.

To estimate quantitative relaxation times for the heteronuclear system one must use a Redfield's formalism in a slightly more complicated form than that outlined in 3.1.1. Second-order truncation in eq. (3.4) dictates a need to transform the Hamiltonian into a double interaction frame; one frame rotating at the proton Larmor frequency via the propagator $\exp(-i\omega_I^0 I_z t)$ and the other at the Larmor frequency of ^{13}C, via $\exp(-i\omega_S^0 S_z t)$, where I denotes proton and S carbon. Solution of the relaxation problem, however, has

Isotopomer	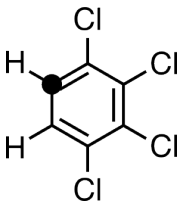	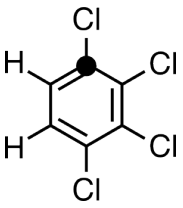	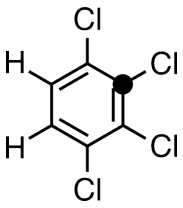	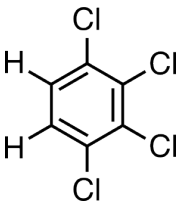
Experimental relaxation times (MeOD, 9.4 T)				
T_S (s)	2.2	(72 ± 5)	(140 ± 10)	–
T_1 (s)	2.8	8.7	9.0	9.2
T_S/T_1	0.8	(8.3 ± 0.4)	(15.5 ± 1)	–
Predicted lifetime ratio, pure DD mechanism + short τ_c				
T_S/T_1	0.7	11-12	> 170	–

Table 3.3: Experimental decay constants, T_S, measured under resonant proton spin locking at 9.4 T, and T_1, by inversion-recovery/INEPT in d_4-methanol for the protons in 1,2,3,4-TCB. For detail on the measurements, see §2.3. The black dots indicate the position of the ^{13}C nucleus, if present, in each isotopologue. The quoted error in T_S is the uncertainty in exponential fitting of experimental decays. Below are listed the theoretical lifetime ratios T_S/T_1 for each geometry predicted by the Redfield theory.

some simplifications: (i) that under resonant spin locking of either the I or S nuclei, (but not both), the heteronuclear couplings are averaged, and may be neglected from calculation; (ii) that due to the secular approximation $\gamma_I \neq \gamma_S$, the operator basis is diagonal in the coherence orders (m_I, m_S) of the I and S spins. Together these validate use of Liouvillian perturbation theory for T_S. Assuming a pure dipole-dipole relaxation mechanism, for sake of simplicity, the rate formula obtained is

$$\begin{aligned} \frac{1}{T_S} &\approx (T_{00}^{12}|\hat{\Gamma}^{(\mathrm{DD_{total}})}T_{00}^{12}) && (3.68)\\ &= \frac{1}{15}(b_{13}^2 + b_{23}^2 - 2b_{13}b_{23}d_{00}^2(\beta_{132})) && (3.69)\\ &\qquad \times(2j(0) + 3j(\omega_I^0) + 3j(\omega_S^0) + j(|\omega_I^0 - \omega_S^0|) + 6j(|\omega_I^0 + \omega_S^0|)). \end{aligned}$$

where the subscript '3' is used to denote the ^{13}C spin and '1' and '2' the protons. In extreme narrowing for the small molecule, this condenses to

$$\text{eq. (3.69)} \quad \Rightarrow \quad (b_{13}^2 + b_{23}^2 - 2b_{13}b_{23}d_{00}^2(\beta_{132}))\tau_c. \qquad (3.70)$$

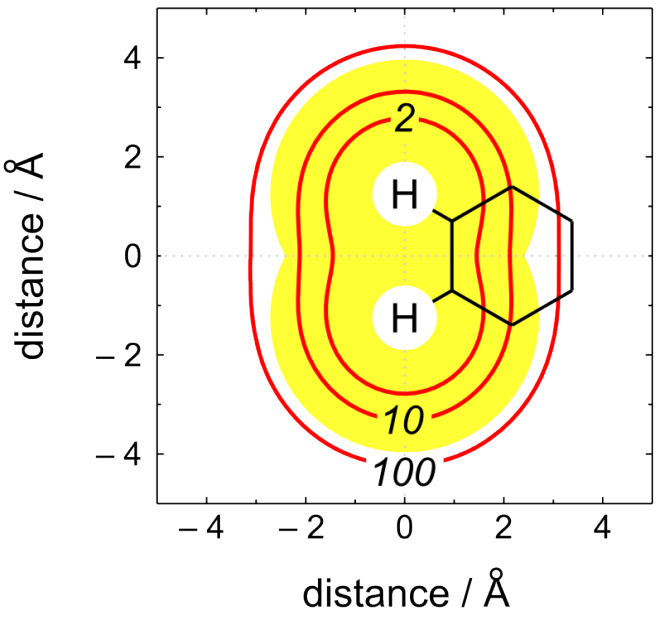

Figure 3.5: Contour plot showing τ_c-independent intramolecular dipole-dipole relaxation ratio T_S/T_1 against position of a ^{13}C nucleus for the two protons in 1,2,3,4-TCB, $d_{12} = (d_{\mathrm{CH}} + d_{\mathrm{CC}}) \approx 2.5$ Å. The yellow region indicates space that is physically inaccessible to the nucleus of a non-bonded carbon atom, assuming standard van der Waals radii for non-bonded carbon ($r_{\mathrm{VdW}}(\mathrm{C}) \approx 1.7$ Å) and hydrogen atoms ($r_{\mathrm{VdW}}(\mathrm{H}) \approx 1.2$ Å).

This is the same formula derived for homonuclear out-of-pair dipolar interactions (compare eq. (3.64)). The formula for the proton T_1, in the case of 1,2,3,4-TCB, is likewise identical to eq. (3.62).

The above formula is evaluated for the ^{1}H relaxation of 1,2,3,4-TCB and plotted in fig. 3.5. The contour lines indicate the theoretical T_S/T_1 at arbitrary position of the ^{13}C nucleus relative to the two protons whose separation is $d_{12} = (d_{\mathrm{CH}} + d_{\mathrm{CC}}) \approx 2.50$ Å, assuming standard bond lengths $d_{\mathrm{CC}} = 1.40$ Å and $d_{\mathrm{CH}} = 1.10$ Åand 120° bond angles. Superimposed upon the contour plot is a diagram showing the location of carbon sites in the 1,2,3,4-TCB, within this model. Precise ratios T_S/T_1 at these positions are listed at the bottom of table 3.3.

The calculated estimates of T_S/T_1 are very close to the experimental results for isotopomers where the ^{13}C nucleus is within one or two sigma bonds from the proton pair, suggesting in these geometries that the dipole-dipole mechanism is the dominant singlet relaxation source. The experimental T_S/T_1 for the more-remote three-bond isotopomer, however, is much shorter than the predicted ratio. The likely situation is that other re-

laxation mechanisms, such as CSA, limit the singlet lifetime from being longer, and are more influential than the ^{1}H-^{13}C dipolar coupling over the three-bond distance. A study of T_S/T_1 versus B^0 field may resolve this hypothesis.

The yellow region in fig. 3.5 marks the area around the proton pair that is inaccessible to the nuclei of non-bonded carbon atoms. This indicates that out-of-pair spins influence singlet relaxation only at very short range, and that intermolecular dipole-dipole contributions make a negligible contribution to T_S.

3.2.3 Singlet relaxation in paramagnetic-containing solutions

The final part of this thesis reports the influence of paramagnetic agents on singlet lifetimes. These are substances that contain one or more unpaired electrons, arising usually as either transition metal complexes or free radicals.

Introduction

Paramagnetism-induced relaxation is a complicated phenomenon.[14] The unpaired electron-spin momentum of paramagnetic species interacts with nuclear spins in quite a different way to inter-nuclear dipole couplings. The gyromagnetic ratio of the electron is much larger than of atomic nuclei, approximately 650 times the gyromagnetic ratio of a ^{1}H nucleus. Firstly this means that even lone-unpaired electrons may induce rather strong relaxation on the nuclear spins. The large electron magnetism is also strong enough to couple to other components of the system, including external magnetic fields (Curie effect) and the molecular orbital angular momenta. Spatial delocalisation of the electron wavefunction adds some further complication. Charged radical ions may additionally distort the nuclear chemical shieldings (chemical shifts), causing additional relaxation through a mechanism similar to intermolecular chemical exchange.

In the present section this mechanical detail of paramagnetic relaxation is for the most part ignored. I focus more on a basic questions of interest: is paramagnetic relaxation of the singlet order slower or faster than the T_1 of longitudinal magnetisation? By how much?

The above questions may be asked in view of the possible *in vivo* applications of nuclear singlet states where in blood there is the invariable large presence of metallo-proteins, such as haemoglobin, dissolved metal complexes and free radicals *e.g.* $^{\bullet}$NO and $O_2^{\bullet\bullet}$. As an

example, the T_1 of ^{129}Xe is more than 12 times faster dissolved in blood than dissolved in a saline solution.[138] Long singlet lifetimes in proximity to these paramagnetic substances may help preserve nuclear spin order during transport through a living animal's or human being's circulatory system. This may apply to spin order that is hyperpolarised outside the body, for instance by DNP[47] or PHIP[57], then injected, which must then survive transport until the point of interest in the body where it is imaged by MRI, or otherwise detected.

A well known example of paramagnet-induced singlet relaxation is the ortho-para conversion in dihydrogen. Conversion between spin isomers of H_2 may be catalysed through non-bonding near-approach to paramagnetic surfaces and complexes,[139, 64] where instantaneous differences in the local magnetic field are experienced by the hydrogen nuclei, inducing instantaneous magnetic inequivalence and singlet-to-triplet transitions. Ortho-para conversion in free H_2 has been studied extensively in solution, both experimentally and theoretically.[54, 140, 141] More recently ortho-para conversion has been studied for H_2 encapsulated in C_{60}.[142, 143, 144]

Relaxivity measurements

The relaxation influence of paramagnetic agents was studied in aqueous solution for the diastereotopic glycine protons of the dipeptide alanylglycine (AG), whose structure and basic NMR spectrum is displayed in fig. 3.6. This small and simple molecule has been the subject of several previous singlet NMR studies.[30, 145, 66, 83] The decay constant T_S in water, in the absence of dissolved paramagnetic substances, is almost 40 times T_1, which is due to the dominant dipole-dipole relaxation mechanism of the relatively isolated proton pair and fast correlation time τ_c.

The glycyl relaxation in AG was verified as a starting point for the present study. Singlet T_S and longitudinal T_1 decay times at a field of 9.4 T were measured in a solution containing 40 mM AG dissolved in 500 μL D_2O. Before the NMR measurements, the solutions were thoroughly degassed using the freeze-pump-thaw technique to eliminate dissolved paramagnetic oxygen. Singlet order was excited using Sarkar's pulse sequence (see §2.2.2 and ref. [24]) with optimal durations $\tau_a = 14.5$ ms and $\tau_b = 10.0$ ms. The singlet order was sustained during a relaxation period τ_{relax} by applying a WALTZ-16 modulated rf field at an amplitude of 2.5 kHz. Signal amplitudes were fitted to a monoexponential

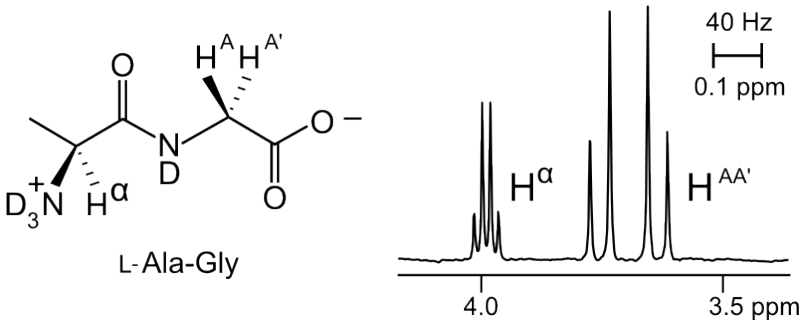

Figure 3.6: Molecular structural diagram and ^{1}H NMR spectrum (9.4 T, D_2O, room temperature) of the Ala-Gly peptide. The proton chemical shift is referenced to tetramethylsilane.

curve $\exp(-\tau_{\text{relax}}/T_S)$ giving $T_S = (32\pm2)$ seconds. A spin-lattice constant $T_1 = (1.4\pm0.1)$ seconds was then measured by inversion-recovery. These data confirm relaxation is caused predominantly by the dipole-dipole coupling in the glycyl proton pair.

The paramagnetic relaxation influence was determined for a small selection of transition metal ions, Cu^{II} (electron spin = 1/2), Mn^{II} (spin 5/2), the lanthanide ion Gd^{III} (spin 7/2) and the organic radical TEMPO (= 2,2,6,6-tetramethyl piperidine N-oxide, electron spin 1/2). A stock solution for each of these agents was prepared by dissolving each species, or its corresponding chloride salt, in D_2O to a suitable concentration.

Proton lifetimes T_S and T_1 were measured versus each paramagnetic substance over a concentration range 0 to 0.4 mM by adding aliquots of the paramagnetic stock to the starting AG solution (= 40 mM AG in 500 μL degassed D_2O). In all experiments the signal was fitted successfully by monoexponential relaxation curves. No noticeable line broadening or paramagnetic shifts were observed.

As shown by Fig. 3.7, the rate constants $1/T_S$ and $1/T_1$ were observed to increase linearly with paramagnet concentration $[X]$ according to the law

$$\frac{1}{T_i([X])} = k_i[X] + \frac{1}{T_i(0)} \tag{3.71}$$

where the coefficient of proportionality is called the 'relaxivity'.[14] The relaxivities k_1 and k_S, for the longitudinal and singlet relaxation, were fitted from the slopes of the $1/T_1$ and T_S data and are tabulated in table 3.4.

The table shows the T_1 relaxivity occupies a wide range of values and it can be seen that k_1 increases approximately in proportion to the square of the electron magnetic moment

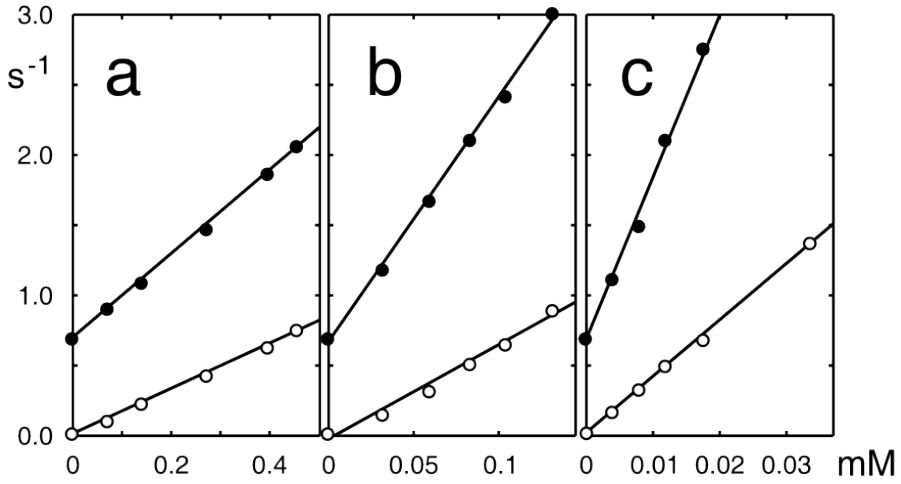

Figure 3.7: Longitudinal ($\bullet\, T_1^{-1}$) and singlet ($\circ\, T_S^{-1}$) relaxation rate constants in D_2O for the glycine protons in AG as a function of metal ion concentration as measured for paramagnetic species: (a) $Cu^{II}Cl_2$; (b) $Mn^{II}Cl_2$; (c) $Gd^{III}Cl_3$. Time constants at zero concentration are $T_S(0) = 32$ seconds and $T_1(0) = 1.4$ seconds. Relaxivities are equal to the respective slopes of each line.

X	k_1 ($mM^{-1}s^{-1}$)	k_S ($mM^{-1}s^{-1}$)	k_S/k_1
$Cu^{2+}_{(aq)}$	3.0 ± 0.1	1.6 ± 0.08	0.51 ± 0.04
$Mn^{2+}_{(aq)}$	17.4 ± 1.0	6.7 ± 0.3	0.38 ± 0.02
$Gd^{3+}_{(aq)}$	115 ± 5	40 ± 2	0.35 ± 0.02
TEMPO	2.0 ± 0.1	0.6 ± 0.05	0.28 ± 0.02

Table 3.4: Experimental singlet and longitudinal relaxivities for the methylene protons in AG (9.4 T, D_2O, 293 K), and the ratio between.

for each species. This pattern agrees with the relaxation mechanism involving the proton-paramagnet hyperfine coupling.[2, 141] The singlet relaxivities k_S also follow this trend, but are typically a factor of 2 to 3 smaller. This states the nuclear singlet order is much less susceptible to paramagnet-induced relaxation than ordinary nuclear magnetisation.

The singlet relaxivities k_S for metal ions are more than 10^5 times those for the analogous ortho-para conversion in dihydrogen,[140] and ortho-para conversion in endohedral-hydrogen fullerenes.[142, 144] This probably arises because the interaction between AG and the metal ions can involve partial coordination with the carboxyl groups of the peptide, which results in a much stronger relaxation on AG through a much longer correlation time compared to H_2. Spin isomer interconversion in H_2 is slow due to the very large ortho-para energy splitting, which is the order 120 cm^{-1} (= 3500 GHz), or twice the rotational constant of the diatomic.[54] Ortho-para relaxation requires fluctuations at this frequency while fluctuation at the much slower Larmor frequency (400 MHz) is required by AG.

Oxygen

Oxygen gas was bubbled from a cylinder through an initially degassed solution of AG, again 40 mM in 500 μL D_2O, and the relaxation constants measured at 9.4 T. Additions of O_2 were made until no changes were observed in T_1 and T_S. At this point the solution was assumed to be saturated with O_2.

It was not possible to measure the levels of dissolved oxygen explicitly in this setup, and values for k_S and k_1 were not obtained. However, the data still allow one to calculate the concentration-independent ratio $k_S/k_1 = 0.55 \pm 0.03$ by plotting the slope of $1/T_1$ against $1/T_S$. From eq. (3.71):

$$\Big(\frac{1}{T_S([X])} - \frac{1}{T_S(0)}\Big)/\Big(\frac{1}{T_1([X])} - \frac{1}{T_1(0)}\Big) \;=\; \frac{k_S}{k_1}. \tag{3.72}$$

This experimental ratio shows the singlet relaxation is also about two-times less sensitive to dissolved O_2 than ordinary magnetisation.

Note, while it was not possible to determine explicit relaxivities, an estimate is possible from the relaxation constants at saturation using eq. (3.71). The shortest singlet relaxation constant recorded was $T_S = 1.4$ seconds, which on assuming a saturation of 40 mg/L (1.2 mM) O_2 in D_2O at 293 K[146] gives a value of $k_S = O(1)$ $mM^{-1}s^{-1}$. This is a similar

order of magnitude to the relaxivity of dissolved TEMPO radicals.

Interpretation

The ratio k_S/k_1 can be loosely interpreted within a random-field relaxation model.[82, 2] This ignores the physical detail of the intermolecular nucleus-electron interaction and assumes the dissolved paramagnetic species induce randomly fluctuating magnetic fields at each of the glycyl protons. The relaxation-causing Hamiltonian is thus assumed to be

$$H^{\mathrm{ERF}}(t) = \sum_{j=1}^{2} \gamma_{\mathrm{H}} \boldsymbol{B}_j^{\mathrm{ERF}}(t) \cdot \boldsymbol{I}_j \tag{3.73}$$

$$= \gamma_{\mathrm{H}} \sum_{j=1}^{2} \left(B_{jx}^{\mathrm{ERF}}(t) I_{jx} + B_{jy}^{\mathrm{ERF}}(t) I_{jy} + B_{jz}^{\mathrm{ERF}}(t) I_{jz} \right) \tag{3.74}$$

where $\boldsymbol{B}_j^{\mathrm{ERF}}(t)$, $\boldsymbol{B}_k^{\mathrm{ERF}}(t)$ are the random time-fluctuating fields at the proton sites 'j' and 'k' and can be thought to be proportional in magnitude to the concentration of the dissolved paramagnet; ERF stands for 'external random field'. This Hamiltonian corresponds to a scalar product between rank-1 spherical tensors

$$\text{eq. (3.74)} = \sum_{j=1}^{2} \sum_{m,m'=-1}^{1} (-)^m [A_{1m'}^{\mathrm{ERF},j}]^M(t) D_{m'm}^1(\Omega^{(M\to L)}(t)) [T_{1-m}^{\mathrm{ERF},j}]^L \tag{3.75}$$

whose space-field components are defined [82]

$$[A_{1\pm1}^{\mathrm{ERF},j}]^M(t) = \mp\gamma_{\mathrm{H}} (B_{jx}^{\mathrm{ERF}}(t) \pm B_{jy}^{\mathrm{ERF}}(t))/\sqrt{2} \tag{3.76}$$

$$[A_{10}^{\mathrm{ERF},j}]^M(t) = \gamma_{\mathrm{H}} B_{jz}^{\mathrm{ERF}}(t) \tag{3.77}$$

and the spin components are

$$[T_{1\pm1}^{\mathrm{ERF},j}]^L = \mp(I_{jx} \pm I_{jy})/\sqrt{2} \tag{3.78}$$

$$[T_{10}^{\mathrm{ERF},j}]^L = I_{jz}. \tag{3.79}$$

To obtain the ERF relaxation superoperator the above Hamiltonian is plugged through the Redfield theory. In the ensemble average step, one assumes that the ERF amplitude, which is most likely due to the intermolecular motion, can be separately averaged from the

molecular motion, such that

$$\overline{[A^{\mathrm{ERF},j}_{1m'}]^M(t)[A^{\mathrm{ERF},j}_{1\mu'}]^M(t+\tau)D^1_{m'm}(\Omega^{(M\to L)}(t))D^1_{\mu'\mu}(\Omega^{(M\to L)}(t+\tau))} \equiv \frac{1}{3}\delta_{m-\mu}\delta_{m'-\mu'}G(\tau)\overline{[A^{\mathrm{ERF},j}_{1\mu'}]^M(t)[A^{\mathrm{ERF},j}_{1m'}]^M(t+\tau)}. \quad (3.80)$$

The above may simplify on assuming the fields at sites 'j' and 'k' are orientationally isotropic with root-mean-square (rms) amplitude given by $\overline{(B^{\mathrm{ERF}}_{jx})^2} = \overline{(B^{\mathrm{ERF}}_{jy})^2} = \overline{(B^{\mathrm{ERF}}_{jz})^2} = B^{\mathrm{ERF}}_{j,\mathrm{rms}}$, and defining a correlation parameter $C_{jk} = \overline{\boldsymbol{B}^{\mathrm{ERF}}_j \boldsymbol{B}^{\mathrm{ERF}}_k}/(B^{\mathrm{ERF}}_{j,\mathrm{rms}}B^{\mathrm{ERF}}_{k,\mathrm{rms}})$:

$$\text{eq. (3.80)} = \delta_{m-\mu}G(\tau)B^{\mathrm{ERF}}_{j,\mathrm{rms}}B^{\mathrm{ERF}}_{k,\mathrm{rms}}C_{jk}. \quad (3.81)$$

A value of $C_{jk} = 0$ on the two sites indicates that the fields $\boldsymbol{B}^{\mathrm{ERF}}_j$ $\boldsymbol{B}^{\mathrm{ERF}}_k$ are completely uncorrelated at each molecule, whilst $C_{jk} = \pm 1$ indicates that the two fields are always parallel, or antiparallel to one another respectively.

After making all of these assumptions the relaxation superoperator is given by

$$\hat{\Gamma}^{\mathrm{ERF}} = -\gamma^2_{\mathrm{H}}\sum_{j,k}B^{\mathrm{ERF}}_{j,\mathrm{rms}}B^{\mathrm{ERF}}_{k,\mathrm{rms}}C_{jk}\sum_{m=-1}^{1}(-)^m j(m\omega^0)[T^{\mathrm{ERF},j}_{1m}]^L[T^{\mathrm{ERF},k}_{1-m}]^L. \quad (3.82)$$

The diagonal matrix elements for I_z and T_{00} give a first-order approximation to the relaxivities k_1 and k_S, respectively. These give the equations

$$k_S \propto 1/T^{\mathrm{ERF}}_S = (T_{00}|\hat{\Gamma}^{\mathrm{ERF}}|T_{00}) = 2\gamma^2_{\mathrm{H}}\big((B^{\mathrm{ERF}}_{j,\mathrm{rms}})^2 + (B^{\mathrm{ERF}}_{k,\mathrm{rms}})^2 - 2C_{jk}B^{\mathrm{ERF}}_{j,\mathrm{rms}}B^{\mathrm{ERF}}_{k,\mathrm{rms}}\big)(j(0) + 2j(\omega^0)) \quad (3.83)$$

$$k_1 \propto 1/T^{\mathrm{ERF}}_1 = (I_z|\hat{\Gamma}^{\mathrm{ERF}}|I_z) = \gamma^2_{\mathrm{H}}((B^{\mathrm{ERF}}_{k,\mathrm{rms}})^2 + (B^{\mathrm{ERF}}_{k,\mathrm{rms}})^2)j(\omega^0). \quad (3.84)$$

One may see that in the extreme narrowing approximation $j(\omega^0) = j(0) = \tau_c$ of this model the ratio k_S/k_1 depends only upon the field correlation, C_{jk}. If the fields are completely uncorrelated ($C_{jk} = 0$), then $k_S = 2k_1$, meaning that the paramagnet accelerates relaxation of singlet order (coupled spin order) twice as strongly as the longitudinal magnetisation (single-spin order). At the opposite extreme $C_{jk} = +1$, the relaxivity ratio k_S/k_1 tends to zero. This outcome arises since the ERF Hamiltonian is always symmetric under

permutation, meaning singlet-triplet transitions are forbidden. The findings $k_S \ll k_1$ in table 3.4 thus confer a strong correlation in the induced fields. Consistent values of C_{jk} are ≈ 0.8 to 0.9 for the ratio $k_S/k_1 \approx 0.3$ to 0.5, under the assumption of extreme narrowing.

Similar random-field correlation parameters have been obtained by Wokaun and Ernst [147] for paramagnetic relaxation by comparing zero-quantum, single-quantum and double-quantum linewidths of a proton pair. Their observations, similar to the experimental data presented here, have suggested that a lower correlation parameter C_{jk} indicates a closer mean-approach distance of the paramagnet to the nuclear spins. In table 3.4, for example, the value of k_S/k_1 is lower for molecular oxygen in solution than for TEMPO, which is consistent the relatively small molecular radius of oxygen. The mean approach distance, however, also depends on how strongly the dissolved paramagnet binds or associates with AG, which may well be significant in the case of the solvated transition metal ions. With a sufficiently elaborate relaxation analysis, one may eventually be able to quantify the proton-paramagnet distances, if desired.[14]

Counteraction of paramagnetic relaxation

Relaxation induced by paramagnetic metal ions may be suppressed by addition of suitable chelating agents to the solution. As shown in fig. 3.8a, the singlet lifetime of AG in the presence of 0.1 mM $MnCl_2$ is $T_S = (1.5 \pm 0.1)$ seconds. This improves to $T_S = (37 \pm 2)$ seconds on adding a tenfold molar excess (=1 mM) of ethylenediamine tetra-acetic acid (EDTA). A similar effect is observed for Cu^{II} ions.

Suppression of the paramagnetic relaxation in this way supports a hypothesis that the relaxation mechanism involves transient complexation between the ions and AG. A cartoon representation is shown in fig. 3.9(a). On addition of EDTA, the metal ions remain physically present in solution but form strong hexadentate chelates with the complexing agent. This prevents their association with AG (fig. 3.9(b)), resulting in relaxation times that are comparable to those in a paramagnet-free solution.

Alternatively one may add a chemical agent that transforms the paramagnetic relaxing agent into a diamagnetic form. Fig. 3.8 also shows that ascorbate[145] in molar excess significantly reduces the relaxation effect of dissolved O_2. Ascorbate is well-known to reduce superoxide ($O_2^{\bullet -}$), hydroperoxide ($HOO^{\bullet}$) and $O_2^{\bullet\bullet}$ radicals in aqueous solution.[83, 145]

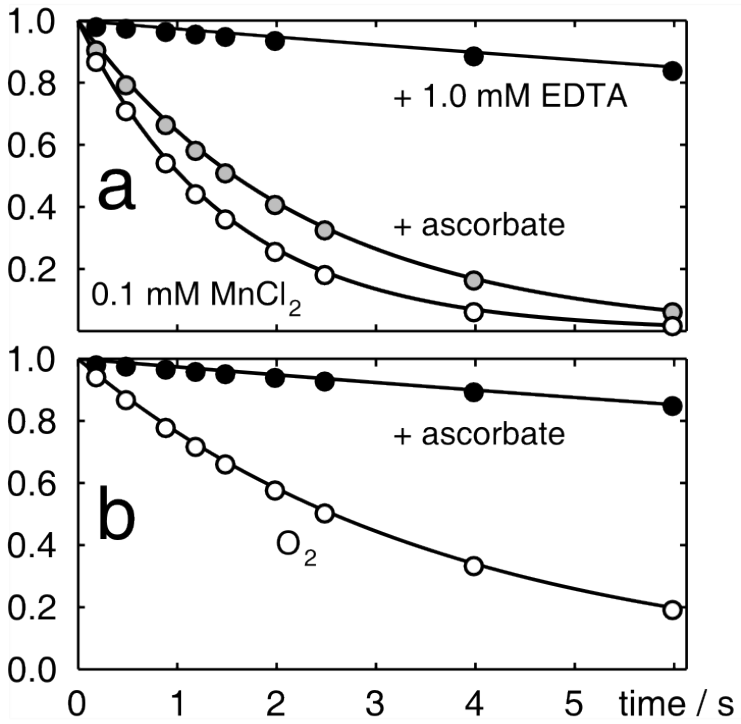

Figure 3.8: Quenching of paramagnetic relaxation agents. Curves show the nuclear singlet decay $\propto \exp(-\tau/T_S)$ at 9.4 T for solutions of 40 mM AG plus (a) 0.1 mM $MnCl_2$ only (open circles, $T_S = 1.5 \pm 0.1$ s), with sodium ascorbate (grey circles, $T_S = 2.3 \pm 0.1$ s), with 1 mM EDTA (black circles, $T_S = 37 \pm 2$ s); (b) dissolved oxygen (open circles, $T_S = 3.9 \pm 0.1$ s), then following addition of ascorbate[83, 145] (black circles, $T_S = 40 \pm 3$ s)

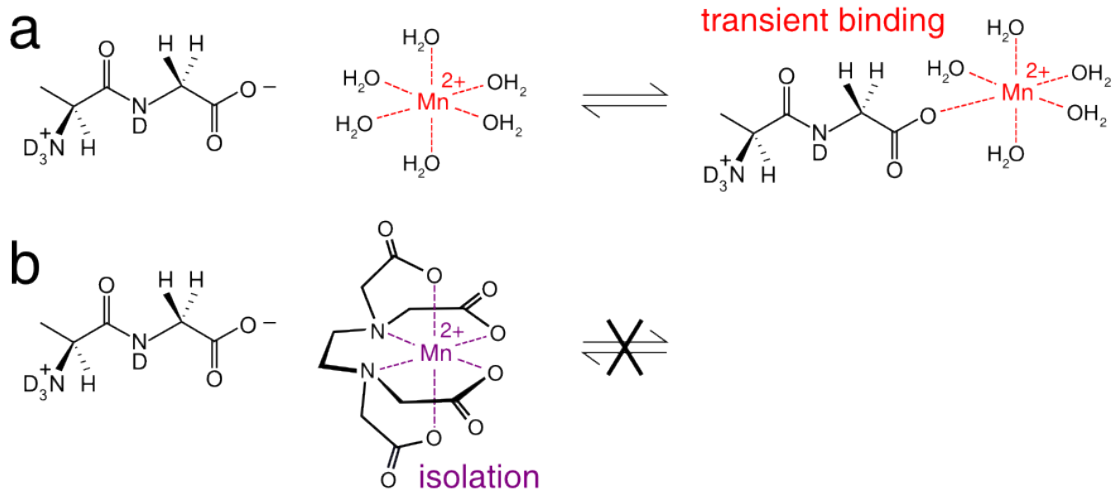

Figure 3.9: Suggested transient-binding interaction between AG and transition metal ions. Close approach of the two species in (a) results in strong relaxivities k_1 and k_S. On addition of EDTA, as shown in (b), the species no longer bind, resulting in much weaker relaxivity.

4 Perspectives

Magnetic resonance imaging (MRI) and spectroscopy (NMR) are unique tools in the study of chemical substances in that they provide an interactive form of 'molecular tagging'. Unlike radioactive labelling, or fluorescence methods, which may be regarded as scalar-like labels, magnetic resonance exploits the phenomenon of nuclear spin, which as a vector property can behave more like a memory. Magnetic resonance relies upon manipulation of *spin order*, which is the net alignment of nuclear spin across the bulk sample. Information may be encoded upon the spin order, then be read out by spectroscopy at a later time. For instance in MRI, information of the molecular position is encoded at one time point, then at a later time imaged, allowing rich information about molecular self-diffusion, flow, and other motion to be determined. Since magnetic resonance detects the chemical environment of nuclei, one may also follow the chemical changes occurring during reactions, such as metabolic outcomes *in vivo*.

This thesis seeks to deal with an Achilles heel of these techniques: the finite lifetime of spin order. Small fluctuations in the magnetic environment of the nuclei eventually cause decoherence of the spins, returning ordered states to thermal equilibrium. In a practical context the maximum storage time of spin order is time until which NMR readout falls below thermal noise of the system. To some extent, this may be lengthened by using very highly ordered (or 'hyperpolarised') initial states, such as provided by dynamic nuclear polarisation, or more sensitive hardware, but the intrinsic decay rate of spin order remains unchanged.

4.1 Summary of concepts

Long relaxation times are possible by exploiting nuclear singlet states between pairs of spin-1/2 nuclei.[16, 17] For isolated spins, the slowest decay process is the relaxation of longitudinal polarisation, (time constant T_1), namely the population asymmetry across the Zeeman states $|\alpha\rangle$ and $|\beta\rangle$. In systems containing two spin-1/2 nuclei, singlet spin order may outlast T_1. The singlet has the non-magnetic configuration $(|\alpha_j\beta_k\rangle - |\beta_j\alpha_k\rangle)\sqrt{2}$, where spins are polarised in opposite directions with respect to the quantisation axis. Singlet order is invariant under conditions that preserve magnetic equivalence of the pair and is therefore slow provided: (i) the nuclei inhabit magnetically similar environments; and (ii) the decay mechanisms involve strong correlation across the pair. This is true of most relaxation in solution, including for intramolecular-[19, 62, 82] and intermolecular- [79] dipole-dipole coupling, paramagnetic [111] and spin-rotation relaxation mechanisms.[20] Nuclei with low gyromagnetic ratio (*e.g.* ^{13}C and ^{15}N) are encouraging, where T_S may approach several tens of minutes, under favourable conditions.[22, 23]

4.2 Summary of outcomes

To set up a foundation for future applied work, the main goals of this work were to (i) consolidate and (ii) extend the NMR methodology and concepts for exploiting nuclear singlet states. The main outcomes are summarised as below:

Resume of chapter 2

- An in-depth study was made on singlet preparation and readout. Singlet order can be prepared on a spin-1/2 pair starting from a state of longitudinal polarisation provided the nuclei are magnetically inequivalent. The coherent evolution can be broken down into chains of transformations within the singlet-triplet Hilbert space. Spin-symmetry-breaking interactions usually induce transformations within two-dimensional (two-level quantum state) ket subspace, which can be visualised as rotations on a Bloch sphere.

- The most appropriate 'magnetisation-to-singlet'-converting pulse sequence for a given molecule depends whether the spin pair is strongly or weakly coupled (how close or

far from equivalence). However, all sequences excite singlet order with the same efficiency, and obtain the maximum singlet order accessible through unitary evolution.

- For all the sequences examined that excite singlet order from a thermally polarised sample, the final detectable signal is two-thirds the intensity of that obtainable from the initial magnetisation. This is the theoretical maximum ignoring all relaxation effects. The recovered magnetisation may be slightly higher in samples with unity-order polarisation, but requires some careful consideration about the direction of the subspace-specific rotations.

- Long-lived singlet order is accessible in the 'near-equivalence' regime, where symmetry-breaking interactions are weak compared to the intra-pair spin-spin coupling. This avoids use of spin-locking and the associated complications. Demonstrations have been made for weak asymmetric induction on an otherwise equivalent spin pair by a remote chiral centre,[88] and $^{18}O/^{16}O$ isotopic substitution.[102]

- Singlet NMR of chemically equivalent nuclear spin pairs is facilitated also by heteronuclear symmetry-breaking.

- Hyperpolarised singlet order is shown to be available immediately after dissolution DNP, avoiding altogether the need for pulse sequence preparations. While this 'brute-force' method generates a relatively small singlet polarisation scaling as $p_S = -p^2/3$, it may save against the resources, time and delicate control involved in hardware and pulse sequences for magnetisation-singlet conversion.[32]

- Singlet-triplet rotations may be induced by weak, transition-selective rf field pulses. This method, however is inferior to the synchronised spin echo method, as its performance is extremely sensitive to homogeneity of the static B^0 field.

- Singlet order of an ensemble of two spin-1/2 nuclei behaves as the unique rotation-invariant (rank-zero) operator, which allows one to obtain NMR spectra containing only singlet-derived signals.

Resume of chapter 3

- Relaxation in solution NMR proceeds by rotational modulation of anisotropic spin interactions, for example dipole-dipole couplings. Spherical tensor operators trans-

form as irreducible representations of the rotation group SO(3) and are therefore a natural language of the density operator when analysing relaxation.

- In the extreme-narrowing regime, most relaxation mechanisms behave as scalar superoperators and cannot induce cross relaxation between tensor operators of different ranks, *i.e.* cannot change the total angular momentum of spin order. This allows numerous shortcuts to be taken in Redfield's formalism and leads to concise analytical formulae for both singlet and longitudinal relaxation rates.

- An experimental study is made for dipolar-dipole relaxation influence on singlet relaxation in systems of three and four nuclei. Relaxation rate contributions from a given nucleus in a molecule are obtainable, within reasonable approximation, by rate difference with a spin-zero isotopologue. Singlet relaxation rates depends strongly on the relative geometry between the spin pair and other magnetic particles, in general decreasing with the inverse eighth power with distance from the centre of the spin pair.

  Redfield theory says the ratio T_S/T_1 for protons in the extreme-narrowing limit is purely a function of geometry between the spins. For rigid molecules, the measured value of T_S/T_1 therefore allows a basic form of conformational analysis. The ratio T_S/T_1 in general provides structural restraints that are complementary to other structure determination methods in solution NMR, including vicinal J-couplings and the nOe. Singlet relaxation may also be less-susceptible to spin diffusion than the nOe.

- Experimental relaxation rates $1/T_1$ and $1/T_S$ are found to be proportional to the concentration of paramagnetic transition metal ion or radical dopants in solution, but the slope with respect to concentration, or 'relaxivity', is lower for the singlet. This means that singlet order is less-sensitive to paramagnetic relaxation than the T_1 of the pair. In general, the ratio depends on the nature of the interaction between the paramagnetic species and the nuclear spin pair. Singlet relaxivity of the methylene protons in Ala-Gly in a solution containing dissolved transition metal ions is found to be two to three lower than the T_1 relaxivity.

- The effect of accelerated relaxation due to paramagnetic metal ions by can be re-

moved by addition of EDTA or similar multi-dentate complexing agents. In the case of radicals the same outcome is achieved by adding a mild reducing agent, such as ascorbate.[111] The magnetism of transition metal ions may also be altered by suitable reducing or oxidising agents, where the number of unpaired electrons depends on oxidation state.

4.3 An outlook for singlet NMR

The most interesting area for future study is singlet relaxometry. While in this thesis the singlet lifetimes have been analysed for several mechanisms, many variables remain unexplored.

Perhaps the most obvious is the B^0 field dependence. Spin relaxation via the chemical shielding anisotropy mechanism (CSA) increases in importance at higher B^0 field as CSA-CSA auto-correlation terms scale quadratically in γB^0. Cross-correlated CSA-dipole relaxation scales linearly with γB^0. Both mechanisms are significant for essentially all spin-1/2 isotopes except protons, which have large shielding anisotropies (*e.g.* ^{13}C, ^{31}P; CSA of order 10 to 200 ppm). A separate issue at high B^0 fields is the exit from extreme-narrowing, where molecular tumbling appears slow on the Larmor frequency timescale and may not sample the spectral density uniformly for all coherence orders. In the Redfield treatment, nonuniform spectral density adds complication in the form of cross-relaxation between spin ranks, so that concise rate formulae may not be obtainable analytically. In general, both $1/T_S$ and $1/T_1$ rates are expected to decrease outside extreme narrowing, increasing lifetimes as a result. The overall ratio T_S/T_1, however is likely to fall, since singlet relaxation may be mediated through transitions at the zero-quantum frequency (spectral density $j(0) = \tau_c$ is always finite), while longitudinal relaxation is not.

There is also a lot to care about besides fluctuating interactions on the molecular rotation timescale. At low enough B^0 field the Larmor frequency may fall within frequency of slow motions that include intermolecular processes, for instance chemical exchange, which may be explored through pH, temperature and solvent-dependence studies. In non-rigid molecules there may be conformational exchange and fluxionality such as ring flips, inversion and other functional group jumps. These may cause sizeable relaxation and result in problems for storing singlet order in low or zero magnetic field, or transporting through

low-field regions.

A better knowledge of singlet relaxation through such studies may help one design molecules with the longest possible lifetimes, by minimising relaxation sources under a given set of conditions. This may help assess potential for singlet NMR applications in vivo, for instance in tracking the progress of metabolites across longer timescales, or as a tool in transporting exogenous hyperpolarised substances through the body to a site of interest, whereupon MRI is performed.

In contrast one may ask which systems exhibit strong singlet relaxation, and may be used to yield useful information. For instance, is paramagnetic singlet relaxation a viable tool for molecular geometry and dynamics determination in metallo-proteins, or a tool for measuring that oxidation state of a dissolved complex?

References

[1] K. Pearson, "The problem of the random walk", *Nature*, vol. 72, pp. 294, 1905.

[2] A. Abragam, *Principles of nuclear magnetism*, Clarendon Press, Oxford, England, 1961.

[3] R. R. Ernst, G. Bodenhausen, and A. Wokaun, *Principles of nuclear nagnetic nesonance in one and two dimensions*, Clarendon Press, Oxford, England, 1987.

[4] M. H. Levitt, *Spin dynamics: basics of nuclear magnetic resonance*, John Wiley and Sons, Chichester, England, 2001.

[5] R. Freeman, *A handbook of nuclear magnetic resonance*, Longman Scientific, 1988.

[6] M. Goldman, *Quantum description of high-resolution NMR in liquids*, Clarendon Press, Oxford, England, 1988.

[7] R. A. de Graaf, *In vivo NMR spectroscopy. Principles and techniques*, John Wiley and Sons, 2 edition, 2007.

[8] D. P. DiVincenzo, "Quantum computation", *Science*, vol. 270, pp. 225–261, 1995.

[9] R. Taylor, J. P. Hare, A. K. Abdul-Sada, and H. W. Kroto, "Isolation, separation and characterisation of the fullerenes C_{60} and C_{70}: The third form of carbon", *J. Chem. Soc. Chem. Commum.*, pp. 1423–1425, 1990.

[10] H. W. Kroto, "Symmetry, space, stars and C_{60}", Nobel lecture, 1996.

[11] R. R. Ernst, "Nuclear magnetic resonance Fourier-transform spectroscopy", Nobel lecture, 1991.

[12] K. Wüthrich, "NMR studies of structure and function of biological macromolecules", Nobel lecture, 2002.

[13] P. Mansfield, "Snap-shot MRI", Nobel lecture, 2003.

[14] J. Kowalewski and L. Mäler, *Nuclear spin relaxation in liquids*, Taylor and Francis, 2006, Chap. 15.

[15] E. Hahn, "Spin echoes", *Phys Rev.*, vol. 80, pp. 580–594, 1950.

[16] M. H. Levitt, *Singlet and other states with extended lifetimes*, in Encyclopedia of Magnetic Resonance, volume 9, John Wiley & Sons, Ltd, 2010.

[17] M. H. Levitt, "Singlet nuclear magnetic resonance", *Annu. Rev. Phys. Chem*, vol. 63, pp. 89–105, 2012.

[18] M. Carravetta and M. H. Levitt, "Long-lived nuclear spin states in high-field solution NMR", *J. Am. Chem. Soc.*, vol. 126, no. 20, pp. 6228–6229, 2004.

[19] M. Carravetta, O. G. Johannessen, and M. H. Levitt, "Beyond the t_1 limit: singlet nuclear spin states in low magnetic fields", *Phys. Rev. Lett.*, vol. 92, no. 15, pp. 153003, 2004.

[20] G. Pileio, "Relaxation theory of nuclear singlet states in two spin-1/2 systems", *Prog. Nucl. Magn. Reson. Spectrosc.*, vol. 56, pp. 217–231, 2010.

[21] R. Sarkar, P. Ahuja, P. R. Vasos, A. Bornet, O Wagnieres, and G. Bodenhausen, "Long-lived coherences for line-narrowing in high-field NMR", *Prog. Nucl. Magn. Reson. Spectrosc.*, vol. 59, pp. 83–90, 2011.

[22] G. Pileio, M. Carravetta, E. Hughes, and M. H. Levitt, "The long-lived nuclear singlet state of ^{15}N-nitrous oxide in solution", *J. Am. Chem. Soc.*, vol. 130, no. 38, pp. 12582–12583, 2008.

[23] R. K. Ghosh, S. J. Kadlecek, J. H. Ardenkjær-Larsen, B. M. Pullinger, G. Pileio, M. H. Levitt, N. N. Kuzma, and R. R. Rizi, "Measurements of the persistent singlet state of $^{15}N_2O$ in blood and other solvents: potential as a magnetic tracer", *Magn. Reson. in Med.*, vol. 66, pp. 1177–1180, 2011.

[24] R. Sarkar, P. R. Vasos, and G. Bodenhausen, "Singlet-state exchange NMR spectroscopy for the study of very slow dynamic processes", *J. Am. Chem. Soc.*, vol. 129, no. 2, pp. 328–334, 2007.

[25] R. Sarkar, *Long-lived states in high-field NMR spectroscopy for the study of very slow dynamic processes in solution state*, PhD thesis, Ecole Polytechnique Fédérale de Lausanne, August 2009.

[26] P. Ahuja, *Applications of long-lived spin states to high-resolution NMR studies of biomolecules*, PhD thesis, Ecole Polytechnique Fédérale de Lausanne, November 2010.

[27] A. Bornet, P. Ahuja, R. Sarkar, L. Fernandes, S. Hadji, S. Y. Lee, A. Haririnia, D. Fushman, G. Bodenhausen, and P. R. Vasos, "Long-lived states to monitor protein unfolding by proton NMR", *ChemPhysChem*, vol. 12, no. 15, pp. 2729–2734, 2011.

[28] S. Cavadini, J. Dittmer, S. Antonijevic, and G. Bodenhausen, "Slow diffusion by singlet state NMR spectroscopy", *J. Am. Chem. Soc.*, vol. 127, no. 45, pp. 15744–15748, 2005.

[29] S. Cavadini and P. R. Vasos, "Singlet states open the way to longer time-scales in the measurement of diffusion by NMR spectroscopy", *Conc. Magn. Reson. A*, vol. 32A, no. 1, pp. 68–78, 2008.

[30] P. R. Vasos, A. Comment, R. Sarkar, P. Ahuja, S. Jannin, J. P. Ansermet, J. A. Konter, P. Hautle, B. van den Brandt, and G. Bodenhausen, "Long-lived states to sustain hyperpolarized magnetization", *Proc. Natl. Acad. Sci. USA*, vol. 106, no. 44, pp. 18469–18473, 2009.

[31] W. S. Warren, E. Jenista, R. T. Branca, and X. Chen, "Increasing hyperpolarized spin lifetimes through true singlet eigenstates", *Science*, vol. 323, no. 5922, pp. 1711–1714, 2009.

[32] M. C. D. Tayler, I. Marco-Rius, M. I. Kettunen, K. M. Brindle, M. H. Levitt, and G. Pileio, "Direct nuclear singlet hyperpolarisation via dynamic nuclear polarisation", *J. Am. Chem. Soc.*, vol. 134, pp. 7668–7671, 2012.

[33] M. E. Rose, *Elementary theory of angular momentum*, John Wiley and Sons, New York, 1957.

[34] C. Cohen-Tannoudji, B. Diu, and F. Laloë, *Quantum mechanics*, Wiley-Interscience -Hermann, Paris, 1977.

[35] R. Shankar, *Principles of quantum mechanics*, Plenum Press, New York, 2 edition, 1994.

[36] U. Fano, "Description of states in quantum mechanics by density matrix and operator techniques", *Rev. Mod. Phys.*, vol. 29, no. 1, pp. 74–93, 1957.

[37] J. Jeener, "Superoperators in magnetic resonance", *Adv. Magn. Reson.*, vol. 10, pp. 1–51, 1982.

[38] A. D. Bain, "The superspin formalism for pulse NMR", *Prog. Nucl. Magn. Reson. Spectrosc.*, vol. 20, pp. 295–315, 1988.

[39] I. Kuprov, N. Wagner-Rundell, and P.J. Hore, "Polynomially scaling spin dynamics simulation algorithm based on adaptive state-space restriction", *J. Magn. Reson.*, vol. 189, no. 2, pp. 241–250, 2007.

[40] M. Krzystyniak, L. J. Edwards, and I. Kuprov, "Destination state screening of active spaces in spin dynamics simulations", *J. Magn. Reson.*, vol. 210, no. 2, pp. 228 – 232, 2011.

[41] A. G. Redfield, "The theory of relaxation processes", *Adv. Magn. Reson.*, vol. 1, pp. 1–132, 1965.

[42] S. Szymanski, A. M. Gryff-Keller, and G. Binsch, "A Liouville space formulation of Wangsness-Bloch-Redfield theory of nuclear spin relaxation suitable for machine computation. I. fundamental aspects", *J. Magn. Reson.*, vol. 68, no. 3, pp. 399 – 432, 1986.

[43] P. A. M. Dirac, "The quantum theory of the emission and absorption of radiation", *Proc. R. Soc. Lond. A*, vol. 114, no. 767, pp. 243–265, 1927.

[44] O. W. Sørensen, G. W. Eich, M. H. Levitt, G. Bodenhausen, and R. R. Ernst, "Product operator formalism for the description of nmr pulse experiments", *Prog. Nucl. Magn. Reson. Spectrosc.*, vol. 16, pp. 163–192, 1983.

[45] H. Kovacs, D. Moskau, and M. Spraul, "Cryogenically cooled probes – a leap in NMR technology", *Prog. Nucl. Magn. Reson. Spectrosc.*, vol. 46, pp. 131–155, 2005.

[46] R. G. Griffin and T. F. Prisner, "High field dynamic nuclear polarization-the renaissance", *Phys. Chem. Chem. Phys.*, vol. 12, pp. 5737–5740, 2010.

[47] J. H. Ardenkjær-Larsen, B. Fridlund, A. Gram, G. Hansson, L. Hansson, M. H. Lerche, R. Servin, M. Thaning, and K. Golman, "Increase in signal-to-noise ratio of $>$ 10,000 times in liquid-state NMR", *Proc. Natl. Acad. Sci. USA*, vol. 100, no. 18, pp. 10158–10163, 2003.

[48] J. Wolber, F. Ellner, B. Fridlund, A. Gram, H. Jóhannesson, G. Hansson, L. H. Hansson, M. Lerche, S. Månsson, R. Servin, M. Thaning, K. Golman, and J. H. Ardenkjær-Larsen, "Generating highly polarized nuclear spins in solution using dynamic nuclear polarization", *NIMA*, vol. 36, pp. 173–181, 2004.

[49] M. D. Lingwood and S. Han, "Solution-state dynamic nuclear polarization", *Ann. Rep. NMR Spectrosc.*, vol. 73, pp. 83–126, 2011.

[50] W. Happer, "Optical pumping", *Rev. Mod. Phys.*, vol. 44, pp. 169–249, 1972.

[51] H. Middleton, R. D. Black, B. Saam, G. D. Cates, G. P. Cofer, R. Guenther, W. Happer, L. W. Hedlund, G. Alan Johnson, K. Juvan, and J. Swartz, "MR imaging with hyperpolarized ^{3}He gas", *Magn. Reson. in Med.*, vol. 33, no. 2, pp. 271–275, 1995.

[52] M. Salerno, T. A. Altes, J. P. Mugler, M. Nakatsu, H. Hatabu, and E. E. de Lange, "Hyperpolarized noble gas MR imaging of the lung: Potential clinical applications", *Europ. J. Radiol.*, vol. 40, no. 1, pp. 33–44, 2001.

[53] H. D. Roth, *Chemically induced dynamic nuclear polarisation*, vol. 2, in Encyclopedia of Magnetic Resonance, John Wiley & Sons, Ltd, 1996.

[54] A. Farkas, *Ortho-hydrogen, para-hydrogen and heavy hydrogen*, Cambridge University Press: Cambridge, U.K., 1935.

[55] C. R. Bowers and D. P. Weitekamp, "Parahydrogen and synthesis allow dramatically enhanced nuclear alignment", *J. Am. Chem. Soc.*, vol. 109, no. 18, pp. 5541–5542, 1987.

[56] M. G. Pravica and D. P. Weitekamp, "Net NMR alignment by adiabatic transport of parahydrogen addition products to high magnetic field", *Chem. Phys. Lett.*, vol. 145, pp. 255–258, 1988.

[57] C. R. Bowers, *Sensitivity enhancement using parahydrogen*, in Encyclopedia of Magnetic Resonance, John Wiley & Sons, Ltd, 2007.

[58] V. A. Norton, *Efficient generation of hyperpolarised molecules utilizing the scalar order of parahydrogen*, PhD thesis, California Insitute of Technology, May 2010.

[59] R. A. Green, R. W. Adams, S. B. Duckett, R. E. Mewis, D. C. Williamson, and G. G. R Green, "The theory and practice of hyperpolarization in magnetic resonance using parahydrogen", *Prog. Nucl. Magn. Reson. Spectrosc.*, p. in press, 2012.

[60] M. H. Levitt, "Composite pulses", *Prog. Nucl. Magn. Reson. Spectrosc.*, vol. 18, pp. 61–122, 1986.

[61] P. Ahuja, R. Sarkar, P. R. Vasos, and G. Bodenhausen, "Molecular properties determined from the relaxation of long-lived spin states", *J. Chem. Phys.*, vol. 127, no. 13, pp. 134112, 2007.

[62] M. C. D. Tayler, S. Marie, A. Ganesan, and M. H. Levitt, "Determination of molecular torsion angles using nuclear singlet relaxation", *J. Am. Chem. Soc.*, vol. 132, no. 24, pp. 8225–8227, 2010.

[63] L. Buljubasich, M. B. Franzoni, H. Spiess, and Münneman, "Level anti-crossings in parahydrogen-induced polarization experiments with c_s-symmetric molecules", *J. Magn. Reson.*, vol. 219, pp. 33–40, 2012.

[64] R. W. Adams, J. A. Aguilar, K. D. Atkinson, M. J. Cowley, P. I. P. Elliott, S. B. Duckett, G. G. R. Green, I. G. Khazal, J. López-Serrano, and D. C. Williamson,

"Reversible interactions with para-hydrogen enhance NMR sensitivity by polarization transfer", *Science*, vol. 323, no. 5922, pp. 1708–1711, 2009.

[65] G. Pileio and M. H. Levitt, "Theory of long-lived nuclear spin states in solution nuclear magnetic resonance. II. singlet spin locking", *J. Chem. Phys.*, vol. 130, no. 21, pp. 214510, 2009.

[66] P. Ahuja, R. Sarkar, P. R. Vasos, and G. Bodenhausen, "Diffusion coefficients of biomolecules using long-lived spin states", *J. Am. Chem. Soc.*, vol. 131, no. 22, pp. 7498–7499, 2009.

[67] N. N. Yadav, A. M. Torres, and W. S. Price, "NMR q-space imaging of macroscopic pores using singlet spin states", *J. Magn. Reson.*, vol. 204, pp. 346–348, 2010.

[68] G. Pileio, M. Carravetta, and M. H. Levitt, "Extremely low-frequency spectroscopy in low-field nuclear magnetic resonance", *Phys. Rev. Lett.*, vol. 103, no. 8, pp. 083002, 2009.

[69] G. Pileio, M. Carravetta, and M. H. Levitt, "Storage of nuclear magnetization as long-lived singlet order in low magnetic field", *Proc. Natl. Acad. Sci. USA*, vol. 107, no. 40, pp. 17135–17139, 2010.

[70] E. Vinogradov and A. K. Grant, "Long-lived states in solution NMR: selection rules for intramolecular dipolar relaxation in low magnetic fields", *J. Magn. Reson.*, vol. 194, pp. 46–57, 2008.

[71] E. Vinogradov and A. K. Grant, "Hyperpolarized long-lived states in solution NMR: three-spin case study in low field", *J. Magn. Reson.*, vol. 194, pp. 46–57, 2008.

[72] A. K. Grant and E. Vinogradov, "Long-lived states in solution NMR: theoretical examples in three- and four-spin systems", *J. Magn. Reson.*, vol. 193, pp. 177–190, 2008.

[73] A. A. Karabanov, C. Bretschneider, and W. Köckenberger, "Symmetries of the master equation and long-lived states in NMR", *J. Chem. Phys.*, vol. 131, pp. 204105, 2009.

[74] P. Ahuja, R. Sarkar, P. R. Vasos, and G. Bodenhausen, "Long-lived states in multiple-spin systems", *ChemPhysChem*, vol. 10, no. 13, pp. 2217–2220, 2009.

[75] H. Hogben, P. Hore, and I. Kuprov, "Multiple decoherence-free states in multi-spin systems", *J. Magn. Reson.*, vol. 211, pp. 217 – 220, 2011.

[76] G. Pileio, M. Concistre, M. Carravetta, and M. H. Levitt, "Long-lived nuclear spin states in the solution NMR of four-spin systems", *J. Magn. Reson.*, vol. 182, no. 2, pp. 353–357, 2006.

[77] G. Pileio and M. H. Levitt, "J-stabilization of singlet states in the solution NMR of multiple-spin systems", *J. Magn. Reson.*, vol. 187, no. 1, pp. 141–145, 2007.

[78] G. Pileio, "Singlet state relaxation via scalar coupling of the second kind", *J. Chem. Phys.*, vol. 135, no. 17, pp. 174502, 2011.

[79] G. Pileio, "Singlet relaxation via intermolecular dipolar coupling", *J. Chem. Phys.*, vol. 134, pp. 214505, 2011.

[80] K. Gopalakrishnan and G. Bodenhausen, "Lifetimes of the singlet states under coherent off-resonance irradiation in NMR spectroscopy", *J. Magn. Reson.*, vol. 182, pp. 254–259, 2006.

[81] R. Sarkar, P. Ahuja, D. Moskau, P. R. Vasos, and G. Bodenhausen, "Extending the scope of singlet-state spectroscopy", *ChemPhysChem*, vol. 8, no. 18, pp. 2652–2656, 2007.

[82] M. Carravetta and M. H. Levitt, "Theory of long-lived nuclear spin states in solution nuclear magnetic resonance. I. Singlet states in low magnetic field", *J. Chem. Phys.*, vol. 122, no. 21, pp. 214505, 2005.

[83] A. Bornet, R. Sarkar, and G. Bodenhausen, "Life-times of long-lived coherences under different motional regimes", *J. Magn. Reson.*, vol. 206, pp. 154–156, 2010.

[84] R. Sarkar, P. Ahuja, P. R. Vasos, and G. Bodenhausen, "Long-lived coherences for homogeneous line narrowing in spectroscopy", *Phys. Rev. Lett.*, vol. 104, no. 5, pp. 053001, 2010.

[85] A. Bornet, S. Jannin, J. A. Konter, P. Hautle, B. van den Brandt, and G. Bodenhausen, "Ultra high-resolution NMR: sustained induction decays of long-lived coherences", *J. Am. Chem. Soc.*, vol. 133, no. 39, pp. 15644–15649, 2011.

[86] T. F. Segawa, A. Bornet, N. Salvi, P. Miéville, V. Vitzthum, D. Carnevale, S. Jannin, M. A. Caporini, S. Ulzega, P. R. Vasos, M. Rey, and G. Bodenhausen, "Extending timescales and narrowing linewidths in NMR", *Chimia*, vol. 65, no. 9, pp. 652–655, 2011.

[87] R. Sarkar, P. Ahuja, P. R. Vasos, A. Bornet, O. Wagnières, and G. Bodenhausen, "Long-lived coherences for line-narrowing in high-field NMR", *Prog. Nucl. Magn. Reson. Spectrosc.*, vol. 59, pp. 83–90, 2010.

[88] M. C. D. Tayler and M. H. Levitt, "Singlet nuclear magnetic resonance of nearly equivalent spins", *Phys. Chem. Chem. Phys.*, vol. 13, pp. 5556–5560, 2011.

[89] D. Varshalovich, A. Moskalev, and V. Khersonskii, *Quantum theory of angular momentum*, World Scientific, Singapore, 1988.

[90] O. W. Sørensen, "A universal bound on spin dynamics", *J. Magn. Reson.*, vol. 86, pp. 435–440, 1990.

[91] M. H. Levitt, "Unitary evolution, Liouville space, and local spin thermodynamics", *J. Magn. Reson.*, vol. 99, pp. 1–17, 1992.

[92] S. J. Nelson, D. Vigneron, J. Kurhanewicz, A. Chen, R. Bok, and R. Hurd, "DNP-hyperpolarised ^{13}C magnetic resonance metabolic imaging for cancer applications", *Appl. Magn. Reson.*, vol. 34, pp. 533–544, 2008.

[93] S.J. Kohler, Y. Yen, J. Wolber, A.P. Chen, M.J. Albers, R. Bok, V. Zhang, J. Tropp, S. Nelson, D.B. Vigneron, J. Kurhanewicz, and R.E. Hurd, "In vivo ^{13}carbon metabolic imaging at 3 T with hyperpolarized ^{13}C-1-pyruvate", *Magn. Reson. Med.*, vol. 58, no. 1, pp. 65–69, 2007.

[94] K. Golman, R. In't Zandt, M. Lerche, R Pehrson, and J. H. Ardenkjær Larsen, "Metabolic imaging by hyperpolarised ^{13}C magnetic resonance imaging for in vivo tmnor diagnosis", *Cancer Res.*, vol. 66, pp. 10855–10860, 2006.

[95] A. P. Chen, R. E. Hurd, M. A. Schroeder, A. Z. Lau, Y.-p. Gu, W. W. Lam, J. Barry, J. Tropp, and C. H. Cunningham, "Simultaneous investigation of cardiac

pyruvate dehydrogenase flux, Krebs cycle metabolism and pH, using hyperpolarized [1,2-$^{13}C_2$]pyruvate in vivo", *NMR Biomed.*, pp. 305–311, 2012.

[96] S. E. Day, M. I. Kettunen, F. A. Gallagher, D.-E. Hu, M. Lerche, J. Wolber, J. H. Golman, K. Ardenkjær-Larsen, and K. M. Brindle, "Detecting tumor response to treatment using hyperpolarized ^{13}C magnetic resonance imaging and spectroscopy", *Nature Med.*, pp. 1382–1387, 2007.

[97] R. Sarkar, P. Ahuja, P. R. Vasos, and G. Bodenhausen, "Measurement of slow diffusion coefficients of molecules with arbitrary scalar couplings via long-lived spin states", *ChemPhysChem*, vol. 9, no. 16, pp. 2414–2419, 2008.

[98] M. J. Thrippleton and J. Keeler, "Elimination of zero-quantum interference in two-dimensional NMR spectra", *Angew. Chem. Int. Ed.*, vol. 42, pp. 3938–3941, 2003.

[99] M. J. Thrippleton, R. A. E. Edden, and J. Keeler, "Suppression of strong coupling artefacts in *J*-spectra", *J. Magn. Reson.*, vol. 174, pp. 97–109, 2005.

[100] U. Haeberlen, "High resolution NMR in solids: selective averaging", *Adv. Magn. Reson. suppl.*, 1976.

[101] M. H. Levitt, "Spindynamica", www.spindynamica.soton.ac.uk, June 2012, version 2.4 for Mathematica 8.0.

[102] M. C. D. Tayler and M. H. Levitt, "Long-lived nuclear spin order accessed via isotope-induced symmetry breaking", *Nature Chem.*, 2012, submitted.

[103] P. E. Hansen, "Isotope effects in nuclear shielding", *Prog. Nucl. Magn. Reson. Spectrosc.*, vol. 20, pp. 207–255, 1988.

[104] A. D. McNaught and A. A. Wilkinson., *IUPAC Compendium of Chemical Terminology*, Blackwell Scientific Publications, Oxford, 2 edition, 1997.

[105] J. M. Risley and R. L. van Etten, "^{18}O-isotope effect in ^{13}C nuclear magnetic resonance spectroscopy. 2. The effect of structure.", *J. Am. Chem. Soc.*, vol. 102, no. 14, pp. 4609–4614, 1980.

[106] R. N. Moore, J. Diakur, T. T. Nakashima, S. L. McLaren, and J. C. Vederas, "Isotope shifts in ^{13}C-NMR spectra of ^{18}O-labelled acetals; multiple labelling effects at β-carbons", *J. Chem. Soc. Chem. Comm.*, vol. 155, pp. 501–502, 1980.

[107] C. A. Bunton, J. H. Carter, D. R. Llewellyn, C. O'Connor, A. L. Odell, and S. Y. Yih, "The reactivity of coordinated oxalate. Part 1. Oxygen-18 exchange studies on oxalic acid, the trisoxalatochromium(III) anion, and the trisoxalatocobalt(III) anion", *J. Chem. Soc.*, pp. 4615–4622, 1964.

[108] J. M. Risley, *Oxygen-18 in biological NMR*, in Encyclopedia of Magnetic Resonance, John Wiley & Sons, Ltd, 2007.

[109] J. D. van Beek, M. Carravetta, G. C. Antonioli, and M. H. Levitt, "Spherical tensor analysis of nuclear magnetic resonance signals", *J. Chem. Phys.*, vol. 122, pp. 244510, 2005.

[110] J. A. Aguilar, R. W. Adams, S. B. Duckett, G. G. R. Green, and R. Kandiah, "Selective detection of hyperpolarised NMR signals derived from para-hydrogen using the Only Para-hydrogen SpectroscopY (OPSY) approach", *J. Magn. Reson.*, vol. 208, pp. 49–57, 2011.

[111] M. C. D. Tayler and M. H. Levitt, "Paramagnetic relaxation of nuclear singlet states", *Phys. Chem. Chem. Phys.*, vol. 13, pp. 9128–9130, 2011.

[112] Y. S. Greenberg, "Application of superconducting quantum interference devices to nuclear magnetic resonance", *Rev. Mod. Phys.*, vol. 70, pp. 175–222, 1998.

[113] A. J. Shaka, "Composite pulses for ultra-broadband spin inversion", *Chem. Phys. Lett.*, vol. 120, no. 2, pp. 201–205, 1985.

[114] A. J. Shaka, Barker. P. B., and R. Freeman, "Experimental demonstration of wide-band spin inversion", *J. Magn. Reson.*, vol. 67, pp. 580–584, 1986.

[115] A. J. Shaka and A. Pines, "Symmetric phase-alternating composite pulses", *J. Magn. Reson.*, vol. 71, pp. 495–503, 1987.

[116] N. Chandrakumar and S. S. Velan, "Separation of longitudinal multispin order by frequency cycling", *J. Magn. Reson. A.*, vol. 104, pp. 363–365, 1993.

[117] H. Geen and R. Freeman, "Band-selective radiofrequency pulses", *J. Magn. Reson.*, vol. 93, no. 1, pp. 93–141, 1991.

[118] L. T. Kuhn, U. Bommerich, and J. Bargon, "Transfer of parahydrogen-induced hyperpolarization to ^{19}F", *J. Phys. Chem. A*, vol. 110, pp. 3521–3526, 2006.

[119] E. Y. Chekmenev, V. A. Norton, D. P. Weitekamp, and P. Bhattacharya, "Hyperpolarized ^{1}H NMR employing low-γ nucleus for spin polarization storage", *J. Am. Chem. Soc.*, vol. 131, no. 9, pp. 3164–3165, 2009.

[120] M. Haake, J. Natterer, and J. Bargon, "Efficient NMR pulse sequences to transfer the parahydrogen-induced polarization to hetero nuclei", *J. Am. Chem. Soc.*, vol. 118, no. 36, pp. 8688–8691, 1996.

[121] M. Goldman, H. Jóhannesson, O. Axelsson, and M. Karlsson, "Design and implementation of ^{13}C hyper polarization from para-hydrogen, for new MRI contrast agents", *C. R. Chimie*, vol. 9, pp. 57–363, 2006.

[122] M. Goldman, H. Jóhannesson, O. Axelsson, and M. Karlsson, "Hyperpolarization of ^{13}C through transfer from parahydrogen: A new contrast agent for MRI", *Magn. Reson. Imag.*, vol. 23, pp. 153–157, 2005.

[123] M. Goldman and H. Jóhannesson, "Conversion of a proton pair para order into ^{13}C polarization by rf irradiation, for use in MRI", *C. R. Physique*, vol. 6, pp. 575–581, 2005.

[124] E. Chekmenev, P. Bhattacharya, and B. D. Ross, "Development of hyperpolarized metabolic contrast agents using PASADENA", Cambridge Isotope Laboratories, application note 21.

[125] S. Kadlecek, K. Emami, M. Ishii, and R. Rizi, "Optimal transfer of spin-order between a singlet nuclear pair and a heteronucleus", *J. Magn. Reson.*, vol. 205, no. 1, pp. 9–13, 2010.

[126] T. Theis, P. Ganssle, G. Kervern, S. Knappe, J. Kitching, M. P. Ledbetter, D. Budker, and A. Pines, "Parahydrogen-enhanced zero-field nuclear magnetic resonance", *Nat. Phys.*, vol. 7, pp. 571–575, 2001.

[127] J. H. Keeler, *Phase cycling procedures in multi-pulse NMR spectroscopy of liquids*, in Multinuclear magnetic resonance in liquids and solids: chemical applications, Kluwer, Dordrecht, 1990.

[128] M. H. Levitt, P. K. Madhu, and C. E. Hughes, "Cogwheel phase cycling", *J. Magn. Reson.*, vol. 155, pp. 300–306, 2002.

[129] G. Pileio and M. H. Levitt, "Isotropic filtering using polyhedral phase cycles: Application to singlet state NMR", *J. Magn. Reson.*, vol. 191, no. 1, pp. 148–155, 2008.

[130] W. H. Press, S. A. Teukolsky, W. T. Vetterling, and B. P. Flannery, "Numerical recipes in C: The art of scientific computing. Second edition", 1992.

[131] M. Abramowitz and I. A. Stegun, *Handbook of Mathematical Functions with Formulas, Graphs, and Mathematical Tables*, Dover Publications, New York, 9 edition, 1964.

[132] C. Laustsen, G. Pileio, M. C. D. Tayler, L. J. Brown, R. C. D. Brown, M. H. Levitt, and J.-H. Ardenkjær Larsen, "Hyperpolarized singlet NMR on a small animal imaging scanner", *Magn. Reson. Med.*, 2012, accepted.

[133] S. Singha Roy and T. S. Mahesh, "Density matrix tomography of singlet states", *J. Magn. Reson.*, vol. 206, no. 1, pp. 127–133, 2010.

[134] S. Singha Roy and T. S. Mahesh, "Initialization of NMR quantum registers using long-lived states", *Phys. Rev. A.*, vol. 82, pp. 052302, 2010.

[135] A. R. Al-Karaghouli and T. F. Koetzle, "Neutron diffraction study of L-phenylalanine hydrochloride", *Acta Crystallogr.*, vol. E31, pp. 2461 – 2465, 1975.

[136] C. M. Gall, A. DiVerdi, J, and S. J. Opella, "Phenylalanine ring dynamics by solid-state deuterium NMR", *J. Am. Chem. Soc.*, vol. 103, pp. 5039–5034, 1981.

[137] A. Demarco, M. Llinás, and K. Wüthrich, "Analysis of the ^{1}H-NMR spectra of ferrichrome peptides. I. the non-amide protons", *Biopolymers*, vol. 17, no. 3, pp. 617–636, 1978.

[138] B. M. Goodson, "Nuclear magnetic resonance of laser-polarized noble gases in molecules, materials, and organisms", *J. Magn. Reson.*, vol. 155, pp. 157–216, 2002.

[139] K. F. Bonhoeffer and P. Z. Harteck, "Para and ortho hydrogen", *Z. Phys. Chem.*, vol. 84, pp. 113–141, 1929.

[140] L Farkas and H. Sachsse, "Homogeneous catalysis of the para- ortho-hydrogen conversion under the influence of paramagnetic molecules", *Z. f. Phys. Chem.*, vol. B23, pp. 1–18, 1933.

[141] P. W. Atkins and M. J. Clugston, "Ortho-para hydrogen conversion in paramagnetic solutions", *Mol. Phys.*, vol. 27, no. 6, pp. 1619–1631, 1974.

[142] E. Sartori, M. Ruzzi, R. G. Lawler, and N. J. Turro, "Nitroxide paramagnet-induced para-ortho conversion and nuclear spin relaxation of H_2 in organic solvents", *J. Am. Chem. Soc.*, vol. 130, no. 38, pp. 12752–12756, 2008.

[143] J. Y. C. Chen, A. A. Martí, N. J. Turro, N. Komatsu, Y. Murata, and R. G. Lawler, "put the title here", *J. Phys. Chem. B*, vol. 114, pp. 14689–14695, 2010.

[144] N. J. Turro, A. A. Martí, J. Y. C. Chen, S. Jockusch, R. G. Lawler, M. Ruzzi, E. Sartori, S. C. Chuang, K. Komatsu, and Y. Murata, "Demonstration of a chemical transformation inside a fullerene. the reversible conversion of the allotropes of H_2 at C_{60}", *J. Am. Chem. Soc.*, vol. 130, pp. 10506–10507, 2008.

[145] P. Miéville, P. Ahuja, R. Sarkar, S. Jannin, P. R. Vasos, S. Gerber-Lemaire, M. Mishkovsky, A. Comment, R. Gruetter, O. Ouari, P. Tordo, and G. Bodenhausen, "Scavenging free radicals to preserve enhancement and extend relaxation times in NMR using dynamic nuclear polarization", *Angew. Chem. Int. Ed.*, vol. 49, no. 35, pp. 6182–6185, 2010.

[146] P. Scharlin and R. Battino, "Solubility of 13 nonpolar gases in deuterium oxide at $15-45°C$ and 101.325 kPa. thermodynamics of transfer of nonpolar gases from H_2O to D_2O", *J. Solution Chem.*, vol. 21, pp. 67–91, 1992.

[147] A. Wokaun and R. R. Ernst, "The use of multiple quantum transitions for relaxation studies in coupled spin systems", *Mol. Phys*, vol. 36, pp. 317–341, 1978.